NASA Technical Memorandum 104813

Penetration Experiments in Aluminum 1100 Targets Using Soda-Lime Glass Projectiles

Friedrich Hörz
Mark J. Cintala
Ronald P. Bernhard
Frank Cardenas
William E. Davidson
Gerald Haynes
Thomas H. See
Jerry L. Winkler

June 1995

NASA Technical Memorandum 104813

Penetration Experiments in Aluminum 1100 Targets Using Soda-Lime Glass Projectiles

Friedrich Hörz and Mark J. Cintala
Lyndon B. Johnson Space Center
Houston, Texas

Ronald P. Bernhard, Frank Cardenas, William E. Davidson
Gerald Haynes, Thomas H. See, and Jerry L. Winkler
Lockheed Engineering and Sciences Company
Houston, Texas

June 1995

ABSTRACT

The cratering and penetration behavior of annealed aluminum 1100 targets, whose thickness was systematically varied from several centimeters to ultra-thin foils < 1 μm thick, were experimentally investigated using 3.2 mm diameter spherical soda-lime glass projectiles at velocities from 1-7 km/s. The objective was to establish quantitative, dimensional relationships between initial impact conditions (impact velocity [V], projectile diameter [D_p] and target thickness [T]) and the diameter of the resulting crater (D_c) or penetration hole (D_h). Such dimensional relationships and calibration experiments are needed to extract the diameters and fluxes of hypervelocity particles from space-exposed surfaces and to predict the performance of certain collisional shields. The purpose of this report is to document in detail, primarily via photographs, the experimental results and some dimensional analyses.

The cratering behavior of aluminum 1100 is fairly well predicted by previous works (*e.g.*, of Cour-Palais, 1987 or Watts *et al.*, 1993); crater diameter scales with $V^{0.58}$. However, crater depth (P) is modestly deeper ($P/D_c = 0.58$), for our silicate impactors, than the canonical value of $P/D_c = 0.5$ based on aluminum projectiles and aluminum 6061-T6 targets. Furthermore, the ballistic-limit thickness (T_{BL}) at 6 km/s was found to be $T_{BL} = 1.4P$, rather than the traditional $T_{BL} = 1.8P$ used by many. These differences attest to the great sensitivity of detailed crater geometry and penetration behavior on the physical properties of both the target and impactor.

The D_h systematically decreases, essentially as a continuum, with decreasing T. Penetration-hole dimensions for massive targets ($D_p/T < 1$) are close to that of a standard crater ($D_h \sim D_c$) at any given V; this relationship may be understood from considerations of shock-wave velocity and associated duration(s) of the shock-pulse in both the target and projectile, a concept that is used to extrapolate the laboratory findings to velocities as high as 20 km/s. An important boundary condition, where $D_h = D_p$, is typically reached at $D_p/T > 50$, regardless of V. The relationship of D_h and V over the range in T from $1 < D_p/T < 50$ is demonstrably complex; the experimental data form well defined curves of variable slopes in this D_p/T range, suggesting (highly) variable exponents of V over relatively narrow intervals in D_p/T. The empirical relationships found in this study may, nevertheless, be used to obtain unique solutions for D_p from the measurement of D_h and T on space-retrieved membranes (and the assumption of an impact velocity). This capability renders the interpretation of individual penetration holes totally akin to that of D_c in semi-infinite targets.

Each penetration experiment was equipped with a witness plate to monitor the nature of the debris plume emanating from the rear of the target. This plume consists of both projectile fragments and target debris. Projectile fragments typically occupy the central portions of this debris cloud, dispersing distinctly less than target debris. The relative proportions of projectile fragments and target debris systematically vary in response to D_p/T, because variable T and an associated D_h produce variable volumes of displaced target for a given projectile volume. Very thick targets only shed debris in the form of low-velocity, massive spall fragments. T must be less than P, for any given V, for impactor material to reach the witness plate, either as fine-grained, unmelted fragments (at V < 3 km/s), or in the form of melts at higher velocities. However, for thin targets most projectile material forms a tight cluster of unmelted fragments. Conversely, the PT states of the target debris vary from unmolten spalls, for massive targets, to melts and vapors for very thin targets, because the latter become progressively more subjected to the (maximum) shock stresses typical of the target/projectile interface.

In summary, both D_h and witness-plate spray patterns systematically evolve in response to D_p/T. The relative dimensions of the projectile and target (D_p/T) totally dominate the experimental products documented in this report; impact velocity is an important contributor as well to the evolution of penetration holes, but is of subordinate significance for the witness-plate spray patterns.

TABLE OF CONTENT

ABBREVIATIONS

T	=	Absolute target thickness
T_{BL}	=	Target thickness at ballistic limit
t_t	=	Shock-pulse duration in target
t_p	=	Shock-pulse duration in projectile
T_{bg}	=	Target thickness where rear surface exhibits bulging
T_i	=	Target thickness that permits impactor fragments to exit the rear
T_{HR}	=	Target thickness where onset of hole-saw rings first occurs
T_{RS}	=	Target thickness where first radial patterns occur
D_c	=	Crater Diameter (measured at original target surface)
D_r	=	Crater Rim Diameter (measured from center-of-rim to center-of-rim)
D_l	=	Crater Lip Diameter (measured at periphery of overturned crater lip)
D_h	=	Penetration-Hole Diameter (minimum, physical opening)
D_p	=	Projectile Diameter
H_r	=	Rim Height (from original target surface)
P	=	Crater Depth (measured from original target surface)
V	=	Velocity
L	=	Standoff Distance of witness plate from target's rear surface
v_c	=	Crater Volume (calculated from measured geometry)
m_t	=	Dislodged Target Mass (determined by measured weight difference)
m_p	=	Projectile Mass

INTRODUCTION

A detailed understanding of hypervelocity impact into both massive and relatively thin targets is needed to characterize the natural and man-made particle environment in low-Earth orbit (LEO) from the analysis of space-exposed surfaces (*e.g.*, Levine, 1992, 1993; McDonnell, 1992; Flury, 1993). To date, most available surfaces have represented targets of opportunity. Dedicated flight instruments are currently under development that aim at measuring the trajectories of individual particles and at decelerating particles in such a fashion that their residues may be returned to Earth for analysis of the mineralogic and chemical compositions, isotopic characteristics and organic molecules (CDCF, 1990). The trajectory information will serve to reconstruct the potential source of each particle, such that the detailed laboratory characterizations may be interpreted within the astrophysical context of comets and asteroids, or relative to man-made objects and associated operational procedures in Earth orbit. The methods and objectives of such instrument developments overlap with cratering and penetration studies of long-standing military interest, and especially with the more recent developments of hypervelocity collisional shields for the protection of spacecraft in Earth orbit (*e.g.*, Anderson, 1990, 1993; Flury, 1993).

The mass-frequency distribution of hypervelocity particles in LEO has a steep mass index, typical of comminution products (*e.g.*, Grun *et al.*, 1985; Kessler, 1993). Every single penetration hole in a space-exposed membrane, such as a thermal blanket or a spacecraft hull, of thickness T, will be accompanied by numerous, relatively small hypervelocity craters of depth $P << T$. The desire to understand the transition from genuine cratering to penetration processes in a wide variety of target materials becomes the common denominator among most of the above flight-instrument and collisional-shield developments.

The dependence of collisional outcomes in targets of highly variable thickness is conceptually illustrated in Figure 1. This diagram may also be viewed as an experimental matrix that is capable of yielding the relationships between crater (D_c) and/or hole diameter (D_h), target thickness (T) and projectile diameter (D_p) for any given impact velocity (V). These relationships are crucial to extracting projectile dimensions and associated masses from the measurement of individual craters and penetration holes in space-exposed surfaces (*e.g.,* Warren *et al.*, 1989; Humes, 1992; McDonnell and Sullivan, 1992; Coombs *et al.,* 1993). Conversely, from the knowledge (or assumption) of D_p and T, one may calculate the resulting crater or penetration-hole size in the context of collisional hazard assessments, or one may define specific shielding requirements (Christiansen, 1993). Consequently, such experiments are frequently referred to as calibration experiments.

A projectile of constant diameter (D_p) and of constant impact velocity (V) is allowed to encounter targets of systematically decreasing thickness T. Very massive, infinite halfspace targets will sustain a fully grown or *standard* crater of diameter (D_c) and depth P. The *ballistic limit* marks the transition from such infinite halfspace targets to those of finite thickness which will be perforated and possess penetration holes of diameter D_h. A target at the exact ballistic limit (T_{BL}) will ideally sustain a full cratering event and be characterized by a penetration of size $D_h = 0$. All collisions at $T < T_{BL}$ will result in the physical penetration of the target. We define *marginal* penetrations as those events that are characterized by $D_h < D_p$; this condition is distinctly unique for targets subtly thinner than T_{BL}. Still thinner targets will develop penetration holes of $D_h > D_p$, possibly as large as D_c, (*i.e.*, $D_h \sim D_c$; Hörz *et al.*, 1994) for $T > D_p$. At conditions of $T < D_p$, the diameter of penetration holes will gradually decrease until the condition of $D_h = D_p$ is reached at some characteristic T.

Possible observations related to the fate of the impactor are indicated in Figure 1 as well. Such observations may address the size, energy or velocity distribution of projectile fragments and their geometric dispersion, the onset of melting and vaporization, or the mass fraction of the initial projectile that will reach a collector substrate located behind a penetrated target. All projectile material is ejected uprange during hypervelocity cratering events, but as increasingly thinner targets are encountered, successively larger mass fractions of projectile and target will continue downrange. Is the projectile residue concentrated in specific areas? Under what conditions can one expect solid fragments, melts or

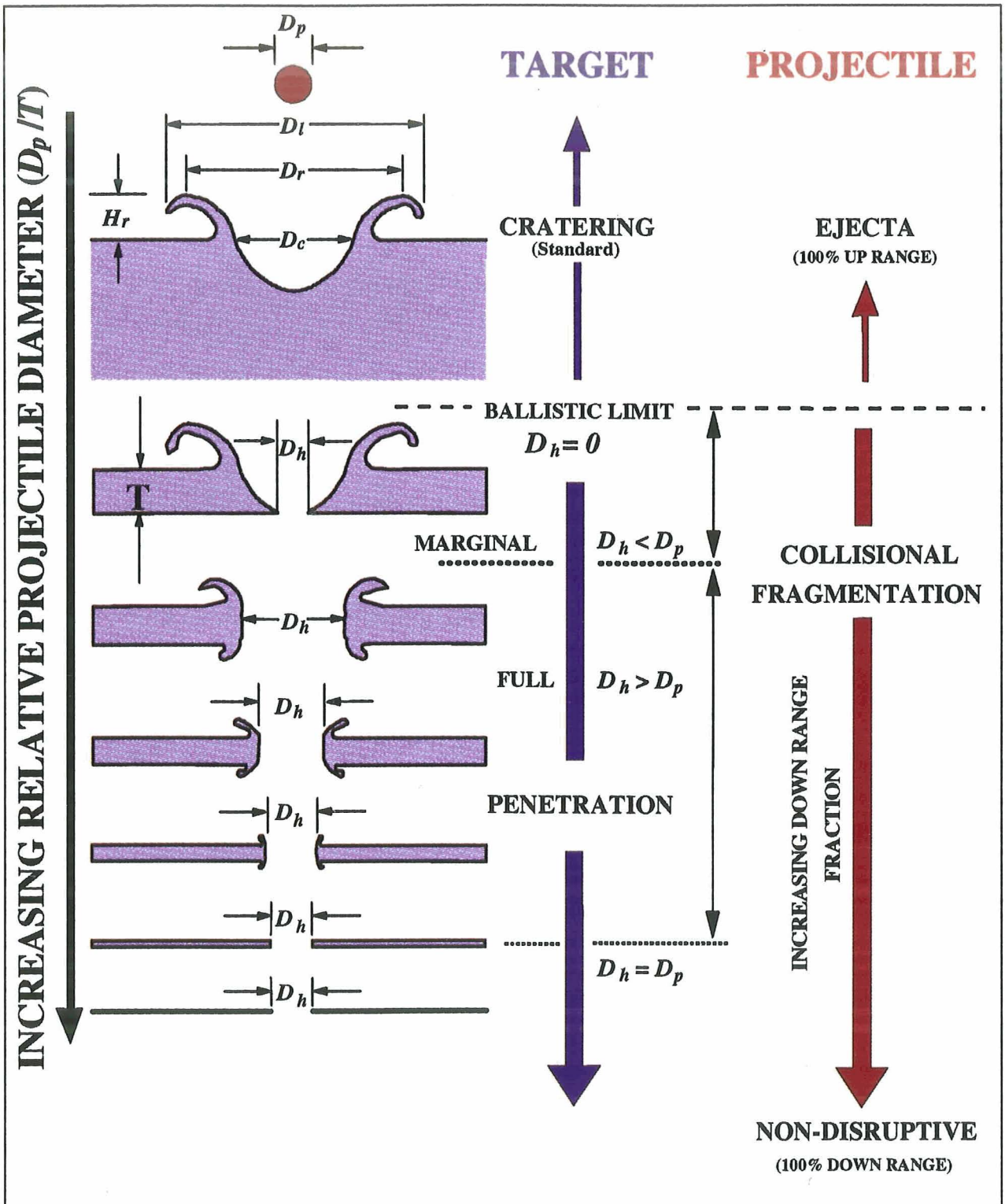

Figure 1. Conceptual illustration of diverse collisional outcomes that result from the impact of a model projectile of diameter (D_p) with targets of widely variable thickness (T). The resulting crater diameter (D_c) is always measured at the initial target surface, while the hole diameter (D_h) refers to the average diameter of the physical opening generated, regardless of vertical position within the target. Note that penetrations in massive targets may be characterized by both a D_c and D_h measurement. This figure also serves to define some of the terminology used throughout this report (*e.g.*, ballistic limit at D_h =0; marginal penetration at $D_h < D_p$).

vapors? These are critical questions for the optimization of capture-cell devices and the associated concentration of, and search for impactor residues during detailed compositional analysis. In addition, for exceedingly thin targets, a condition is reached where T is too thin to collisionally fracture or deform the impactor, which continues on its initial trajectory at approximately its initial velocity. This condition is of critical interest for trajectory sensors in future flight experiments that will monitor the magnitude and location of impact-triggered plasma generated during encounters with thin films, or that may measure the change in polarization of thin PVDF foils (CDCF, 1990).

The fate of the impactor following penetration of relatively thin films ($D_p/T > 10$) recently became of interest to collisional bumper and shield developments (Cour-Palais and Crews, 1990). Any number of such thin targets may be stacked to efficiently decelerate or annihilate the impactor, because successive, multiple collisions with large numbers of bumper elements will incrementally raise the projectile's entropy to cause melting, or even vaporization. Deliberate compromises between the degree of projectile fragmentation, heating, deceleration and dispersion will have to be made when selecting the number, thickness and separation distances of individual thin films used in multiple-foil capture devices, or of individual components composing a multi-shock bumper (*e.g.,* Hörz *et al.,* 1986; CDCF, 1990; Cour-Palais and Crews, 1990; Hörz *et al.,* 1993; Christiansen and Kerr, 1993).

This report describes cratering and penetration experiments in aluminum targets consistent with Figure 1. Target thickness was varied by approximately three orders of magnitude, from $D_p/T < 0.1$ to $D_p/T > 100$. Impact velocities were varied from ~2 to 7 km/s, using powder-propellant and light-gas gun ballistic ranges. The purpose of these experiments was to quantify velocity dependent trends and to derive an empirical database from which to extrapolate to velocities typical for LEO. Such extrapolations are needed for the optimum design of cosmic-dust flight instruments, the major concern in this study. Consistent with these objectives, the alloy of choice was aluminum 1100 (annealed). This relatively soft and pure (>99% Al) alloy is a good analog material for the pure aluminum foils contemplated in the above cosmic-dust flight instruments. In addition, this alloy was used in the manufacture of the Solar Maximum satellite thermal louvers (Warren *et al.*, 1989) and some surfaces exposed on the Long Duration Exposure Facility (Hörz *et al.*, 1992a). Soda-lime glass spheres were used as projectiles to represent brittle silicate impactors. Witness plates were utilized in all penetration experiments to facilitate characterization of the debris cloud emanating from the target's rear (*e.g.,* Pietkutowsky, 1990, 1993; Stilp *et al.*, 1990; Hörz *et al.*, 1994a, 1994b).

Clearly, the present work is highly complementary to a large number of previous investigations that employed different metals or aluminum alloys and/or projectiles as summarized by Pailer and Grun (1980), Carey *et al.* (1985), Herrmann and Wilbeck (1986), Cour-Palais (1987), Humes (1992), or Watts *et al.* (1993). However, none of these earlier studies varied T and impact velocity as widely and as systematically as the present work. Note that Hörz *et al.* (1994a) experimented with aluminum 1100 and soda-lime glass projectiles of different sizes at constant encounter velocity (~6 km/s) to isolate the effects of absolute impactor size. In contrast, the present study predominantly explores the effects of impact velocity (1-7 km/s) at constant impactor dimensions (D_p = 3.175 mm; 1/8").

The specific purpose of this extensive report is to document the experimental conditions, products and findings of ~100 impact experiments in more detail than would be possible via traditional journal articles of limited volume. Furthermore, detailed photo-documentation is frequently the only means to convey to the reader some sense for the complex morphologies of craters and penetration holes, and especially the complexity of some spray patterns on the witness plates. Detailed photographic illustrations seems to be the best way to communicate how some morphologic characteristics may or may not depend on the development of others. This interdependence and gradual development of all morphologic features comprising a crater, a penetration hole, or a witness-plate spray pattern is difficult to describe qualitatively, much less quantitatively (and especially within the scope of this study). Detailed photo-documentation of all experimental products will hopefully stimulate and guide hydrocode computer simulations, a powerful tool to scale from limited laboratory capabilities (*i.e.,* velocity) to those occurring in space. Development and verification of such hydrocodes requires that experimental evidence be duplicated with some degree of fidelity, before extrapolating with confidence to unknown

conditions. This photo-documentation is accomplished in two ways: (a) composite, photographic plates that are part of the text and which illustrate any number of experiments in such a fashion that specific trends are illustrated and (b) detailed photo-documentation, on an experiment by experiment basis, in the form of an Appendix, which is an important and integral part of this report.

Organization of this report proceeds from experimental objectives and procedures, to the analysis and interpretation of craters in infinite halfspace targets, to the description of penetrations in targets of highly variable thickness and their dimensional characteristics and associated interpretations which focus on some first-order suggestions for velocity scaling. We conclude with a descriptive chapter of witness plates and associated implications for the debris cloud. Throughout this report, the descriptions and discussion will proceed from low- to high-impact velocities. It is highly recommended that the Appendix be frequently consulted for details; when this seems highly advisable, a specific experiment number will be called out throughout this report. The introduction to the Appendix provides guidelines how to efficiently locate any specific experiment within the Appendix.

EXPERIMENTAL OBJECTIVES

Consistent with Figure 1, we employed aluminum 1100 targets that ranged in thickness from infinite halfspace to ultra-thin foils. Massive targets were machined from a single round stock of ~8 cm diameter. Targets of thickness $T = D_p = 3.175$ mm (1/8") and smaller were punched or cut from commercially available sheet stock. Foils thinner than 12.5 μm (0.0005"; $D_p/T > 250$) were cut from pure aluminum (>99.9%) foils. The following detailed objectives were pursued as a function of impact velocity.

Establish the ballistic-limit thickness (T_{BL}) of aluminum 1100 where $D_h = 0$ – An experimental sequence typically started by generating a standard crater in an infinite halfspace target. We then proceeded to the conditions of $D_p/T = 0.5$ and 1.0 in order to develop a general strategy for all subsequent experiments of $D_p/T < 1$ conditions. Depending on the results, T was adjusted in small increments based on two criteria that bracket T_{BL}: (a) The onset of bulging or spallation of the target's rear surface precedes actual perforation and occurs at $T > T_{BL}$. (2) The onset of physical penetration occurs only at $T < T_{BL}$. Penetration holes very close to the T_{BL} have dimensions $D_h < D_p$. Hörz *et al.* (1994a) demonstrated that a series of such *marginal* penetrations may be used to extrapolate to the condition of $D_h = 0$, thereby yielding the exact ballistic-limit thickness T_{BL}.

Establish the range of T where $D_h < D_c$ – Penetration holes in massive targets, typically at $D_p/T < 1$, approach the diameter of standard craters (*i.e.*, $D_h \sim D_c$) and are best interpreted as representing truncated cratering events (Hörz *et al.*, 1994a). As demonstrate below, genuine penetration formulas, for purposes of extracting projectile sizes from penetration holes, seem to only apply for the condition $D_h < D_c$ and for T much thinner (typically by a factor of 2-3) than the T_{BL}. The transition from the condition of $D_h = D_c$ to $D_h < D_c$ delineates the transition from applicable cratering to penetration equations when interpreting projectile sizes on space-exposed surfaces; this transition does not occur at T_{BL} (Hörz *et al.*, 1994a, 1994b), as is commonly assumed in the literature.

Determine the T which yields the condition $D_h = D_p$ – Experiments were conducted with successively thinner targets aimed at monitoring the gradual decrease of D_h until the condition of $D_h = D_p$ was reached (see Figure 1). When this important threshold condition occurs, the projectile dimensions may be directly equated to the measured penetration hole(s). At this condition the impactor may or may not be collisionally disrupted; such non-disruptive penetrations (see Figure 1 and Figure 13 in Hörz *et al.*, 1994a) at exceedingly thinner foils were not part of this study.

Determine the size distribution, geometric dispersion and physical state of projectile fragments – Such an objective serves to evaluate the ability of locating and analyzing the remnants of collisionally disrupted projectiles that will be produced by capture cells (CDCF, 1990). Selection of appropriate foils depends on an understanding of projectile disruption as a function of T (Pietkutowsky, 1994) For these reasons each experiment employed a witness plate -- at an essentially constant standoff distance (L) --

located behind the target. Note that the debris cloud consists of projectile fragments as well as debris dislodged from the target, and that the cumulative mass of the target debris frequently exceeds that of the projectile (Pietkutowsky, 1990, 1994; Stilp *et al.*, 1990; Hörz *et al.*, 1994a, 1994b).

Determine the diameter and depth of craters in aluminum 1100 targets – A separate series of cratering experiments was conducted utilizing projectile velocities from 1 to 7 km/s, primarily to assist in the interpretation of depth/diameter measurements obtained from LDEF surfaces (Love *et al.*, 1995; Bernhard and Hörz, 1995). However, such craters are also useful for evaluating D_c as a function of V (see Watts *et al.*, 1993). In addition, these cratering experiments were highly suitable to study loss-mechanisms of impactor materials from the growing cavity of hypervelocity craters as described by Bernhard and Hörz (1995). Photo-documentation of these craters was included into this report for completeness of our impact simulations with aluminum 1100 targets and soda-lime glass projectiles.

EXPERIMENTAL PROCEDURES

All experiments were carried out in the Experimental Impact Laboratory, SN4, NASA-Johnson Space Center, Houston, Texas. The Vertical Impact Facility, a powder-propellant gun, is equipped with a 7.2 mm diameter bore barrel, and was used for all experiments requiring velocities < 3 km/s. Two essentially identical, light-gas guns (5 mm bore) were used for all high velocity (> 3 km/s) experiments. Projectile velocities were determined by the occultation of LED-IR lasers trained onto arrays of photodiodes. Three such velocity stations were attached to the free-flight chamber (beyond the sabot stripper) of the vertical powder-propellant gun; the velocity is measured to < 1%. Four velocity stations are installed along the free-flight chambers of both light-gas guns, yet in front of the sabot stripper. In addition, both light-gas guns employ photodiodes that pick up the separate light flashes generated by the impact of the sabot with the sabot stripper and the primary impact of the projectile with the actual target, which is ~8 m downrange from the muzzle. One of the light-gas guns is also equipped with devices that monitor impact-produced plasma; these charge sensors were used in many, but not all experiments as additional velocity sensors. Internal consistency between these velocity sensors, responding to completely different and separate physical phenomena, was < 2%, and typically < 1%.

Spherical soda-lime glass projectiles were utilized as reasonable analogs to natural silicate impactors, which are of major interest in this study aimed at an improved understanding of cosmic-dust impacts on space-exposed surfaces. The glass spheres were individually hand-picked under the binocular microscope to eliminate flawed specimen that possessed either surface chips, internal bubbles and/or cracks. Even modestly flawed spheres resulted in excessively large data scatter, including non-reproducible penetration and fragmentation results.

The disc-shaped targets were mounted in circular clamping devices, ~7.5 cm inside diameter. The witness plates were mounted at a standoff distance (L) of 12-13 cm, depending on absolute T, from the target's rear surface. The ~29 cm square witness plates were fabricated from aluminum 1100 (annealed), either 7.3 mm (1/4") or 3.17 mm (1/8") thick, depending on expected fragmentation products. All witness plates were blued with alcohol-based lay-out ink, which was found to vastly improve recognition of subtle witness-plate features compared to a bare, metallic plate. In contrast to most paints, this ink neither peels nor spalls, or measurably affect the surface properties of the witness plate.

A minimum of two observers independently performed the dimensional measurements of crater diameter (D_c), crater depth (P), and penetration-hole diameter (D_h), generally utilizing a binocular microscope or, for small-scale events, a Scanning Electron Microscope (SEM). D_c and P measurements refer to the initial target surface as reference datum. A custom-made, mechanical device was used to measure P and to scribe the elevation of the reference plane onto the crater walls; the scribe-mark can be seen on many photographs, especially those at SEM scales. Following measurement and photo-documentation, most craters and penetration holes were cross-sectioned for additional observations, in part via SEM-methods.

Any systematic and quantitative measurements of the complex damage and spray patterns exhibited by the witness plates are very time consuming, and such analyses were substantially beyond the scope of this effort. This is unfortunate because important information about the size-frequency distribution of the debris cloud emanating from a penetrated target could be obtained. As described by many (*e.g.*, Schomberg and Taylor, 1989; Pietkutowsky, 1990, 1993, 1994; Stilp *et al.*, 1990; Hörz *et al.*, 1994a, 1994b), this cloud consists of target and projectile fragments. The trained eye can, in many cases, distinguish secondary impacts on the witness plate that were made by aluminum (target) and glass (projectile) fragments. In the present series, the aluminum target fragments caused secondary craters with shiny, metallic interiors, whereas the glass fragments resulted in gray-colored (sometimes beige) crater interiors with low reflectivity. Such distinctions are readily made for the largest craters, yet they become increasingly more difficult as witness-plate crater sizes decrease; generally, for crater < 100 μm in size it is not possible to assign the features to either (aluminum) target or (glass) projectile origins. However, we are confident that we can assign the dominant spatial distribution of target and projectile species as a result of the optical inspection of the dominant large crater population. To verify such assignments, we conducted penetration/fragmentation tests utilizing copper witness plates, making the distinction between aluminum and glass fragments easier (Hörz *et al.*, 1994a, and to be published). Until we developed sufficient skill and confidence in our ability to differentiate among the fragment sources by purely optical techniques, we verified some of the optical assignments with SEM Energy Dispersive X-ray (EDS) methods. It is possible -- in principle -- to map the distribution of target- and projectile-specific elements on every witness plate using SEM-EDS. If target and projectile were to differ by some diagnostic element(s), one could trace their spatial distribution with considerable precision, including the smallest craters. Nevertheless, given our initial conditions, the majority of projectile and target mass could be, in many cases, readily identified via color of the witness plate craters.

Throughout this report many individual photographs were combined into photographic plates to illustrate specific trends. However, such plates may not be assembled and reproduced without loss of detail and spatial resolution. Consequently, the Appendix contains, in a systematic fashion, photographs of each individual experiment at the best optical resolution available. Even these reproductions suffer from substantial degradation relative to the original photographs, and even more so relative to the actual experimental products; photographic renditions of the witness plates are particularly degraded. Each of the photographic plates presents a number of individual experiments to essentially identical scales; this scale can vary considerably from plate to plate. Generally, however, the front and rear views of a target, at any given velocity, are of the same scale. The approximate dimensions for an individual frame within a given photographic plate may be derived from the thinnest films depicted, because the condition of $D_p \sim D_h \sim 3.175$ mm is approximated at $D_p/T > 20$. All cross-section plates contain the case of $D_p/T \sim 1$ (*i.e.*, $T \sim 3.175$ mm), which can be used as an internal standard from plate to plate. Unless otherwise noted, all witness plates were 29 cm square. Note that our objects of interest ranged in absolute dimensions from microns to centimeters, and that there is simply no good method to portray all experiments at the same scale with a single photographic method. Some features are too small for close-up optical photography, while others are too large to permit convenient SEM documentation.

EXPERIMENTAL RESULTS

The initial impact conditions and major results for all individual experiments are listed in Table 1 (at the end of the Appendix), which establishes groups of experiments based on specific experimental objective and velocity. The cratering experiments in infinite halfspace targets are listed first and arranged with increasing velocity. The subsequent groups of penetration experiments are tabulated with increasing impact velocity. Within an individual penetration series at constant, nominal velocity, individual experiments are ranked in order of decreasing T, no matter what the velocity. Importantly, the sequence of experimental groups and individual experiments portrayed in Table 1 reflects the organization and sequence of descriptions to follow.

Note that the Appendix exactly duplicates Table 1 in the sequencing of individual experiments. This organization by topic simply enables relative efficient comparison of many related experiments, especially for the casual reader. However, it will make the search for any specific test somewhat cumbersome. To facilitate the latter, we provide Table 2 (at the end of the Appendix), which lists all experiments in numerical order, together with the nominal impact velocity and relative target thickness (D_p/T). The intent of Table 2 is to enable efficient cross referencing with Table 1 by identifying the first-order initial conditions; the latter should assist in rapidly locating any individual experiment within the Appendix. Throughout this report, the laboratory experiment number is the sole identifier for each test. It refers to the chronological sequence of tests, with the two light-gas guns identified as *O* (old) and *N* (new), and the Vertical Gun as *V*. Also note that some cratering shots are listed twice in Table 1 to reflect that they are integral parts of both the cratering and penetration series.

Standard Craters

A major objective of the present study is to delineate the transition from cratering to penetration phenomena and processes. Consequently, we first describe a series of 24 craters in infinite halfspace targets at velocities ranging from 1 to 7 km/s (see Table 1; also see Bernhard and Hörz, 1995). *T* was typically 2.5 cm or more, to inhibit bulging of the target's rear side. As demonstrated by Hörz *et al.* (1994a), even subtly bulged targets display appreciably deeper craters than in the standard case.

Figures 2a and 2b display representative craters in plan view and cross-section, respectively, and vividly illustrate how crater size increases with increasing velocity. From the cross-sections in Figure 2b, the relative extent and geometry of the crater lips seem to be invariant at $V > 3$ km/s. Craters at $V < 3$ km/s, and especially at $V < 2$ km/s are relatively deep, consistent with previous descriptions of cratering phenomena at modest impact velocity (*e.g.*, Hermannn and Wilbeck, 1986 or Cour-Palais, 1987). It is widely acknowledged and understood in ballistic-limit work that low-velocity impactors, generally < 3 km/s, are much better penetrators than high-velocity projectiles (*e.g.*, Christiansen, 1993 or Schmidt *et al.*, 1994). Note that these low-velocity craters exhibit substantially straighter walls and a cone-like appearance in cross-section, unlike the paraboloid profile of high-velocity craters (Sapp *et al.*, 1993).

Detailed measurements of crater diameters, normalized to projectile dimensions, are illustrated in Figure 3a. An exponential regression line through the experimental data reveals that they scale with $V^{0.59}$, at otherwise identical conditions. A comparison of our experimental data with those of Cour-Palais (1987) and Watts *et al.* (1993) is presented as well in Figure 3a. Detailed discussion about the general utility of diverse cratering equations currently in use and their differences exceeds the essentially descriptive nature of this report and will be published elsewhere. Nevertheless, we note the excellent agreement of Watts *et al.* (1993) with our experimental data.

Figure 3b illustrates the relative crater depth (P/D_p), measured with a mechanical device from the original target surface to the bottom of the crater. Again, note the good agreement with Watts *et al.* (1993). During the cross-sectioning and polishing processes care was exercised to assure that (1) little or no projectile material was dislodged from the crater (in some cases we employed epoxy to stabilize the fragmented impactor residue) and (2) each cross-section runs through the geometric center of the crater cavity. The low-velocities craters (< 3 km/s) possess a significant and reproducible plug of projectile material in the bottom of the crater cavity, to be described later, that can affect the measurement of crater depth. As a result, *P* measured to the bottom of the aluminum surface in the cross-sectioned craters is deeper than the corresponding plan-view measurements, which were made the top of this projectile plug. The differences in these measurements is illustrated in Figure 3c. This distinction between the apparent and true crater depth is important for low-velocity craters, and can only be accomplished in cross-section. None of the existing cratering equations reproduce our observations at < 3 km/s. However, the formalisms of Watts *et al.* (1993) best fit the experimental evidence at $V > 4$ km/s, where we observe an average of $P/D_c = 0.57$. This value is distinctly different from the relationship of $P = 0.5D_c$ that is commonly used for hypervelocity impact craters in aluminum (*e.g.*, Cour-Palais, 1987 or Christiansen, 1993).

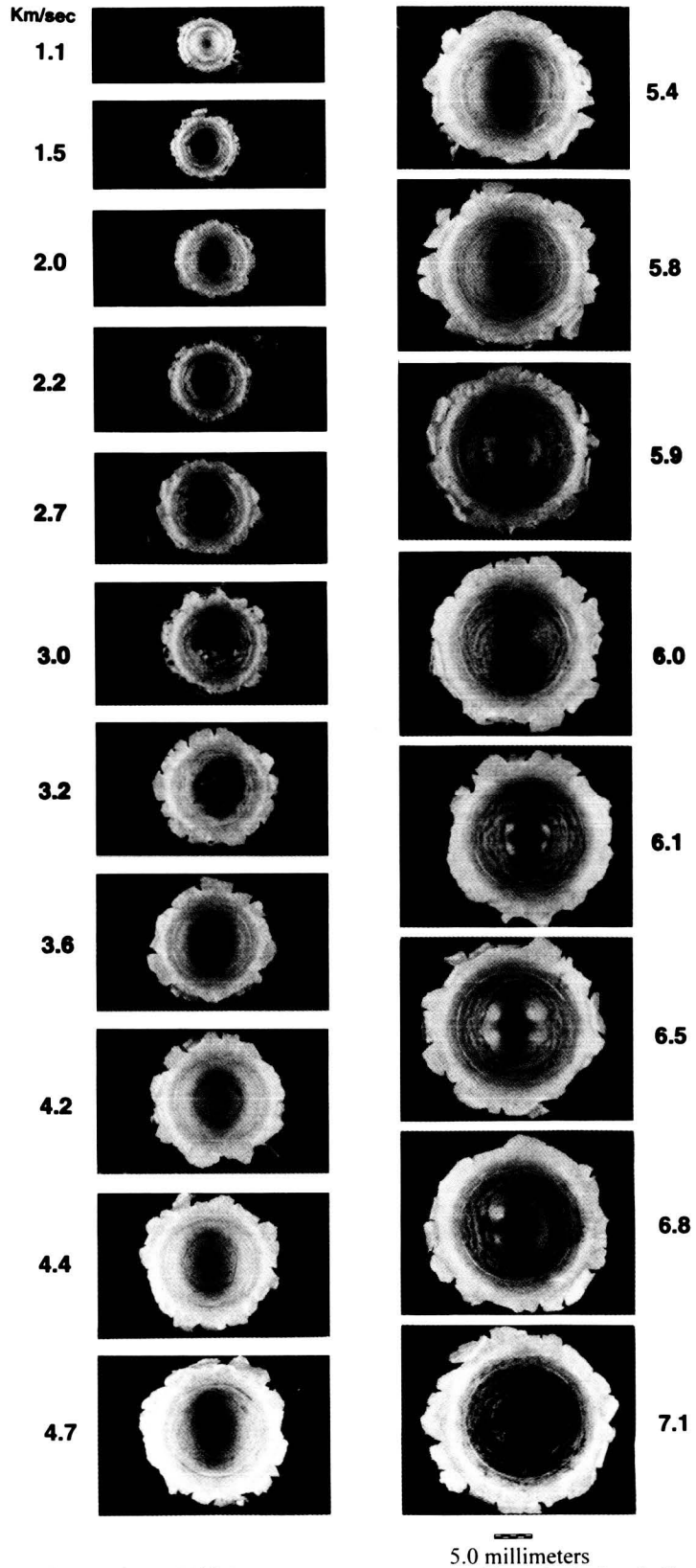

Figure 2a. Plan view of craters in aluminum 1100 (annealed) targets generated by spherical soda-lime glass projectiles of 3.175 mm (1/8") diameter impacting at 1-7 km/s. All images are to identical scale illustrating the progressive increase of crater diameter with increasing encounter velocity (see text for details).

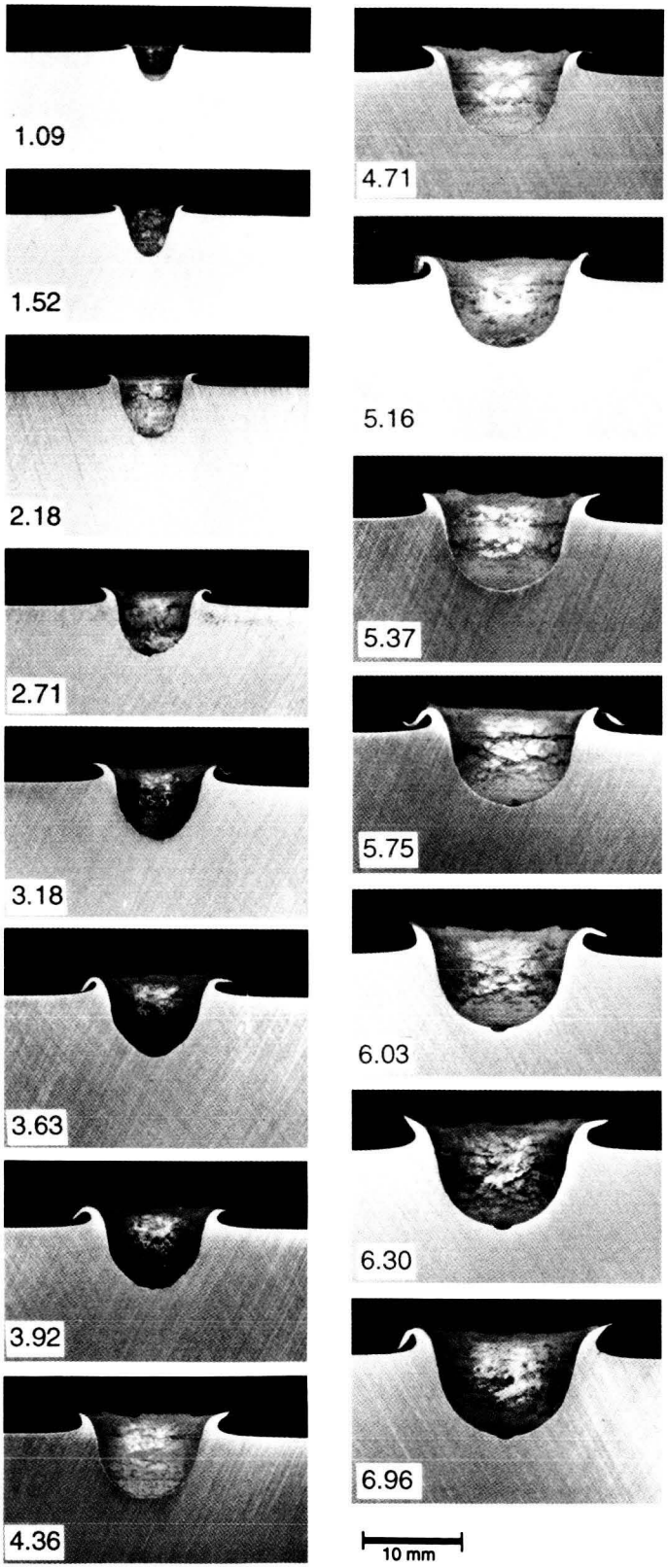

Figure 2b. Cross-sections of craters in aluminum 1100 targets generated by spherical soda-lime glass projectiles at 1-7 km/s. Note the unusually deep craters formed at < 3 km/s, and that the relative crater shape remains fairly constant at $V > 5$ km/s (see text for details).

As part of the post-retrieval analyses of our LDEF experiment, we recently determined the aspect ratios of hundreds of highly circular craters, to avoid the effects of oblique impact (*e.g.*, Christiansen *et al.*, 1993), on space-exposed aluminum surfaces (1100 and 6061-T6; Love *et al.*, 1995; Bernhard and Hörz, 1995). The majority of these craters were formed at $V > 10$ km/s, including some cases where mean encounter velocity approached 20 km/s, such as in the ram direction of the non-spinning LDEF platform (Zook, 1992). The average P/D_c of these LDEF craters is distinctly > 0.5, typically 0.56-0.58 (Newman, 1992; Love *et al.*, 1995; Bernhard and Hörz, 1995). Igelseder and Igenbergs (1990) suggest that P/D_c continually increases with increasing velocity. From the experimental and empirical LDEF data this does not appear to be correct and is due to the curve-fittings procedures of Igelseder and Igenbergs (1990). The experimental data of Igelseder and Igenbergs (1990; soda-lime glass into aluminum) are actually consistent with a constant P/D_c ~0.6 for $V > 8$ km/s

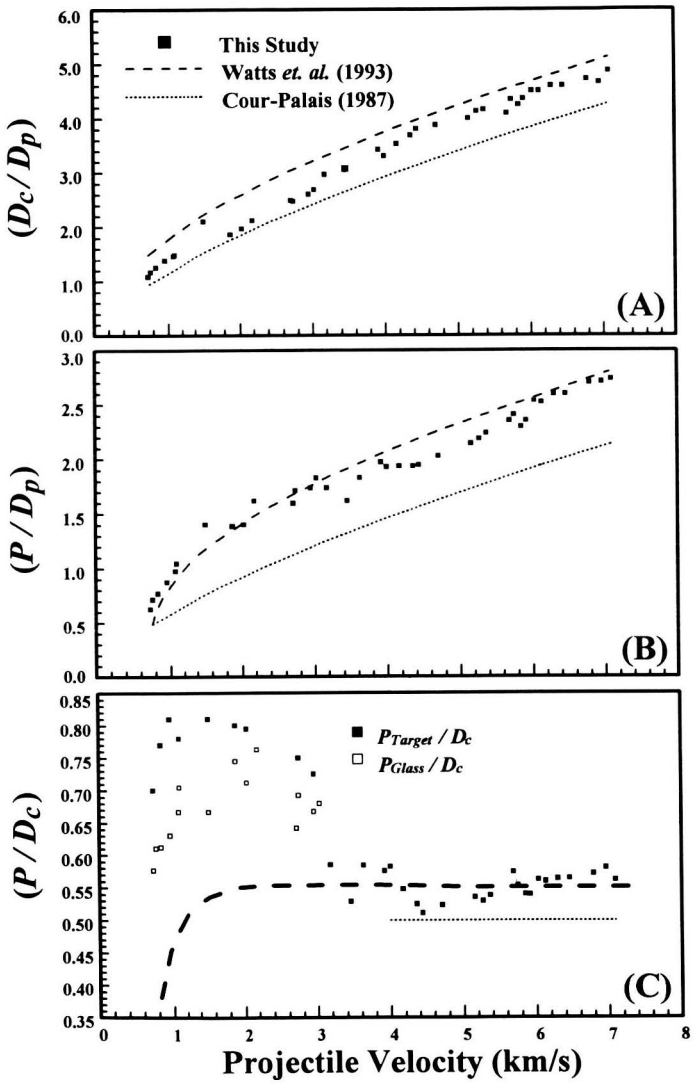

Figure 3. Diameters (A) and depths (B), normalized to projectile diameter (D_p), for craters produced by soda-lime glass projectiles into aluminum 1100 targets. Note the generally good agreement of the experimental results with Watts *et al.* (1993). (C) Depth/diameter ratios of experimental craters. Note the difference between depth measurements in plan view to the top of the projectile residue (open symbols) and the true crater depth in the aluminum target (solid symbols) revealed in cross-section. In addition, note that the crater depth at $V > 5$ km/s is distinctly deeper than $P/D_c = 0.5$.

Our observations agree with previous proposals that advocated a constant P/D_c relationship at all velocities > 4 km/s. However, we disagree with the specific, commonly used value of $P/D_c = 0.5$ and suggest somewhat deeper structures which result in an average P/D_c of 0.58. This value is consistent with LDEF observations, which empirically extend the experimental (< 7 km/s) aspect ratios to velocities > 10 km/s, and approaching 20 km/s. Regardless, a $P/D_c = 0.58$ applies to typical craters produced in LEO, and P/D_c of 0.6 does not appear to be unreasonable for perpendicular impacts at $V > 10$ km/s. Consequently, we suggest that the essentially hemispherical aspect ratio of 0.5 that is commonly advocated for space-produced craters, be modified to a $P/D_c = 0.58$, for aluminum 1100 and 6061-T6 targets.

Figure 4 presents our measurements of rim diameter (D_r), crater-lip width (D_l) and rim height (H_r), all normalized to D_p. The rim diameter represents the distance from rim-crest to rim-crest, while the lip width represents the average radial extent of the very periphery of the bent and thinned crater lip; the rim height is the average elevation of the rim crest above the initial target surface. All three parameters where obtained by making a number of measurements per crater, typically 4-6, which were averaged. These averages are plotted in Figure 4 to evaluate whether any of these morphologic elements varies with V. As can be seen, all three parameters cluster along essentially horizontal lines, at least at velocities > 2 km/s. Consequently, they do not appear to constitute useful velocity indicators. Combined with essentially constant P/D_c

from Figure 3b, it appears that the morphology of craters in aluminum 1100 targets does not vary as a function of velocity, at least for velocities > 4 km/s, and most likely including cosmic velocities. The average values for these morphologic elements are: P/D_c = 0.58; D_r/D_c = 1.3; D_l/D_c = 1.5, and H_r/D_c = 0.25. We recommend that these relative dimensions be used to describe typical hypervelocity craters from space-retrieved aluminum (1100) surfaces.

The pre- and post-experimental target weights were obtained (via a micro-balance) to determine the total target mass loss, a parameter of interest to model the potential production of orbital-debris fragments (*e.g.*, Potter, 1993). A few targets sustained impacts from general gun-debris and were discarded as unsuitable for this purpose. In addition, an additional batch of targets were, inadvertently, not weighed prior to cross-sectioning and could not be included in the database. The low mass loss observed from these weighing operations was somewhat surprising. Therefore, we calculated an approximate crater volume (v_c) assuming a hemispherical geometry of $r = 0.5D_c$; this simplified geometry was deemed sufficient to illustrate the substantial differences in dislodged target mass resulting from (1) the actual weight measurements (m_t) and (2) post-mortem crater volume (v_c) considerations. The values m_t and v_c are compared in Figure 5, with both parameters normalized to the projectile. Note that the largest crater dislodged ~5 times the impactor mass, yet its volume is > 50 times larger than that of the impactor. Similar results were found with penetrated targets (Hörz *et al.*, 1994). Therefore, we conclude that only measured weight differences can correctly reveal the cumulative mass of dislodged target material, and that volume-based mass estimates can be in serious error. The apparent discrepancy results from the fact that most of the crater volume is the result of plastic deformation and material displacement (*i.e.*, raised crater rims and surroundings will accommodate the formation of substantial crater volume[s], without actual mass loss and associated liberation of particulates). These effects are important when estimating the development of orbital-debris population by cratering events in infinite halfspace targets.

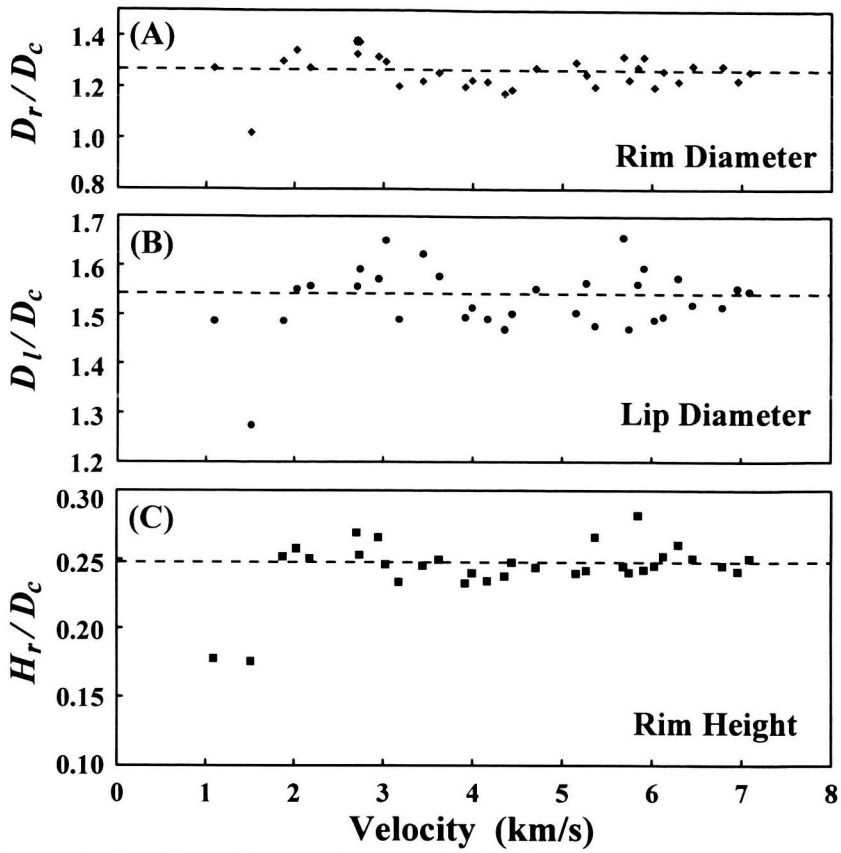

Figure 4. The effects of impact velocity on (A) rim diameter, (B) diameter of the crater lip, and (C) rim height for craters in aluminum 1100 targets generated by soda-lime glass impactors.

Representative SEM images that reveal details of the crater shape and the distribution and physical state of the soda-lime glass impactor can be seen in Figure 6 (consultation of the Appendix is recommended for all SEM images). Note the distinctly hummocky and irregular crater bottoms in the velocity range of ~2-3 km/s. Some small scale, highly localized depressions modulate the general crater profile. Similar structures were observed from modestly fractured projectiles following thin film penetration (*e.g.*, Figure 13 in Hörz *et al.*, 1994a), or from cratering experiments at very oblique angles (Christiansen *et al.*, 1993). Craters with such highly localized depressions are common on space-exposed

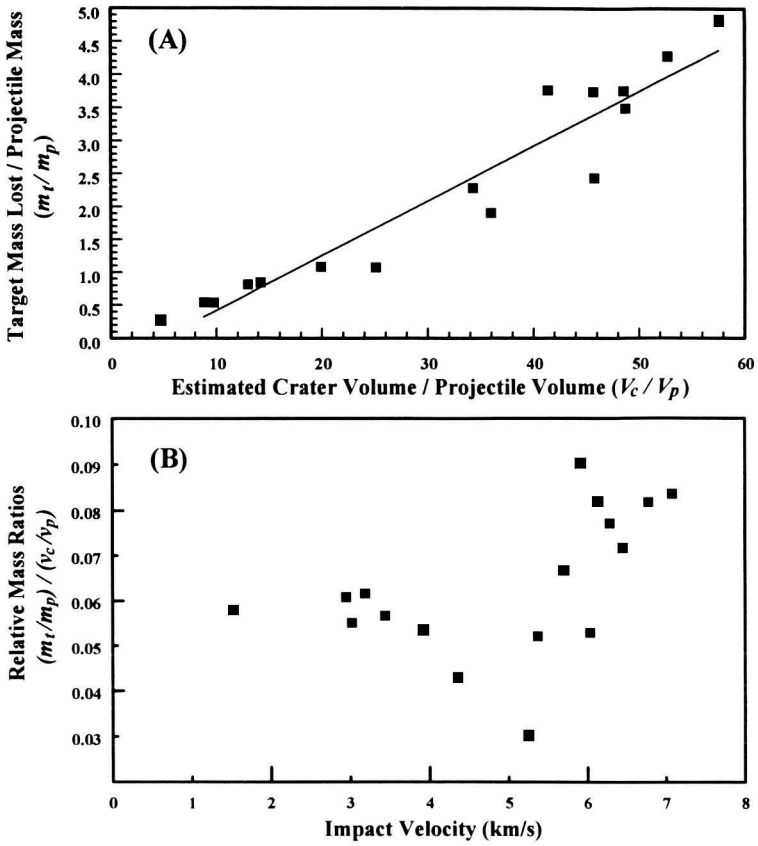

Figure 5. Mass loss measurements by weight difference (m_t/m_p) for impact craters into aluminum 1100 versus estimates for dislodged mass based on (hemispherical) crater volume (V_c/V_p). Figure 5a shows the actual measurements and volume calculations, while Figure 5b illustrates the relative mass ratios as a function of impact velocity.

surfaces as well (see the pictorial catalogues of LDEF craters by Bernhard and Hörz, 1992 or Bernhard and Zolensky, 1993). Generally, such structures suggest a projectile that has an intrinsically heterogeneous mass distribution, such as an aggregate structure or because of internal fractures, possibly being in a state of disaggregation due to oblique impact (Schulz and Gault, 1982; Christiansen *et al.*, 1993) or upon thin-film penetrations (Hörz *et al.*, 1994a). Obviously, the present projectiles were neither initially fragmented nor heterogeneous aggregates, yet heterogeneous mass distribution seems manifested by these localized depressions. Therefore, we tentatively suggest that the projectile fragmented upon collisional contact, and that a few, large fragments were able to penetrate noticeably deeper than their finer-grained counterparts of the impactor. It seems possible that (the leading) part of the projectile was shocked into the solid/liquid mixed-phase regime at these velocities (2-3 km/s), and that a few remaining solid fragments penetrated deeper than the melts. The point is that the "hummocky" experimental crater floors must result from heterogeneous mass distributions, and it is suggested that homogeneous impactors may disaggregate differentially upon impact at modest velocities (< 3 km/s). If any hummocky crater bottom were also associated with a relatively deep and cone-shaped crater on a space-exposed aluminum surface, a strong argument could be made for relatively low-velocity impactor. Most impact features with multiple, localized depressions on LDEF surfaces are invariably of a (very) shallow nature (*e.g.*, Bernhard and Hörz, 1992; Bernhard and Zolensky, 1993; Christiansen *et al.*, 1993).

A totally different type of localized depression occurs in craters formed at $V > 5.5$ km/s (Figure 9; also see experiment 1247 in the Appendix, page A23). A small, very regular and symmetrical depression resides at the very center of the crater bottom. This regular "dimple" feature is readily reproduced, yet only with spherical soda-lime glass impactors encountering aluminum 1100. It does not form with nylon, aluminum or steel projectiles at otherwise identical conditions, nor did such dimples occur in other aluminum alloys with soda-lime glass impactors, or any other projectile. Formation of the dimples commences when the projectile melt liner (see below) starts to detach from the center of the crater bottom. To date, we have not seen a corresponding feature on any space-exposed surface, and do not have an explanation for its origin, yet it is a very idiosyncratic, reproducible phenomenon associated with our specific impact conditions. Qualitatively similar features have been produced in some computer simulations, yet they were interpreted as artifacts (Allahdadi, 1992, personal communications).

As to the fate of the impactor, we mentioned above that a substantial mass of unmelted projectile occupies the crater bottoms at impact velocities < 2 km/s. Figure 7 illustrates that substantially different fragmentation processes operated within the brittle glass projectile, one producing a coarsely fractured,

yet otherwise substantially coherent, central core, and another an intensely comminuted, wedge-shaped annulus surrounding this core. The contact between these two fragmentation regimes is stunningly sharp. The fine-grained annulus appears intensely sheared and contains distinct linear zones or bands of especially severe comminution. In addition, the rear portion of the projectile core (see Figure 7) is intensely comminuted as well, yet the fragments have a distinct two-dimensional, flat and platy appearance that is very different from the other comminution products. Much of the platy material, as well as the fragments constituting the core and the sheared annulus, seem to have fractured in-situ, with little rotation, mixing and mass movement. The average fragment size varies dramatically in these deformation zones, yet all of the fragments interlock and match the outlines of their neighbors. There is no fine-grained intergranular debris, much less any rounding of components or other evidence of relative motion. We have no ready explanation for the occurrence of these features, other than that dramatically different stress regimes must exist within the impactor that seem to have stunningly sharp contacts. Interestingly, Pietkutowsky (1995) describes the collisional break up of low-velocity aluminum spheres following thin-film penetration as resulting in three distinct fragment populations: (1) an inner, essentially intact core that is surrounded by (2) a disk-shaped cloud of fine-grained debris and (3) a trailing plume of spallation-produced fragments derived from the projectile's rear. These basic fragmentation regimes are possibly manifested by the in-situ materials illustrated in Figure 7. However, the brittle glass impactor does not retain an intact core and is coarsely fragmented, as are some of the high-velocity aluminum spheres of Pietkutowsky (1995). The platy nature of the rear portion of our glass-impactors is consistent with spallation processes as well. The fine-grained annulus seems to result from intensive shear. We will return to these observations during the discussion of the witness-plate crater populations.

Figures 8 and 9 are intended to augment Figure 6 in a discussion on the formation and distribution of impact melts within the craters. Note the presence of irregular clumps of fine-grained, unmelted material in the bottom of the 1.88 km/s crater (Figure 8a), and how these masses move up the crater wall as V increases (*i.e.*, 2.74 km/s; Figure 8b), and especially at $V > 4$ km/s (Figure 8c). It is obvious, from Figures 8b and 8c that a substantial fraction of the impactor is molten and forms a melt liner that drapes the entire crater cavity. Beginning at ~2.5 km/s some fraction of this melt may escape the crater and be lost via ejection. It is difficult to determine the role of molten material at these velocities, yet we suspect that thin films and minor quantities of melt promote the mass movement along the crater wall (and beyond the rim?). Clearly, at $V > 3.5$ km/s the entire crater was, at some stage, draped by melt. However, the post-mortem melt distribution is uneven because of the effects of surface tension upon cooling and the associated contraction of the liquid. Note that those portions of the crater walls that seem devoid of melt in Figures 8c or 8d are still draped by an exceedingly thin veneer of melt that is readily revealed by SEM-EDS analysis. We ascribe the scouring of the crater walls, which results in the prominent, radial streaks visible in Figures 8d and 8e, to be caused by solid fragments that were mixed with the melt. Evidence suggest that the entire crater cavity was completely lined with a coherent melt layer at some stage, and that increasing fractions of this melt (and accompanying solids?) escaped the growing crater cavity at velocities > 3.5 km/s. Note a relatively small, melt-free"window" in the bottom of the 5.7 km/s crater depicted in Figure 9a, and how increasingly larger fractions of relatively pure melt move up the crater wall. This melt-free window systematically enlarges with increasing velocity, and could (possibly) be used as a velocity indicator for our specific, experimental conditions (see Appendix, pages A22 - A32). Upon cooling, the (most-likely continuous) melt liners have contracted into highly irregular lumps and masses, as illustrated by the cross-sections of the 6.5 and 7 km/s cases in Figures 9e and 9f. Such spatially heterogeneous lumps and blebs of melt are typical of space-produced microcraters, attesting to their high impact velocities. Clearly, progressively larger fractions of the impactor escape a growing crater cavity in the form of melts as impactor velocity increases. It is not necessary to invoke vaporization as a (dominant; exclusive?) loss mechanism for impactor materials on space-exposed surfaces, as advocated by Bernhard *et al.*, 1993. Escape of molten material -- as suggested by Watts *et al.* (1993) -- may suffice to account for the observation that ~50% of all LDEF craters contain impactor residues below the detection threshold of our SEM-EDS techniques, if any projectile residue (Bernhard and Hörz, 1992; Bernhard and Zolensky, 1993; Simon *et al.*, 1993).

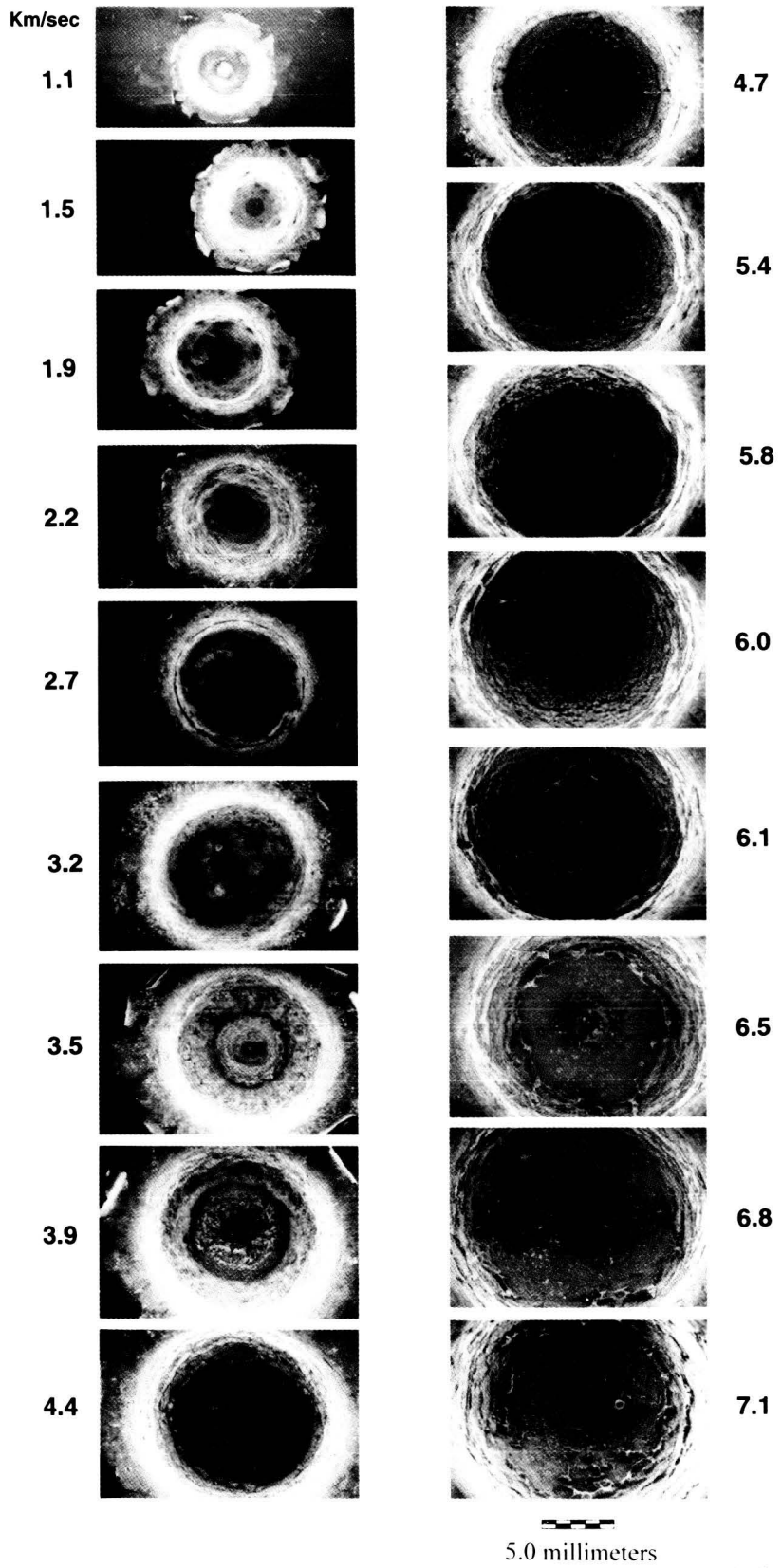

Figure 6a. Detailed SEM images of representative craters in aluminum 1100 targets generated by soda-lime glass projectiles of 3.175 mm diameter at 1-7 km/s. Note the mixture of melts and fragments at velocity ranges between 3 and 5 km/s, and how the initially contiguous melt liner leaves an increasingly larger window at the crater bottom at $V > 5.5$ km/s. Note further that the remaining melt coagulates into irregular blobs and lumps at $V > 6$ km/s.

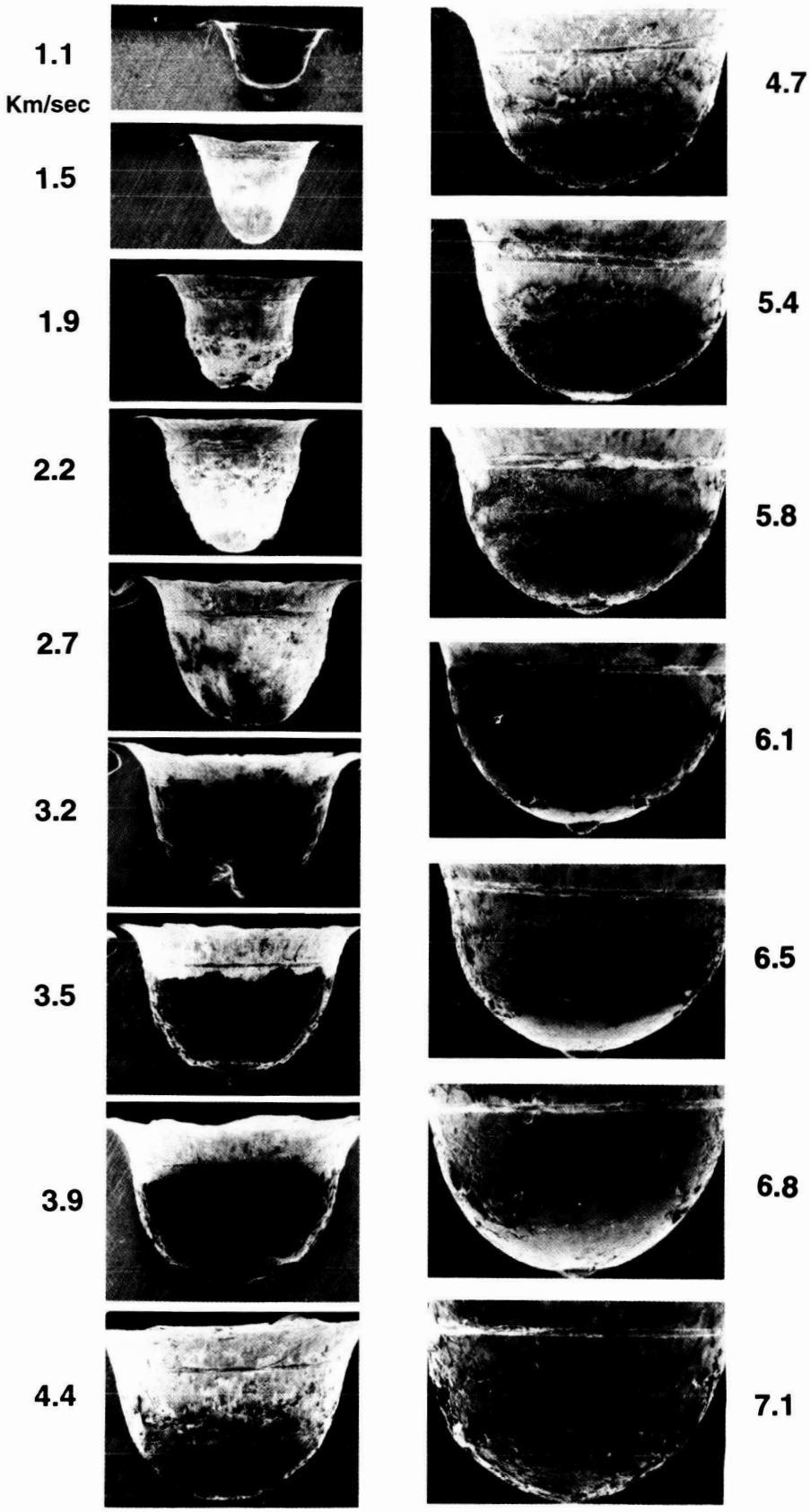

Figure 6b. Detailed SEM images of cross-sectioned craters that correspond to Figure 6a. Note the unusually deep craters at $V < 3$ km/s, the relatively irregular crater bottoms at velocities between 2 and 4 km/s, the typical melt texture governed by surface tension at velocity ranges from 4 to 6 km/s, and the formation of a central dimple at the crater bottom at $V > 5.5$ km/s.

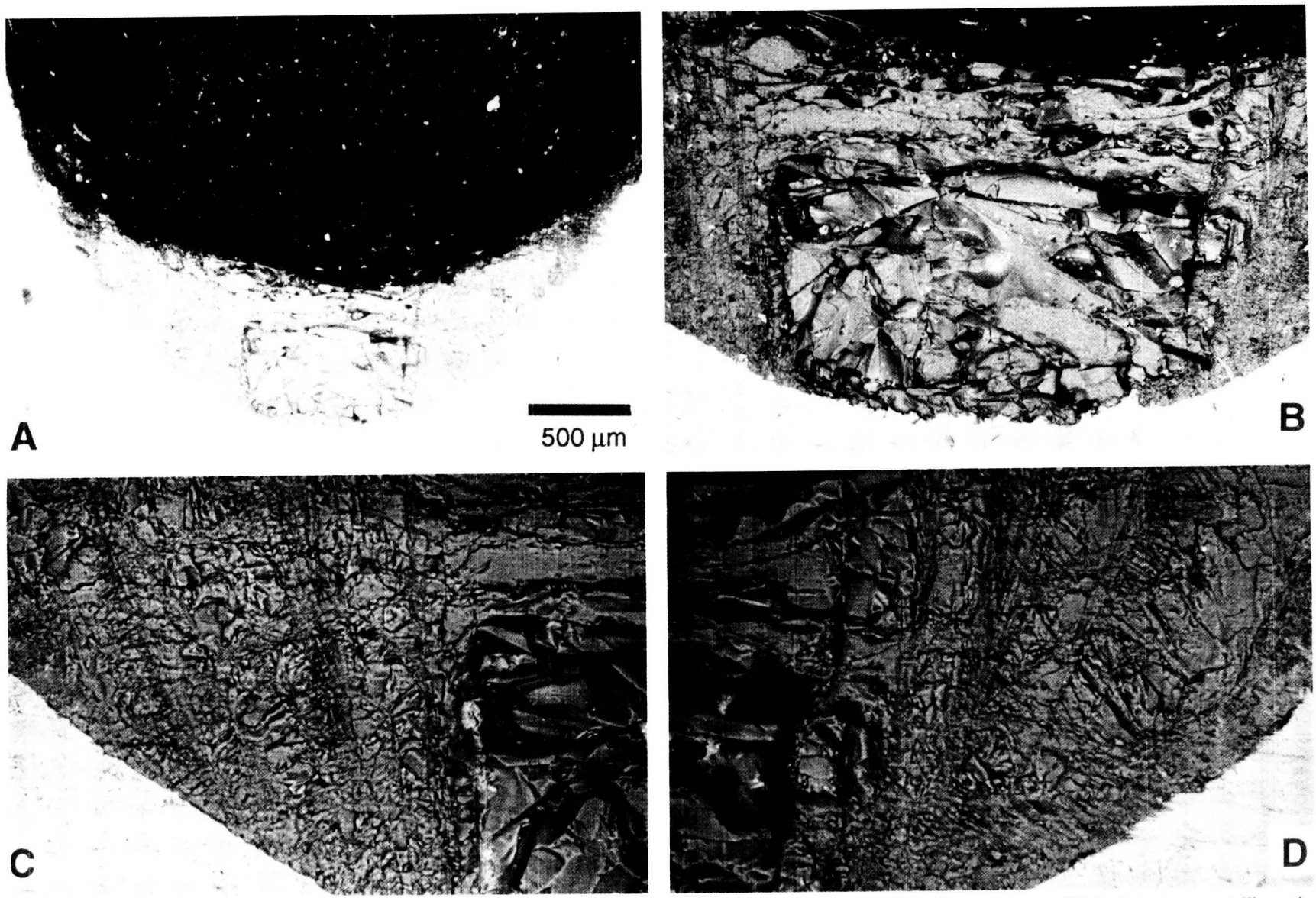

Figure 7. Detailed SEM photographs of highly fractured projectile residue in experiment 3604 at 1.09 km/s. (A) Overview of crater bottom. (B) Partial enlargement illustrating three distinctly different deformation regimes in the form of (1) a relatively coarsely fractured core, (2) intensely cominuted annulus and (3) distinctly platy fragments towards the projectile's rear volume. Note the stunningly sharp contacts between these fragmentation regimes, especially between core and the fine-grained annulus. (C) and (D) Enlarged views of the three fragmentation regimes illuminating details of the highly comminuted lateral portions of the soda-lime glass sphere, characterized by highly localized, two-dimensional zones of severe comminution which we interpret as shear bands. The latter are initially straight and parallel to the central core/annulus contact, but become increasingly curved with lateral distance to parallel the curved crater walls.

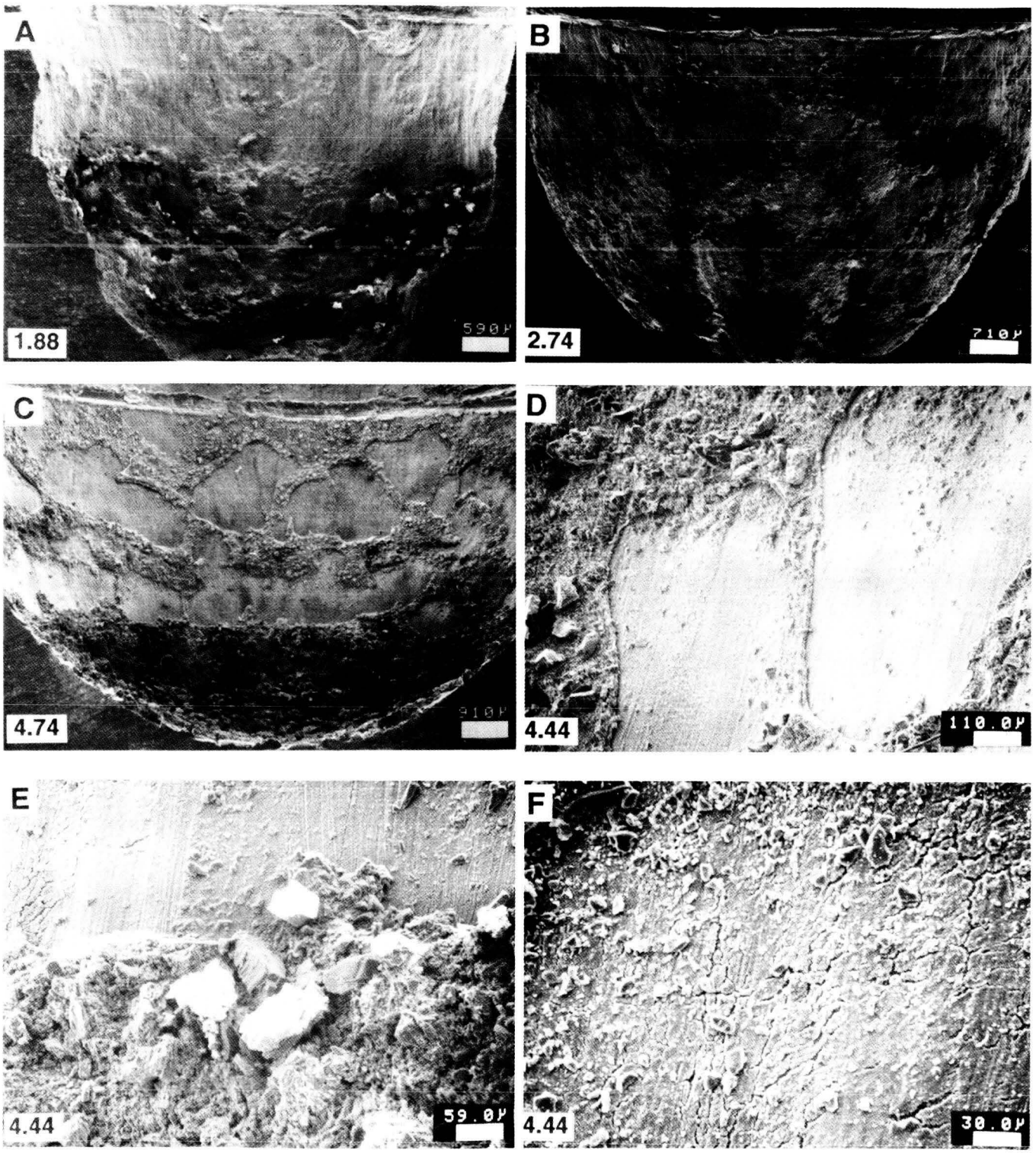

Figure 8. Detailed SEM images of crater interiors. Numbers in lower left-hand corner refer to velocity. (A) Highly fractured and dissagregated projectile plug and irregular crater bottom (1.88 km/s). (B) Mixture of fragments and melt moving up the crater wall and over the rim. (C) Mixture of predominantly molten impactor and fine-grained projectile detritus. (D) Details of fragment-laden melt liner and scoured aluminum crater walls. (E) Contact between melt-liner and scoured wall area. (F) Enlarged view of a scoured crater wall (see text for discussion and consult Appendix for additional SEM photographs).

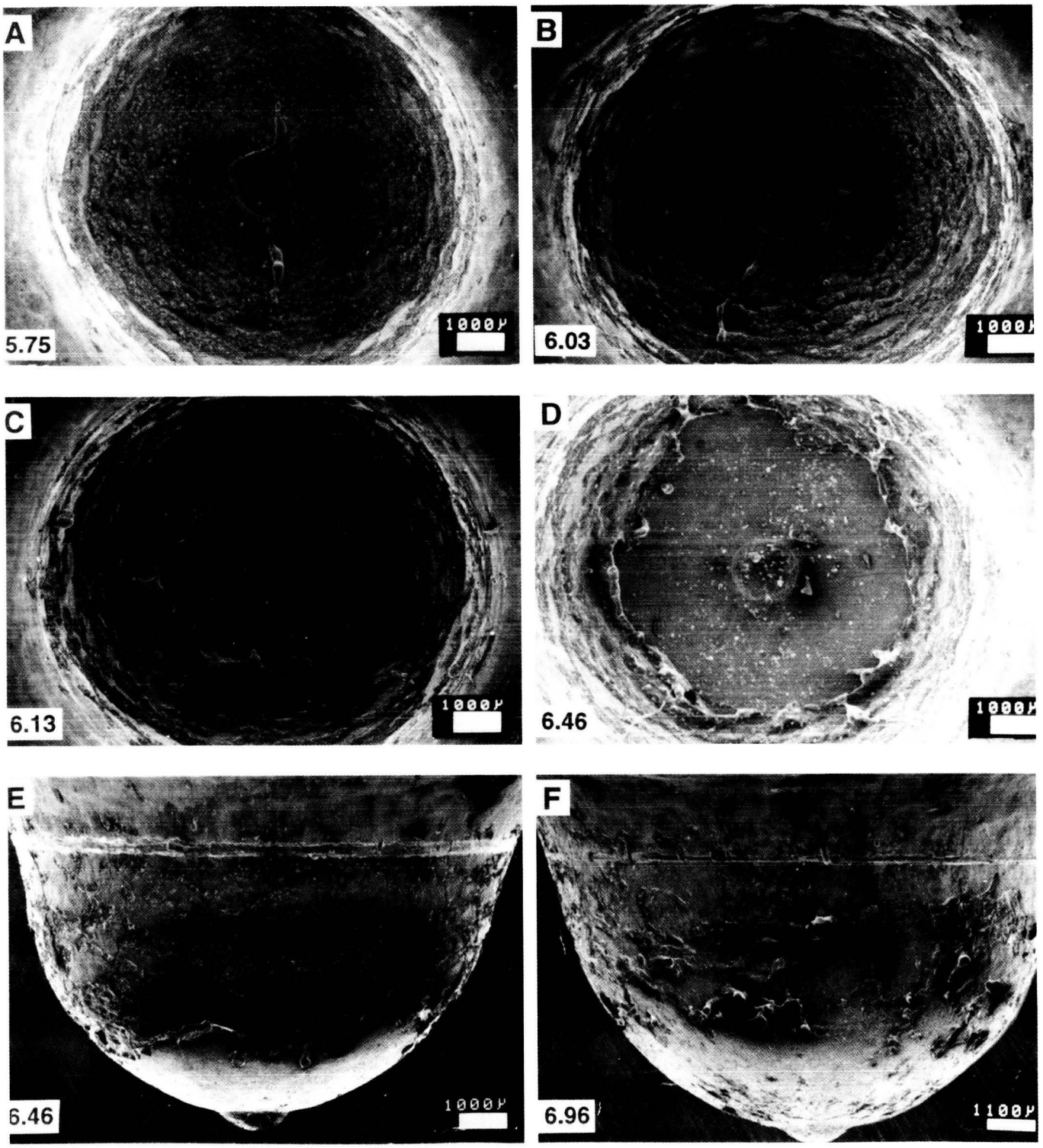

Figure 9. Detailed SEM views of projectile melts for cratering events of $V > 5.5$ km/s. Note the increasingly larger window in the melt liner as V increases, and the loss of increasingly larger fractions of melt. Photographs (E) and (F) illustrate the presence of an unusual dimple feature in the crater bottom (additional SEM photographs can be found in the Appendix).

It is not possible, in the context of this study, to quantify the projectile mass loss as a function of impact velocity. The spatial distribution of the residues inside the craters are simply so geometrically complex that their volume cannot be measured with confidence. It is not practical to accurately measure the projectile residue volume in most space-retrieved craters and, thus, to derive initial impactor size or mass from such a potential measurement, as suggested by some. Even if accurate volume determinations of the projectile residue were possible, it would still only represent an unknown fraction of the total impactor, given the fairly unconstrained initial conditions responsible for space-retrieved craters.

While any series of cratering experiments will reveal substantial idiosyncrasies due to the specific impactor and target materials used, we may, nevertheless, summarize this cratering section with the following, general conclusions. Crater diameters in aluminum are reasonably well predicted by the cratering equations of Cour-Palais (1985, 1987), or Watts *et al.* (1993), but crater depth seems to be deeper, at velocities < 4 km/s, than is predicted by Cour-Palais (1987). The above experimental craters, combined with observations from LDEF (Love *et al.*, 1995; Bernhard and Hörz, 1995), and the latest cratering equations by Watts *et al.* (1993) all suggest that a value for P/D_c of 0.58 is more applicable to craters on space-exposed aluminum surfaces than is the more traditional aspect ratio of 0.5. The experiments also demonstrate that projectile melts are efficiently ejected from the growing crater cavity and that it is not necessary to invoke vaporization processes to explain why ~50% of all space-produced craters from LDEF contain little or no detectable impactor residues, at least within the detection threshold of SEM-EDS methods employed.

Penetration Holes: Morphologic Elements and Their Evolution

The morphologies of penetration-holes in aluminum 1100 targets of variable thickness can be seen in Figures 10 and 11. Figures 10a - 10h show the projectile entrance and exit sides at specific velocities, while Figure 11 presents the corresponding cross-sections. The latter illustrations are limited to relatively massive targets, as very thin films are not very informative in cross-section. Note, for scale in Figures 10a - 10h, that the penetration-hole diameters for the thinner foils (*i.e.*, $D_p/T \geq 25$) are not substantially larger (< 50%) than the impactor, and that the condition of $D_h = 3.175$ mm $= D_p$ is approached at $D_p/T > 50$. Similarly, the cross-section summaries (Figures 11a - 11e) contain the case of $D_p/T \sim 1.0$, and thus, a scale for $T = D_p = 3.175$ mm. For most photographic plates only representative experiments are shown, rather than all experiments; for a detailed photo-documentation of all experiments see the Appendix.

To facilitate the descriptions, comparisons and discussions, we will categorize the target thickness (T) into three major classes: (1) *massive* ($D_p/T < 1$), (2) *thin* ($1 < D_p > 10$) and (3) *foils* ($D_p/T > 10$). This classification is highly arbitrary and has no significance other than to provide a convenient classification for descriptive purposes and clarity.

The most important, first-order result of these penetration experiments relates to the systematic dependence of hole diameter on target thickness, as reported earlier for the 6 km/s case by Hörz *et al.* (1994a). Penetrations in massive targets typically exhibit dimensions approaching that of the standard crater, with D_h systematically decreasing in thinner targets, and especially in foils. The end-member condition of $D_h = D_p$ is generally reached at $D_p/T > 50$. Indeed, all morphologic elements that one may wish to use in the characterization of these features, such as hole size, details of rim and lip features, the bulging of massive targets close to the ballistic limit, and all spallation features at the target's rear, evolve gradually and systematically as a function of T. They are an integral part of a continuum that is characterized by the two end-member cases of (1) the standard crater in infinite halfspace targets and (2) the penetration of an ultra-thin foil where $D_h = D_p$. This systematic dependence on absolute and relative T provides strong evidence and encouragement that absolute impactor dimensions can be extracted from unknown, space-produced penetrations.

Another first-order observation illustrated by Figures 10 and 11 is that the low-velocity experiments not only produce smaller diameter craters, but smaller diameter penetration-holes compared to the high-velocity impacts. Furthermore, T_{BL} increases with velocity. In general, these features were all expected, yet had not been systematically investigated over such a wide range of experimental conditions. For

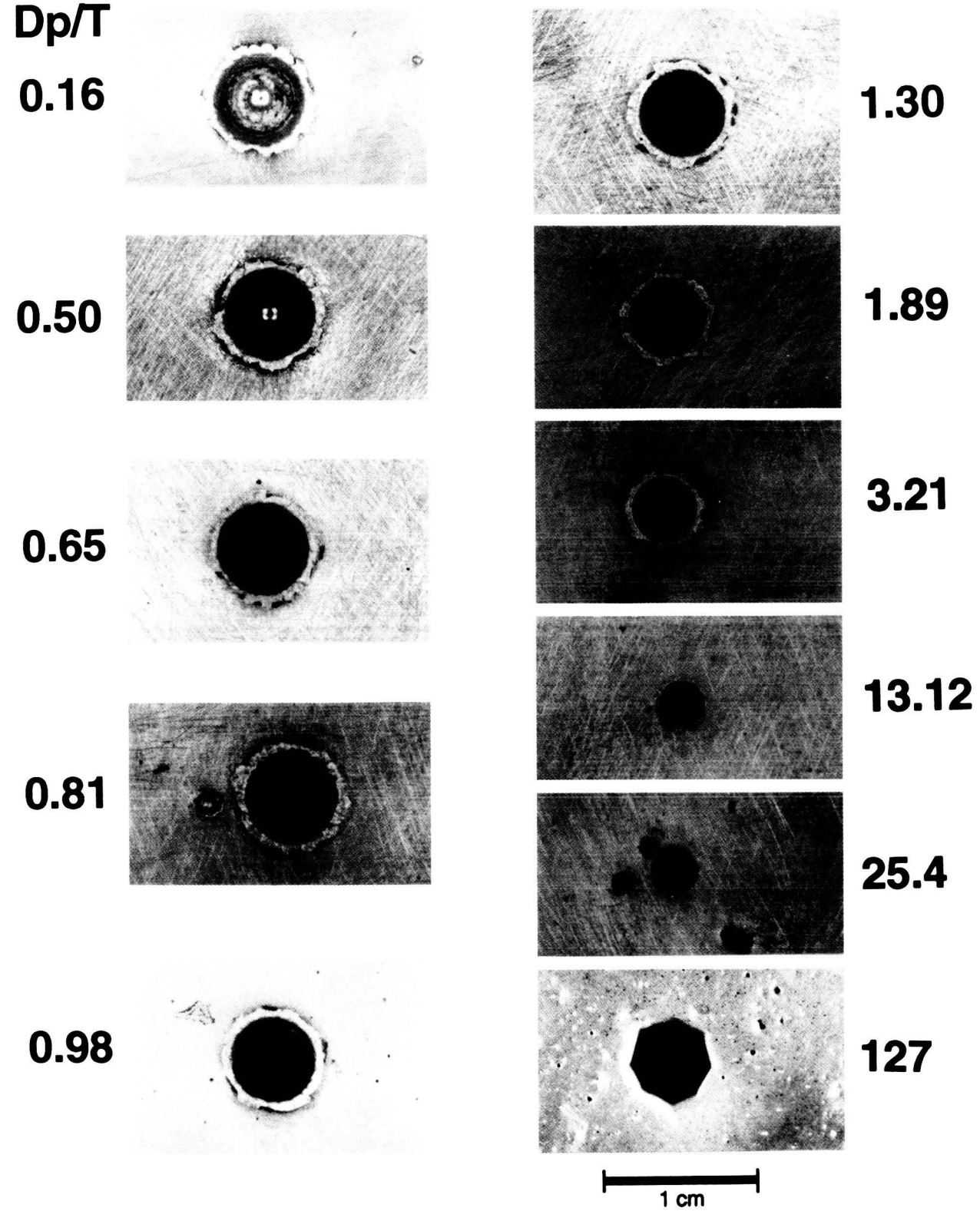

Figure 10a. Front-side views of 2 km/s penetrations of aluminum 1100 targets of widely variable thickness (D_p/T) by soda-lime glass impactors. Note that the detailed rim and lip dimensions for $D_p/T < 1$ are essentially that of the standard crater, and how the penetration hole systematically decreases with decreasing T. The case of $D_p/T = 127$ is anomalous due to tearing of the thin target foil.

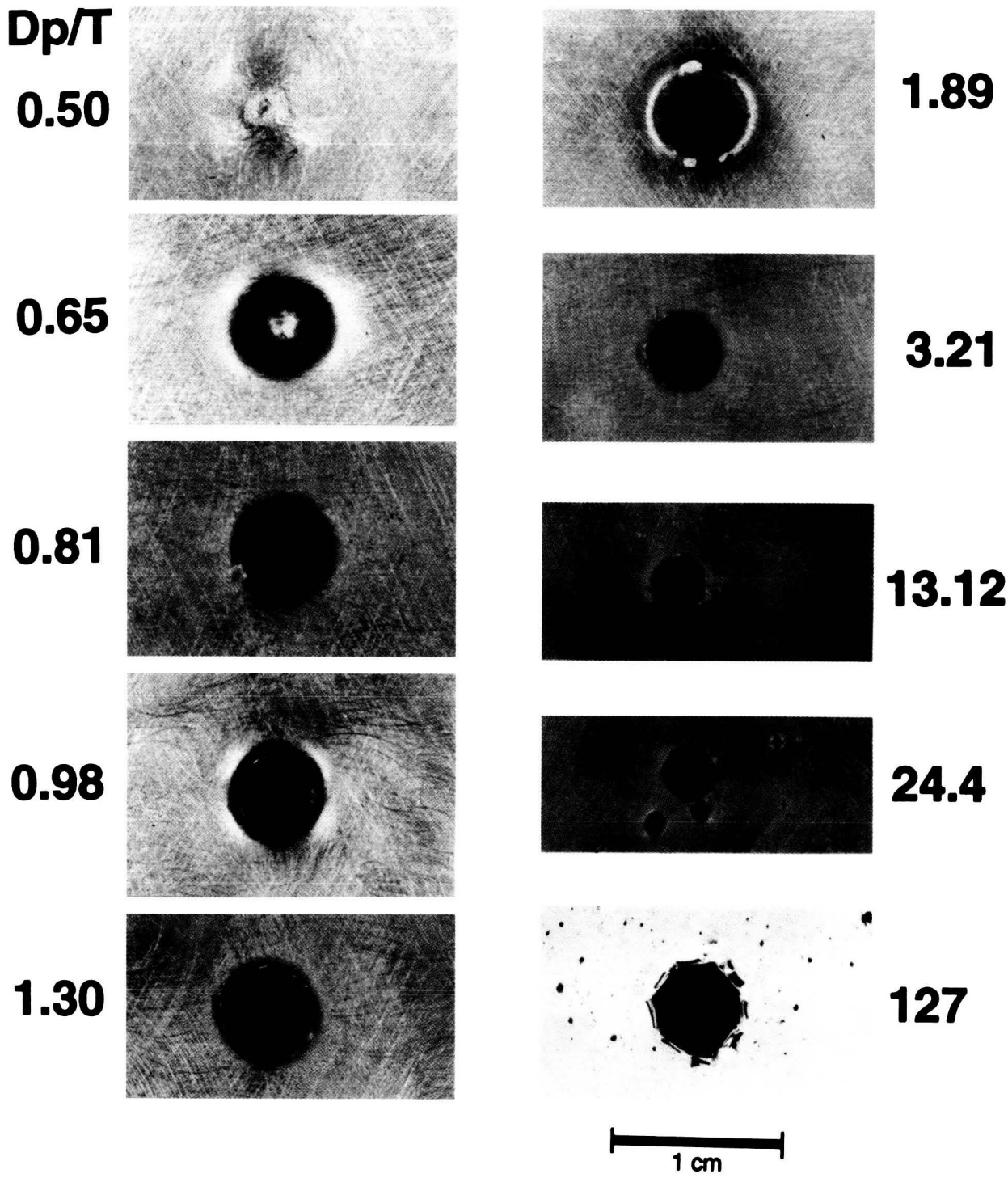

Figure 10b. Back-side views of the 2 km/s penetrations illustrated in Figure 10a.

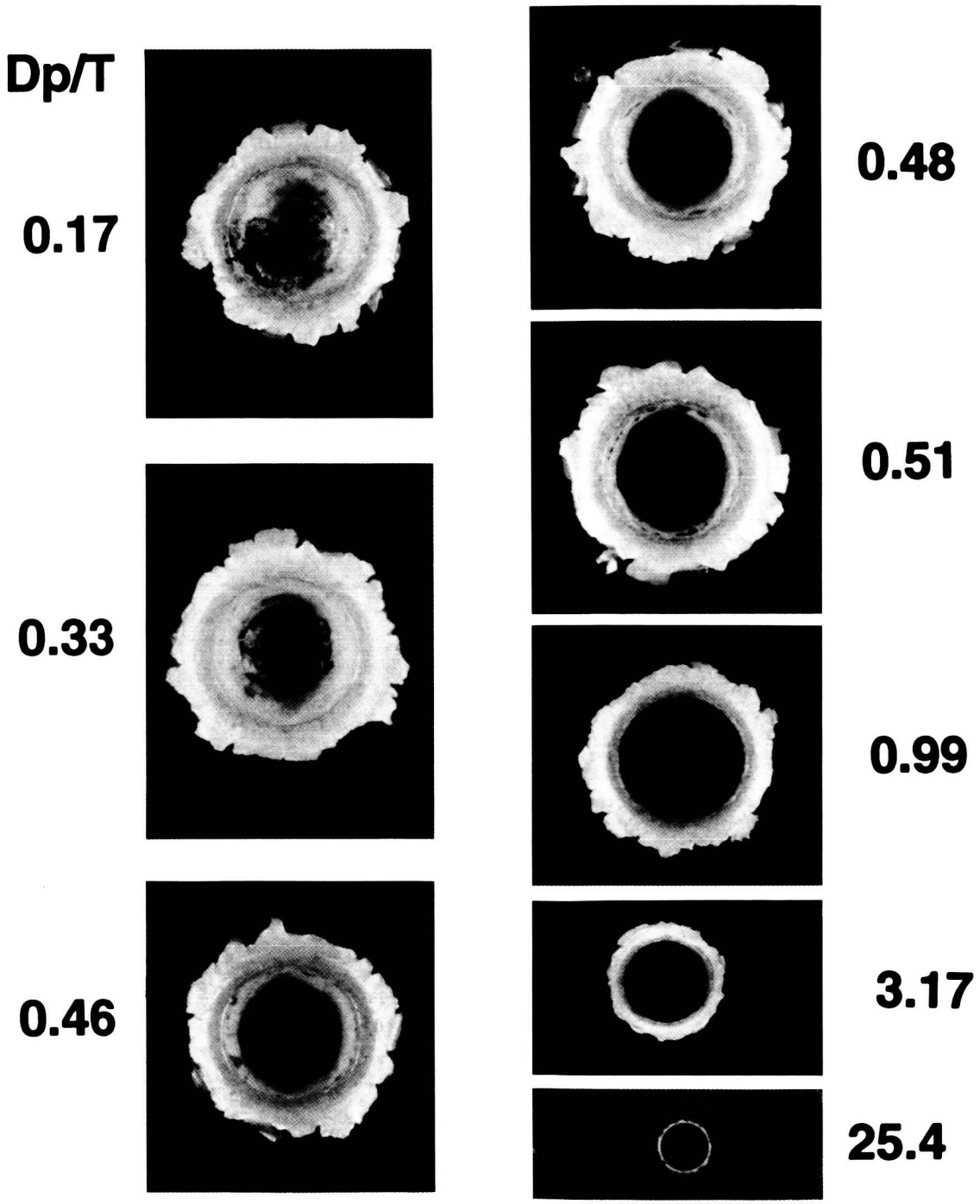

Figure 10c. Front-side views of 4 km/s penetrations of aluminum 1100 targets of widely variable thickness (D_p/T) by soda-lime glass impactors.

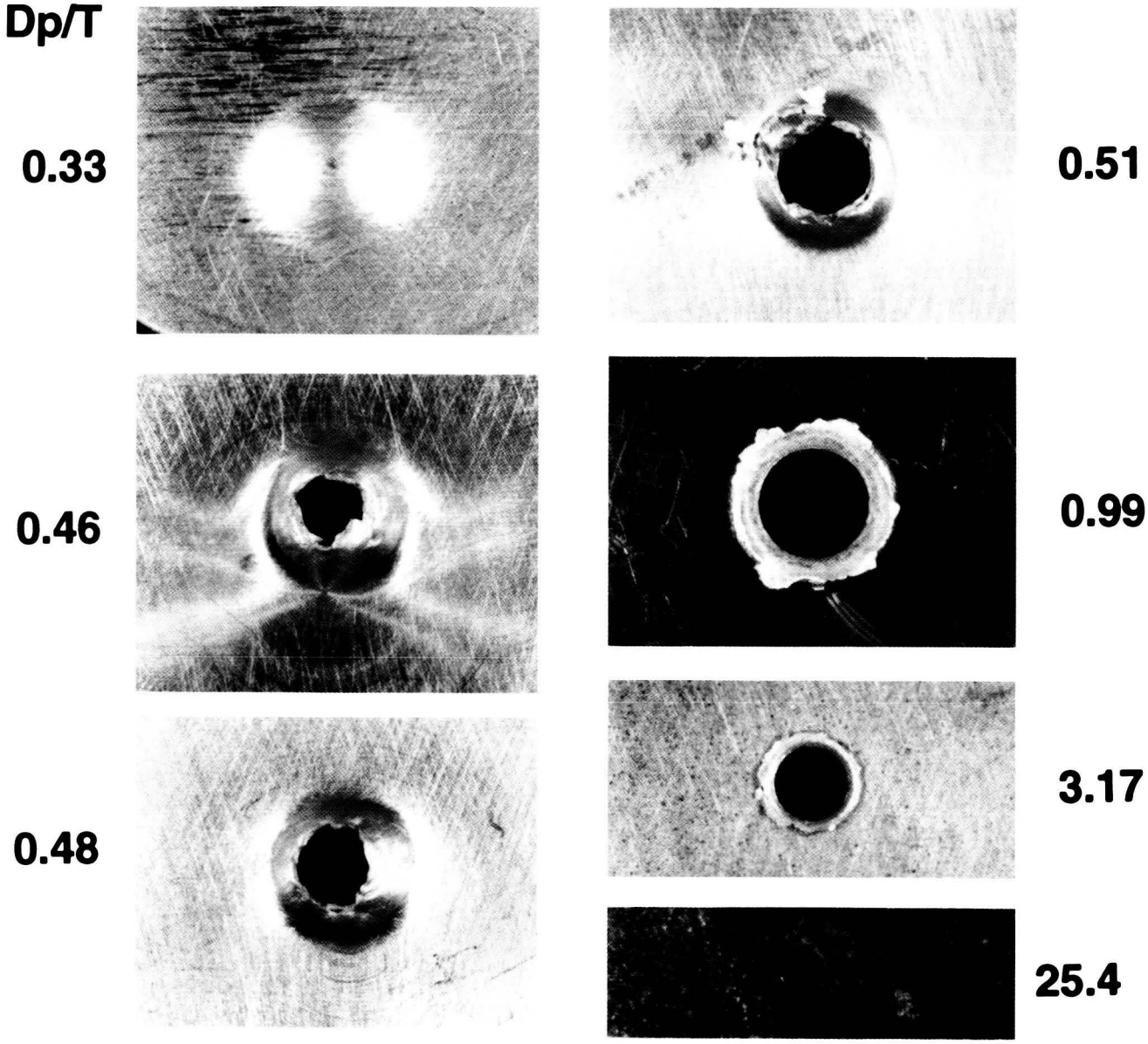

Figure 10d. Back-side views of the 4 km/s penetrations illustrated in Figure 10c. Note the bulging of the target's rear surface and the development of a lip-like structure at the exit side for $D_p/T > 1$.

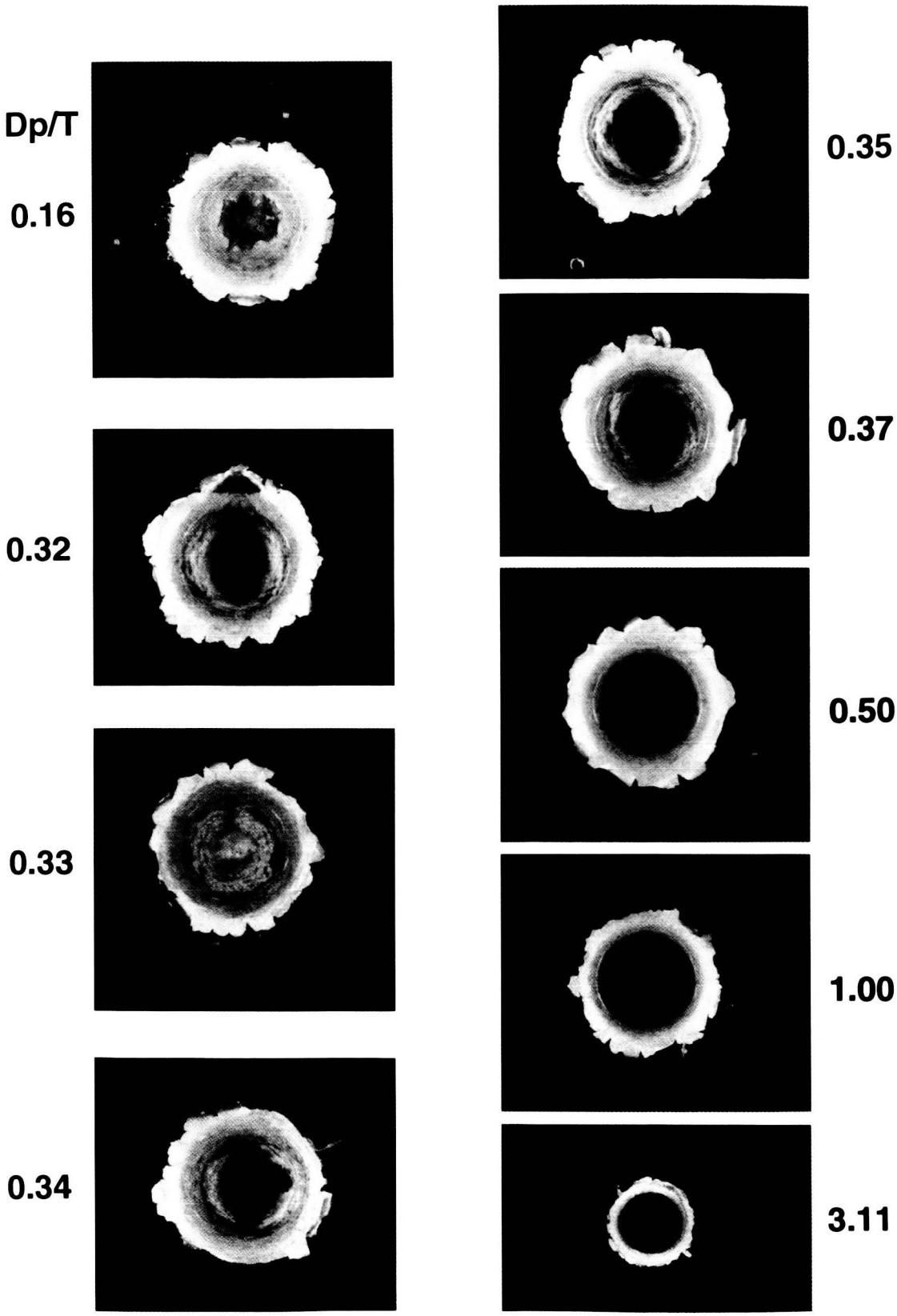

Figure 10e. Front-side views of 5 km/s penetrations of aluminum 1100 targets of widely variable thickness (D_p/T) by soda-lime glass impactors. Note grossly similar morphologies of crater rims and lips for all conditions of $D_p/T < 1$.

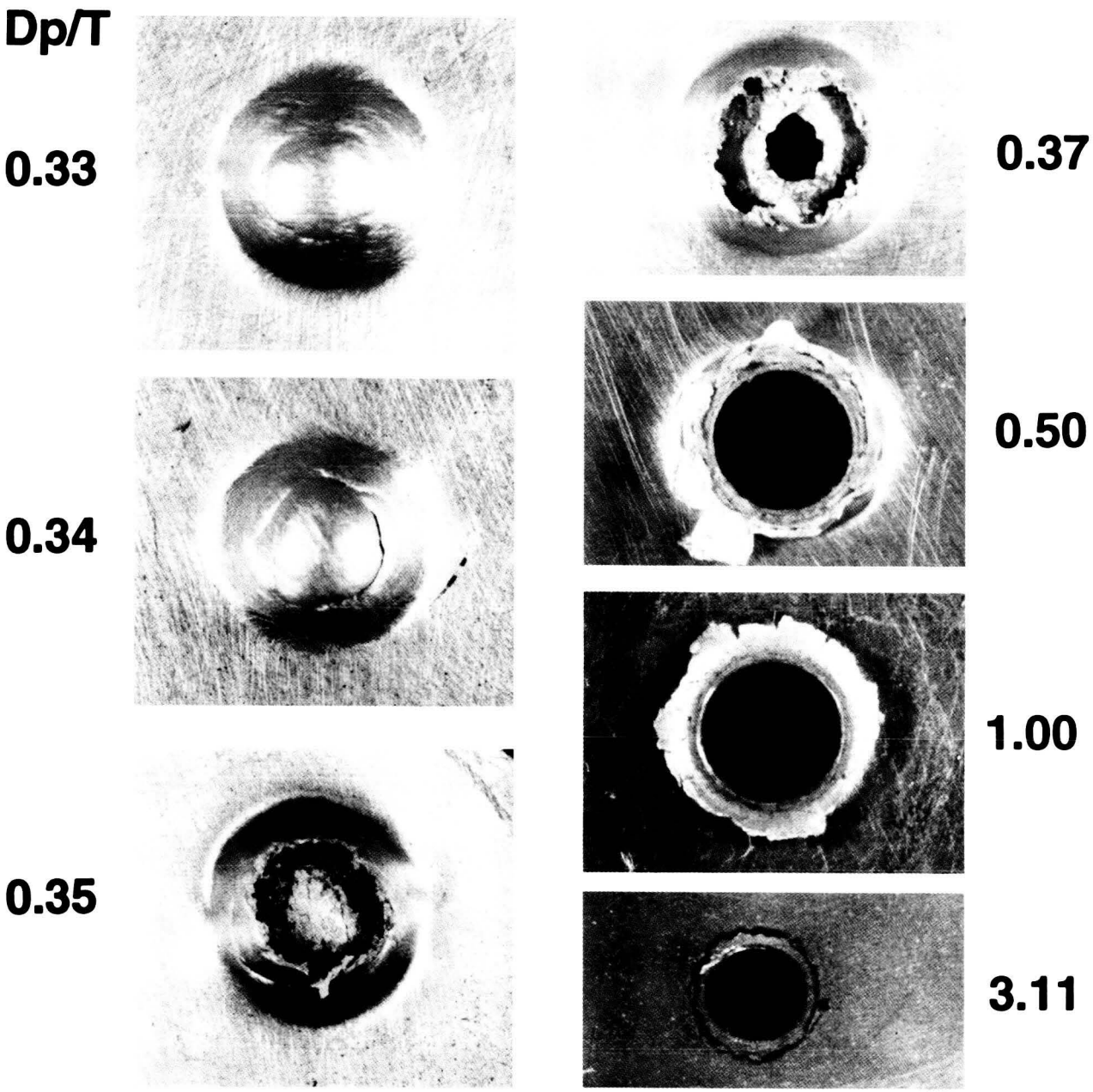

Figure 10f. Back-side views of the 5 km/s penetrations illustrated in Figure 10e. Note the incipient, concentric fracture at $D_p/T = 0.33$ that is further developed at $D_p/T = 0.34$, and that subsequently failed completely at $D_p/T > 0.35$. The formation of, and subsequent failure along the crack attest to the prominent effects of very subtle changes in T close to the ballistic limit (T_{BL}).

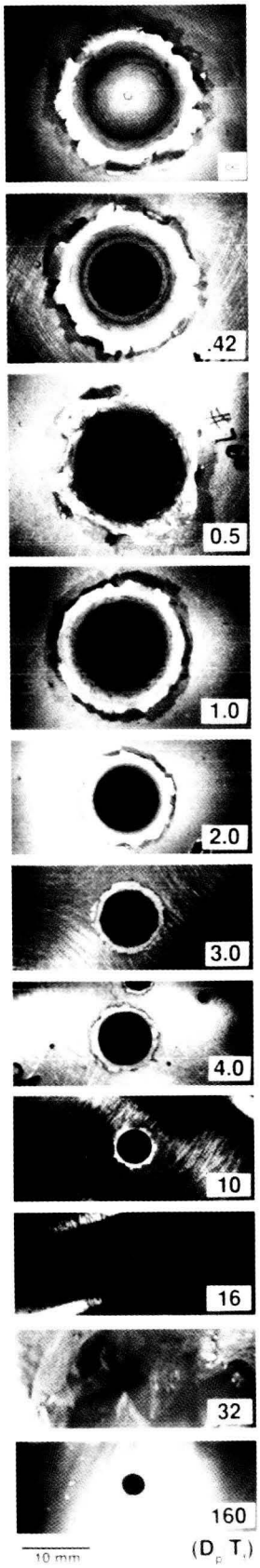

Figure 10g. Front-side views of 5.9 km/s penetrations of aluminum 1100 targets of widely variable thickness (D_p/T) by soda-lime glass impactors. Note how rapidly the size of the penetration holes decreases at $D_p/T > 1$. The condition of $D_h = D_p$ is reached at $D_p/T = 160$. Unfortunately, there are no rear-side views for the 5.9 km/s series.

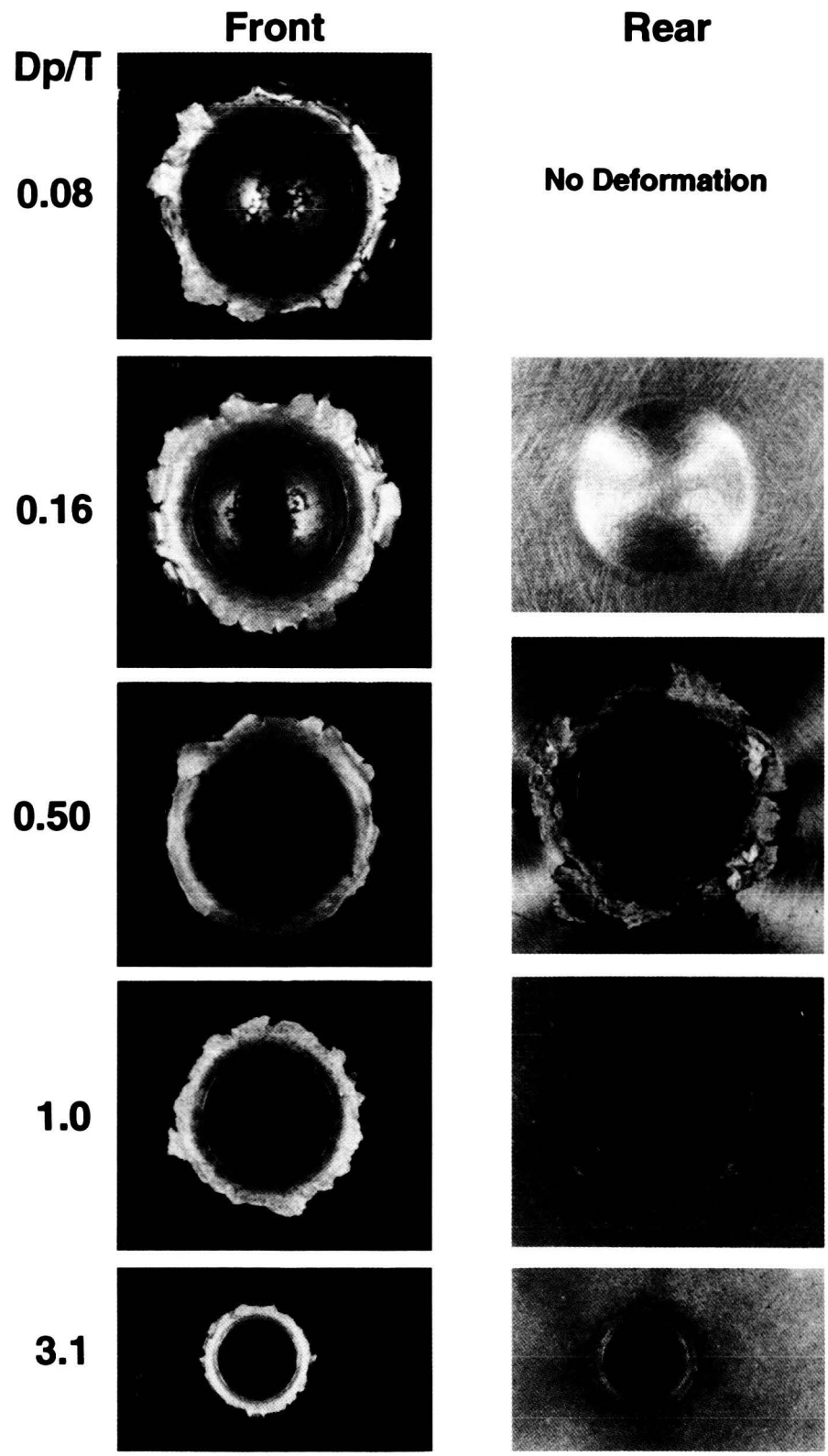

Figure 10h. Front and back-side views of 6.7 km/s penetrations of aluminum 1100 targets of widely variable thickness (D_p/T) by soda-lime glass impactors.

example, compare all cases of $D_p/T \sim 1$ in Figures 11a - 11e for absolute or relative hole size, or compare D_h with the diameter of the standard crater, recalling that its size systematically varies with velocity ($V^{0.59}$; Figure 3a).

Examination of Figures 10a, 10c, 10e and 10g reveals that the relative width of the raised rims and associated lips decreases with decreasing T for all velocities. These effects were noted earlier, and actually measured for the 6 km/s case (Figures 3 & 8 in Hörz *et al.*, 1994a). Measurement of the relative lip width can be a useful, secondary criterion to deduce D_p/T for unknown cases, however, penetration-hole size (D_h) is less ambiguous and the more useful parameter. The extent of the lips in many of these plan views appear more irregular than they are in reality. This is because certain lip sectors may be more vertical (or horizontal) than the average, resulting in irregular outlines in these normal views. Note the substantially torn foil at $D_p/T = 127$ in Figure 10a. Obviously, the low-velocity impactor initiated modest tearing of the foil, with the individual tears bending backwards (Figure 10b). These curled flaps were

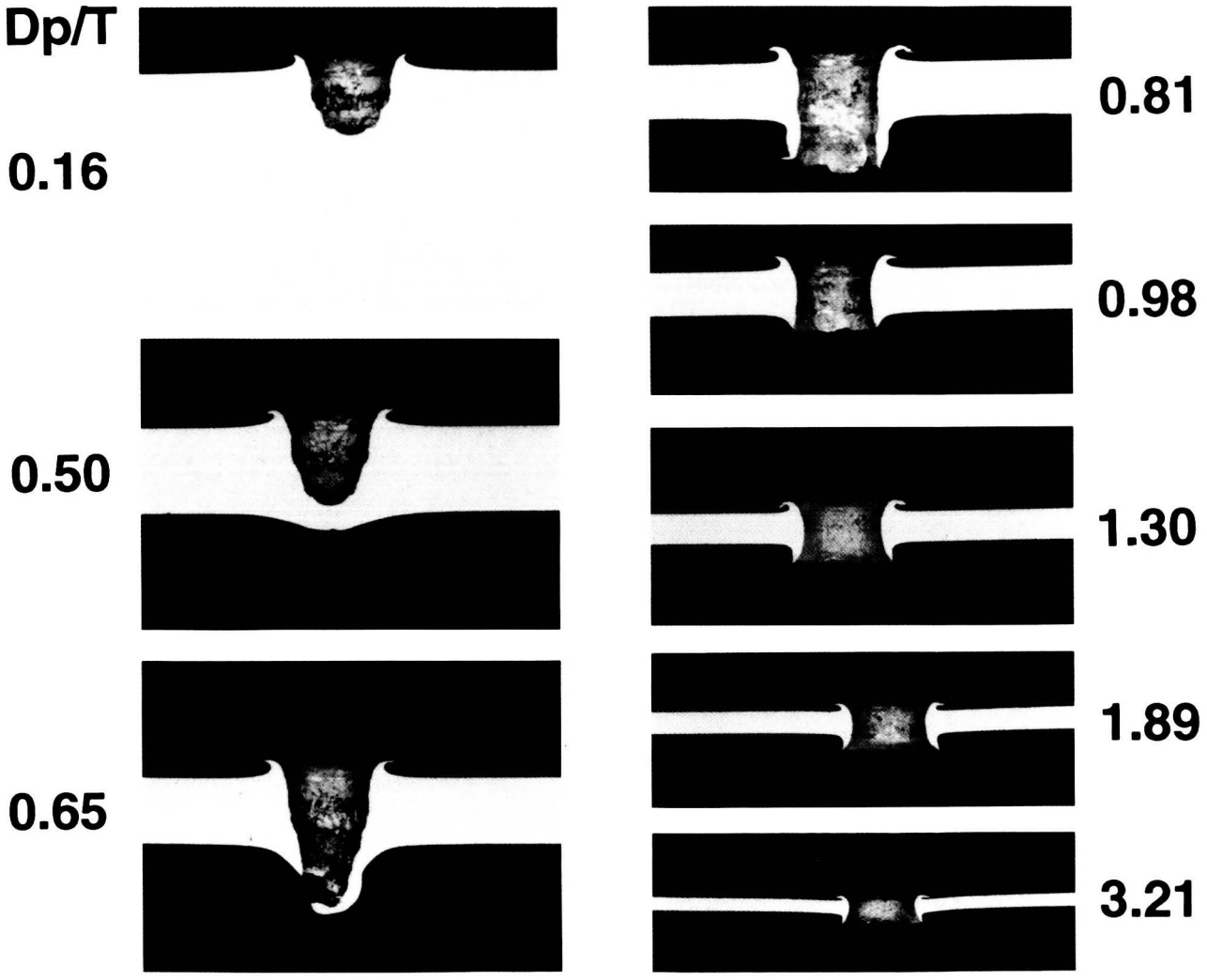

Figure 11a. Cross-sections of craters and penetrations in aluminum 1100 targets of widely variable thickness (D_p/T) by 2 km/s soda-lime glass impactors. Note the substantially deeper crater close to the T_{BL} (*e.g.*, $D_p/T = 0.50$) compared to the standard crater ($D_p/T = 0.16$). In addition, note the, more or less, straight walls of penetration holes at $D_p/T < 0.8$. $D_p/T = 0.98$ can be used for scale in this, and subsequent photographs (*i.e.*, $D_p = 3.175$ mm ~ T).

rotated back to their initial, flat position to facilitate reconstruction and analyses of the actual penetration hole. Such tearing was not observed at higher velocities (*e.g.*, at 6 km/s, $D_p/T = 160$; Figure 10g), nor in penetrated space-exposed foils (*e.g.*, Solar Max thermal louvers), and appears to be a distinctive low-velocity phenomenon.

The rear sides of many targets display prominent bulging prior to physical perforation occurs (*e.g.*, $D_p/T = 0.50$, Figure 10b; $D_p/T = 0.33$, Figure 10d; $D_p/T = 0.16$, Figure 10f). The absolute thickness where such bulging commences is highly dependent on impact velocity, consistent with ballistic limit investigations (*e.g.*, Christiansen, 1993 or Schmidt *et al.*, 1994). No bulging was observed at 2 km/s at $D_p/T = 0.16$ (Figure 10b), yet is very prominent at 6.7 km/s for similar targets (Figure 10f).

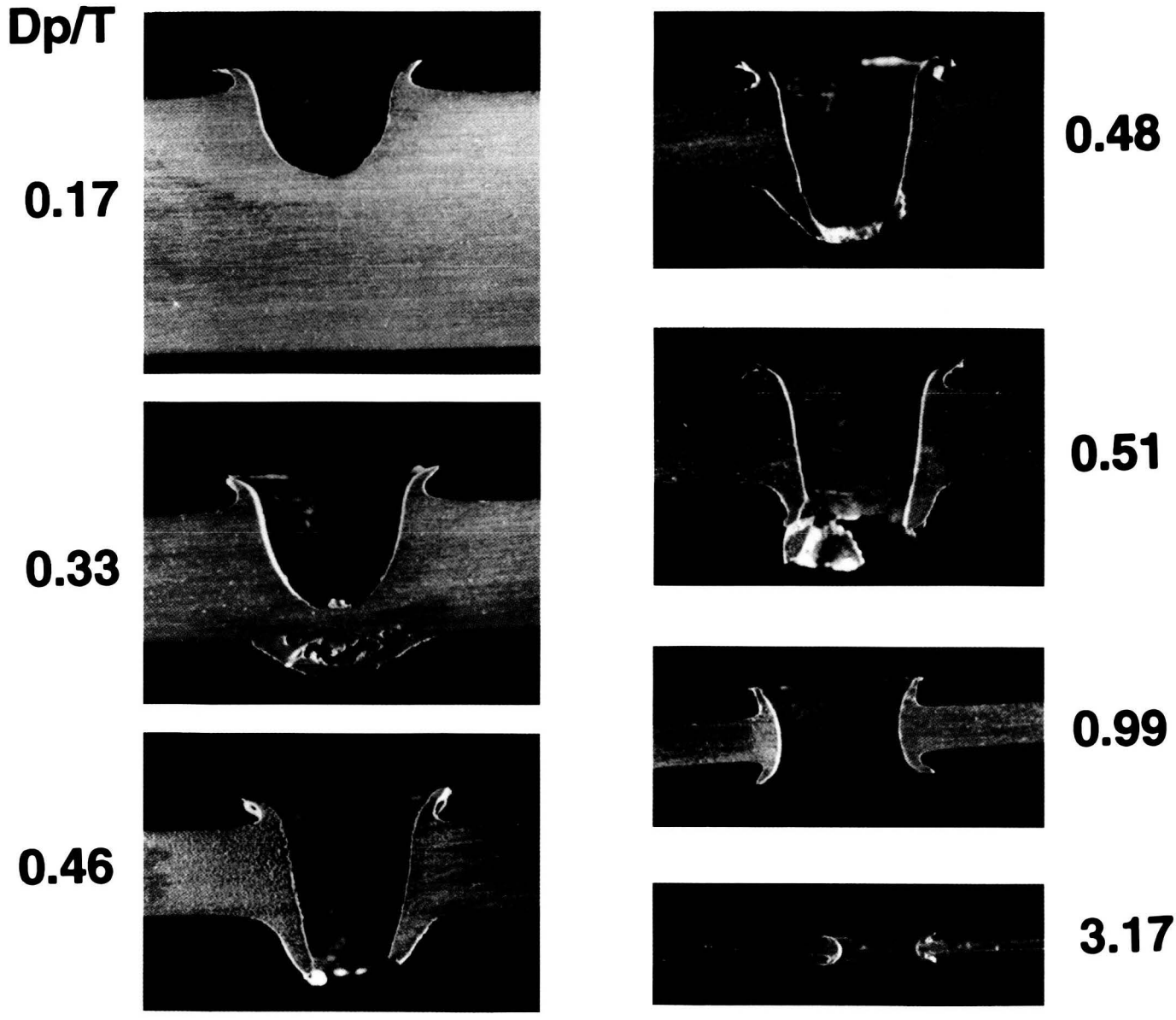

Figure 11b. Cross-sections of craters and penetrations in aluminum 1100 targets of widely variable thickness (D_p/T) by 4 km/s soda-lime glass impactors. Note the bulging of the rear surface and delamination within the target interior at $D_p/T = 0.33$.

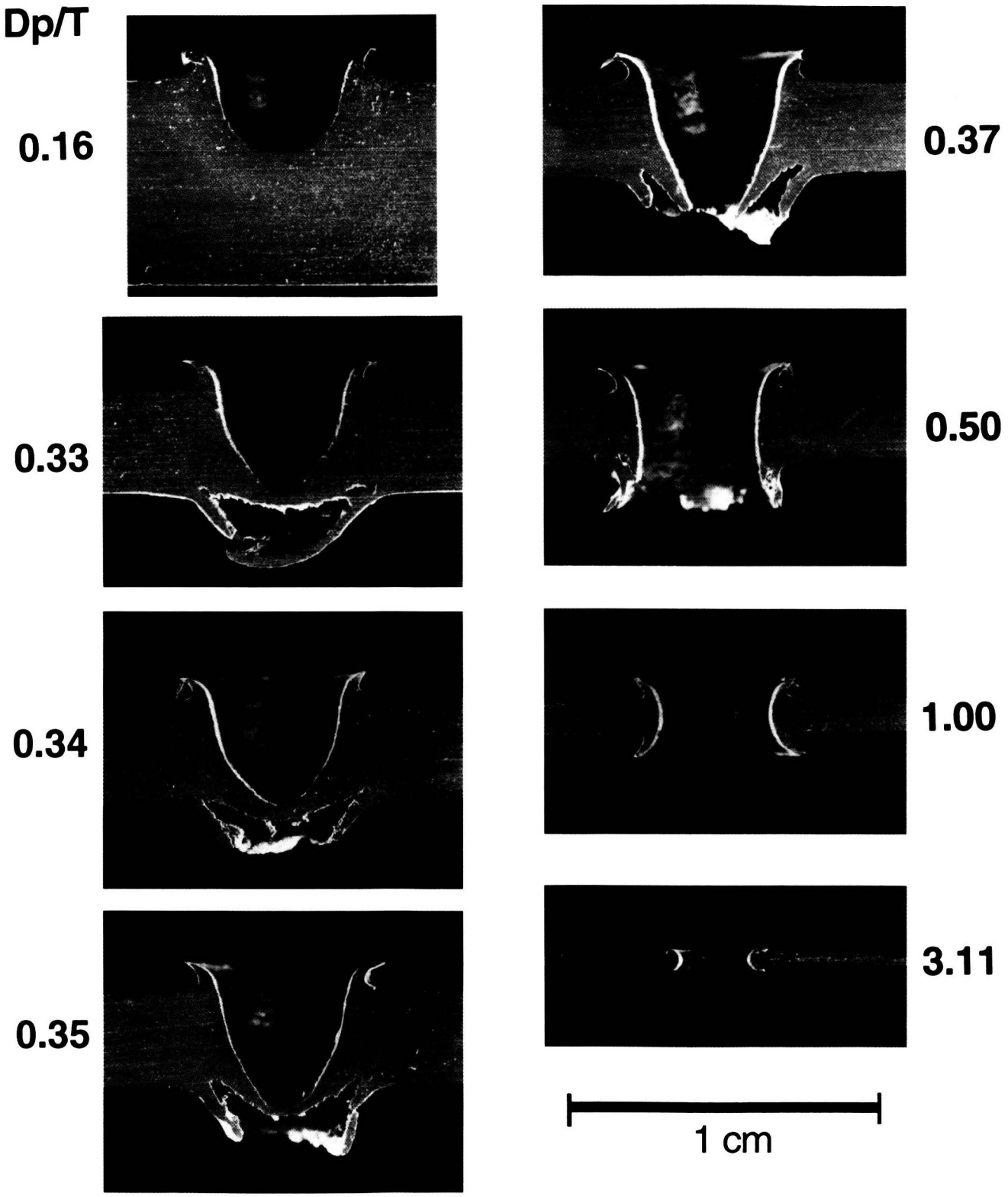

Figure 11c. Cross-sections of craters and penetrations in aluminum 1100 targets of widely variable thickness (D_p/T) by 5 km/s soda-lime glass impactors. Note the removal of a substantial spall plate at the target's rear surface (*e.g.*, $D_p/T = 0.34$ and 0.35) prior to physical penetration at $D_p/T = 0.37$. Compare this case to similar D_p/T values at 2 km/s (Figure 11a).

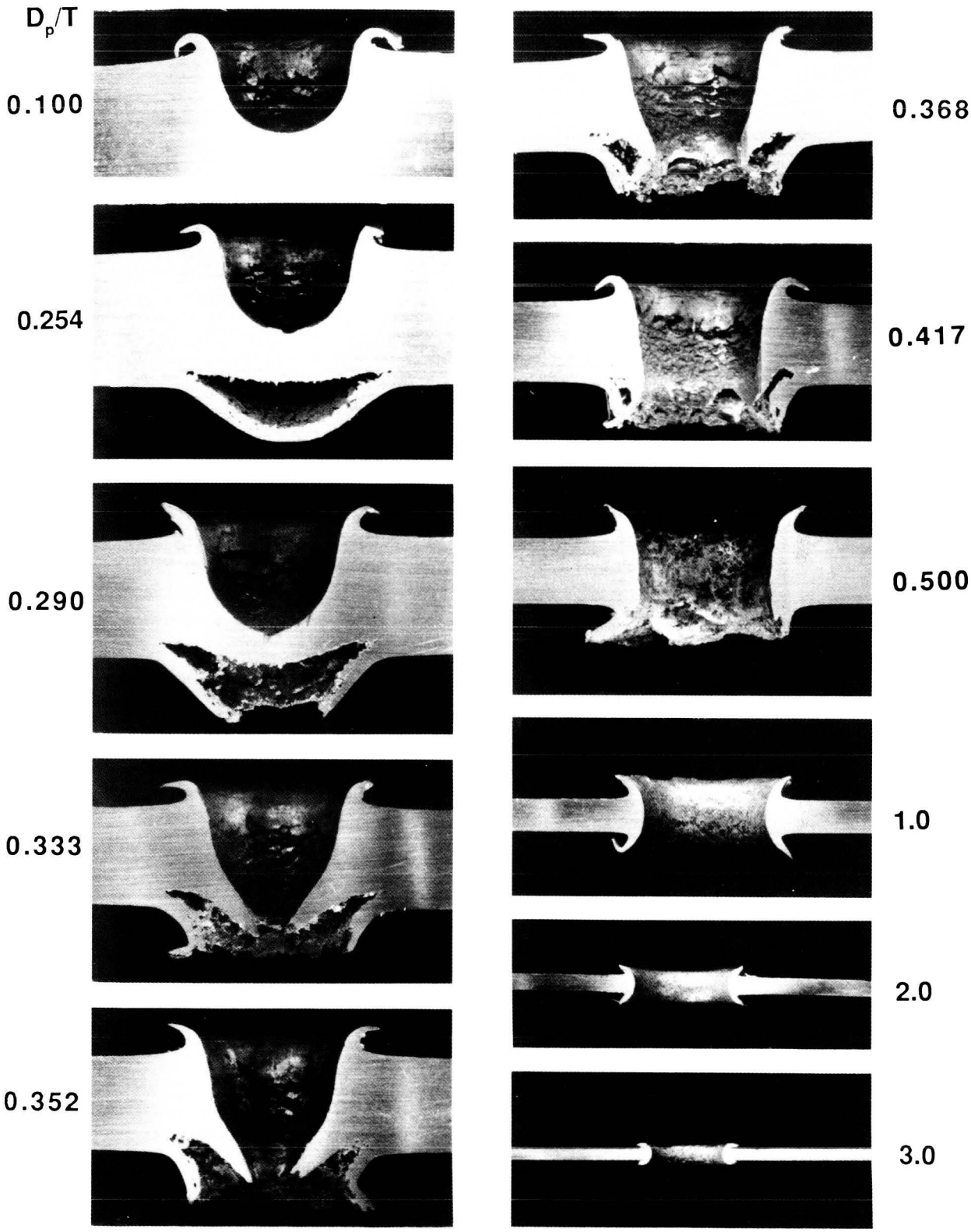

Figure 11d. Cross-sections of craters and penetrations in aluminum 1100 targets of widely variable thickness (D_p/T) by 5.9 km/s soda-lime glass impactors. Note the penetration hole of $D_h << D_p$ at $D_p/T = 0.33$. The initial delamination surface, where bulging of the rear surfaces commences, is relatively straight at $D_p/T = 0.25$, but bulging and deformation of this delamination surface increases rapidly at modestly thinner targets, resulting in anomalously deeper craters.

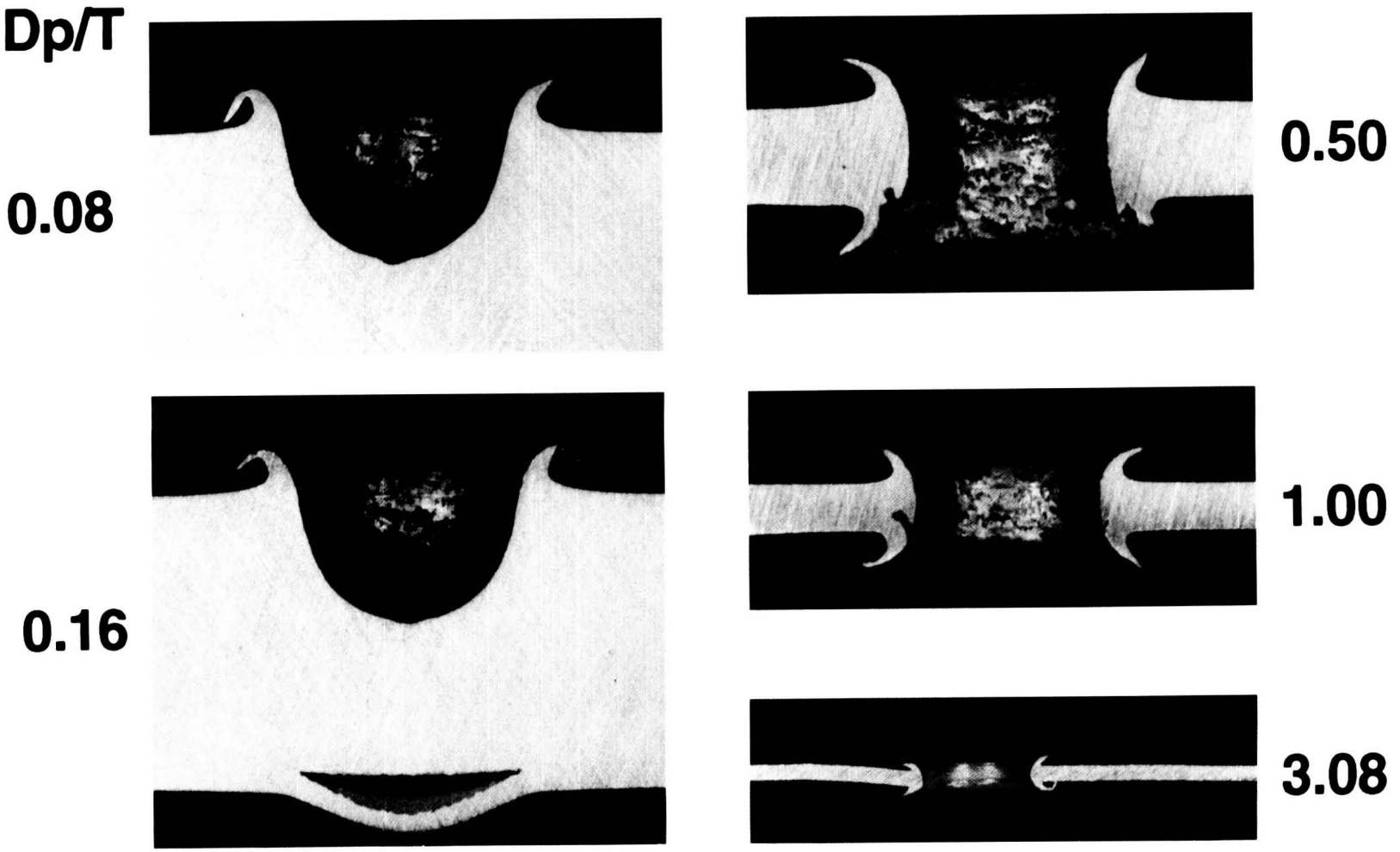

Figure 11e. Cross-sections of craters and penetrations in aluminum 1100 targets of widely variable thickness (D_p/T) by 6.7 km/s soda-lime glass impactors. Compare the D_p/T = 0.16 case with the identical thickness in Figure 10a, as well as the absolute size of penetration holes at $D_p/T \sim 1$ in Figures 10a - 10f.

The cross-sectional views of these targets (Figures 11a - 11e) are the most informative illustrations in discussing the morphologic evolution of penetration holes as a function of T. However, foils of $D_p/T > 10$ are not included in these figures; the reader should consult the Appendix for such thin targets. Targets of $D_p/T < 0.5$ are generally close to the ballistic limit and exhibit especially dramatic variation in delamination, spallation, and penetration phenomena (*e.g.*, Gehrig, 1970). Note the case of constant $D_p/T = 0.33$ in Figures 11b - 11d, which illustrates progressive rear-surface spallation with increasing V. Conversely, consult the range of $0.33 < D_p/T < 0.37$ at 5 km/s (Figure 10c), or $0.25 < D_p/T < 0.36$ at 6 km/s (Figure 11d) to gain an appreciation for the rapid morphologic developments over very subtle differences in T.

As targets approach the ballistic limit they exhibit rear-surface bulging, which is the manifestation of a single lamina that separates from the remainder of the target along a fracture paralleling the target's rear surface. This lamina is substantially stretched and thinned, the amount of which increases with decreasing T. While this lamina increasingly deforms with thinner targets, the actual fracture and delamination surface in the target's interior remains completely undeformed and horizontal over a considerable D_p/T range (*e.g.*, $D_p/T = 0.33$, Figure 11c; $D_p/T = 0.25$, Figure 11d; $D_p/T = 0.16$, Figure 11e). When the target thickness becomes thin enough for this horizontal fracture surface to deform as well, the geometry of the standard crater begins to modify and becomes measurably deeper. Up to this point, the growing crater did not sense the proximity of the target's rear surface, developing a standard crater geometry. However, once the interior delamination surface deforms, crater depth becomes anomalous and increases rapidly until the ballistic limit is exceeded and physical perforation of the entire target is accomplished (*e.g.*, Figure 11d). Note that the 2 km/s case (Figure 11a) did not develop prominent spallation (the rarefaction wave did not exceed the target's tensile failure strength), but it does show the progressive deepening of the crater in response to progressive deformation of the target's rear surface. From these observations it becomes apparent that caution should be exercised in the interpretation of depth measurements for craters that possess bulged and/or spalled rear surfaces, suggesting target thickness close to T_{BL}.

Examination of the lower velocity series reveals that the penetration holes possess relatively straight and inclined walls, resulting in cone-shaped penetration holes at T modestly thinner than T_{BL} (*e.g.*, $D_p/T = 0.65$ and $D_p/T = 0.46$, Figures 11a and 11b, respectively). In contrast, high-velocity penetrations result in curved wall segments in massive targets (*e.g.*, $D_p/T = 0.33$ and 0.35, Figure 11d). However, at $D_p/T > 1$, all targets possess similar, convex wall geometries, irrespective of V. It is suggested that detailed morphological properties of penetration holes in massive targets may contain velocity-sensitive information, yet additional experiments are needed to generate quantitative relationships. Clearly, the target front and exit sides become progressively more difficult to distinguish as T decreases to $D_p/T > 2$, even for the trained eye. It does not appear that penetrations of very thin targets contain any velocity information.

The qualitative observations offered during discussion of Figures 10 and 11 attest that a wide diversity of morphological phenomena are being produced during the penetration of aluminum 1100 targets. These morphologic characteristics, without exception, are part of a continuum that strongly depends on T, for otherwise identical impact conditions. This continuum is bound on one end by the standard crater in infinite halfspace targets, and on the other by the ultra-thin foil that yields the condition of $D_h = D_p$. The various morphological elements seem to develop gradually, in a systematic and predictable fashion as a function of the relative dimensions D_p/T. The hole diameters are so systematically dependent on D_p/T, that quantitative relationships emerge for the reconstruction of typical projectile dimensions from the measurement of D_c or D_h, and knowledge of T and V. Similar, systematic behavior was found for cratering and penetration processes in Teflon^{FEP} targets (Hörz *et al.*, 1994b), as well as lead, inconel, aluminum 6061 and other metals that we have experimented with (Watts *et al.*, 1995; in preparation).

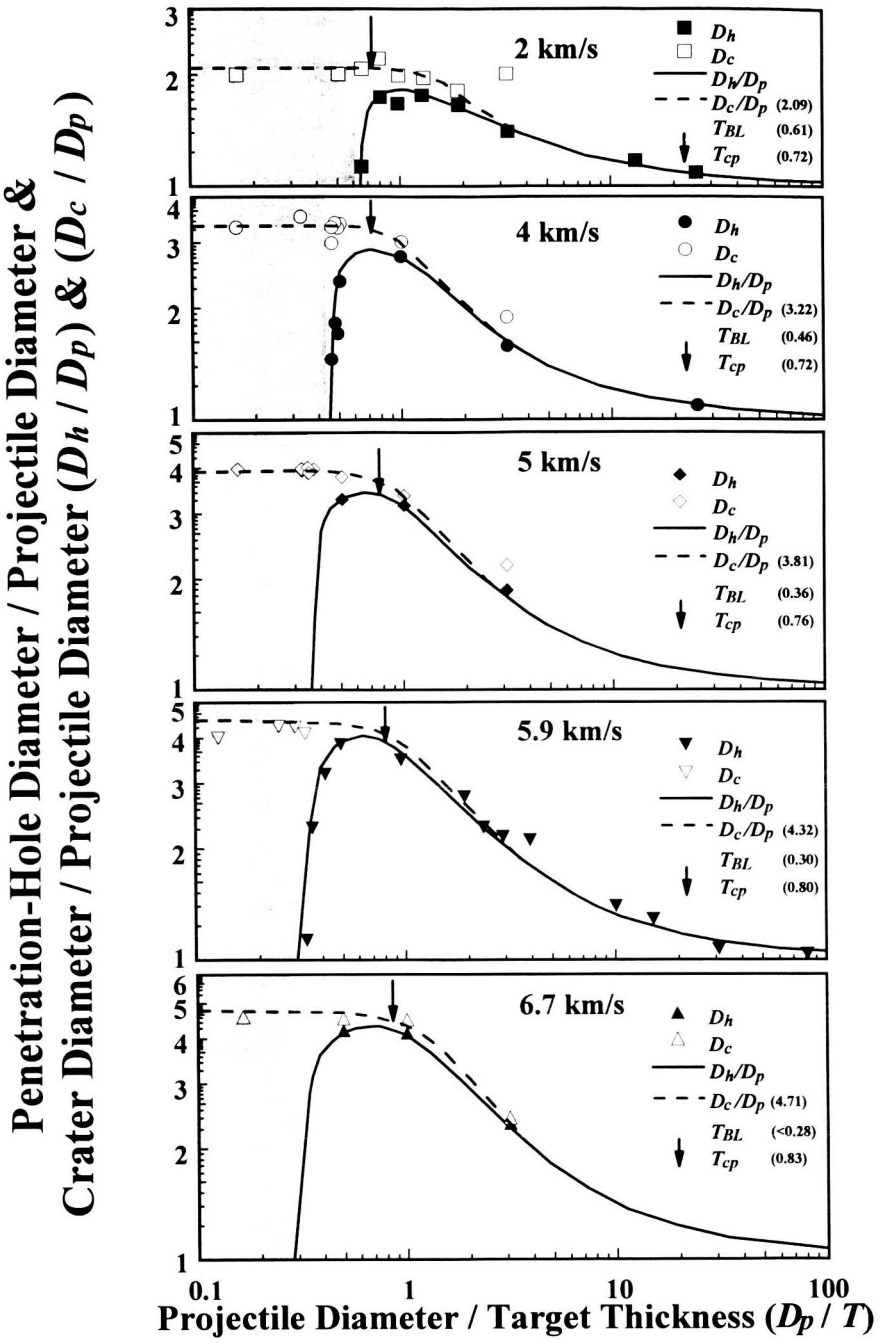

Figure 12. Plot depicting crater diameter (D_c) and penetration hole (D_h) measurements, normalized to impactor dimensions (D_p), as a function of relative projectile and target dimensions (D_p/T) for aluminum 1100 targets at impact velocities of 2, 4, 5, 5.9 and 6.7 km/s. The D_c/D_p ratio for the standard crater (in parentheses) is a constant at any given velocity forming a horizontal line. Note that D_h for massive targets varies greatly over relatively small intervals in D_p/T, and that it is measurably smaller than D_c in most cases; this demonstrates that D_c is the more diagnostic measurement relating to projectile size. The steeply dipping curve of D_h measurements for massive targets extrapolates to the ballistic-limit thickness (T_{BL} at D_h = 0) on the D_p/T axes (values given in parentheses). Table 1 lists the few experiments that produced $D_h < D_p$ which were deleted from these plots for brevity/space considerations, given the log-scales. The stippled area reflects the target thickness that can sustain full cratering events. Thus, all targets to the right of the stippled area will be perforated. The arrow indicates the D_p/T values where the pulse duration in the target and projectile are equal ($t_p = t_t$) with the corresponding D_p/T values given in parentheses.

Penetration-Holes: Measurements and Interpretations

All dimensional measurements are summarized in Table 1. Figure 12 present the detailed diameter measurements for craters (D_c) and penetration holes (D_h), plotted as a function of the relative target dimensions (D_p/T) for each of the five experimental velocities. These measurements and plots constitute the essence of the present investigations, because we consider D_c and D_h to be the primary measurements for estimating projectile sizes from space-retrieved surfaces. Similar to Hörz *et al.* (1994a, 1994b), we found that measurements of such features as D_l or D_r to be less informative and/or mimic the trends observed in the D_c and D_h measurements (see Table 1). In addition, note that we now refer to the 6 km/s case more appropriately as 5.9 km/s, consistent with the average experimental encounter velocities.

Returning to Figure 12, the standard craters in infinite halfspace targets are represented by the horizontal, dashed line, because the D_c/D_p ratio (value given in parentheses) remains a constant for any given velocity. Importantly, the D_c measurements associated with standard craters are also typical (up to $\sim D_p/T = 1$) for the entrance side of penetrations in relatively massive targets. Consequently, the horizontal, dashed line of constant D_c/D_p, appropriate for standard craters, extends substantially into the penetration regime. It is only at conditions of $\sim D_p/T > 1$, that the surface diameter for penetrations becomes noticeably smaller than that of the standard crater (*i.e.*, $D_{c_{penetration}} < D_{c_{crater}}$). Distinction between D_c and D_h is essentially impractical and not necessary at $D_p/T > 5$, as both dimensions are virtually identical. However, by definition, D_c is always somewhat larger than D_h, given the convex walls of all penetration holes at $D_p/T > 1$.

The D_h measurements for the more massive targets define a steeply dipping curve in Figure 12 that is largely driven by the condition of $D_h = 0$ at the exact ballistic limit (T_{BL}). This slope becomes ideally vertical at T_{BL} and separates the cratering field (stippled in Figure 12) from that of physical perforation (all events to the right of the stippled area). Clearly, the steepening of this curve is predominantly defined by penetrations of $D_h < D_p$ (off scale in this figure, see Table 1), and more generally by features of $D_h << D_c$ (see Hörz *et al.*, 1994a and 1994b). Any curve fitting procedure through these data will yield an intercept on the D_p/T axis that defines T_{BL} (value given in parentheses), in terms of D_p/T. Note how T_{BL} systematically increases with increasing impact velocity, being at $D_p/T = 0.62$ for 2 km/s and at $D_p/T = 0.27$ for 6.7 km/s (*i.e.*, more than a factor of two difference in T over the velocity range investigated, consistent with previous studies [*e.g.*, Hermannn and Wilbeck, 1986 or Cour-Palais, 1987]).

General ballistic-limit determinations remain largely empirical due to idiosyncrasies in the dynamic response, primarily of tensile failure strength, of many commercial materials. Such experiments can be time-consuming and costly. The extrapolation of measured penetration-hole diameters to the ballistic limit ($D_h = 0$), as illustrated in Figure 12, permits T_{BL} to be determined with relatively few experiments. By varying T in sufficiently small increments one needs to produce (1) a standard crater in an infinite halfspace target yielding a measure of D_c, (2) one marginal penetration ($D_h < D_p$), and (3) several substantial penetrations, all of $D_h << D_c$. All holes of $D_h << D_c$ are of use for some graphic (or rigorous) curve-fitting procedure to obtain a precise intercept on the D_p/T axis for $D_h = 0$, and thus, an exact T_{BL}. This includes rather large penetration holes that may have been previously discarded as having significantly overshot the ballistic limit. We suggest that this is a relatively efficient way, necessitating less than ten experiments, to produce T_{BL} for many engineering applications.

As discussed in detail by Hörz *et al.* (1994a, 1994b), penetrations of massive targets must be viewed, to first order, as craters that had their bottoms truncated. This argument derives primarily from the transitional nature of cratering and penetration processes, as illustrated in Figures 10 and 11. The quantitative argument is based on Figure 12, which demonstrates that penetrations in massive targets have entrance-hole morphologies and dimensions (D_c) essentially identical to those of a standard crater in the same material. The cratering flow fields set in motion according to the prevalent initial conditions do not appear to be disturbed by the rarefaction waves from the target's rear surface. As T decreases, this flow field is modified and essentially terminated at increasingly closer distances to the target's front side. For massive targets, the initial flow field may grow to full standard crater size, yet material motions in deep-

seated target volumes, occupying the prospective crater bottoms, are severely affected and essentially terminated by the rarefaction wave.

This behavior may be understood by considering the duration of the shock-pulse (t) in both the target (t_t) and projectile (t_p). The shorter of the two pulses defines the duration of the compressive phase of any collisional event. In a typical cratering event in infinite halfspace targets, this pulse duration is completely controlled by the comparatively small impactor (*i.e.*, $t_p << t_t$). As T decreases, a condition will be reached where $t_t = t_p$; if the target and projectile are composed of the same material, this condition applies at $D_p/T = 1$. As T decreases to $D_p/T >> 1$, the pulse duration in the target will become (much) shorter than that in the impactor (*i.e.*, $t_p >> t_t$). Obviously, such an event cannot produce cratering motions within the target that are characteristic of full-fledged cratering events in infinite halfspace targets (*e.g.*, Maxwell, 1977). The flow field will have smaller dimensions in thin targets and foils, resulting in penetration-holes that will have radial [and vertical] dimensions much smaller than the standard crater.

Following these considerations we used the equation-of-state data by Marsh (1980) for quartz glass and aluminum 1100, and the computational method of Cintala (1992) to calculate shock velocities and associated pulse durations in the projectiles and targets at our specific impact velocities, and to determine their relative dimensions (D_p/T) that satisfy the condition of $t_p = t_t$. This condition is indicated by the vertical arrows in Figure 12 and it is termed T_{cp}, because it corresponds to the *transition of cratering to penetration* following the above considerations of pulse duration. The position of T_{cp} in D_p/T space (given in parentheses) closely conforms to our postulate of a relatively constant diameter D_c for craters and penetrations at all conditions of $t_p < t_t$. Note that hole diameters approximate crater dimensions at D_p/T values that are close to the T_{cp} arrow, and that D_c and D_h systematically decrease at target thickness of $t_p > t_t$. We consider this evidence that the condition of $t_p = t_t$ constitutes a useful criterion in distinguishing -- at the target surface via measurement of D_c -- between crater-like structures and genuine penetration holes when interpreting impactor sizes for unknown events on space-retrieved surfaces.

Therefore, the parameter of interest to obtain projectile dimensions from unknown penetrations is D_c, measured at the original target surface, rather than D_h, measured at some arbitrary target depth. The penetration hole changes almost arbitrarily in size relative to actual initial conditions, especially for the condition of $D_h << D_c$ in massive targets. The range in D_p/T over which $D_h << D_c$ applies is substantially beyond T_{BL}, typically by factors of 2 to 3. The preferred and diagnostic measurement for all penetrations that possess rim morphologies at the target front side which closely resemble that of a standard crater is D_c, and not D_h. This specifically includes the most massive penetrations simulated (see Figure 11), as already detailed by Hörz *et al.* (1994a, 1994b). In practice, such truncated cratering events may be recognized by the fact that the rear side is still dominated by spallation processes, at least in annealed aluminum 1100. Once crater-like rims and associated lips develop on the rear surface of aluminum 1100 targets the event may be classified as a true penetrations.

The penetration behavior of aluminum 1100 at $D_p/T > 1$ is akin to that of Teflon (Hörz *et al.*, 1994b) and many other materials (*e.g.*, Carey *et al.*, 1985; Hermannn and Wilbeck, 1987); D_h systematically decreases with decreasing T. However, none of the previous reports, except Hörz *et al.* (1994a, 1994b), appear to have utilized targets of $D_p/T > 100$. Note that the condition of $D_p/T = 10$ yields penetration holes in aluminum 1100 approximately a factor of two larger than D_p (at ~6 km/s). From Figure 12 we also conclude that the important boundary condition of $D_p/D_h = 1$ is reached, for most practical purposes, at $D_p/T \sim 100$. This condition is virtually independent of impact velocity, a very important result to which we will return later.

Figure 13 summarizes the most pertinent measurements, either D_c or D_h, in a single plot for ease of comparison, and additionally presents our suggestions for extrapolating the experimental results at < 7 km/s to higher model velocities of 10, 15 and 20 km/s. The rationale to plot either D_c or D_h only relates to our perception of what constitutes the most diagnostic measurement at any given D_p/T that is readily obtained from space-produced penetrations.

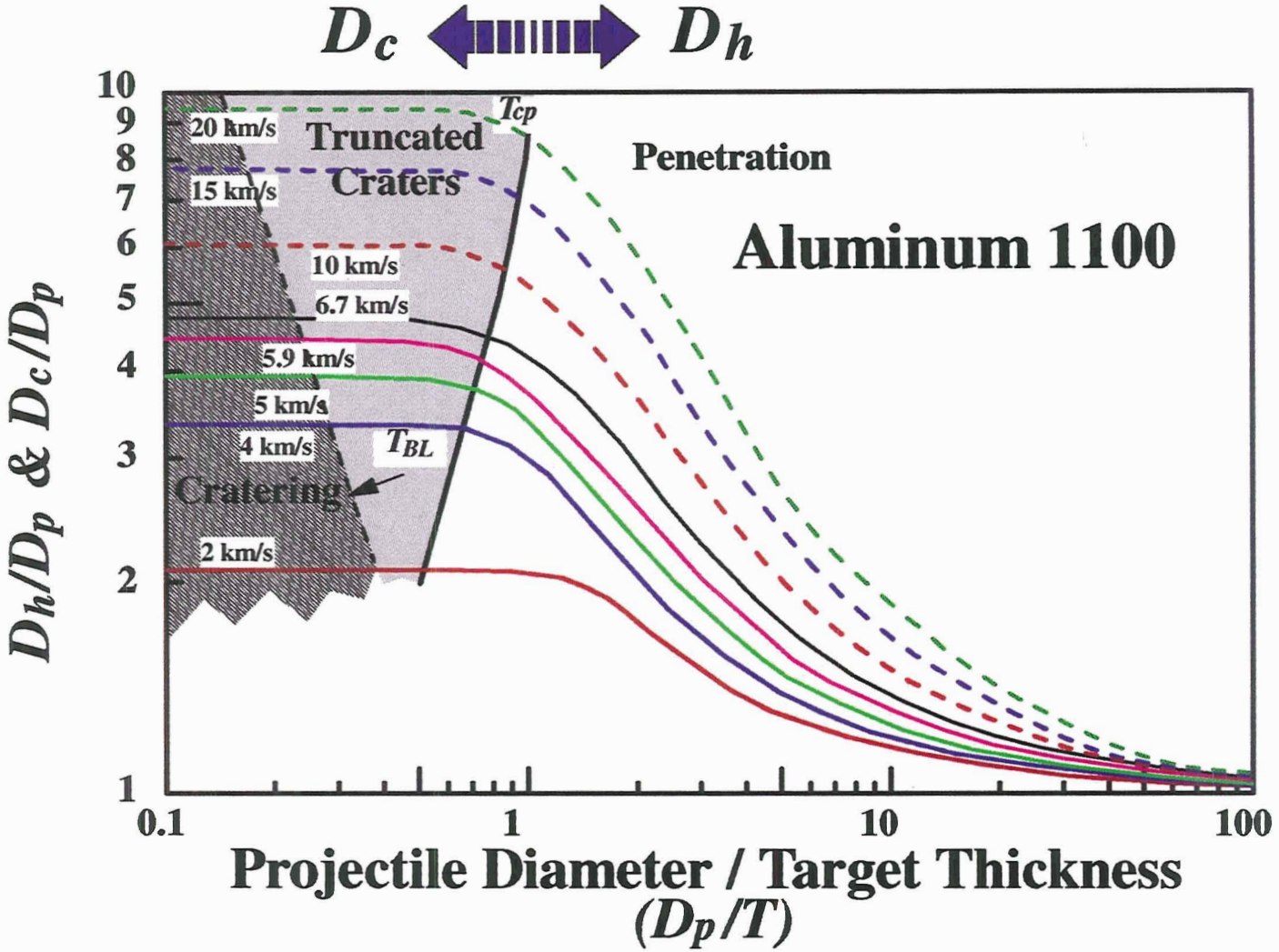

Figure 13. Summary of experimental observations (D_c and D_h) for the velocity range of 2 to 7 km/s as a function of target thickness, and extrapolation to higher velocities using the concept of relative pulse duration as discussed in the text.

The experimental data verify the strong velocity dependence of cratering and penetration phenomena in massive targets, typically of $D_p/T < 1$. In contrast, projectile velocity seems to be of little consequence in producing a hole approximately the size of the impactor at $D_p/T \sim 100$. Therefore, we reach the important conclusion that the relative dimensions of the projectile and target (D_p/T) are important considerations in the velocity-scaling of penetration phenomena. The variable slopes displayed at any constant velocity imply that there is not a single, constant velocity exponent with which to scale penetrations in widely variable target thickness. Such exponents depend on the V and D_p/T. Obviously, cratering and penetrations in massive targets are more sensitively related to V than are penetrations in thin foils.

Extrapolation of the experimental data to higher velocities is based on a number of assumptions, first detailed by Hörz *et al.* (1994a). The present extrapolations in aluminum 1100 targets rely exclusively on experiments at $V > 5$ km/s, because the experiments of $V < 4$ km/s, and especially those at 2 km/s, are unsuitable for describing the hydrodynamic behavior of aluminum at very high velocities. The relative crater diameter (D_c/D_p) at $V > 10$ km in Figure 13 is based on Figure 3 and an associated velocity dependence of $V^{0.59}$. Also shown in Figure 13 is a ballistic-limit line based Cour-Palais (1987) and Christiansen (1993), who suggest that $T_{BL} = 1.8P$ with $P = 0.5D_c$ at $V > 5$ km/s and increasing with $V^{2/3}$. The purpose of the T_{BL} curve in Figure 13 is to merely delineate the boundary between cratering and incipient perforation, and is not critical for the discussion(s) that follow. At any given velocity, all targets to the left of this line will act as infinite halfspace targets, while those to the right will be perforated.

Consistent with Figure 12, we extend a constant, relative crater size (D_c/D_p) into the field of (massive) penetrations in Figure 13. Furthermore, we calculated the shock velocities for both the projectile and target, at encounter velocities up to 20 km/s, to determine T_{cp}, for the condition of $t_p = t_t$. Following Figure 12, this T_{cp} line marks the onset of penetration holes of dimensions $D_h < D_c$. Penetrations to the left of this line should be viewed as truncated cratering events, while events to the right represent genuine penetrations that are -- by definition -- characterized by $t_p > t_t$ and by the observation as having $D_h < D_c$.

Construction of the > 10 km/s penetration curves at $D_p/T > 1$ was accomplished as follows: the constant (horizontal) D_c/D_p line -- appropriate for any given velocity -- was extended into the penetration field until it intersected the T_{cp} curve. This intercept defines the relative target thickness (D_p/T) that classifies all events into truncated craters (characterized by $t_t > t_p$) and as genuine penetrations ($t_t < t_p$) for a given model velocity. This intercept must be viewed as a well defined, velocity-dependent locus through which any cratering and penetration curves must pass. A second locus through which all penetration curves must pass is represented by the condition of $D_h = D_p$ for very thin foils (*i.e.*, $D_h/D_p \sim 1$ at $D_p/T = 100$), regardless of absolute encounter velocity. The actual curves shown for the intermediate target thickness ($1 < D_p/T < 100$) merely connect these two loci by graphical extrapolation that parallels and mimics the empirical, experimental curves as best as possible. While details of the modeled curves are somewhat intuitive, there can be little doubt that their slopes are highly velocity dependent and variable. Even the empirical curves steepen with increasing velocity, because D_c/D_p increases much more rapidly in massive targets than does D_h/D_p in thin films. There appears to be little room for substantially different relationships, at $V > 10$ km/s, other than those shown in Figure 13, if one accepts our concept of pulse duration in distinguishing between cratering and penetrations. Clearly, more rigorous treatment of the experimental data and their extrapolation to higher impact velocities is warranted. As is, Figure 13 merely illustrates some new, conceptual framework for such extrapolations. Hydrocode calculations are particularly well suited to first duplicate the experimental trends and to test our concepts and suggestions embedded in Figure 13.

Consistent with the intended application of these experiments, Figure 14 summarizes the experimental data, and their extrapolations to higher velocities, in such a way as to permit a direct and unique determination of unknown projectile sizes (D_p) from the readily obtained measurements of D_h and T, for any penetration event. Note that the unknown impactor is part of both the abscissa and ordinate in most previous investigations, and that Figure 14 purposely separates the measurable quantities from the unknown(s). Figure 14 is essentially a plot of D_h versus D_p. Therefore, it represents the desired

Page Intentionally Left Blank

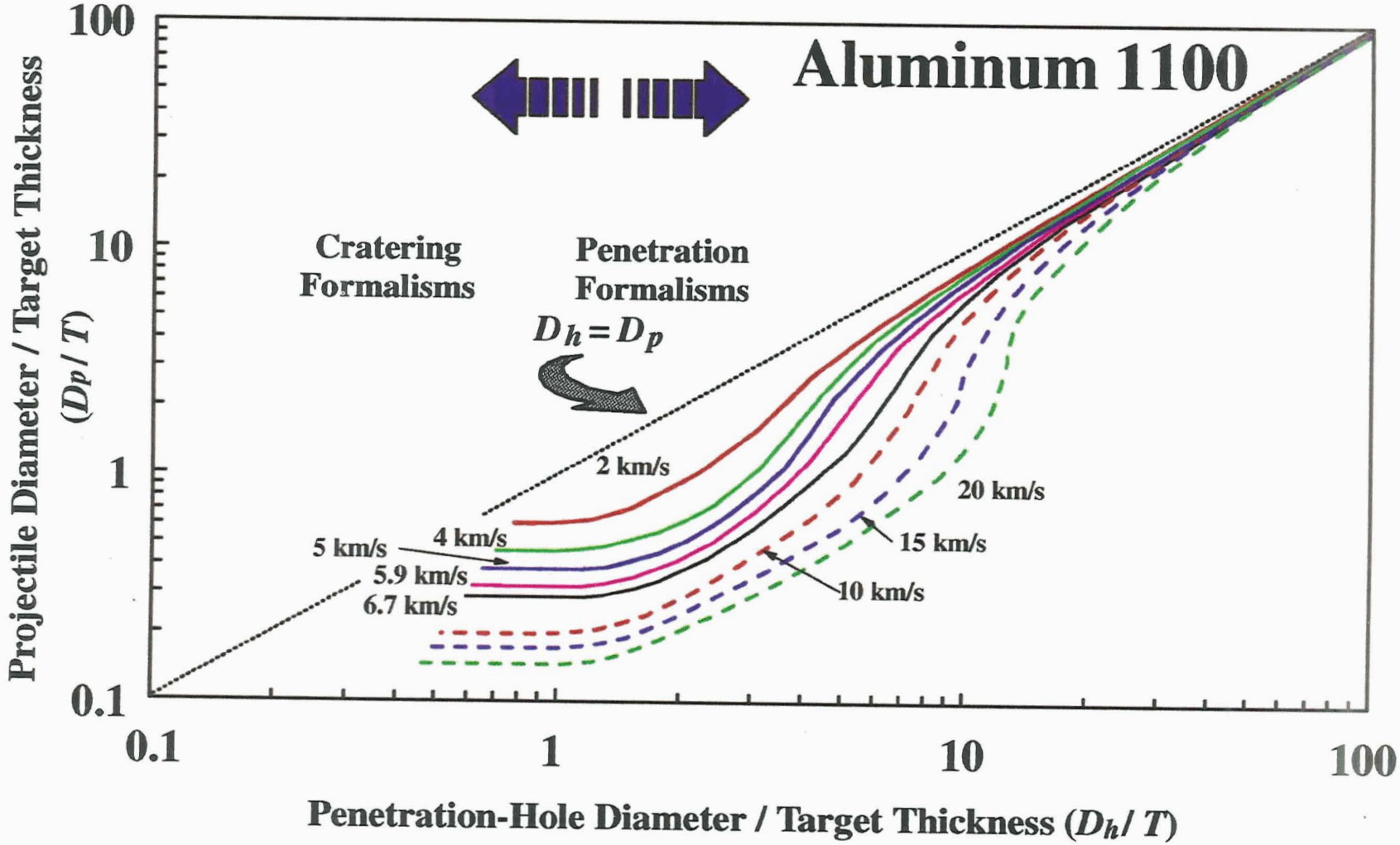

Figure 14. Empirical calibration curves of projectile diameter (D_p) from penetration holes of diameter D_h in targets of thickness T. This graph re-plots the experimental observations and their extrapolations to higher velocities from Figures 12 and 13 so that the readily measured parameter D_h is plotted against the unknown size of the impactor (D_P); both dimensions are normalized to target thickness. This plot yields unique (!) solutions for D_P from the measurement of D_h and T and an assumed or known impactor velocity.

calibration curves for the interpretation of space-produced penetrations in aluminum 1100. Note that all curves become horizontal for massive targets, because the condition of $D_h = 0$ is being approached asymptotically. This horizontal line is the equivalent to the vertical line in Figure 12, and intercepts the D_p/T scale at the T_{BL} value associated with a given V. We disagree with the hydrocode calculations of Tanner *et al.* (1993) that do not produce the curve segments for infinite halfspace targets, and therefore, portray penetrative events in targets that are much thicker than the ballistic limit(s).

The major purpose of Figure 14 is to demonstrate that any specific D_h measurement will yield unique D_p/T values for arbitrary target thickness thinner than the T_{BL}, provided V is either known or assumed. This permits each individual penetration hole to be associated with a specific impactor size. This capability represents substantial progress over the more traditional interpretations of penetration holes that is largely rooted in ballistic-limit considerations. The latter can only solve for the minimum particle size (or energy) that is capable of penetrating a given T (*e.g.*, Pailer and Grun, 1980; Carey *et al.*, 1985; Herrmann and Wilbeck, 1987; McDonnell and Sullivan, 1992). Accordingly, all perforations in a given target must be the result of larger or more energetic impactors than this threshold particle, yet specific dimensions or energies beyond the threshold values may not be determined. As a result, entire populations of penetration holes can only be represented by a single, cumulative datum (*e.g.*, McDonnell and Sullivan, 1992). In stark contrast, the approach illustrated in Figure 14 enables every single penetration hole to be associated with a unique projectile size. Figure 14 may be used to obtain differential projectile-size frequencies from any population of space-produced penetration holes.

Summarizing our quantitative measurements, the calibration data illustrated in Figure 14 make the interpretation of individual penetration holes totally analogous to, and on a par with the extraction of impactor dimensions from diameter and/or depth measurements of individual craters in infinite halfspace targets. Unquestionably, the absolute encounter velocity remains a crucial assumption in both of these interpretations. Presently, there is no direct way to extract absolute impact velocity from the morphology of either craters or penetration holes. Velocity assumptions must largely rely on an understanding of the dynamic behavior of hypervelocity particles in LEO. Any statistically meaningful population of craters and/or penetrations will have to be interpreted via reasonably constrained, mean encounter velocities of natural (*e.g.*, Zook, 1992) and man-made (Kessler, 1993) particles. Additional and prominent uncertainties that are similarly germane to both cratering and penetration events relate to the distribution of projectile densities and impact angles for hypervelocity impacts in space (*e.g.*, Humes, 1992; Christiansen, 1993; Watts *et al.*, 1993).

Witness Plates

Witness plates were placed behind the target foils for all experiments to monitor the debris plume emanating from the target, although it was known that detailed, quantitative analysis of these highly complex spray patterns would exceed the scope of the present study (*e.g.*, Schomberg, 1991; Stilp *et al.*, 1993; Pietkutowsky, 1990, 1993, 1994; Hörz *et al.*, 1994a, 1994b). Nevertheless, we present detailed photographs of these witness plates in this report to support some qualitative descriptions of the collisional history of the projectile and the response of the target. These descriptions will greatly benefit from frequent consultation of the high-resolution, witness-plate photographs contained within the Appendix. In addition, consultation of the cross-sections photographs (Figures 11a - 11f) is recommended in order to develop some sense for the absolute and relative volume or mass that were displaced from the target. Unless otherwise noted, all witness-plate photographs in Figure 15, and in the Appendix, portray the entire witness plate (29 cm square). The witness plates were mounted at a standoff distance (L) of ~12 cm, making dispersion angles of the debris cloud as large as 120° accessible. Undoubtedly, some fragments could have, and did disperse at angles >120°, yet the total mass in this widely dispersed material cannot be significant, as demonstrated by x-ray shadow graph techniques (*e.g.*, Pietkutowksy, 1990, 1993), or by cylindrical witness plates (*e.g.*, Hörz *et al.*, 1992b). For descriptive clarity, we refer to dislodged target material as *debris*, and to projectile particles as *fragments*; both

Page Intentionally Left Blank

46.47

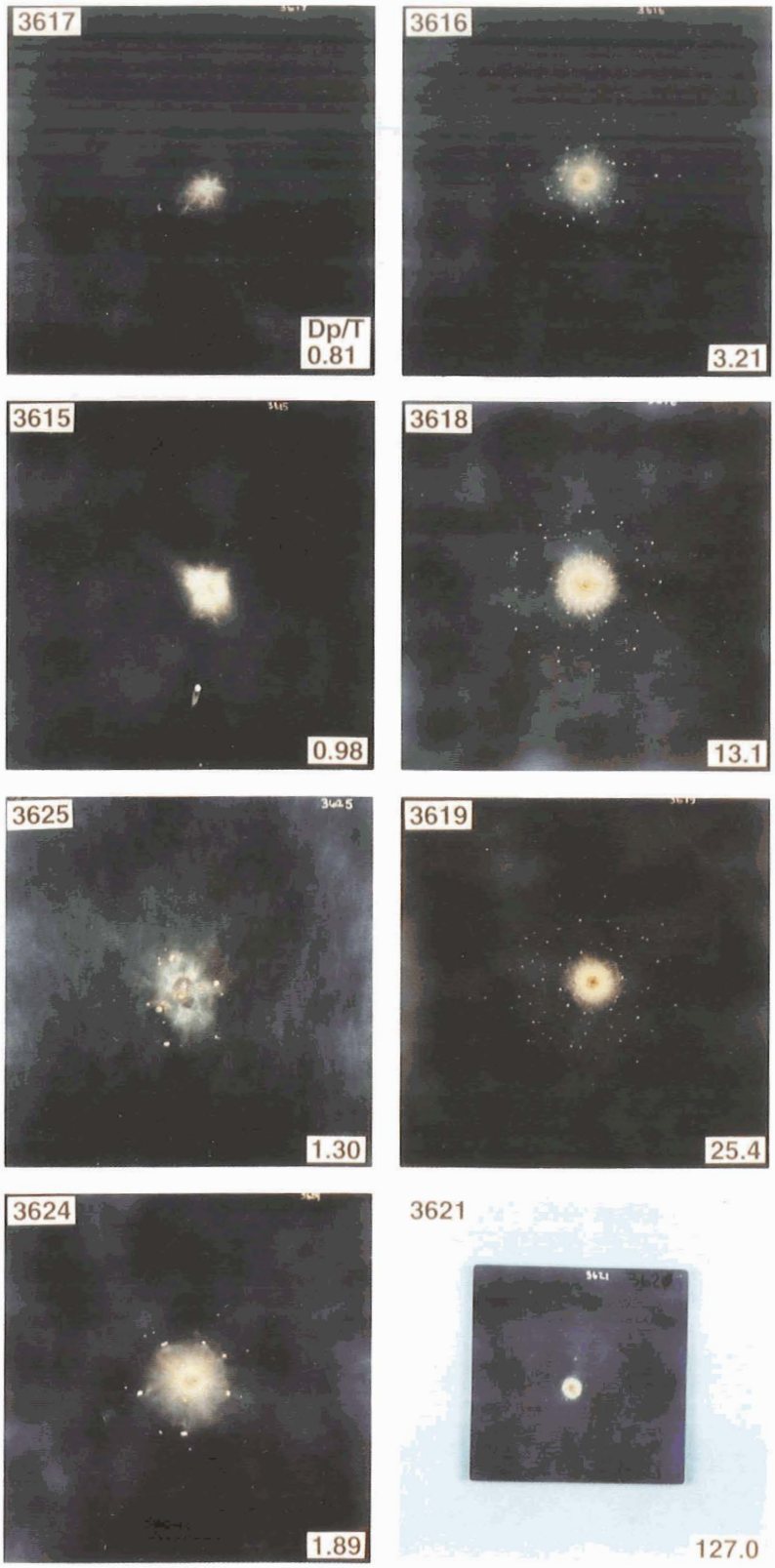

Figure 15a. Photographic summary of witness-plate patterns associated with the 2 km/s penetrations of aluminum 1100 targets of variable thickness by soda-lime glass projectiles. Each plate is 29 cm square (higher resolution photographs of individual experiments can be found in the Appendix).

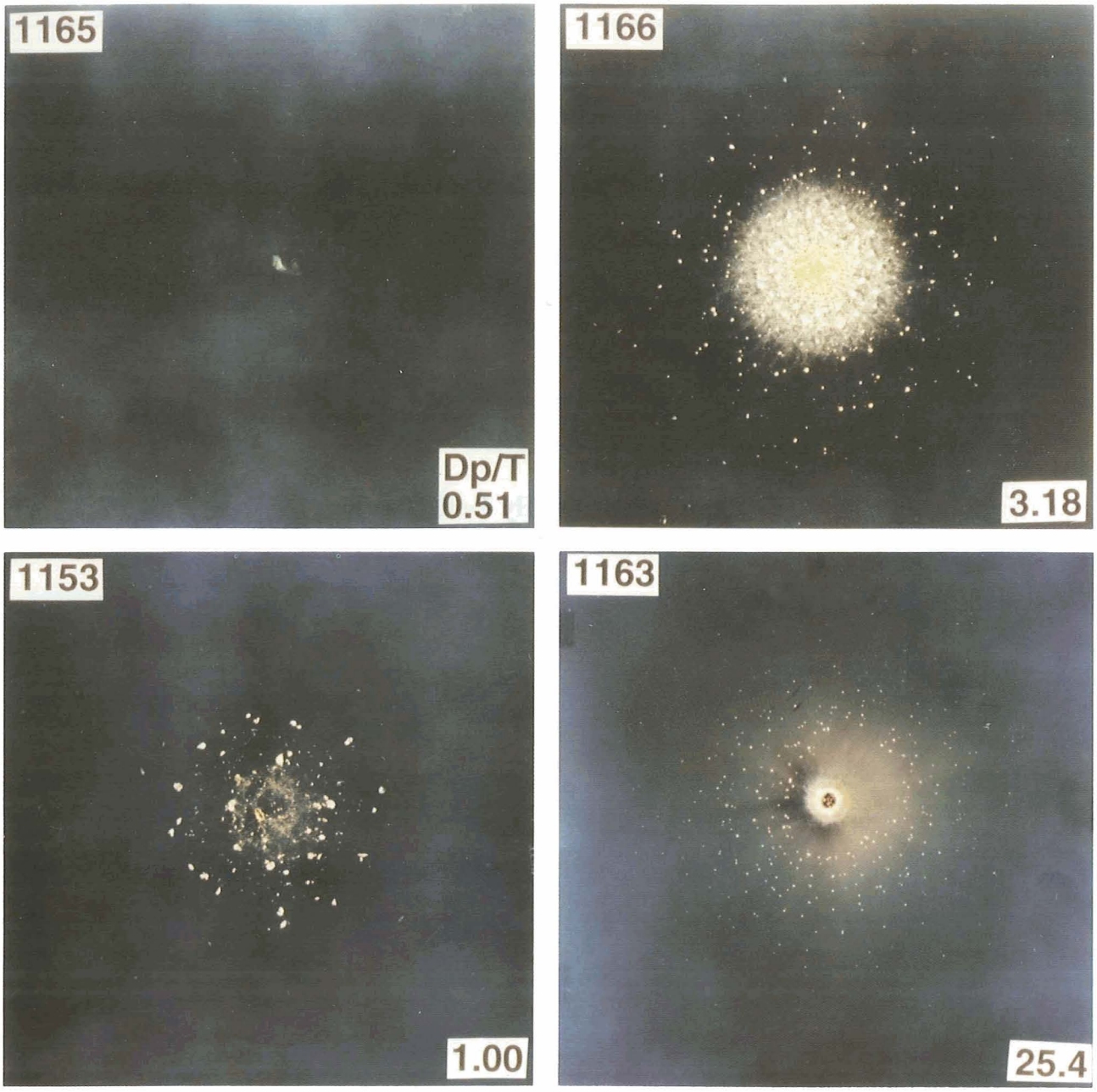

Figure 15b. Photographic summary of witness-plate patterns associated with the 4 km/s penetrations of aluminum 1100 targets of variable thickness by soda-lime glass projectiles.

Page Intentionally Left Blank

Page Intentionally Left Blank

50-51

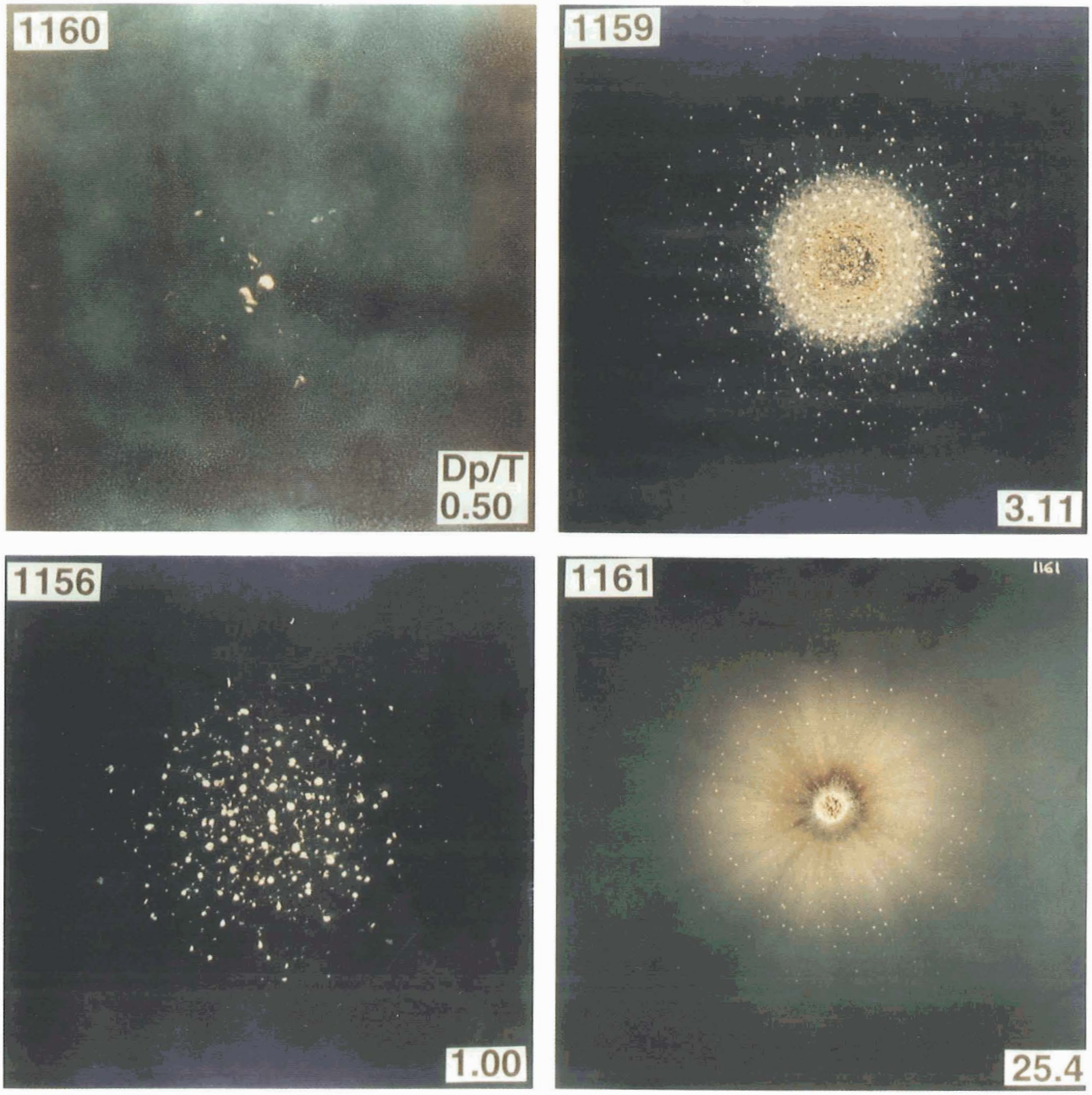

Figure 15c. Photographic summary of witness-plate patterns associated with the 5 km/s penetrations of aluminum 1100 targets of variable thickness by soda-lime glass projectiles.

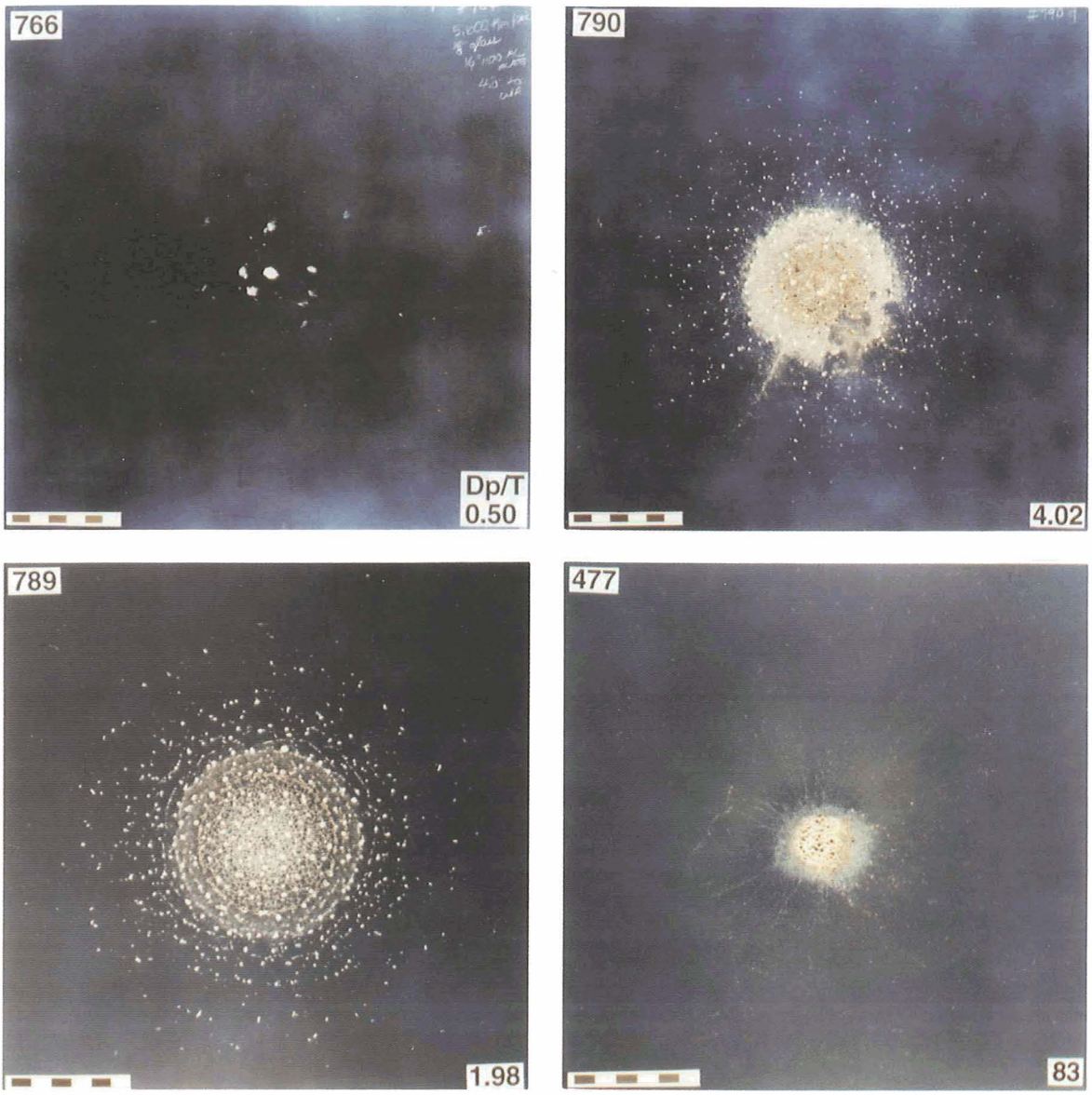

Figure 15d. Photographic summary of witness-plate patterns associated with the 5.9 km/s penetrations of aluminum 1100 targets of variable thickness by soda-lime glass projectiles.

Page Intentionally Left Blank

Page Intentionally Left Blank

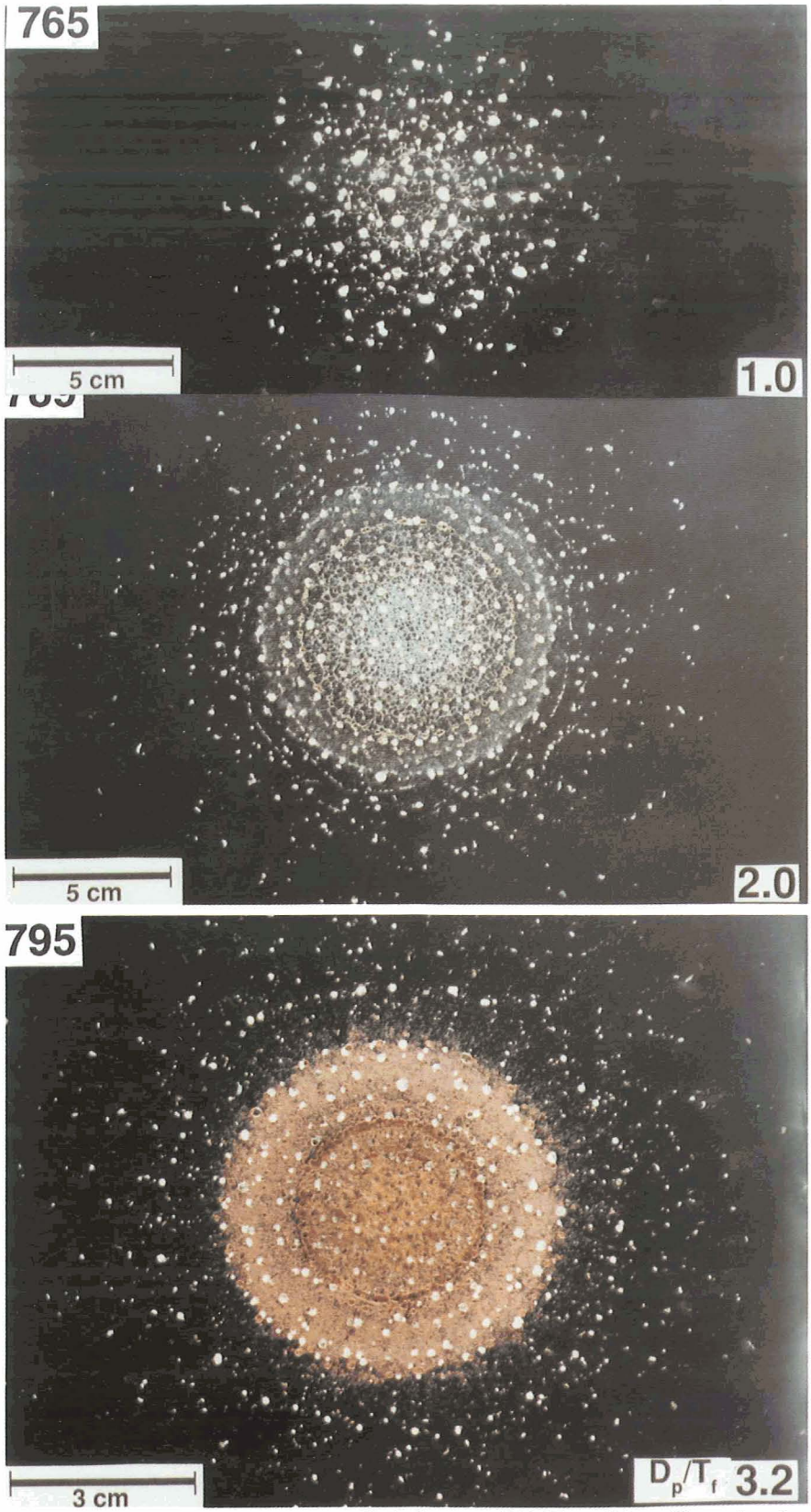

Figure 15e. Details of witness-plate spray patterns over a limited range of D_p/T conditions illustrating the formation of the spider-web patterns (described in the text) resulting from projectile melts at $D_p/T = 1$, and the formation of hole-saw ring patterns at $D_p/T = 2$; the $D_p/T = 3.175$ case employed a copper witness plate to increase visualization of projectile melts (Cu-colored craters), the massive hole-saw ring, and target debris (light-colored craters outside of the major hole-saw ring).

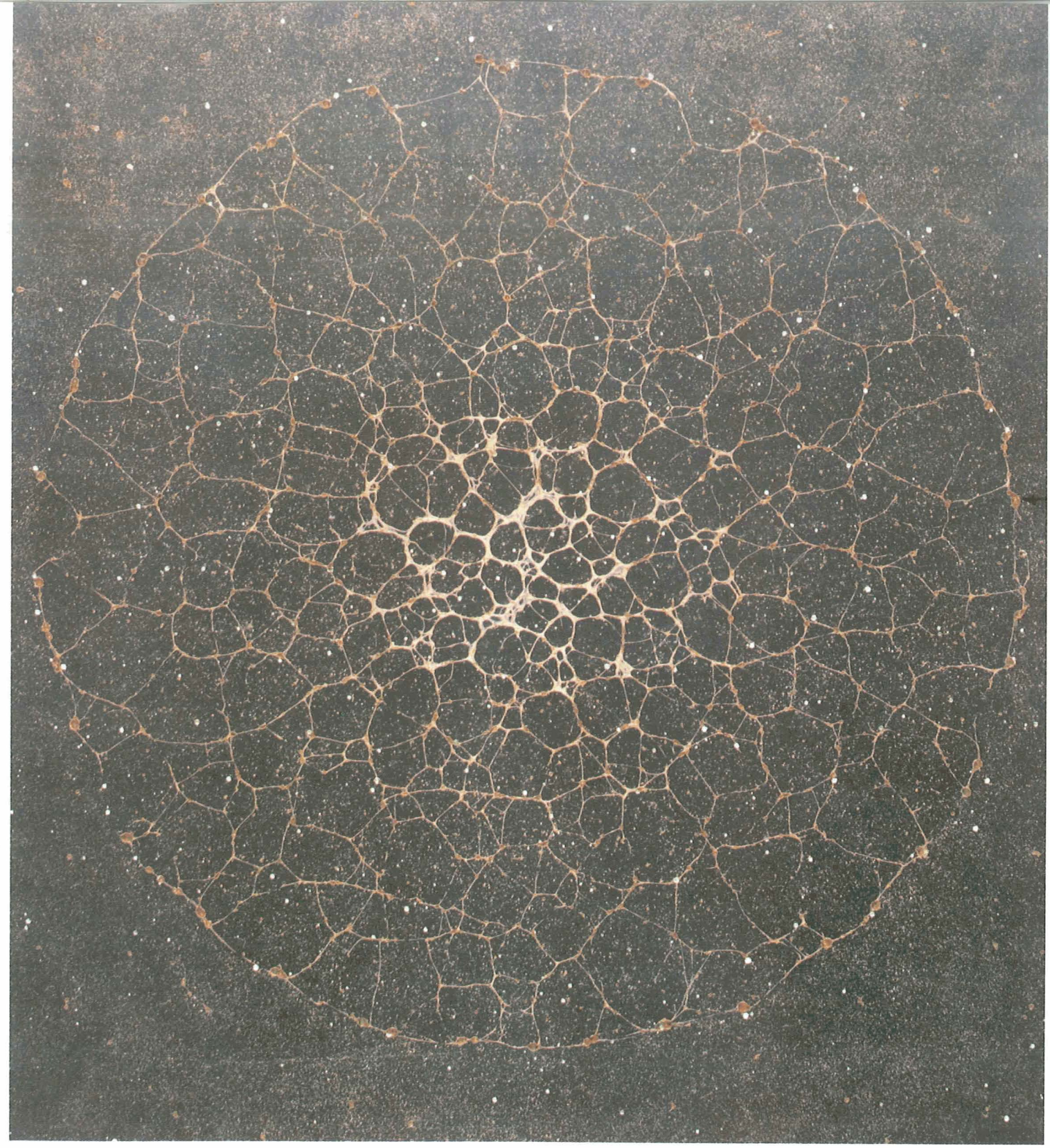

Figure 15f. Copper witness plate at extra-long standoff distance ($L \sim 45$ cm), predominantly recording the projectile melt spray from a 3.175 mm soda-lime glass projectile at 5.9 km/s that had penetrated an aluminum 1100 target of 800 μm thickness ($D_p/T = 3.96$). The Cu-plate permits easier distinction between Cu-colored (largely transparent) projectile melts and white craters (metallic, shinny) caused by aluminum debris. Note the regular distribution of melt stringers and the presence of distinct small craters at the intersections of all stringers. The entire pattern is bounded by a distinct ring of fairly large craters of surprisingly uniform size and highly regular spacing, characteristic for a (geometrically more dispersed) hole-saw rings. In detail, most of these craters are elongate, compound structures resulting from multiple impacts of barely dispersed melt particles, as evidenced by a bulbous, contiguous rim associated with discrete localized depressions that are separated by individual, discrete septa-like ridges. Field of view is ~20 cm across.

Page Intentionally Left Blank

Page Intentionally Left Blank

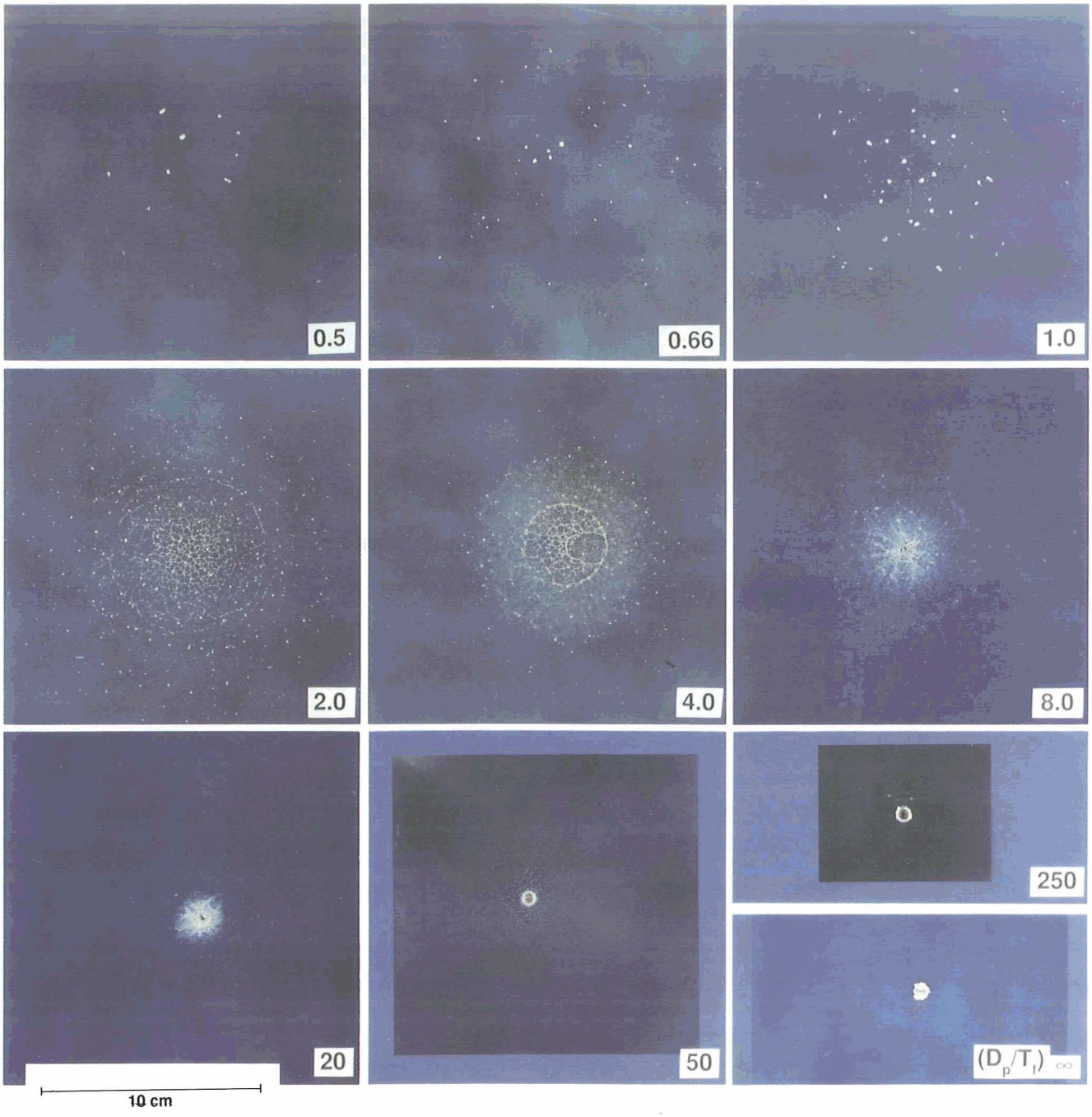

Figure 15g. Overview of witness-plate spray patterns following penetration of aluminum 1100 targets of variable thickness by 1 mm diameter soda-lime glass spheres at a nominal 6 km/s. Note the similarity in the spray patterns with those produced by 3.175 mm spheres at equivalent D_p/T conditions (Figures 15d and 15e).

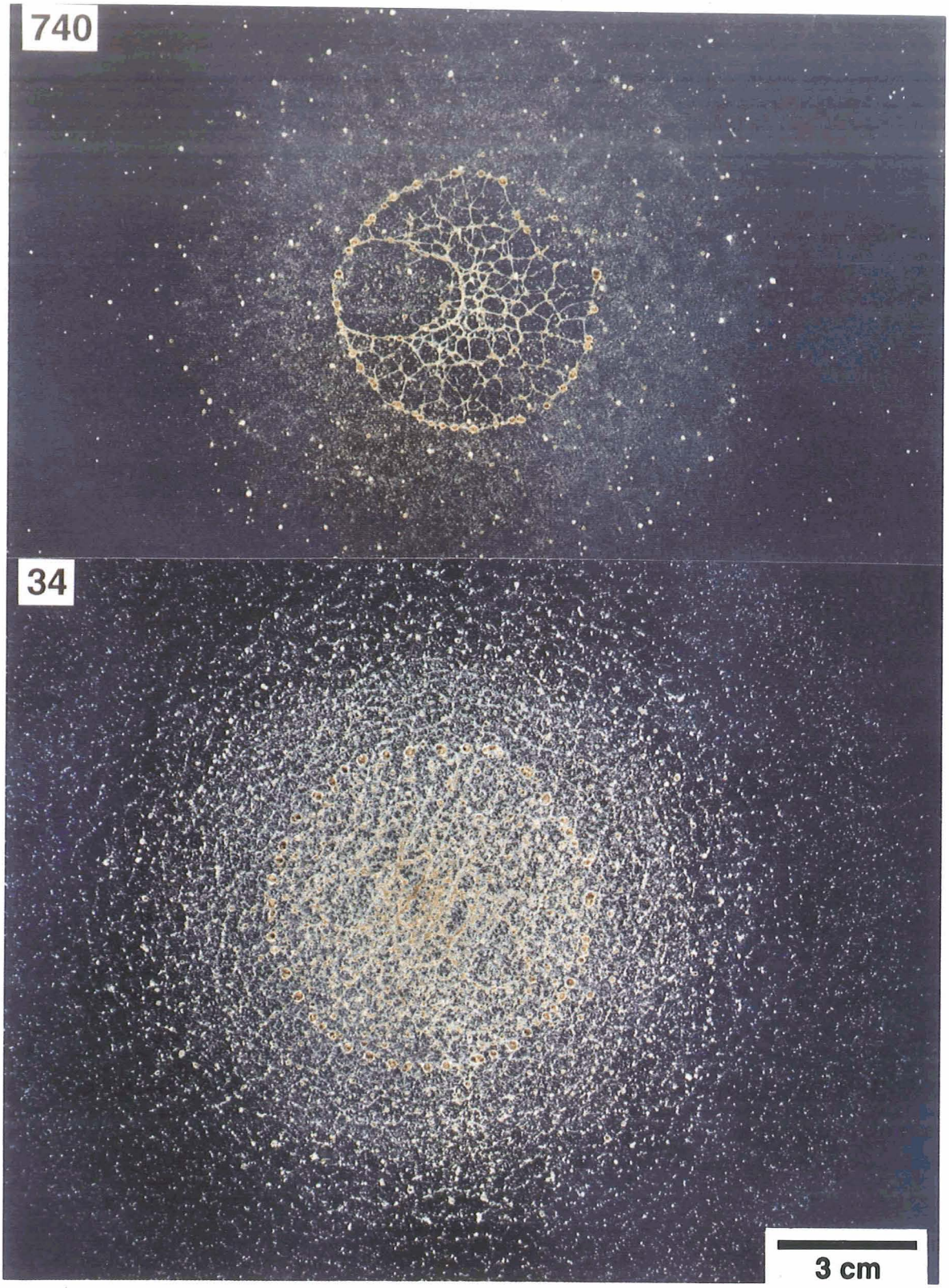

Figure 15h. Atypical witness-plate spray patterns resulting from either the use of a flawed projectile containing a vesicle (# 740; $D_p/T = 4.0$, 1 mm glass projectile at 6 km/s), or from an imperfect target (# 34; $D_p/T = 2$, 3.175 mm glass projectile at 6.3 km/s into a teflon target). Note the anomalous bubble in the projectile melt of # 740, although a seemingly defect-free projectile was selected as per routine procedure. The distinctly curved striae in # 34 reflect minute machine marks on the target's rear surface. Nominal target surfaces did not possess machine marks that coarse. The marks on # 34 were concentric relative to the overall target shape, yet the projectile hit slightly off-center to cause the pronounced arc-segments of target debris.

62-63

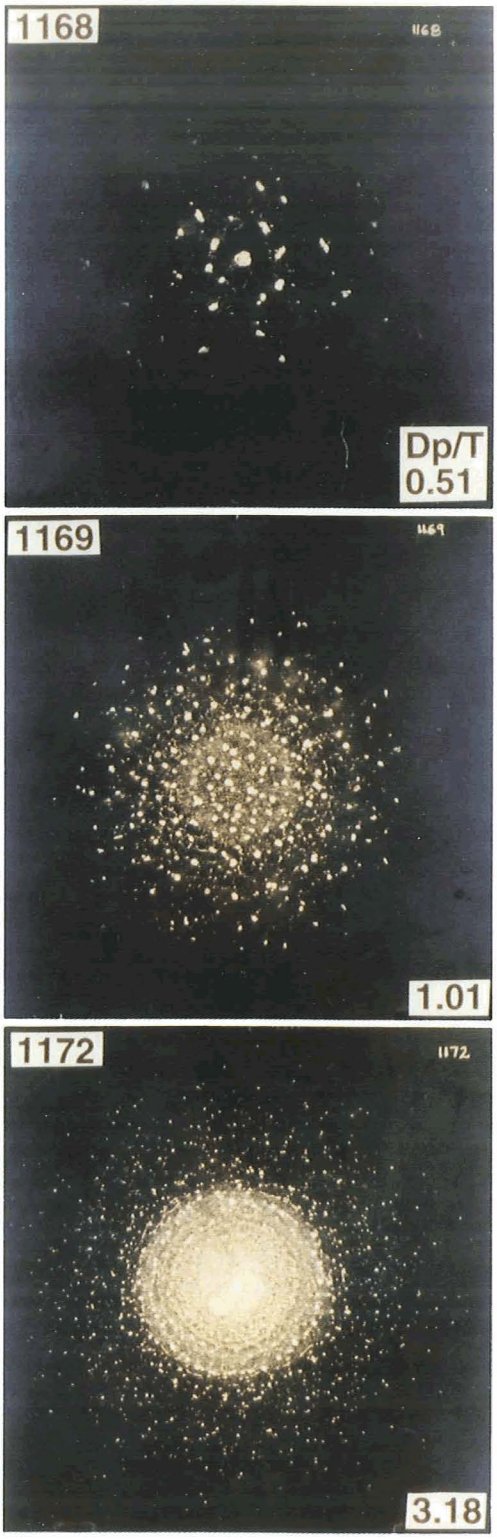

Figure 15i. Photographic summary of witness-plate spray patterns following penetration of aluminum 1100 targets of widely variable thickness by soda-lime glass projectiles at 6.7 km/s.

constitute the general *debris cloud* or *plume* which exits a penetrated target. *Ejecta* refers to target and/or projectile materials emanating uprange from the target.

Distinction between target debris and projectile fragments responsible for secondary craters on the witness-plate(s) will be a major aspect of the following descriptions. This distinction is based on color differences of the crater interiors as described in the Experimental Procedures section. Making this distinction is easy in many cases, yet it can also be difficult, if not impossible in others. However, we feel confident that specific impactor assignment is possible for the majority of large witness-plate craters, and that these assignments relate to the dominant mass fractions of either projectile or target. The color criteria of the crater interior used for these assignments deteriorates with decreasing crater size. Thus, any witness plate will contain a population of very small craters of unknown origin. However, this indeterminate crater population can only represent a minor fraction of the total cloud mass in comparison to those crater populations that can be assigned to their respective source materials. Most comments below regarding the dispersion and nature of projectile fragments and target debris will relate only to the dominant mass fraction.

Our confidence in assigning witness-plate craters to specific source materials is predominantly derived from the gradual development of specific cloud characteristics in systematic response to relative target thickness. While each individual witness plate may reveal diverse and complex features, every detailed structure develops in direct response to D_p/T at any given velocity. Akin to the penetration holes themselves, the witness-plate patterns also form a surprisingly systematic continuum that is totally controlled by D_p/T. Most features develop gradually over a specific range of D_p/T (*i.e.*, have a distinct beginning as well as ending) and an intermediate D_p/T range where they may constitute the dominant feature on the witness plate. This gradual evolution and systematic dependence on D_p/T greatly assists in the differentiation of projectile and target materials as discussed below. It is very easy to define the endmembers of this continuum at very massive and ultra-thin targets that will provide useful guides for the evolutionary trends of the spray patterns at intermediate target thickness. As illustrated in Figure 1, very thick, albeit perforated, targets will not permit any projectile fragment to exit as down-range debris, and all witness-plate damage is exclusively due to target debris. Conversely, for ultra-thin films, the entire impactor mass will interact with the witness plate, and the total target mass associated with such conditions (*i.e.*, $D_p >> T$) will be trivial. It follows that absolute and relative contributions of debris and fragments must vary as a functions of D_p/T. Furthermore, the impactor may be substantially more fragmented and dispersed upon collision with massive targets than it is following thin-film penetration; the latter entails, as its ideal endmember, the passage of a non-fragmented, intact projectile. As a consequence, size-distribution and dispersion angles of projectile fragments must vary in response to D_p/T as already demonstrated by Hörz *et al.* (1984). It is this transitional nature between well defined endmembers of possible exit plumes that can be recognized and traced on the witness plates with a high degree of confidence.

The 2 km/s experiments are summarized in Figure 15a. No visible damage to the witness plate occurred until D_p/T = 0.81 was reached (#3617). This damage is manifested by fine-grained, white (glass) powder that is embedded and deposited onto the witness plate; a few (~20) larger projectile fragments also occurred. The latter clearly penetrate the deposit of glass powder, suggesting that the more massive fragments were late arrivals. Contrary to the above general statement that target debris should dominate projectile debris in massive targets, this is not the case at low velocities. Indeed, we see no evidence of displaced aluminum debris until D_p/T = 1.30 is reached, where target material is represented by a few shallow, irregularly shaped depression a few mm in size. These are clearly low-velocity impacts of irregular aluminum chunks. We conclude -- consistent with experiments at higher velocities -- that the initial debris dislodged from experiment 3617 was of such low velocity that no damage was caused to the witness plate. With increasing D_p/T, the number of target-debris fragments increases, while their sizes decrease, and judging from the circularity of the secondary craters and their depths, the debris velocity must increase with decreasing T. Furthermore, note the excellent reproducibility of these patterns by consulting essentially identical experiments 3620 and 3621 within the Appendix.

The initial projectile powder exhibits a highly irregular geometry at $D_p/T = 0.81$, yet it commences to organize into centrosymmetric geometries at $D_p/T \sim 2$, and increases in granularity as evidenced by numerous, distinct, individual craters (Figure 15a). The latter are erosive features that gradually replace the continuous deposit of fine projectile dust typical for thicker targets. This deposit all but disappears at $D_p/T = 2$. An area of high mass concentration forms in the center that is sharply delineated from a less densely populated annulus; many cratering events overlap in this central area. As T decreases further, this center shrinks in diameter; while simultaneously the number of increasingly larger fragments decreases. Ultimately, at $D_p/T = 13$, sufficient energy is packed into the center of the fragment cloud that a contiguous, macroscopic, very shallow depression forms by a series of overlapping craters of substantial, millimeter-sized fragments. Hörz *et al.* (1994a) termed this feature the *central cluster.* The diameter of this cluster-depression gradually decreases with decreasing T, while depth increases to ultimately form an increasingly crater-like structure at $D_p/T > 127$ (see Figure 13 in Hörz *et al.*, 1994a). We introduced the term *central halo* for the distinctly less populated annulus of fine-grained fragments which surrounds the central cluster (Hörz *et al.*, 1994a, 1994b).

In Figure 15a note that the dispersion angle of the projectile fragments goes through a distinct maximum at thin targets, as described by Hörz *et al.* (1994a). In addition, note the relatively large penetration hole of the $D_p/T = 0.81$ case in Figure 11a, and the relatively small fragment dispersion angle in Figure 15a compared to the $D_p/T > 3$ cases. Obviously, the projectile fragments do not widely disperse for massive targets at low velocities. However, keep in mind that these fragments represent a relatively small (but unknown) fraction of the total impactor mass compared to thinner targets. Increasingly larger fractions of projectile mass will make it onto the witness plate as T decreases, yet at very thin foils the fragmented impactor will barely disperse. In contrast to the project fragments, the total dispersion angle of target debris remains relatively constant for all conditions of $D_p/T > 3$, including thin foils at $D_p/T = 127$. Naturally, less total mass is contained within this debris cloud as T decreases and grain size gets smaller, but dispersion angles seem to remain constant (see Hörz *et al.* (1994a).

Based on these observations it seems obvious that the central portions of the debris cloud are increasingly occupied by projectile fragments as T decreases. This central-fragment population will possess increasingly more kinetic energy, at the expense of the increasingly fewer and smaller target-debris particles, which are progressively residing further out within the peripheral parts of the debris cloud. The central projectile cloud forms an unexpectedly sharp contact with the peripheral target debris. We do not know whether or not any target debris resides within the central cloud portions that appears to be totally dominated by projectile species (see also Pietkutowsky, 1990, 1993, 1994).

Maximum peak stress in the glass projectile at 2 km/s was ~15 Gpa, well below the melting point of soda-lime glass. As a consequence, all projectile impacts are due to unmelted glass fragments. This is also true for all target-debris. The production of target and projectile derived impact melts at higher velocities will lead to substantially different witness-plate patterns than those produced at 2 km/s by the solid fragments and debris.

Figure 15b presents representative witness plates for the 4 km/s series. Note that the $D_p/T = 0.51$ case exhibits a single, irregular dent (~1 cm in size), caused by a single aluminum chunk emanating from the target; consult the corresponding cross-section in Figure 11b. Obviously, a large fraction of the exit lip tore off, impinging at very low velocity onto the witness plate (note that some of the ink is not removed in the dented area, suggesting elastic rebound (see experiment 1165 in the Appendix). Importantly, all targets of $D_p/T < 0.5$ do not display a trace of damage on the witness plate, although they are characterized by sizable holes, as illustrated by Figure 11b and experiment 1186 at $D_p/T = 0.48$ (Appendix). Also note that the deposit of projectile powder, typical for 2 km/s, has totally disappeared at 4 km/s (and all higher V). The $D_p/T \sim 1$ case in Figure 15b is fairly typical for massive penetrations at elevated velocities and displays many millimeter-sized, highly irregular, shallow and essentially rimless indentations, which were unquestionably caused by low-velocity target debris. The distribution of this debris is not chaotic, but tends to concentrate in two (crude) circles that are characterized by fairly equant spacing of individual craters/particles. These distributions are the precursors of some well pronounced ring patterns visible in experiment 1166 at $D_p/T = 3.175$. Some fine-grained target material resides

between these two rings, yet very little mass seems to reside at radial ranges beyond the outer ring. The central portion of witness-plate 1153 (Figure 15b) is totally dominated by small projectile fragments of irregular distribution; they form well defined (deep and circular) craters, down to submicroscopic sizes. The size distribution of the impactor fragments seems distinctly bimodal, consisting of a population of large particles within a background of fine-grained material. As was the case at 2 km/s, these large fragments appear to be largely superposed on the population of small background craters. Consistent with Figure 15a (experiment 3615), there is evidence that relatively large projectile fragments arrive at modestly later times at the witness plate than does the fine-grained debris. Analogous to Pietkutowsky (1994), it is suggested that these late and large fragments derive from the projectile's interior, where as the leading fine-grained material derives from the more highly shocked front-side of the impactor.

Returning to Figure 15b, we observe increased dispersion of both impactor and target particles at $D_p/T = 3.175$ relative to more massive targets. In addition, the target debris becomes progressively finer grained. Again, note (# 1166) the development of substantially centrosymmetric cloud characteristics, including distinct, ring-shaped mass distributions for relatively large target debris (relatively shiny, essentially white craters), as well as for the projectile fragments, which form the inner most ring of well defined, albeit small craters of brownish-yellow hues. The projectile craters are fairly circular, deep structures with substantial rims, whereas the target-debris craters are irregular, shallow and essentially rimless. This suggests dramatically different velocity distributions. A few large target pieces reside in the very central portions of the spray patterns, and many projectile fragments occur in the densely cratered, major damage area. There is evidence that projectile and target species may occur anywhere on the witness plate, and that they may be modestly mixed in the debris cloud. Nevertheless, the inner portions of the debris cloud are dominated by projectile species, while the outer portions are largely occupied by target debris. The latter specifically applies to the highly discontinuous population of craters at the periphery of the witness-plate pattern; they are all lined with aluminum and caused by target debris, no glass impacts can be recognized.

Unfortunately, there is a substantial gap between $D_p/T = 3$ and 25 in the 4 km/s series, which was conducted last to substantiate the general trends at found lower and higher velocities. Experiment 1163 displays a highly confined, centrally located beam of fine-grained projectile fragments, which, in turn, surrounds a central-cluster crater resulting from substantially larger fragments. This entire central-cluster depression is devoid of target debris. As previously noted, a relatively sharp contact between the areas occupied by projectile and target species is found. Target debris makes up a wide annulus of highly discontinuous craters, corroborating the finding that the peripheral portions of the debris cloud are totally dominated by target debris. Note, that the largely centrosymmetric cloud geometry of the $D_p/T = 3.175$ experiment disappeared at $D_p/T = 25$. Instead, a faint pattern of distinct radial geometry is observed; the latter is a deposit, rather than an erosive feature.

Figure 15c depicts the witness plates associated with the 5 km/s series. Not surprisingly, the first signs of witness-plate damage occur at more massive targets, relative to the lower-velocity cases. The first target debris is visible in experiment 1180 (not pictured) at $D_p/T = 0.37$. This damage was caused by a single, exceptionally large aluminum fragment which essentially rebounded elastically, and that was physically recovered. As can be seen in Figure 15c (# 1160), a small number of spall pieces impacted the witness plate at $D_p/T = 0.50$. These particles were highly irregular and of low velocity, judging from the highly irregular crater shapes. Nevertheless, they substantially dented and penetrated the witness plate, unlike the single piece in experiment 1180. Experiment 1156 attests to the fact that the grain size of the target debris decreases very rapidly as T decreases. Also note that large target debris and small projectile fragments are intimately mixed in the inner portions of the 1156 spray pattern. Many small projectile craters are connected by fine stringers; the craters are distinctly elongate and characterized by subsidiary depressions and septa. We interpret these features as the first signs of projectile melt, akin to Figure 15d (at 5.9 km/s; see below).

Again, both impactor and projectile particles are arranged into largely concentric patterns by $D_p/T \sim 3$ in Figure 15c. We termed these distinct features *hole-saw rings*, to emphasize their highly regular, azimuthal separations in addition to their constant radial dispersion (Hörz *et al.*, 1994a). Note that such

rings may either be composed of projectile fragments (innermost ring of deep, circular, tan-colored craters with well developed rims, 1159), as well as of target debris (two prominent rings of white craters at larger radial range). A faint projectile ring, generated by very small fragments, almost coincides with the inner debris ring, and a third projectile ring occurs just barely beyond the larger debris ring (see 1159 in Appendix). Generally, hole-saw rings are characterized by (1) exceptionally uniform radial dispersion, (2) a very restricted and highly uniform crater size compared to the wide spectrum of crater sizes on any given witness plate, and (3) exceptionally equal azimuthal spacing of the individual craters comprising these rings, occasionally even including regularly spaced doublet craters. This implies a mechanism that produces debris and fragments of constant radial and azimuthal dispersion, as well as size. Each individual ring differs in these characteristics from other rings. These rings are highly reproducible and occur in other target materials as well, such as teflon (Hörz *et al.*, 1994b), aluminum 6061-T6, inconel and lead (latter three, unpublished data). While the D_p/T values vary from material to material for the production of these rings, they form only over a limited D_p/T range for any given material. In the case of aluminum 1100, the D_p/T range is approximately $2 > D_p/T < 6$ and only modestly velocity dependent.

Returning to experiment 1159 in Figure 15c, we observe that the area of highly discontinuous craters at very large dispersion angles is largely the result of aluminum impacts from the target. While target and projectile are demonstrably, but modestly, mixed in the inner portions of the 1159 spray, the outer portions appear to be exclusively made up of target debris. Again, a rather abrupt demarcation is evident between continuous versus discontinuous secondary crater fields. This sharp demarcation is largely the result of a well defined and restricted central beam of projectile fragments; only minor target debris may reside in this beam.

Experiment 1161 in Figure 15c is equivalent to the $D_p/T = 25.4$ case at 4 km/s. A substantial central-cluster crater is surrounded by a (small) halo, and the discontinuous craters are exclusively made up of dislodged target particles. A prominent, radial deposit dominates the central portions outside the central-cluster crater. We attribute such radial patterns to hot gases and their condensate deposits as evidenced by ballistic shadowing, These gases and thermal aureole are generated during formation of the central clusters that have absolute diameters of ~ 1 to 2 cm; such radial aureoles do not form when more widely dispersed or more restricted particle beams collide with the witness plate. Undoubtedly, part of these radial patterns are caused by oxidation of the blue ink pigment, and the intensity of this oxidation is geometrically related to the central cluster. Note that the cluster interior itself is not greatly discolored and oxidized, displaying bare aluminum in many places, and especially in the thin halo surrounding the central cluster. We do not think this radial spray originates from, or during the penetration processes of foil targets, because we do not observe it in association with ultra-thin targets (*e.g.*, Figure 15e at $D_p/T =$ 250 or Figure 13 in Hörz *et al.*, 1994a). Hot hydrogen gas, resulting from normal gun operations, as the cause for this thermal aureole/deposits is eliminated as well, because this gas would be free to reach the target in all penetrations cases. None of the standard craters displays this pattern, where the hydrogen gas is totally uninhibited from reaching the target. The basic observation is that such radial patterns, largely of depositional rather than erosional nature, only occur over a limited range of D_p/T, and associated fragment dispersion angles. Accounting for the multitude of neighboring impacts that seem required for the formation of these radial patterns and discolorations/thermal aureole, we suggest that the hot gases emanating from multiple, essentially simultaneous impacts interfere and interact with each other. This interaction is non-existing for widely dispersed and smaller fragments in modestly thicker targets, and is essentially absent for thin film penetrations as well, where a more tightly clustered fragment beam produces a more crater-like structure; ejecta and hot gases associated with the latter more closely resemble that of the standard crater.

The 6 km/s experiments (Figures 15d - 15h) were conducted over a long period of time (2 to 3 years), while many of the systematic experimental conditions (*e.g.*, size and standoff distance of the witness plate) and photographic procedures characterizing all other experiments were being established. Some of the early 6 km/s experiments did not even employ a witness plate, but produced useful penetration-hole data. In addition, a number of witness plates and targets were never photo-documented before they became scratched and otherwise unsuitable for photography. In brief, the photo-documentation of the 6

km/s impacts is, unfortunately, incomplete. For these reasons we will complement the limited witness-plate photography of our nominal 3.175 mm projectiles with a more complete series of experiments that employed 1 mm glass projectiles, also at a nominal 6 km/s and otherwise identical initial conditions. As described by Hörz *et al.* (1994a), such a comparison of projectiles sizes is interesting in itself, and serves the purpose of illuminating the general characteristics of the particle cloud emanating from aluminum 1100 penetrations, regardless of projectile size.

Figure 15d provides an overview for 3.175 mm projectiles. The first signs of target spallation occurred at $D_p/T = 0.33$ (# 785) in the form of a substantial indentation, caused by a large, round spall piece that was physically recovered; it obviously separated from the target along a circular failure surface (see Figure 11d for cross-section). Experiment 786 ($D_p/T = 0.35$) displayed a substantial dent, equivalent to that of 785, as well as a few small indentations which barely penetrated the ink-layer. Similarly, at $D_p/T = 0.37$ (not pictured, see Appendix # 787) a substantial chunk is accompanied by somewhat smaller fragments, all at very low velocity, that were barely capable of damaging the ink layer. Experiment 788 at $D_p/T = 0.42$ is also dominated by one massive piece, and a few smaller ones, yet the velocity was higher and the paint layer was penetrated. Experiment 766 exhibits a similar number and size distribution of fragments at still higher velocity compared to the more massive targets just discussed.

Within the 6 km/s series, experiment 765 at $D_p/T = 1$ shows the first sign of stringers (*i.e.,* highly two-dimensional, linear or curved features). At modestly thinner targets, these features interconnect to form a complex pattern akin to a *spider web* as first described by Lange *et al.* (1982; for soda lime glass spheres colliding with gold foils). A well developed spider web is illustrated in Figure 15f; however, this witness plate represents a dedicated series of experiments (to be published elsewhere) utilizing aluminum 6061-T6 targets and copper witness plates utilizing an exceptionally large standoff distance ($L = 50$ cm), compared to $L = 12$ cm for the typical witness plates configuration in this report. Consequently, Figure 15f portrays the enlarged, central portion of the overall debris cloud typical for $D_p/T \sim 2$. Obviously, these spider webs reflect the dispersion of molten material. Using SEM-EDS methods, Lange *et al.* (1982) and Hörz *et al.* (1994a) demonstrated that these stringers exclusively represent projectile melt. Therefore, the stringers visible at $D_p/T = 1$ in Figure 15e are clearly projectile melt, and the obvious precursors of more fully developed spider webs that are characteristic of modestly thinner targets. In general, the occurrence of stringers constitutes the first, tangible evidence of projectile material reaching the witness plate at high velocities. Obviously, shock pressures became sufficiently high that the finely comminuted projectile powder at 2 km/s is being replaced by melt at the higher velocities.

Importantly, this first evidence of projectile melt occurs at target thickness that result in some of the largest penetration holes possible (see Figure 11d). Despite the formation of substantial penetrations at $D_p/T < 0.7$, no projectile material will reach the witness plate. Indeed, projectile melts may only reach the witness plate if absolute T becomes less than P of a standard crater (*i.e.,* $T < P$; see detailed discussion below). Obviously, all projectile material is entrained in cratering related flows (at $D_p/T < 0.7$ at 6 km/s), to be quantitatively ejected uprange. We take this evidence as yet another sign that penetrations in massive targets may be viewed as truncated cratering events.

Returning to Figure 15f, the pervasive melt stringers turn out to be microscopic gauges. Where such stringers intersect there is invariably a deep, crater-like depression, commonly possessing non-centrosymmetric outlines, yet a substantial rim. This rim is interrupted by the stringers themselves (*i.e.,* the microscopic gauges extend across the rim and into the crater structure itself), as if the stringer were originating in the crater. Commonly, the stringers posses subsidiary craters that are strung out in bead-like fashion. Also note the highly restricted, radial extent of the spray pattern, resulting in an exceptionally abrupt, radial termination of melt impacts. Indeed the outermost ring of relatively large craters is a geometrically enlarged version of the hole-saw ring characteristic for witness plates of shorter standoff distance. Under the binocular microscope many of the craters associated with this ring are now substantially elongate in plan view, because they consist of a small number (typically 2 to 5) of subsidiary depressions that are separated by discrete septa. It seem apparent that projectiles of distinctly homogeneous mass-distribution are responsible, suggesting projectile melt droplets in variable stages of incipient, yet incomplete dispersion. Clearly, many craterlets responsible for beaded stringers also attest

to various degrees of melt dispersion. Without exception, the intercepts of multiple stringers are occupied by craters and the result of tiny melt drops. The relatively massive, central features obviously reflect more massive melt filaments, yet they are also peppered by tiny craterlets. In summary, the spider webs attest to the detailed dispersion processes of projectile melts. Note the presence of widely dispersed, and comparatively few white (shiny) craters made by aluminum debris dislodged from the target in Figure 15f. Obviously, target debris may reside in the central portions of the exit plume at these conditions, yet the projectile melts are the dominant species.

Returning to Figure 15e and experiments 789 and 795 we note the presence of well developed hole-saw rings; experiment 795 also employed a copper witness plate. Specifically, experiment 789 shows one major (innermost) and two minor rings associated with projectile fragments (small, dark-colored craters). The average crater size in all rings decreases with increasing radial range, yet those due to aluminum particles are systematically larger than those caused by projectile fragments. Although we counted them as individual rings, those close to the periphery may actually be a mixture of projectile and target particles (*i.e.,* mixed rings). Thus, these hole-saw rings can form from both target debris and projectile fragments, mandating surprisingly uniform and regular characteristics of the debris cloud. These regular features are stunning, considering the highly dynamic environment in which they are generated. They occur simultaneously with otherwise irregular particle dispersions, as manifested by the peripheral, target-dominated portions of the cloud, as well as the inner parts that mostly consist of projectile fragments.

Hörz *et al.* (1994a) has previously suggested, exclusively using 6 km/s experiments, that the concentric arrangements of projectile fragments may be the first sign of solid fragments reaching the witness plate, with the central-cloud portions still largely molten to account for the webs. These solid particles were thought to have originated by spallation processes at the target's free (spherical) rear surface. The dedicated copper witness-plate series (Figure 15f) at large L, suggests that this view is incorrect. All particles that make up the peripheral ring appear to have been molten, and the equivalent projectile ring (# 789 and 795; Figure 15e) must be caused by silicate-melt droplets, rather than solid particles. We do not know whether the rings made by target material result from solid particles or melt droplets. However, the aluminum craters are not of compound nature, unlike the silicate-melt craters, which suggests, that solid target debris is involved and/or that aluminum melts disperse substantially different than did the molten glass.

Even after performing a fair number of Cu-witness plate experiments that were essentially dedicated to yielding an improved understanding of their formation, we remain thoroughly puzzled about these ring features and have no ready explanation for their existence. While it seems possible to envision scenarios for fairly regular fragmentation or dispersion processes of an essentially spherical impactor, such spherical (or at least centrosymmetric) free surfaces are more difficult to envision for relatively thin, sheet-like targets. It is possible that two different processes are involved, despite the otherwise strikingly similar characteristics of the resulting rings. Obviously, these rings form part of a continuum with regard to the fragmentation and dispersion of both projectile and target material, forming over a characteristic, limited range of D_p/T conditions centered around $D_p/T \sim 2$ to 4 for our specific conditions.

The above observations for penetrations at $D_p/T < 5$ at 6 km/s are thoroughly duplicated at equivalent, scaled dimensions by 1 mm projectiles (Figure 15g), adding substantial credence to the general applicability of the above observations and detailed trends. Note, in Figure 15g, the generation of a few large spall indentations at $D_p/T = 0.5$, the appearance of melt stringers at $D_p/T = 1$, yet their absence at $D_p/T = 0.66$. Also observe the formation of a substantial web structure in the interior portions of the $D_p/T = 2$ case, which is bounded by concentric arrangements at the periphery. Lastly, a prominent hole-saw ring of projectile material forms at $D_p/T = 4$, the interior of which is substantially disturbed by what appears to be a bubble in the projectile melt. Finally, all trends described for the 3.175 mm projectiles in targets of $D_p/T > 4$ are duplicated in Figure 15g, specifically the radial deposits at $D_p/T = 20$, which have all but disappeared at $D_p/T > 50$.

The melt bubble phenomenon of the $D_p/T = 4$ case of Figure 15g is enlarged in Figure 15h. Such bubbles were produced in other experiments as well, albeit rarely. We ascribe them to the presence of

some flaw in the impactors that went unnoticed during the hand-picking of projectiles under the microscope. Demonstrably flawed projectiles, used in the early stages, are prone to yield non-reproducible, non-centrosymmetric witness-plate patterns. Figure 15h illustrates yet another case of a non-typical witness plate at standard conditions and employing a teflon target at $D_p/T = 2$. In this case, the target rear surface was machined more coarsely, albeit in a subtle way, than typical for all other experiments. The witness plate in Figure 15h prominently displays each individual machine mark. The actual impact point was obviously not in the exact center of the concentric grove pattern. The point we are attempting to make with Figure 15h is that even minor imperfections in either the impactor or target will affect the detailed mass loading of the debris cloud, as manifested by atypical witness-plate patterns.

Returning to the 3.175 mm impactors and $D_p/T > 10$ (# 477, Figure 15d), which display distinctive radial patterns, note that a somewhat flawed projectile may have been used as well, causing portions of the pattern to be non-centrosymmetric. Unlike the radial deposits described for experiment 1161 in Figure 15c, the radial streaks in experiment 477 are erosive, again consisting of minute craters that are connected by thin stringers of variable thickness. To some extent such stringers are also visible for experiment 1161 of Figure 15d, yet they are very subtle. These erosive features are made up of minute, linear gauges (stringers) of variable width and depth, frequently encompassing small craters. We suggest -- as previously done by Hörz *et al.* (1994a) -- that they reflect the first signs of target melt. A number of stringers have relatively sizable craters at their termination points, as if delicate melt filaments were shed from large melt droplets. Also, even in the most distal parts of the experiment 477 spray, most damage occurs in the form of highly clustered, secondary impacts without melt stringers. Frequently, a large fragment is associated with any number of minute craters towards the outer edges of plume 477. We suggest that these are small aluminum (target) melt droplets in various stages of disaggregation.

Clearly, the predominantly radial textures cannot be related to some (sudden) change in impact angle of the target debris, as L was held constant in all experiments, and because the streaks occupy the same radial range that was previously occupied by distinct and well-developed craters. Therefore, we infer that these streaks represent target melt, and that they reflect a distinct transition of the physical state of target debris, as suggested by Hörz *et al.* (1994a, 1994b). Absolute T has become so thin that all mass displaced could essentially be shocked into the liquidus field. Clearly, this cannot be the case for more massive targets, where substantial fractions of the displaced target mass were engulfed by isobars below the solid-liquid phase transition at our specific conditions. A large fraction of this target melt will have escaped the growing crater cavity as ejecta for thicker targets . The appearance of radial streaks at some threshold target thickness merely indicates that molten material that was previously ejected uprange may now exit the target's rear side. The overall dispersion angles of this molten debris is akin to that of solids debris at modestly thicker targets, but the melts have sufficient radial momentum to smear out and disperse upon secondary impact to form the distinctive, radial, erosive patterns. Note that such radial morphologies were not produced at velocities < 4 km/s, because shock stresses were insufficient to generate significant target melt. Clearly, such radial streaks are indicative of elevated impact velocities.

The above target-melt observations lead to the interesting concept that relative dimensions will be crucial in controlling the (dominant) physical state of target and/or projectile materials that comprise the exit debris plume of penetrated targets. The target volume displaced in massive targets will be modestly shocked and thoroughly dominated by solids, whereas very thin targets will shed predominantly molten droplets, provided the peak pressure is sufficient to exceed the solid-liquid phase boundary. Conversely, projectile melts dominate the earliest signs of impactor materials on witness plates associated with massive targets, and increasingly more solid fragments result from thin-film penetrations, approaching the endmember condition of a perfectly intact projectile passing through some ultra-thin foil. Such considerations initially constituted the main argument to suggest that the hole-saw rings signal the onset of the arrival of solid projectile fragments on the witness plate (Hörz *et al.*, 1994a). However, we now conclude from the Cu-witness plates (Figure 15f) that we are unable to rigorously differentiate between solid and molten impactor fragments of high encounter velocities. We now suggest that most particles making up the central-cluster impacts may be unmolten projectile fragments, because the endmember of an intact projectile exiting an ultra-thin foil mandates the presence of solid fragments at some thicker

targets. Furthermore, we suggest that the central-cluster fragments reflect this gradual transition. If the central clusters do indeed reflect such fragments, most projectile mass at $D_p/T < 10$ would be molten, at 6 km/s.

Figure 15i displays representative witness plates for the 6.7 km/s experiments. Again, note the irregular, shallow indentations by massive, irregular, and low-velocity target debris at $D_p/T = 0.5$. However, this plate also shows some evidence of widely dispersed projectile-melt craters, mostly elongate and of a compound nature, some associated with modest filaments and stringers of melt suggesting melt droplets in various stages of breakup. It is to be expected that higher velocity impacts permit the passage of impact melts at increasingly thicker targets; consult Figure 11e and note the massive penetration hole produced at $D_p/T = 0.5$, making the relatively few debris fragments and small quantities of impactor material reaching the witness plate somewhat surprising. The $D_p/T = 1.01$ experiment (# 1169) in Figure 14h again displays abundant spider-web structures, yet a relatively large number of aluminum impacts occupy the same area as well. The latter are clearly superposed onto the web and arrived after the projectile melts. Finally, experiment 1172, at $D_p/T = 3.18$ in Figure 15i, is almost a duplicate of the 6 km/s experiment at $D_p/T = 2$ (Figure 15f, # 789; 6 km/s at the same D_p/T is diagnostically different). A substantial, innermost ring and one to two fainter rings are made by projectile material in experiment 1172, yet only one ring is formed by target debris. The outermost projectile ring seems unique in that it displays clear evidence of impactor melt. Unusually elongate, compound depressions of multiple mass centers and associated septa were formed, indicating that melt droplets were in the process of disaggregating. However, substantially concentric stringers were formed in experiment 1172, rather than radial streaks. The prominently concentric patterns of melt spray are unique for this experiment, although some suggestion thereof is present in some 6 km/s experiments. Finally, witness-plate 299 (see Appendix) at $D_p/T = 84.3$ displays a prominent central cluster surrounded by small craters of substantially radial characteristics, consistent with the 6 km/s patterns at $D_p/T > 50$, but not as well developed as in experiment 477 of equivalent D_p/T. In summary, the general trends at 6.7 km/s are consistent with all observations at lower velocities, but modestly concentric melt spray in experiment 1172 seems to suggest that the last remnants of the spider-web patterns (see Figure 15f) persist for thinner targets with increasing V.

Summary of Witness-Plate Observations

A variety of the above observations and interpretations are synthesized in Figure 16 with the specific intent to assist in the comparison of velocity dependent trends, with emphasis on the transition from cratering to penetration. The numbers next to each data point in Figure 16 refer to specific experiments, plotted at their actual, rather than nominal velocities. Relative crater depth (P/D_c; see Figure 3 or P/D_p from Table 1) will constitute an important consideration and datum in this presentation. Because P cannot be normalized to infinite target thickness, all dimensions were normalized to D_p as the common denominator. The purpose of Figure 16 is to plot -- as a function of velocity -- the threshold thickness for the onset of bulging (T_{bg}), the onset of perforation (T_{BL}), and the threshold target thickness (T_i) that permit impactor fragments to exit the rear. Unfortunately, the onset of T_{bg} is not systematically defined, even in this substantial series of experiments. However, the lower boundary between substantially bulged and physically perforated targets is well defined by T_{BL} (Figure 12). As discussed above, a threshold thickness (T_i) may be constructed beyond which the first signs of impactor material, either highly comminuted fragments or melts, will occur on the witness plate. This line separates massive, yet penetrated targets that exclusively produce target-derive debris, from the thinner materials that produce a mixture of target debris and impactor fragments in the debris plume. This T_i boundary is not precisely defined in all cases, yet is sufficiently well defined at a number of velocities to make the following generalization relative to standard crater depth (P/D_p). In all cases where we could observe the first traces of impactor materials -- molten or solid -- the absolute target thickness was modestly smaller than the absolute depth of a velocity-equivalent, standard crater. Experiments 1184, 1160, 766 and 788 demonstrate that T subtly thinner than P exist that do not permit projectile species to exit the rear. T must

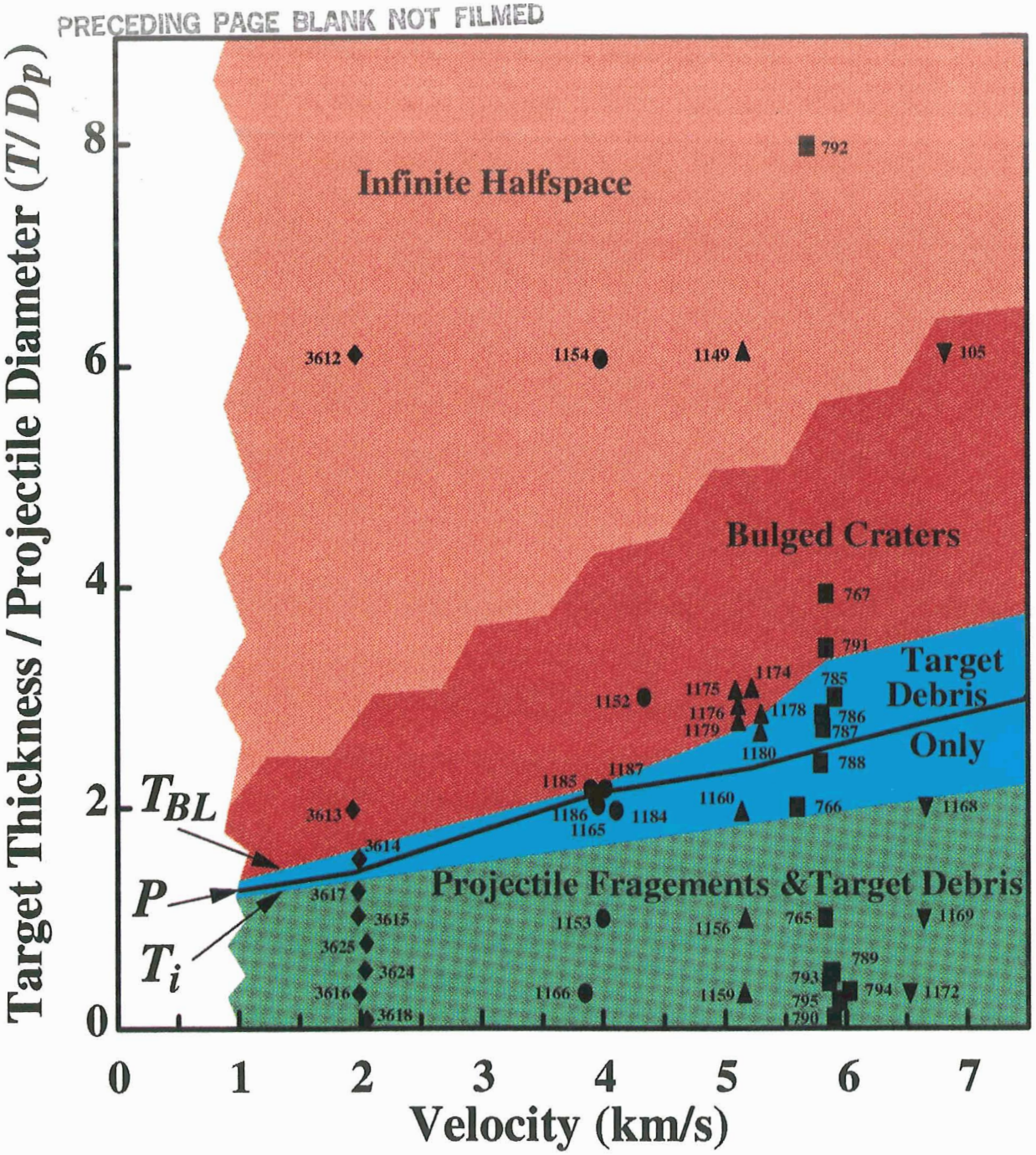

Figure 16. The effects of velocity on ballistic-limit thickness (T_{BL}), crater depth (P) and threshold target thickness (T_i) that permits impactor material to emanate from the rear of the target. Note that this plot normalizes all dimensions to D_p.

be measurably less than P to have impactor species present in the exit plume. The entire projectile mass must be totally entrained in cratering related material flows and essentially ejected uprange for all targets thicker than T_i; only when substantial parts of the prospective crater bottoms are truncated will projectile material escape downrange. On average, $T_i = 0.75 - 0.85P$ at > 5 km/s. Nevertheless, these observations on experimental penetrations may explain why so many substantial spray patterns on the multilayer thermal blankets from Solar Max did not reveal any traces of projectile residues (*e.g.*, Warren *et al.*, 1989).

Note the fairly constant relationship of T_{BL} and P in Figure 16, with $T_{BL} \sim 1.35P$ at > 5 km/s. This is substantially different from the $T_{BL} = 1.8P$ found by Cour-Palais (1987) and Christiansen (1993) for laboratory impacts using predominantly aluminum projectiles. In addition, McDonnell and Sullivan (1992) suggest a $T_{BL} = 1.5P$ for LDEF penetrations in pure aluminum foils, based on electrostatic accelerator experiments using iron projectiles and pure aluminum foils. To our knowledge, the T_{BL}/P ratios characterizing our experiments are the smallest reported to date. They are clearly the result of our specific projectile (silicate glass) and target materials (soft aluminum 1100). The wide range of T_{BL}/P among a variety of studies merely demonstrates that the exact T_{BL} sensitively depends on specific projectile and target materials. Thus, care is necessary when using ballistic-limit considerations to extract particle dimensions on space-exposed surfaces (McDonnell and Sullivan, 1992), or when predicting specific performances of collisional bumpers (Christiansen, 1993).

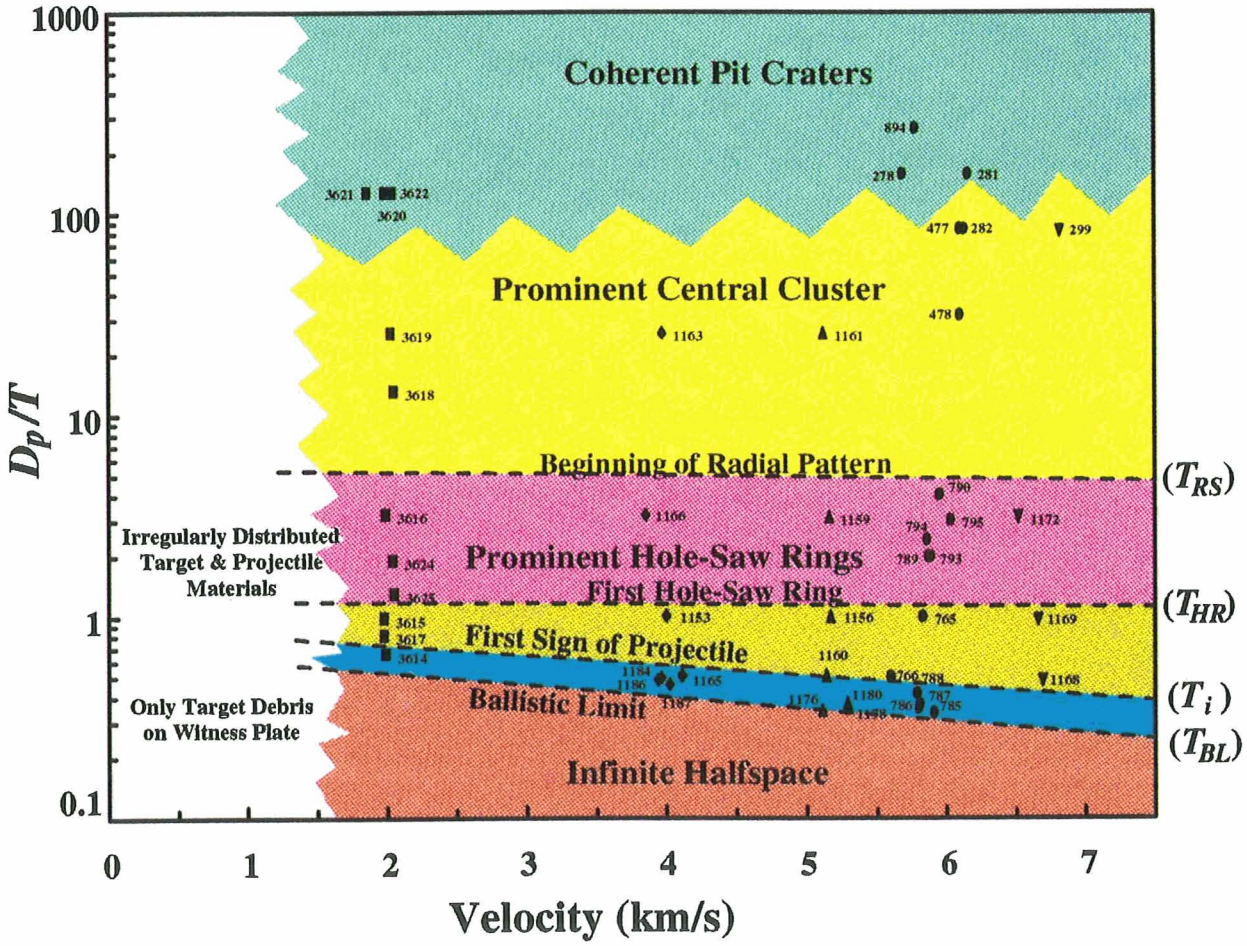

Figure 17. Summary plot of major morphologic trends on witness plates exposed behind aluminum 1100 targets of widely variable thickness that are penetrated by soda-lime glass spheres with velocities ranging from 2 to 7 km/s.

The velocity dependence of detailed witness-plate features as a function of D_p/T is synthesized in Figure 17. We have emphasized throughout this report the continuum nature of the debris cloud. As a consequence, the transition from one field to another is highly gradational. The only sharp discontinuities relate to T_{BL} and T_i, yet they must also be viewed as part of a continuum. The distribution of projectile fragments and target debris is irregular for relatively massive targets, and they begin to arrange into increasingly more centrosymmetric patterns at or close to the first occurrence of the hole-saw rings (T_{HR}). Well developed hole-saw rings occur at $T > T_{HR}$ and begin to be replaced by radial spray patterns at > T_{RS} (beginning of radial patterns) and clustered craters. The latter gradually shrinks in size as T

decreases, until an essentially coherent pit crater is being produced. Clearly, all of these features are transitional, and substantial subjectivity applies to some of the boundaries illustrated in Figure 17a. Nevertheless, the salient point and general purpose of this summary is to again illuminate the systematic nature of the debris clouds and their utter dependence on T. Target thickness is the dominate parameter, while V seems a relatively minor modulator by comparison. However, minor velocity dependent effects exist. For example, the characteristic hole-saw rings occur only over a restricted D_p/T range (*i.e.*, $2 < D_p/T < 6$), but are much better developed at higher velocities. Note that the higher velocities generally result in more numerous and finer-grained target debris, for any given D_p/T. Nevertheless, there does not appear to be a unique tell-tale feature on any given witness plates that would uniquely permit an estimate of initial impact velocity, other than the absence or presence of projectile melts, which may differentiate between low- (< 3 km/s) and high-velocity (> 3 km/s) events.

The major effects of V must relate to the physical state of the dislodged material (*i.e.*, solid or molten). It is exceedingly difficult, if not impractical in most cases, to distinguish the two from the morphology of secondary witness-plate craters. We interpret the onset of specific radial sprays as evidence for aluminum melts, and we recognize projectile melts with relative ease in the specific case of stringers and spider-web like structures. Otherwise, it is not possible to tell solid particles from melts. Our best assessment of these phase transitions is illustrated in Figure 18. Clearly, the peak stress at 2 km/s was insufficient to melt either the projectile or target. All experiments > 4 km/s yield stringers and spider-web structures (*i.e.*, evidence of impactor melt). We also interpret the projectile-derived hole-saw rings as melt. On the other hand, the pit craters must be formed by solids. We do not know the exact locus in D_p/T space where the projectile melts are being replaced and dominated by solid fragments, and the boundary indicated in Figure 18 is more conceptual intuition, rather than factual observation. Similarly, there is no doubt that all spall mass dislodged from massive targets is of low velocity, low shock stress, and consequently, of low temperature (*i.e.*, solid, irrespective of V). Conversely, part of the target must be molten as encounter velocities increase and associated stresses at the target/projectile interface exceed the target's solid/liquid phase boundary. The prominent radial sprays were interpreted as evidence for such melts. Clearly, the target melt volume must increase with increasing V, and increasingly thicker targets will shed molten aluminum as impact velocity increases, as conceptually suggested in Figure 18. The important point to be illustrated by Figure 18 is the fact that the PT states of the target and projectile that compose the exit plume depend not only on the initial impact velocity and associated stresses and the target/projectile interface, but on the relative dimensions of the target and projectile (D_p/T). The materials samples by the witness plate constitute very specific, differential volumes of target and projectile that were engulfed by a specific and restricted range of isobars along the decaying shock front. This leads to the conclusion that one may modulate -- at any given initial condition -- the dominant PT states of the target and projectile species composing the exit plume by prudent selection of relative target and projectile dimensions.

In summarizing this chapter on witness-plate observations, we could demonstrate that the damage patterns and secondary cratering phenomena associated with exit plumes from penetrated targets are sensitively and systematically related to relative target and projectile dimensions (*i.e.*, to D_p/T). Therefore, it seems possible to deduce some estimate of D_p/T and D_p from the morphology of spray patterns on space-exposed surfaces. However, such patterns do not contain very much velocity information, much less unique criteria at very high velocity. The witness-plate sprays are of limited utility in learning about the initial dynamic characteristics of hypervelocity particles in LEO. However, the witness-plate observations are of substantial interest to those involved in the efficient search for projectile residues for compositional analyses on space-exposed substrates. Additionally, witness-plate observations must serve as useful criteria in the development and evaluation of collisional bumpers and shields.

Page Intentionally Left Blank

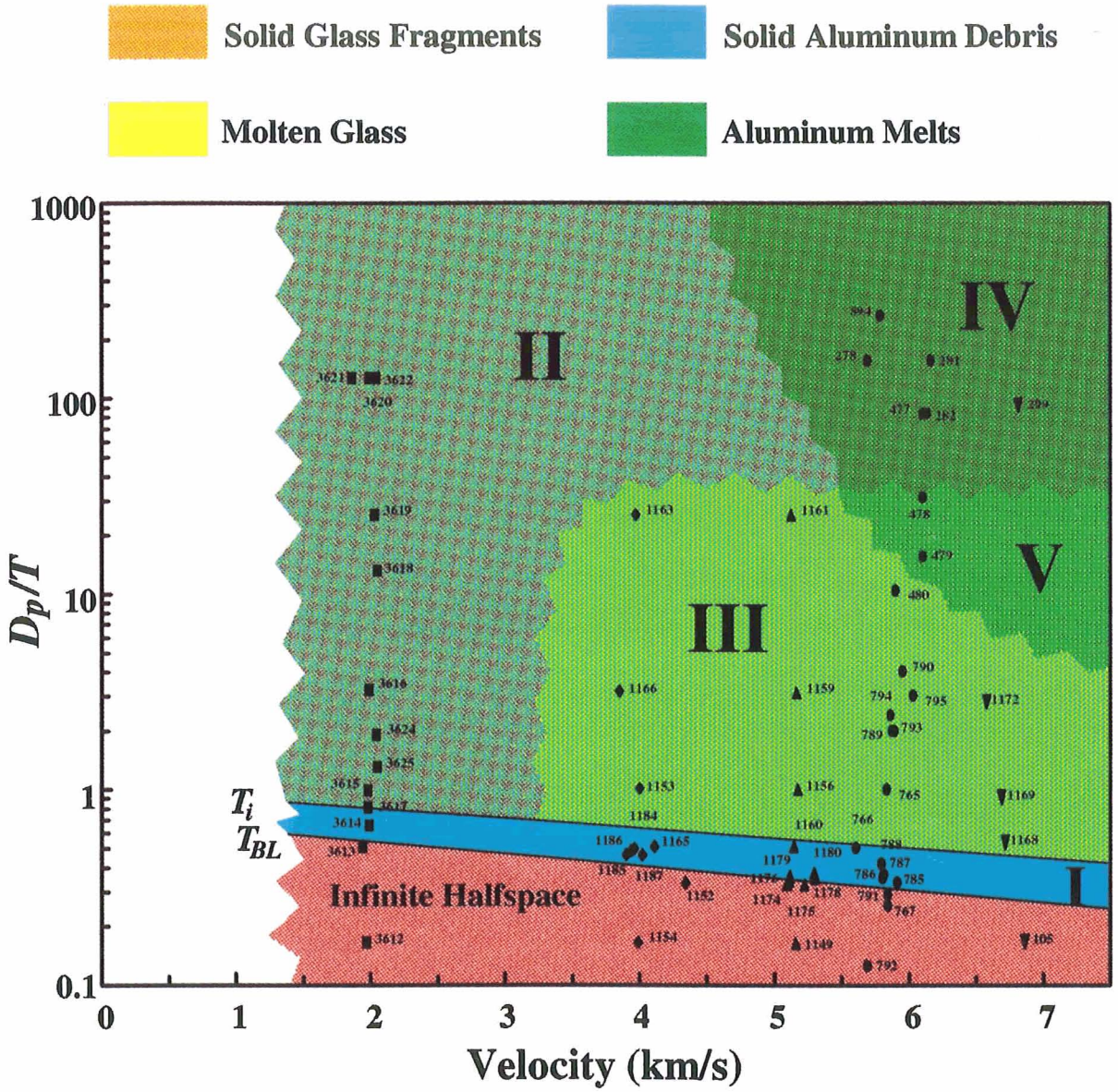

Figure 18. Physical state (*i.e.*, molten or solid) of soda-lime glass projectiles and aluminum 1100 target materials composing the exit cloud of penetrated targets at impact velocities of 2 to 7 km/s. No projectile material exits the penetrated target until target thickness becomes thinner than T_i; depending on the absolute impact velocity and associated peak shock stresses, this material may either be solid (at $V < 4$ km/s) or molten. The transition from molten to solid projectile species, as portrayed in this figure, is substantially intuitive, yet only solids will result from collisions with ultra-thin targets of ~ $D_p/T > 50$, which display substantial central-cluster depressions, if not pitted craters. By the same token, most target mass dislodged from massive targets is solid at all velocities, because most mass dislodged is not shocked beyond the solid/liquid phase transition. Witness-plate evidence for target melt in the form of radial streaks is observed only at $V > 5$ km/s and $D_p/T > 10$. Although the boundaries for these PT states are somewhat intuitive, the important point of this figure is that the PT states of both projectile and target material in a given exit plume depend sensitively and systematically on D_p/T at constant impact velocity.

CONCLUSION

Aluminum 1100 targets which varied over three orders of magnitude in thickness were impacted by soda-lime glass spheres of constant diameter (3.175 mm) at encounter velocities of ~2.0, 4.0, 5.0, 5.9 and 6.7 km/s. In addition, a series of cratering experiments was conducted in infinite halfspace targets over a velocity range of 1 to 7 km/s. Consistent with previous studies (*e.g.*, Cour-Palais, 1987; Watts *et al.*, 1993), crater diameter (D_c) varied systematically as a function of impact velocity, and scales for the given experimental conditions with velocity as $V^{0.59}$. Absolute and relative crater dimensions are in good agreement with the generalized cratering equations for metals of Watts *et al.* (1993). Consistent with Watts *et al.* (1993), the depth/diameter ratios were found to be modestly deeper than the canonical value of $P/D_c = 0.5$ advocated by Cour-Palais (1987) and Christiansen (1993). Importantly, the average depth/diameter ratio for craters in LDEF aluminum panels (6061-T6 and 1100) was found to be $P/D_c = 0.58$ (Love *et al.*, 1995; Bernhard and Hörz, 1995). These LDEF impacts represent events at encounter velocities between 10 and 20 km/s. In particular, we take the new LDEF observations as empirical evidence for a relatively constant crater geometry at elevated encounter velocities beyond those readily obtained with light-gas guns. The typical hypervelocity (> 5 km/s) crater in an aluminum 1100 target has a relative depth of $P/D_c = 0.58$, a rim-to-rim diameter of $D_r \sim 1.2D_c$, a lip diameter of $D_l \sim 1.58D_c$, and a rim height of $H_r = 0.25D_c$. Combining the observations of both experimental craters and those from LDEF verifies the conclusions of many previous studies, that there are no morphologic elements to deduce absolute impact velocity for events between 5 and 20 km/s from craters in aluminum targets.

The penetration experiments demonstrate that there is a remarkable continuum in most morphologic features that is sensitively related to the relative dimensions of the impactor and target (D_p/T). Absolute penetration-hole diameters are dependent on impact velocity at any constant D_p/T, and -- akin to craters -- there is no single morphologic element that would be a diagnostic indicator of V. However, assuming a modeled encounter velocity it is possible to extract impactor sizes from individual penetration holes in (aluminum 1100) targets of arbitrary thickness. Figure 14 demonstrates that unique solutions for projectile size are possible for each individual penetration hole. This renders interpretation of individual penetrations totally analogous to that of individual craters. The latter conclusion applies whether our specific suggestions for velocity scaling (Figure 13) are correct or not.

We emphasize that penetrations in massive targets must be viewed -- from a number of lines of evidence -- as truncated craters, and we merely interpret the actual transition from cratering to penetration processes via the concept of relative pulse duration. Specifically, we propose that the relative shock-pulse duration be used to delineate the transition from catering to penetration phenomena when extracting projectile dimensions from space-exposed surfaces. This transition does not occur at the ballistic limit, as has been assumed by most workers in the past. Instead, we suggest that cratering formalisms apply to all conditions where the shock-pulse duration in the projectile (t_p) is less than the shock-pulse duration within the target (t_t; *i.e.*, $t_p < t_t$), and that penetration equations be used only when $t_p > t_t$. Using this concept we make specific proposals for the dimensional scaling of craters and penetration holes at impact velocities beyond those accessible in the laboratory, resulting in graphical calibration curves that solve for projectile dimensions from impacts into aluminum targets of arbitrary thickness up to 20 km/s. Undoubtedly, the validity of this concept must be verified by additional experiments into different materials, and by theoretical studies that address the implications of pulse duration on cratering-related material motions and flows (*e.g.*, Maxwell, 1977), and on the absolute attenuation rate of a shock wave of fixed, initial amplitude. Additionally, more rigorous analyses and curve-fitting procedures must be applied to the current data for empirical generalizations (Watts *et al.*, 1995).

Akin to the penetration holes themselves, the distribution of materials within debris clouds that emanate from penetrated targets systematically depends on the relative dimensions of the projectile and target, and to a lesser degree, on impact velocity. The continuum nature of this plume, as recorded by witness plates, permits the collection of additional information of relative impactor dimensions (D_p/T) on space-exposed surfaces. However, in practice, such studies are not readily performed because most impacts occur at oblique angles, substantially modifying the witness-plate features resulting from the

vertical incidence impacts described in this report (*e.g.,* Schomberg *et al.*, 1987; Hörz *et al.*, 1992; Christiansen *et al.*, 1993). In addition, the majority of impactors in LEO are relatively small which results in spray patterns on underlying substrates that are very faint and difficult to detect (*e.g.,* Warren*et al.*, 1989).. Furthermore, the scaled standoff distance for space-exposed surfaces is commonly $L > 100D_p$ (*e.g.,* LDEF), as opposed to $L = 30D_p$ for most of the present experiments. Such differences will produce additional dispersion of an already very small, and fine-grained debris cloud. Lastly, most space-produced exit plumes should contain much more vaporized materials than our experiments; the associated condensate deposits are easily overlooked.

Consistent with the major objectives of this work, which is the delineation of impactor dimensions from space-produced craters and penetrations, we have made little reference throughout this report regarding the development of ballistic shields. However, we recognize that some of our results readily apply to such efforts. Most shield developments attempt to predict the collisional damage inflicted upon an operational flight system by an assumed impactor at a given model velocity. This damage may either be defined as the size of the resulting crater or penetration hole from the primary impact, or as the secondary damage inflicted by the debris plume resulting from the deployment of collisional bumpers. As already noted, the calibration curves illustrated in Figure 14 are totally applicable to these shielding issues and may be used to predict the size of penetration holes resulting from model impactors that encounter (aluminum 1100) targets of any thickness over a wide range of velocities, including those typical of LEO. Furthermore, the relatively rapid and economic approach to delineate a ballistic-limit thickness via regression analysis from penetration-hole size in fairly massive targets to the condition of $D_h = 0$ is directly applicable to the development of collisional shields, whether from aluminum 1100 or other candidate shield materials. Lastly, relatively massive, single bumpers constitute a poor choice for collisional protection, because they shed unnecessarily large quantities of material from the bumper itself. The deployment of multiple, thin bumpers (Cour-Palais and Crews, 1990; Hörz*et al.*, 1993; Christiansen and Kerr, 1993) seems a more prudent choice in order to minimize the total number of particles liberated during bumper penetration. Additionally, the debris cloud of massive, single bumpers may contain more dislodged bumper mass than projectile fragments, and may, therefore, contain unnecessarily large, possibly intolerable, amounts of kinetic energy.

The effects of projectile density, tensile and compressive strengths, and shape were not addressed in this work, yet their significance is recognized (*e.g.,* Watts *et al.*, 1993). Additional experiments in aluminum targets using variable projectile densities and other physical properties seem warranted to provide additional insights into the interpretation of craters and penetrations that were produced in space under poorly constrained conditions. Furthermore, additional experiments must be conducted to address the effects of oblique impact. Nevertheless, the current work suggests that interpretation of individual penetration holes may become comparable and equivalent to the analysis and interpretation of individual impact craters on space-exposed surfaces.

REFERENCES

Anderson, C.E. (1990) Hypervelocity Impact, *Proc. of the 1989 Symposium*, San Antonio, TX., *Int. J. Impact Engng. 10.*, 635 p.

Anderson, C.E. (1993) Hypervelocity Impact, *Proc. of the 1992 Symposium*, Austin, TX., *Int. J. Impact Engng., 14.*, 891 p.

Bernhard, R.P. and Zolensky, M. (1994) Analysis of Impactor Residues in Tray Clamps from the Long Duration Exposure Facility, *NASA Technical Memorandum,* 104784, 278 p.

Bernhard, R.P.and Hörz, F. Craters in Aluminum 1100 by Soda Lime Glass Spheres at 1-7 km/s, *Int. J. Impact Engng., in print.*

Bernhard, R.P., T.H. See, and Hörz, F. (1993) Projectile Compositions and Modal Frequencies on the "Chemistry of Micrometeoroids Experiment", in *LDEF-69 Months in Space, Second Post Retrieval Symposium, A. Levine, ed., NASA CP 3194,* 551-573.

Carey, W.C., McDonnell, J.A.M. and Dixon, D.G. (1985) An Empirical Penetration Equation for Thin Metallic Films Used in Capture Cell Techniques, in *Properties and Interactions of Interplanetary Dust,* R.H. Giese and P. Lamy, eds., *Reidel, Dordrecht,* p.131-136.

CDCF (1990), *Cosmic Dust Collection Facility: Scientific Objectives and Programmatic Relations*, CDCF Working Group Report, F. Hörz, ed., *NASA TM 102169*, 14 p.

Christiansen, E. L. (1993) Design and Performance Equations for Advanced Meteoroid and Debris Shields, *Int. J. Impact Engng., 14,* p. 145-156.

Christiansen, E.L. and Kerr, J.H. (1993) Mesh Double-Bumper Shield: a Low-Weight Alternative for Spacecraft Meteoroid and Orbital Debris Protection, *Int. J. Impact Engng. 14*, p. 169-180.

Christiansen, E.L., Cykowsky, E., and Ortega, J. (1993) Highly Oblique Impacts into thick and thin targets, *Int. J. Impact Engng.* 14, 157-168.

Cintala, M.J. (1992) Impact-Induced Thermal Effects in the Lunar and Mercurian Regoliths,*J. Geophys. Res., 97*, p. 947-973.

Coombs, C.R., Watts, A.J., Wagner, J.D. and Atkinson, D.(1993), LDEF Data: Comparison with Existing Models, in *LDEF - 69 Months in Space: Second Post-Retrieval Symposium, NASA CP 3194*, p. 619-664.

Cour-Palais, B. G. (1987) Hypervelocity Impacts in Metals, Glass, and Composites, *Int. J. Impact Engng., 5,* p. 681-692.

Cour-Palais, B.G. and Crews, J.L. (1990) A Multi-Shock Concept for Spacecraft Shielding, *Int. J. Impact Engng., 10*, p. 135-146

Flury, W. ed. (1993) *Proc. First European Conference on Space Debris*, European Space Agency, Paris, *ESA SD-01,* 741 pp.

Gault, D.E. (1973), Displaced Mass, Depth, Diameter, and effects of Oblique Trajectories for Impact Craters Formed in Dense, Crystalline Rocks, *The Moon*, 4, 32-44.

Gehring, J.W. (1970) Theory of Impact on Thin Targets and Shields and Correlation with Experiment, in *High Velocity Impact Phenomena,* Kinslow, R. ed., Academic Press, p. 105-156.

Grun, E., Zook, H.A., Fectig, H. and Giese, R.H. (1985), Collisional Balance of the Meteoritic Complex, *Icarus, 62*, p. 244-272.

Herrmann, W. and Wilbeck, J. (1986) Review of Hypervelocity Penetration Theories, *Sandia National Laboratories Report, SAND -86-1884C,* 29 p.

Hörz, F., Cintala, M.J. and See, T.H. (1986) *Hypervelocity Particle Capture: Some Considerations Regarding Suitable Target Media*, Lunar and Planetary Institute Technical Report, F. Hörz., ed., *LPI TR-86-05*, p. 58-60.

Hörz, F. and Bernhard, R.P. (1992) Compositional Analysis and Classification of Projectile Residues in LDEF Impact Craters, NASA Technical Memorandum 104750, 145 pp.

Hörz, F., Bernhard, R.P., Warren, J., See, T.H., Brownlee, D.E., Laurance, M.R., Messenger, S., and Petersen, R.B.(1992a) Preliminary Analysis of LDEF Instrument AO-187-1, "Chemistry of

Micrometeoroids Experiment", in LDEF-69 Months in Space, First Postretrieval Symposium, A.Levine ed., NASA CP3134, 487-502.

Hörz, F., Cintala, M.J., See, T.H., Bernhard, R.P., Cardenas, F, Davidson, W., and Haynes, G. (1992b) Comparisons of Continuouis and Discontinuous Bumpers: Dimensionally Scaled Impact Experiments into Single Wire Meshes, *NASA Technical Memorandum* 104749, 83p.

Hörz, F., Cintala, M.J., Bernhard, R.P., Cardenas, F., Davidson, W., Haynes, G. and Winkler, J. (1993) Impact Experiments into Multiple mesh Targets: Concept Development of a Light Weight Collisional Bumper, *NASA Techcial Memorandum* 104764, 225 p.

Hörz, F., Cintala, M.J., Bernhard, R. and See, T.H. (1994a) Dimensionally Scaled Penetration Experiments: Aluminum Targets and Glass Projectiles 50 μm to 3.175 mm in Diameter , *Int. J. Impact Engng., 15*, 257-280.

Hörz, F., Cintala, M.J., Bernhard, R.P., Cardenas, F., Davidson, W., Haynes, G., See, T.H., Winkler, G., and Knight, J. (1994) Cratering and Penetration Experiments in Teflon Targets at Velocitoies from 1 to 7 km/s, *NASA Technical Memorandum* 104797, 317 p.

Humes, D.H. (1992) Large Craters on the Meteoroid and Debris Impact Experiment, in *LDEF - 69 Months in Space: First-Post Retrieval Symposium, NASA CP 3134*, p. 399-418.

Igelseder, H., and Igenbergs, E. (1990), Crater Morphology at Impact Velocities between 8 and 17 km/s, *Int. J. Impact Engng.*, 10, 271-280.

Kessler, D.E. (1993) Origin of Orbital Debris on LDEF's Trailing Surfaces, in *LDEF - 69 Months in Space: Second Post-Retrieval Symposium, NASA CP 3194*, p.585-594.

Kipp, M.E., Grady, D.E., and Swegle, J.W. (1993), Experimental and Numerical Studies of High-Velocity Impacr Fragmentation, *SANDIA Report, SAND93-0773. UC-410*, 128 p.

Lange, G.S., Eigner, S., Igenbergs, I., Jessberger, E.K., Kuczera, H., Maas, D., Sutton, S., Weishaupt, U. and Zinner, E. (1986) Ion Microprobe Sensitivities and Their Application to Multi-element Analysis of LDEF Impact Residues (abstract), *Lunar Planet. Sciences XVII,* Abstracts, Lunar Planetary Institute, Houston, p. 456-457.

Levine, A.E. (1992) *LDEF - 69 Months in Space, First Post-Retrieval Symposium, NASA Conference Publication, CP 3134,* 1705 pp.

Levine, A.E. (1993) *LDEF - 69 Months in Space, Second Post-Retrieval Symposium, NASA Conference Publication, CP 3194,* 1572 pp.

Love, S. G., Brownlee, D.E., King, N., and Hörz, F. (1995), Morphology of Meteoroid and Debris Impact Craters Formed in Soft metal targets on the LDEF satellite, *Int. J. Impact Engng.*, in print.

Marsh, S.P. ed. (1980) LASL Shock Hugoniot Data, University of California Press, 658 p.

McDonnell, J.A.M. ed.(1992) *Hypervelocity Impacts in Space*, University of Kent, Canterbury, U.K., 288 pp.

McDonnell, J.A.M. and Sullivan, K. (1992) Hypervelocity Impacts on Space Detectors: Decoding the Projectile Parameters, in *Hypervelocity Impacts in Space*, University of Kent, Canterbury, U.K., p. 39-47.

Pailer, N. and Grun, E. (1980), The Penetration Limit of Thin Films, *Planet. Space Sci., 28*, 321-331.

Pietkutowsky, A.J. (1990) A Simple Dynamic Model for the Formation of Debris Clouds, *Int. J.. Impact Engng., 10,* p. 453-472.

Pietkutowsky, A.J. (1993) Characteristics of Debris Clouds Produced by Hypervelocity Impact of Aluminum Spheres with Thin Aluminum Plates, *Int. J. Impact Engng.*, 573-596.

Pietkutowsky, A.J. (1995) Fragmentation of a Sphere Initiated by Hypervelocity Impact with a Thin Sheet, *Int. J. Impact Engng.*, in press.

Sapp, C.A., See, T.h., Zolensky, M.E. (1993), 3-D Analyseis of LDEF Impact Features from Srereo Imagery, in LDEF-69Months in Space, Second Post Retrieval Sympoium, Levine. A. ed., NASA CP3194, 339-346.

Schmidt, R.M., Housen, K.R., Pietkutowsky, A.J. and Poormon, K.L. (1994) Cadmium Simulation of Orbital Debris Shield Performance to Scaled Velocities of 18 km/s, *J. Spacecraft and Rockets,* in press.

Schneider, E., Stilp, A., Bureo, R. and Lambert, M. (1990) Micrometeoritic and Space Debris Simulation for Columbus Hull Components, *Int. J. Impact Engng., 10*, p. 499-508.

Schneider, E., Stilp, A., Rott, M., Levadou, F. and Schwehm, G. (1993) Hypervelocity Impact Simulation Experiments on LDEF-Foils, *Int. J. Impact Engng., 14*, p. 631-636.

Schultz, P. H. and Lianza, R.E. (1992) Recent Grazing Impacts on the Earth Recorded in the Rio Cuarto Crater Field, Argentinia, *Nature*, Vol. 355., 234-237.

See, T.H., Allbrooks, M.K., Atkinson, D.R., Simon, C.R. and Zolensky, M.E. (1990) *Meteoroid and Debris Impact Features Documented on the Long Duration Exposure Facility, NASA JSC Report # 24608,* 561 pp.

Simon, C. G., Hunter, J.L., Griffis, D.P., Misra, V., Ricks, D.A., Wortman, J.J. anf Brownlee, D.E.(1993), Elemental Analyses of Hypervelocity Microparticle Impact Sites on Interplanetary Dust Experiment Sensor Surfaces, in LDEF-69 Months in Space, Second Post Retrieval Symposium, Levine, A. ed., NASA CP 3194, 677-692.

Stilp, A.J., Hohler, V., Schneider, E., and Weber, K. (1990) Debris Cloud Expansion Studies, *Int. J. Impact Engng., 10,* p. 543-554.

Warren, J.L., Zook, H.A, Allton, J.H., Clanton, U.S., Dardano, C.B., Holder, J.A., Marlow, R.R., Schultz, R.A., Watts, L.A., and Wentworth, S.J. (1989) The Detection and Observation of Meteoroid and Space Debris Impact Features on the Solar Maximum Satellite, *Proc. Lunar Planet. Sci. Conf., 19th*, p. 641-657.

Watts, A., Atkinson, D. and Rieco, S. (1993) *Dimensional Scaling for Impact Cratering and Perforation, NASA JSC Contractor Report, NCR 188259, 170* pp.

Zook, H.A. (1992) Deriving the Velocity Distribution of Meteoroids from the Measured Meteoroid Impact Directionality on the Various LDEF Surfaces, in *LDEF - 69 Months in Space: First Post-Retrieval Symposium, NASA CP 3194*, p. 569-580.

APPENDIX

DETAILED PHOTO DOCUMENTATION OF IMPACT EXPERIMENTS INTO ALUMINUM TARGETS

LEGEND:

SL = Soda-Lime Glass
D_p = Projectile Diameter
V = Impact Velocity
T = Target Thickness

SCALE: Quantitative, dimensional measurements of craters, penetration holes and target thickness are given for each experiment in Table 1. Relative dimensions (D_p/T) are generally given in the legend of each plate; cross-sections and plan-views are generally to the same scale for any given velocity. All witness plates are 29 cm square.

EXPERIMENT IDENTIFICATION: Each experiment is uniquely identified with a laboratory shot number. This number identifies the chronological sequence in which the experiments were conducted utilizing the three different guns within the Experimental Impact Facility, SN4, at the Johnson Space Center:

Shot Numbers 11-114:	New 5 mm Light-Gas Gun
Shot Numbers 428-1316:	Old 5 mm Light-Gas Gun
Shot Numbers >3000:	Powder Propellant, Vertical Impact Facility

ORGANIZATION OF APPENDIX: The appendix is organized by experimental topic and duplicates the sequence of experiments as listed in Table 1 (at the end of the Appendix). For the purpose of comparison, we deemed it useful to organize the photodocumentation by the two variables of prime interest, impact velocity and target thickness. Table 2 (at the end of the Appendix) lists all of the experiments in numerical order and serves as a cross-reference to locate any experiment by shot number.

Cratering events are typically captured with a plan view of the target's front side (forward facing) and a cross-sectional view through the target. Penetrations typically portray the target's front (forward facing) and back sides (rearward facing), and a cross-section; the latter was omitted for targets where $D_p/T > 10$ as such images were not very informative for such thin targets. Penetration experiments are also characterized by witness-plate photographs. However, witness-plate photgraphs were omitted for very massive targets where there was no penetration and, subsequently, no associated damage.

Some judgment had to be exercised in determining when to switch from optical-microscope scales to that of a Scanning Electron Microscope (SEM) for the portrayal of high-resolution details. The time-consuming nature of the SEM limited the high-resolution SEM photography to representative views only.

SHOT # 3604

PROJECTILE: Soda Lime

D_p = 3175 μm

V = 1.09 km/s

TARGET: 1100

T = 12545 μm

FRONT

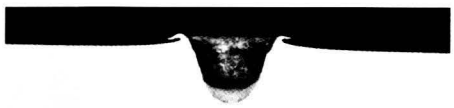

REAR

CLOSE-UP

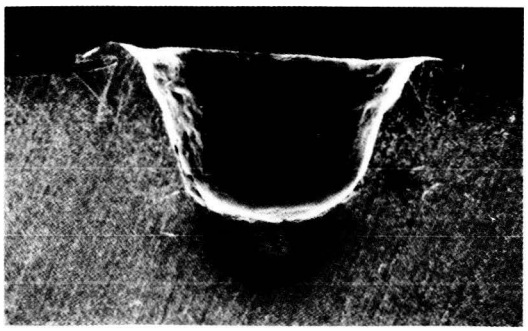

SHOT # 3594

PROJECTILE: Soda Lime

D_p = 3175 μm

V = 1.52 km/s

TARGET: 1100

T = 12471 μm

FRONT

CROSS-SECTION

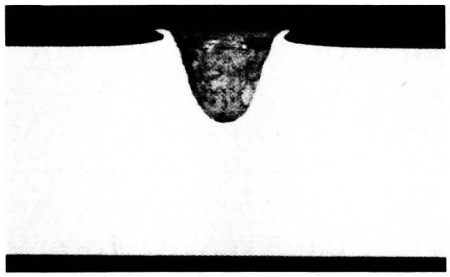

CLOSE-UP

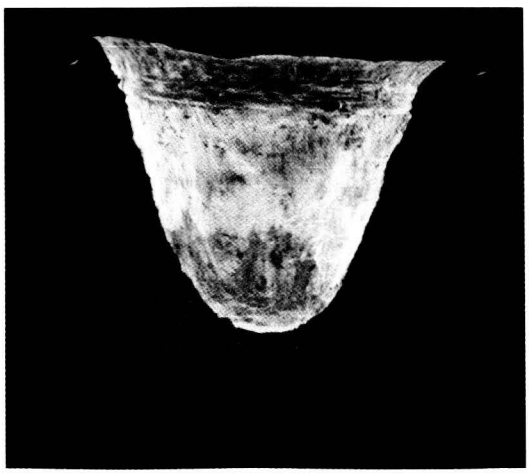

SHOT # 3593

PROJECTILE: Soda Lime

D_p = 3175 μm

V = 1.88 km/s

TARGET: 1100

T = 9761 μm

FRONT

CROSS-SECTION

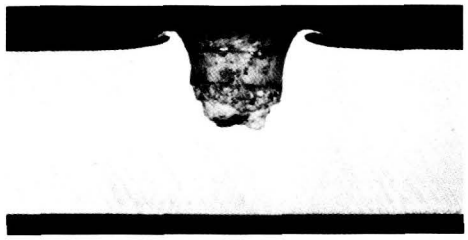

CLOSE-UP

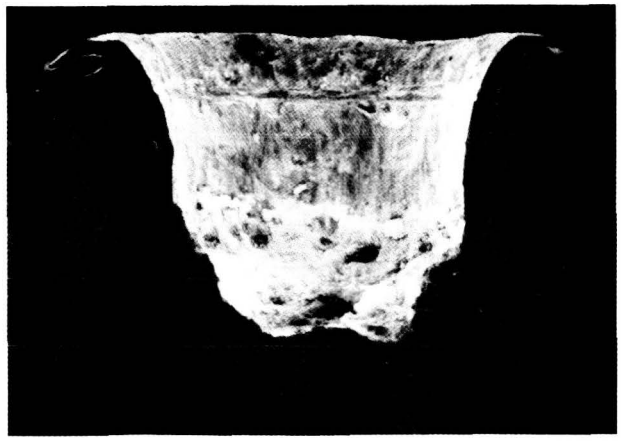

SHOT # 3609

PROJECTILE: Soda Lime

D_p = 3175 μm

V = 2.03 km/s

TARGET: 1100

T = 20455 μm

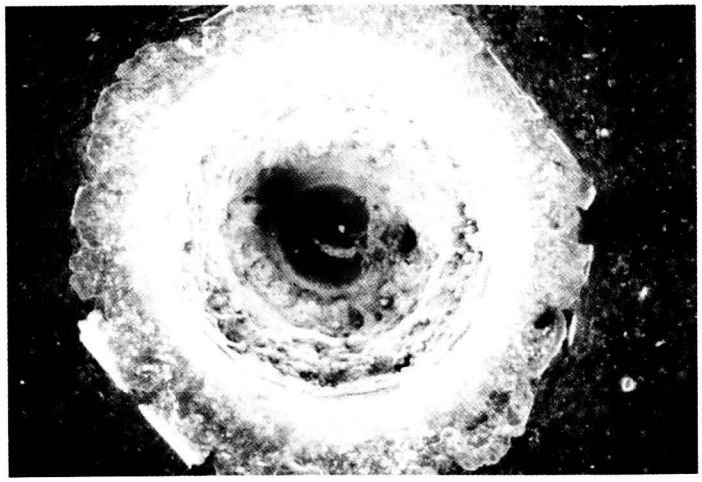

FRONT

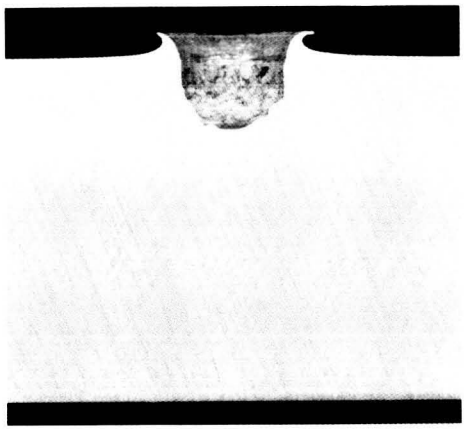

CROSS-SECTION

CLOSE-UP

SHOT # 3610

PROJECTILE: Soda Lime

D_p = 3175 μm

V = 2.18 km/s

TARGET: 1100

T = 24689 μm

FRONT

CROSS-SECTION

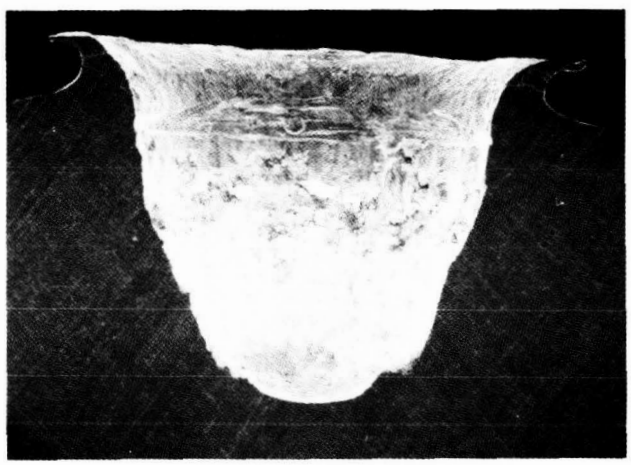

CLOSE-UP

SHOT # 3596

PROJECTILE: Soda Lime

D_p = 3175 μm

V = 2.71 km/s

TARGET: 1100

T = 12621 μm

FRONT

CROSS-SECTION

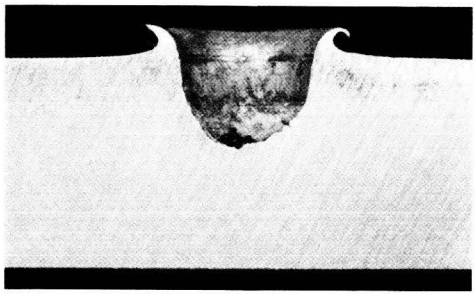

CLOSE-UP

SHOT # 3605

PROJECTILE: Soda Lime

D_p = 3175 μm

V = 2.74 km/s

TARGET: 1100

T = 25044 μm

FRONT

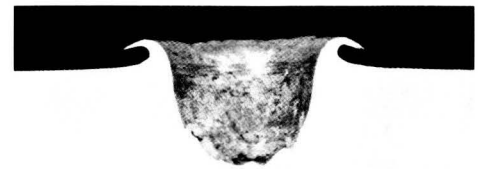

CROSS-SECTION

CLOSE-UP

SHOT # 3606

PROJECTILE: Soda Lime
D_p = 3175 μm
V = 2.95 km/s

TARGET: 1100
T = 25017 μm

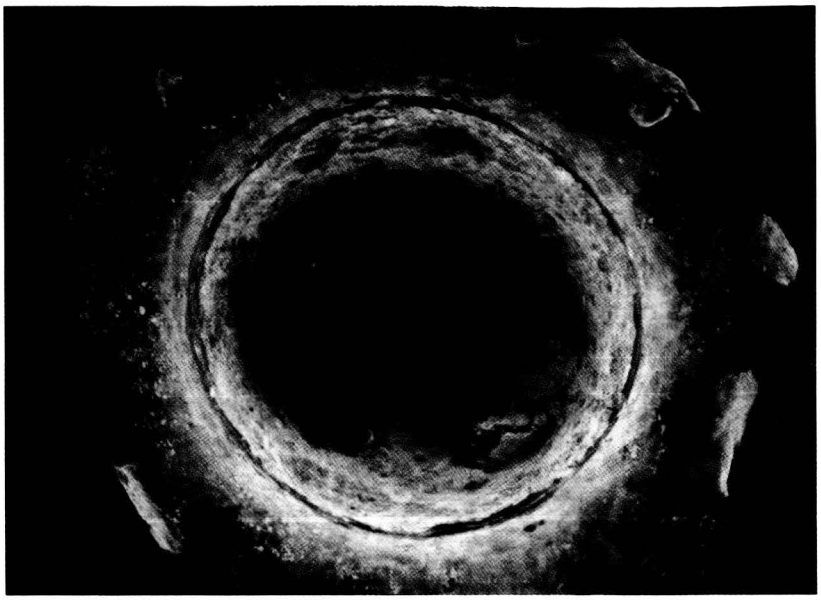

FRONT

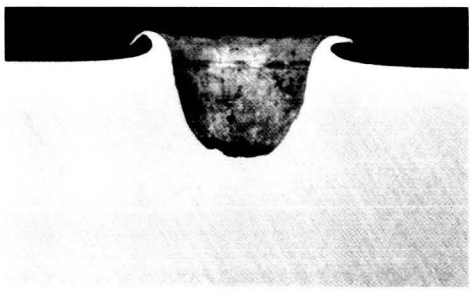

CROSS-SECTION

CLOSE-UP

SHOT # 3607

PROJECTILE: Soda Lime
D_p = 3175 μm
V = 3.03 km/s

TARGET: 1100
T = 24864 μm

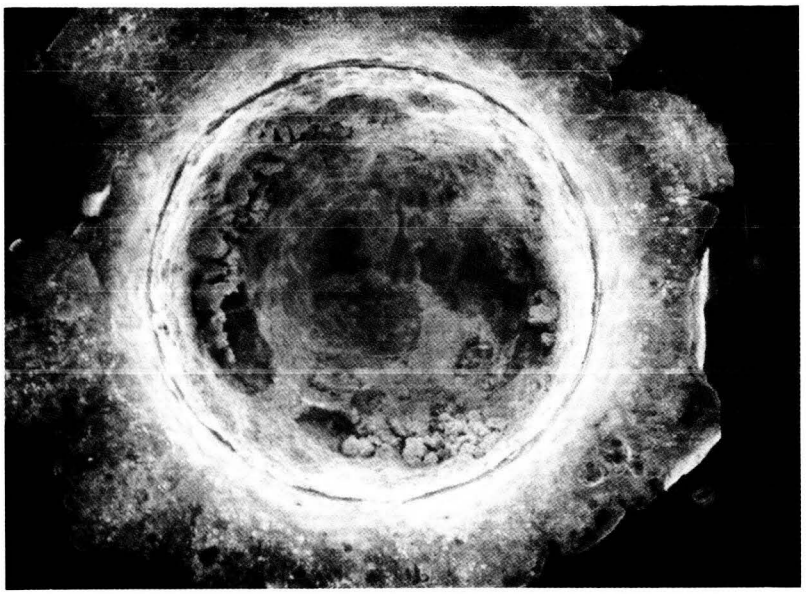

FRONT

CROSS-SECTION

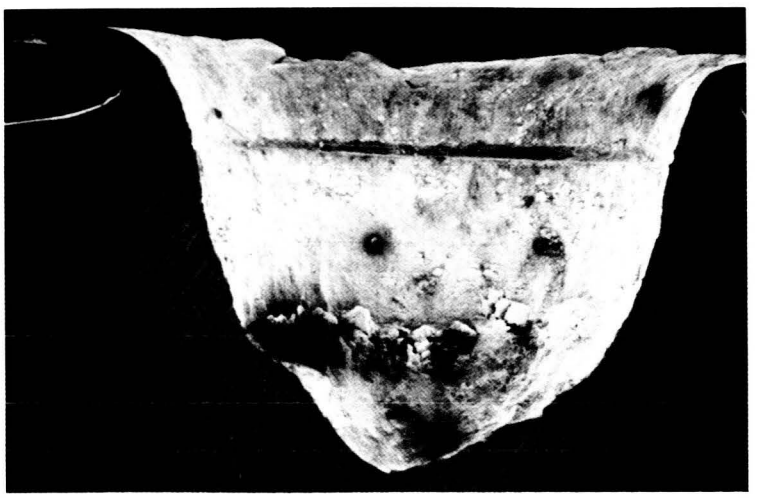

CLOSE-UP

SHOT # 1277

PROJECTILE: Soda Lime

D_p = 3175 μm

V = 3.18 km/s

TARGET: 1100

T = 24359 μm

FRONT

CROSS-SECTION

CLOSE-UP

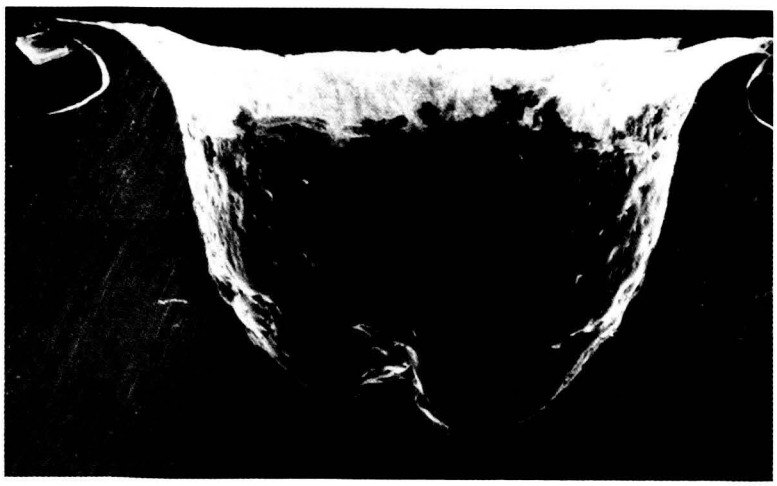

SHOT # 1279

PROJECTILE: Soda Lime

D_p = 3175 μm

V = 3.45 km/s

TARGET: 1100

T = 32029 μm

FRONT

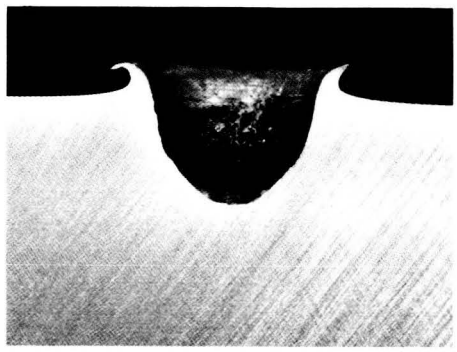

CROSS-SECTION

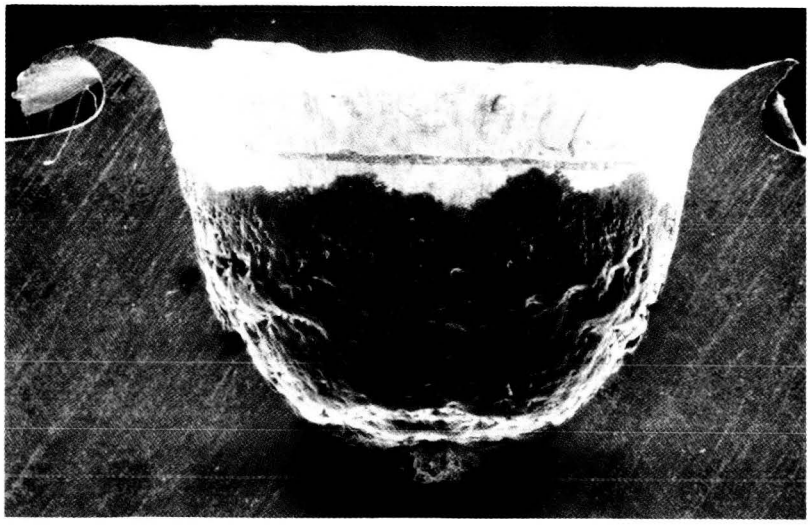

CLOSE-UP

SHOT # 1268

PROJECTILE: Soda Lime

D_p = 3175 μm

V = 3.63 km/s

TARGET: 1100

T = 24536 μm

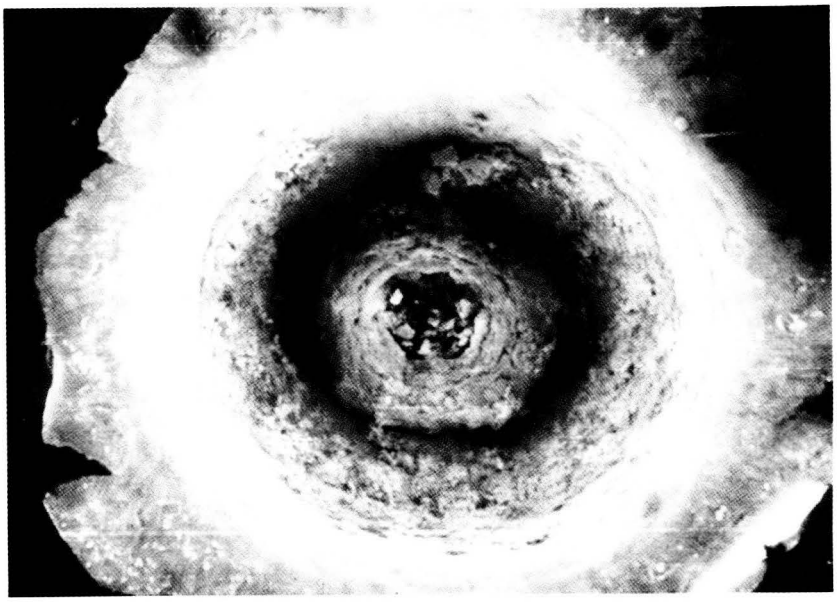

FRONT

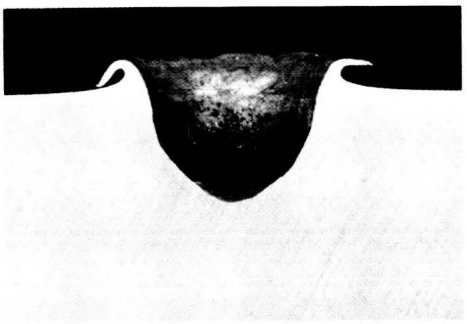

CROSS-SECTION

CLOSE-UP

SHOT # 1278

PROJECTILE: Soda Lime

D_p = 3175 μm

V = 3.92 km/s

TARGET: 1100

T = 24562 μm

FRONT

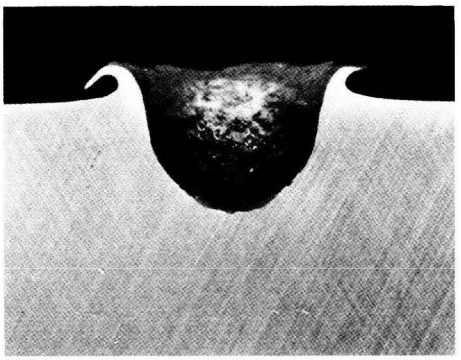

CROSS-SECTION

CLOSE-UP

SHOT # 1154

PROJECTILE: Soda Lime

D_p = 3175 μm

V = 4.00 km/s

TARGET: 1100

T = 19125 μm

FRONT

CROSS-SECTION

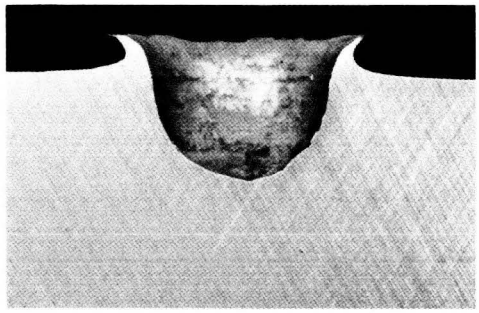

CLOSE-UP

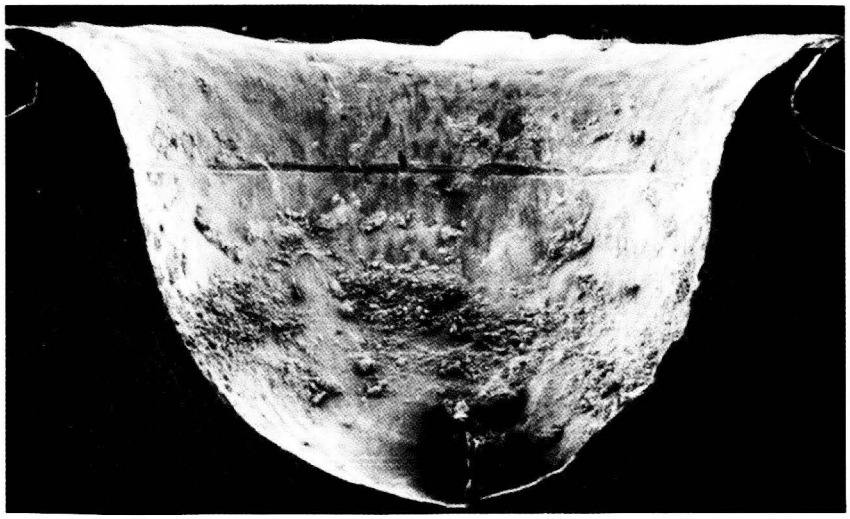

SHOT # 1252

PROJECTILE: Soda Lime

D_p = 3175 μm

V = 4.17 km/s

TARGET: 1100

T = 22600 μm

FRONT

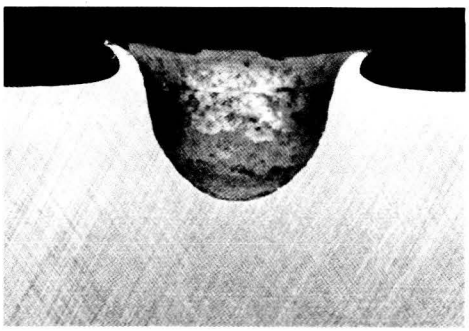

CROSS-SECTION

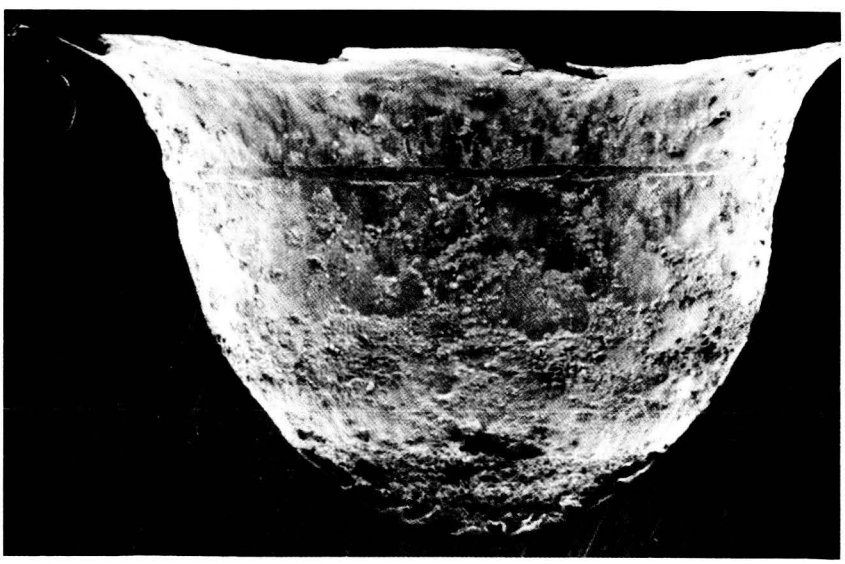

CLOSE-UP

SHOT # 1253

PROJECTILE: Soda Lime

D_p = 3175 μm

V = 4.36 km/s

TARGET: 1100

T = 24700 μm

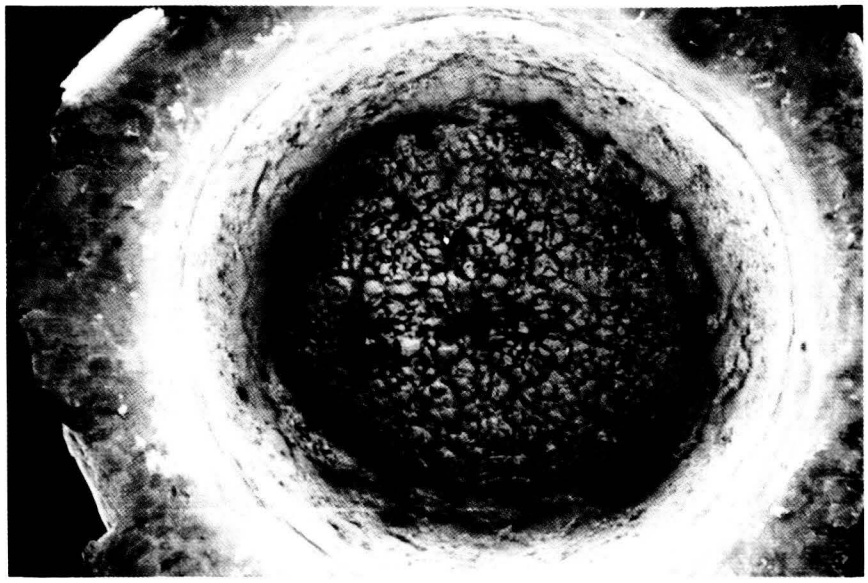

FRONT

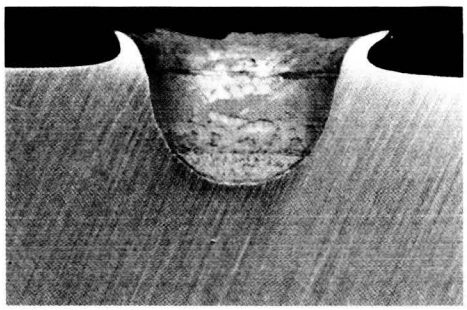

CROSS-SECTION

CLOSE-UP

SHOT # 1266

PROJECTILE: Soda Lime

D_p = 3175 μm

V = 4.44 km/s

TARGET: 1100

T = 37592 μm

FRONT

CROSS-SECTION

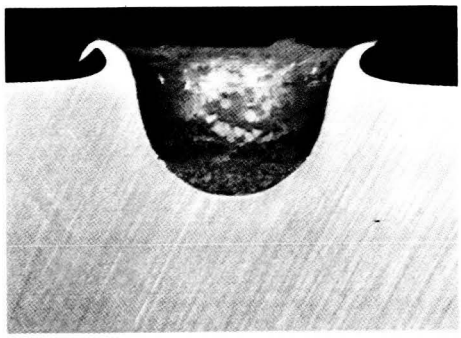

CLOSE-UP

SHOT # 1251

PROJECTILE: Soda Lime

D_p = 3175 μm

V = 4.71 km/s

TARGET: 1100

T = 24600 μm

FRONT

CROSS-SECTION

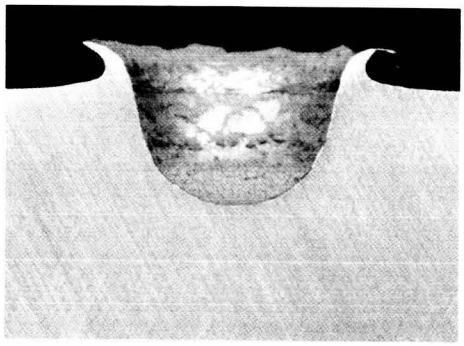

CLOSE-UP

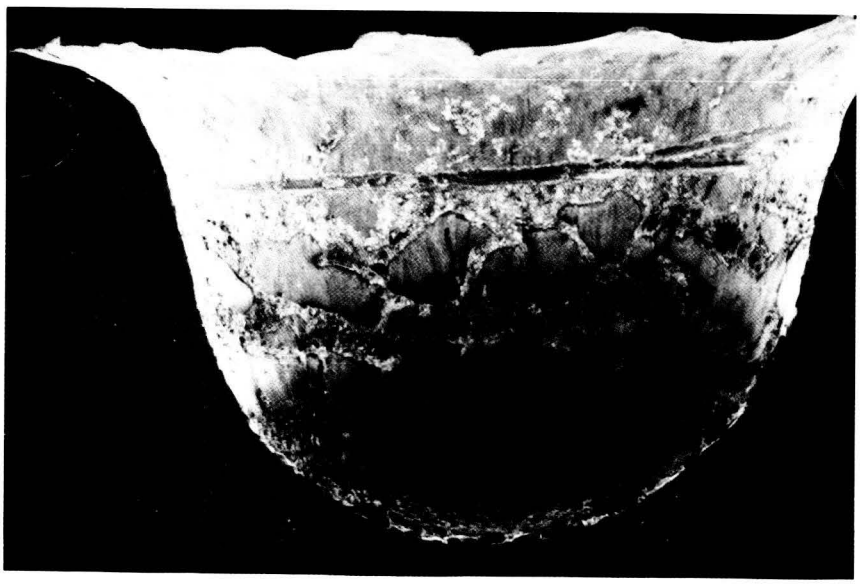

SHOT # 1149

PROJECTILE: Soda Lime

D_p = 3175 μm

V = 5.16 km/s

TARGET: 1100

T = 19500 μm

FRONT

CROSS-SECTION

CLOSE-UP

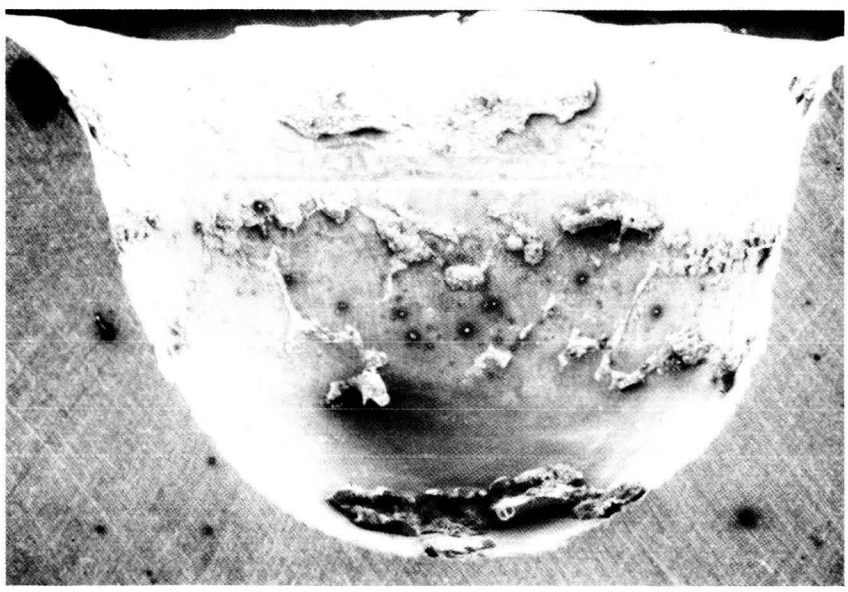

SHOT # 1267

PROJECTILE: Soda Lime
D_p = 3175 μm
V = 5.27 km/s

TARGET: 1100
T = 37643 μm

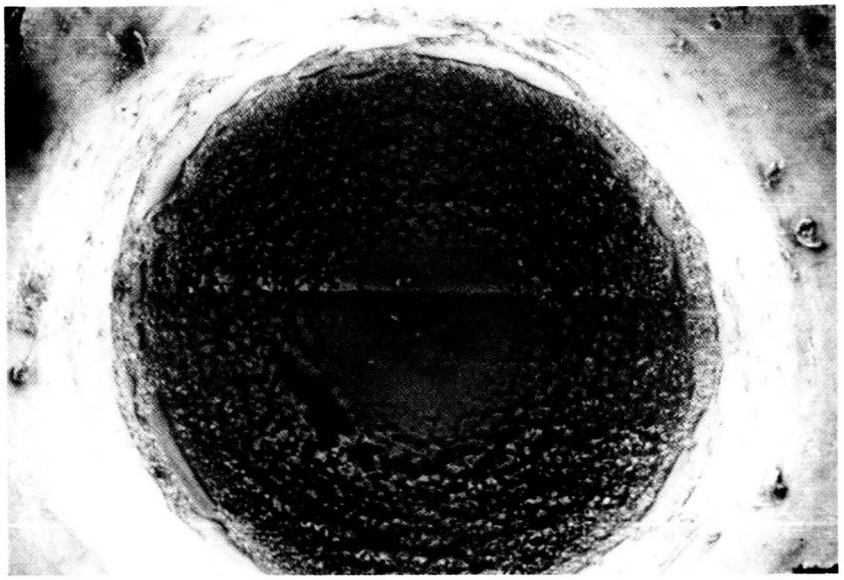

FRONT

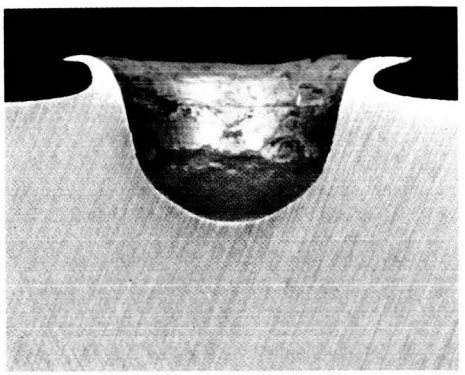

CROSS-SECTION

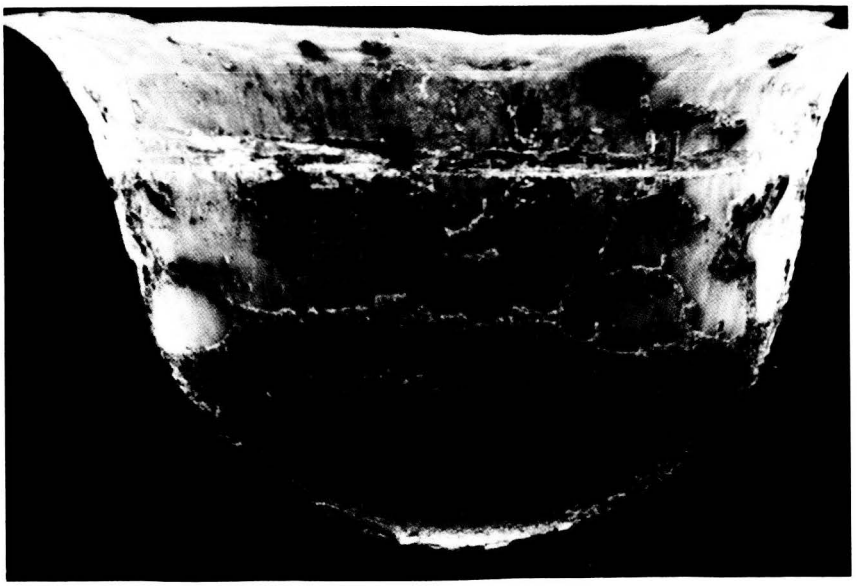

CLOSE-UP

SHOT # 1248

PROJECTILE: Soda Lime

D_p = 3175 μm

V = 5.37 km/s

TARGET: 1100

T = 24800 μm

FRONT

CROSS-SECTION

CLOSE-UP

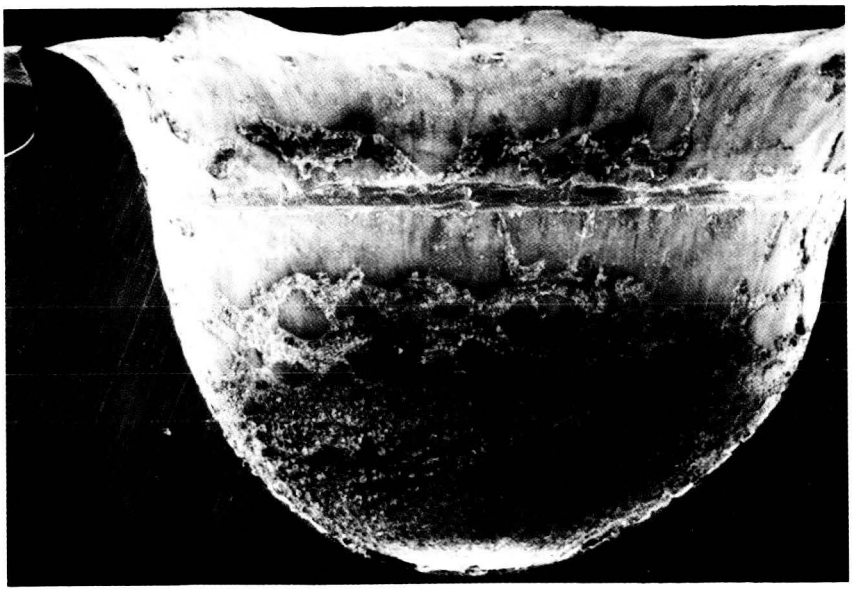

SHOT # 792

PROJECTILE: Soda Lime

D_p = 3175 μm

V = 5.69 km/s

TARGET: 1100

T = 25400 μm

FRONT

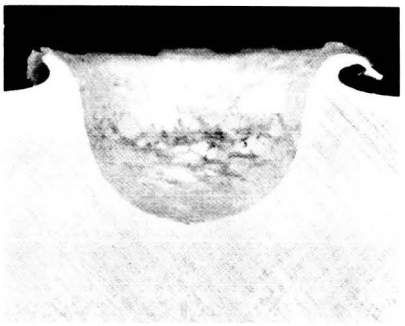

CROSS-SECTION

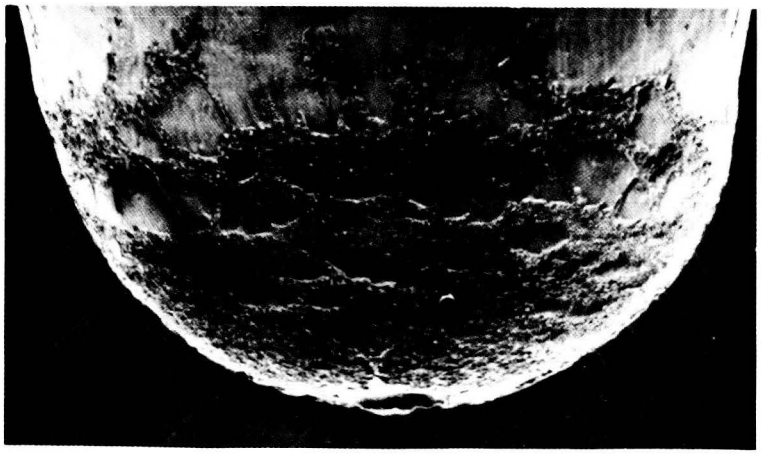

CLOSE-UP

SHOT # 1247

PROJECTILE: Soda Lime

D_p = 3175 μm

V = 5.75 km/s

TARGET: 1100

T = 24800 μm

FRONT

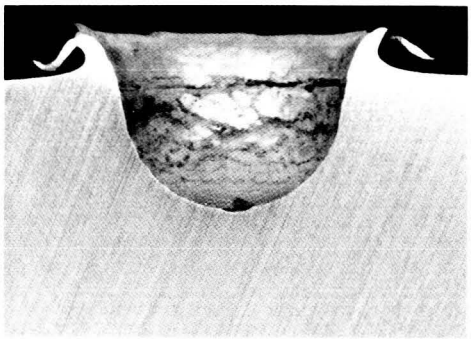

CROSS-SECTION

CLOSE-UP

SHOT # 97

PROJECTILE: Soda Lime

D_p = 3175 μm

V = 5.85 km/s

TARGET: 1100

T = 19660 μm

FRONT

CROSS-SECTION

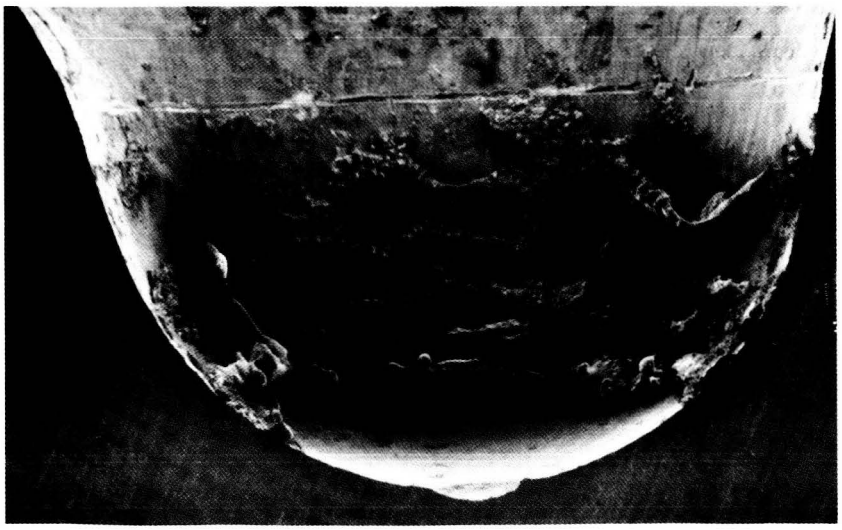

CLOSE-UP

C-2

SHOT # 949

PROJECTILE: Soda Lime

D_p = 3175 μm

V = 5.92 km/s

TARGET: 1100

T = 19500 μm

FRONT

CROSS-SECTION

CLOSE-UP

SHOT # 1249

PROJECTILE: Soda Lime

D_p = 3175 μm

V = 6.03 km/s

TARGET: 1100

T = 24600 μm

FRONT

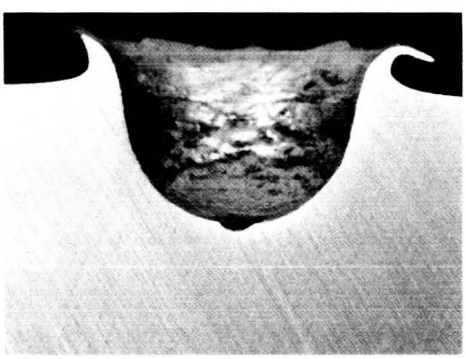

CROSS-SECTION

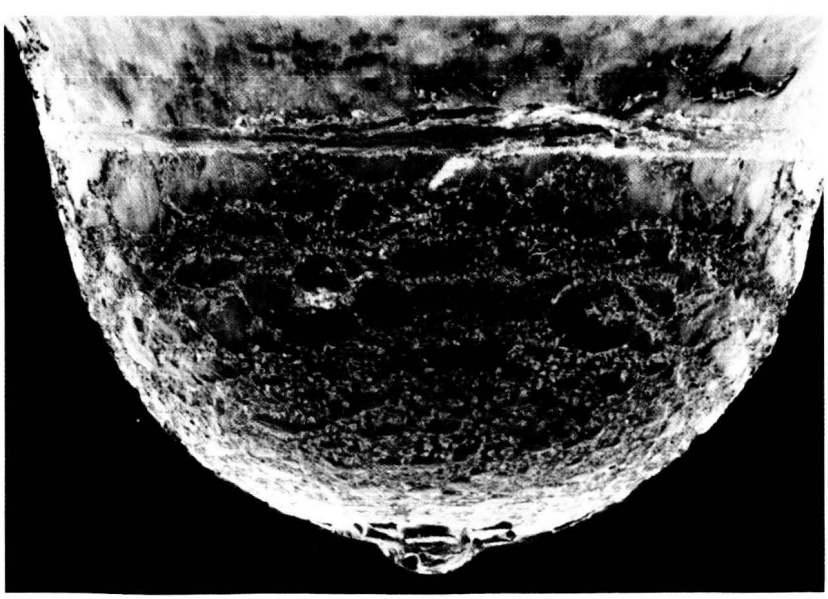

CLOSE-UP

SHOT # 1261

PROJECTILE: Soda Lime

D_p = 3175 μm

V = 6.13 km/s

TARGET: 1100

T = 37643 μm

FRONT

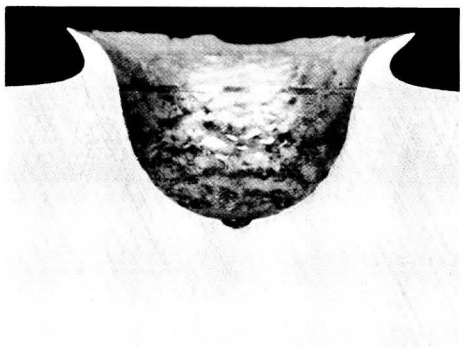

CROSS-SECTION

CLOSE-UP

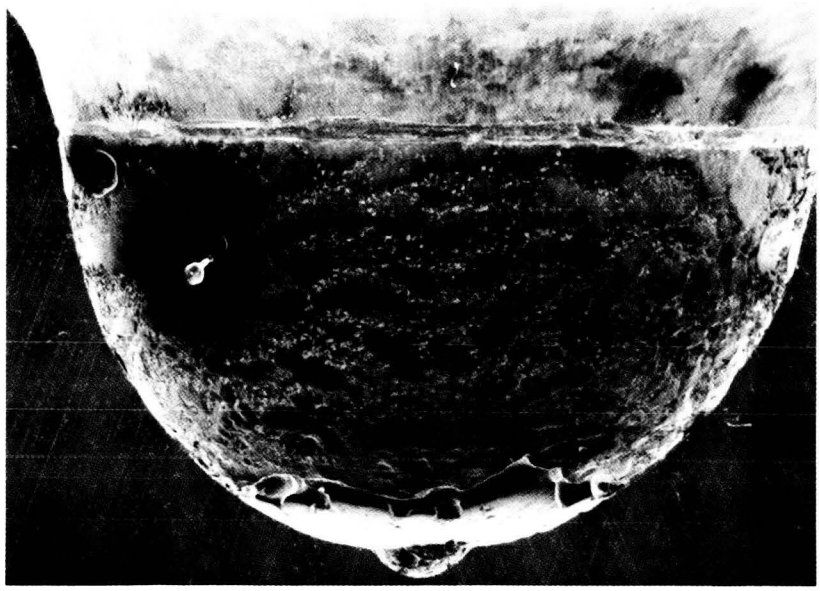

SHOT # 1250

PROJECTILE: Soda Lime

D_p = 3175 μm

V = 6.30 km/s

TARGET: 1100

T = 24700 μm

FRONT

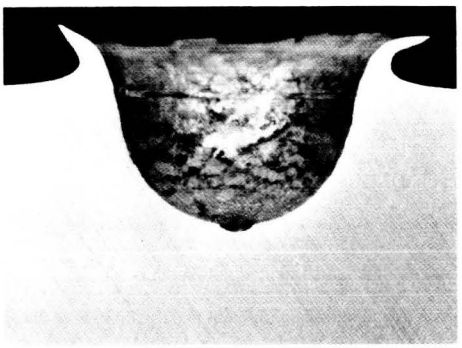

CROSS-SECTION

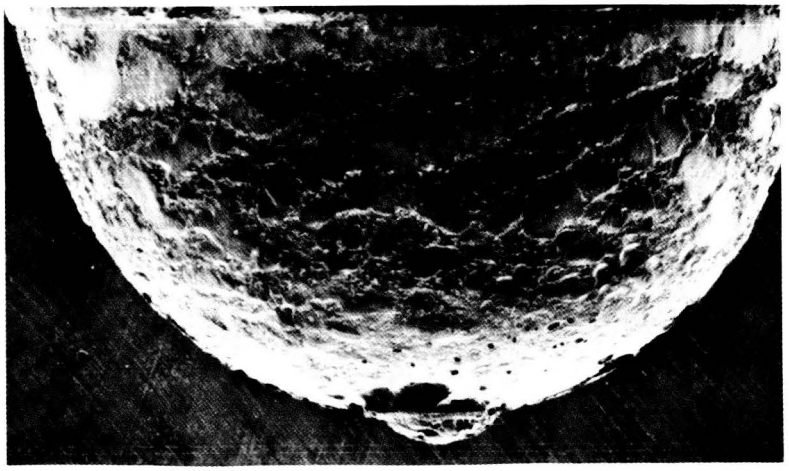

CLOSE-UP

SHOT # 1262

PROJECTILE: Soda Lime

D_p = 3175 μm

V = 6.46 km/s

TARGET: 1100

T = 37668 μm

FRONT

CROSS-SECTION

CLOSE-UP

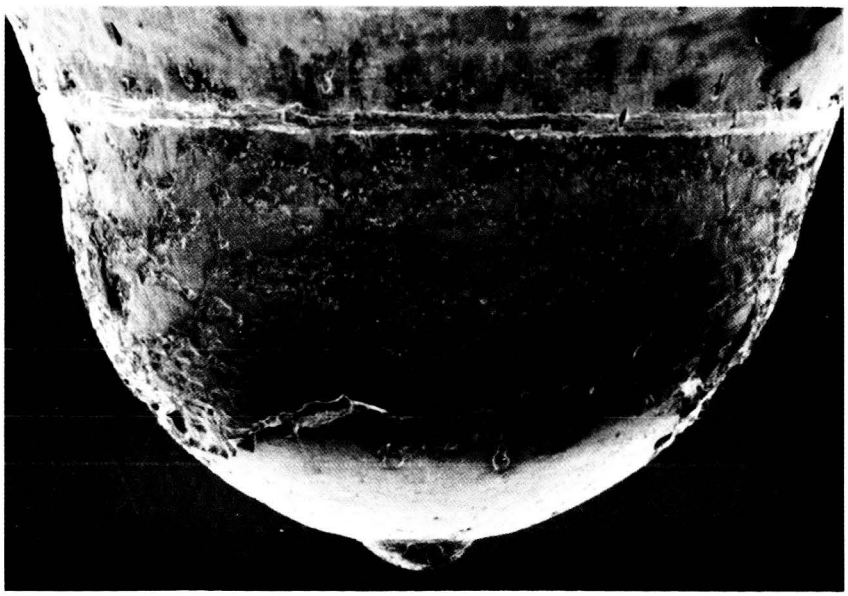

SHOT # 1297

PROJECTILE: Soda Lime

D_p = 3175 μm

V = 6.79 km/s

TARGET: 1100

T = 37287 μm

FRONT

CROSS-SECTION

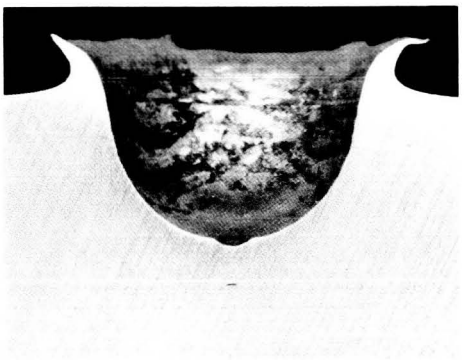

CLOSE-UP

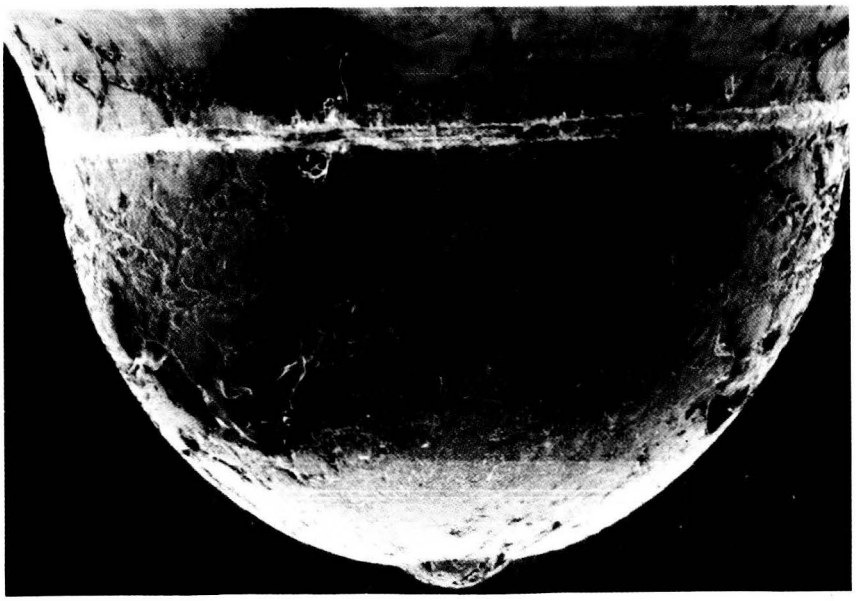

SHOT # 106

PROJECTILE: Soda Lime

D_p = 3175 μm

V = 6.96 km/s

TARGET: 1100

T = 37859 μm

FRONT

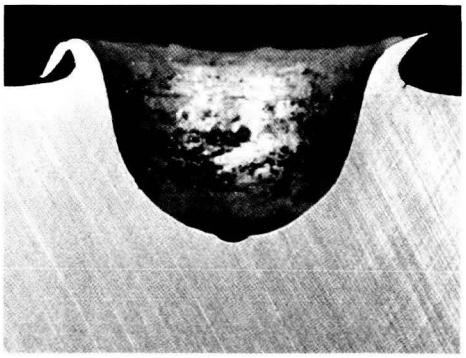

CROSS-SECTION

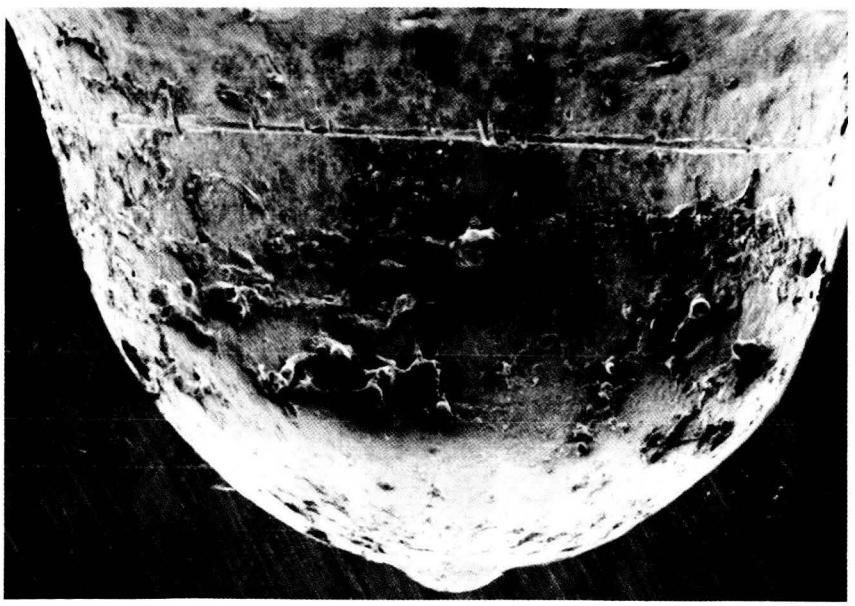

CLOSE-UP

SHOT # 1298

PROJECTILE: Soda Lime

D_p = 3175 μm

V = 7.09 km/s

TARGET: 1100

T = 32338 μm

FRONT

CROSS-SECTION

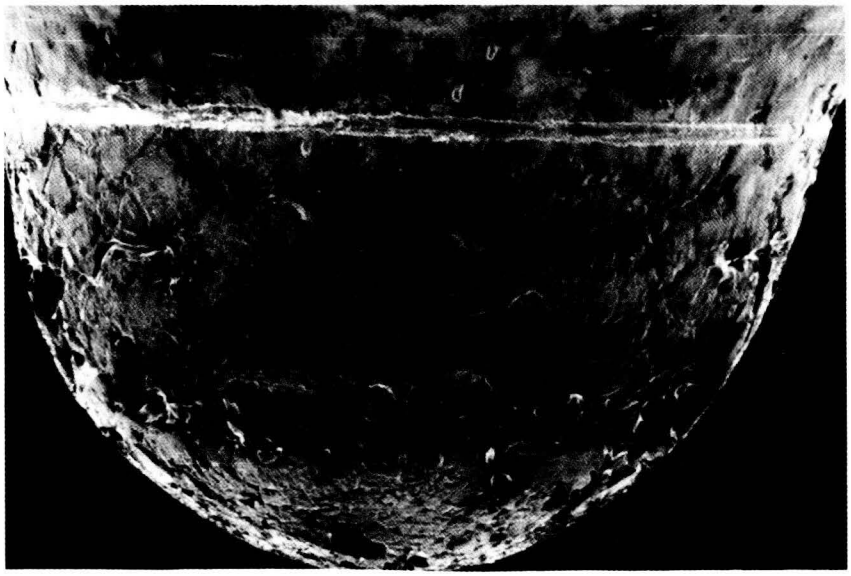

CLOSE-UP

SHOT # 3612

PROJECTILE: Soda Lime

D_p = 3175 μm

V = 1.97 km/s

TARGET: 1100

T = 19400 μm

D_p/T = 0.16

FRONT

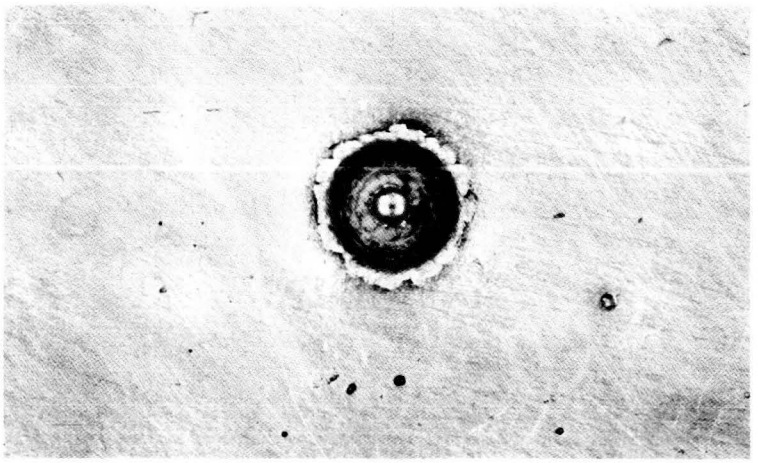

REAR

CROSS-SECTION

SHOT # 3613

PROJECTILE: Soda Lime

D_p = 3175 μm

V = 1.94 km/s

TARGET: 1100

T = 6300 μm

D_p/T = 0.50

FRONT

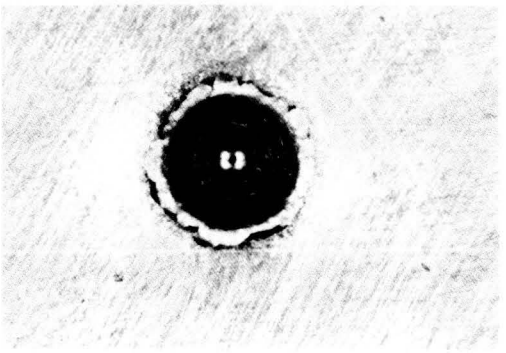

REAR

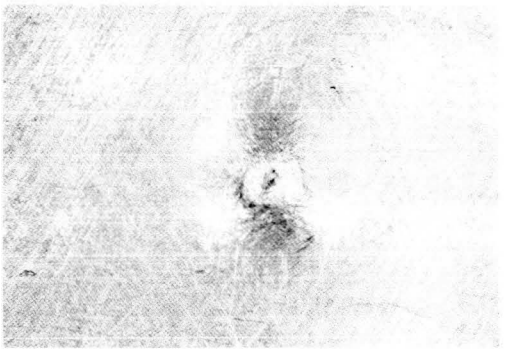

CROSS-SECTION

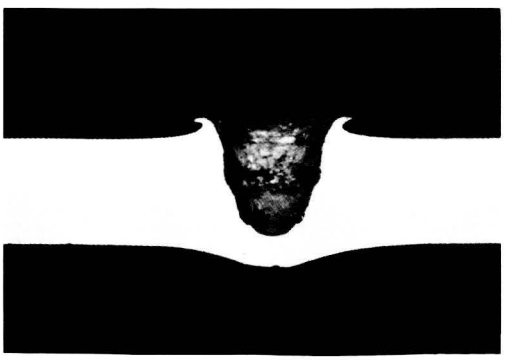

SHOT # 3614

PROJECTILE: Soda Lime

D_p = 3175 μm

V = 1.99 km/s

TARGET: 1100

T = 4870 μm

D_p/T = 0.65

FRONT

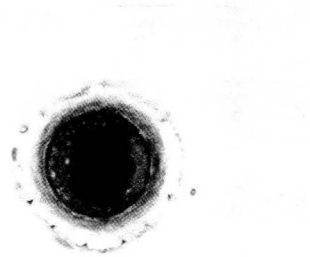

REAR

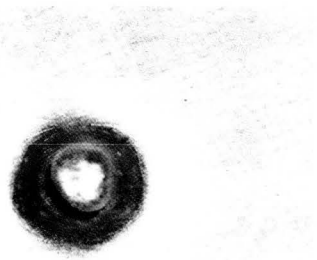

CROSS-SECTION

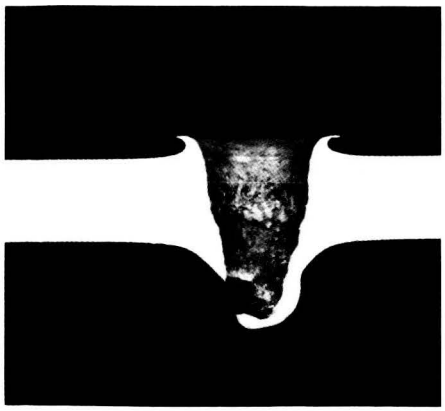

SHOT # 3617

PROJECTILE: Soda Lime

D_p = 3175 μm

V = 1.98 km/s

TARGET: 1100

T = 3937 μm

D_p/T = 0.81

FRONT

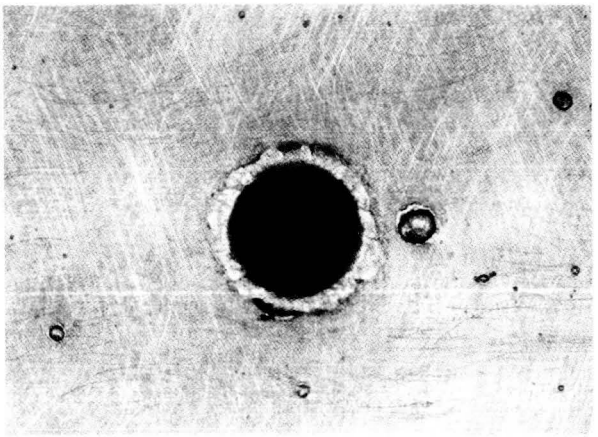

REAR

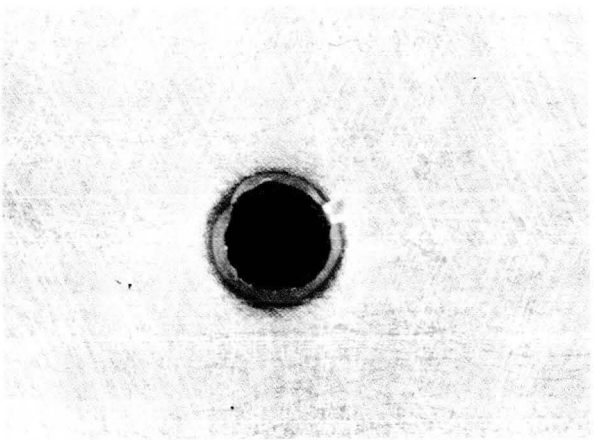

CROSS-SECTION

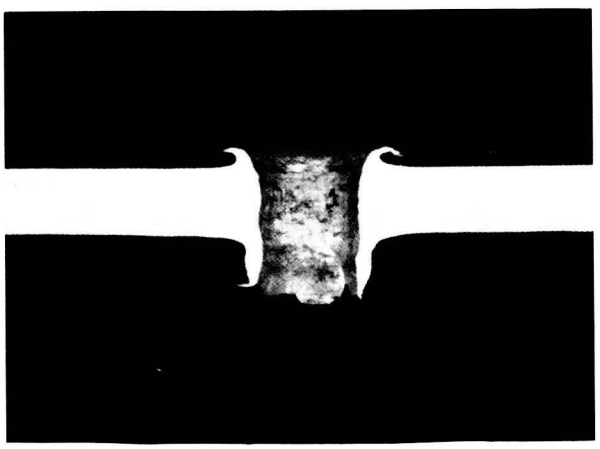

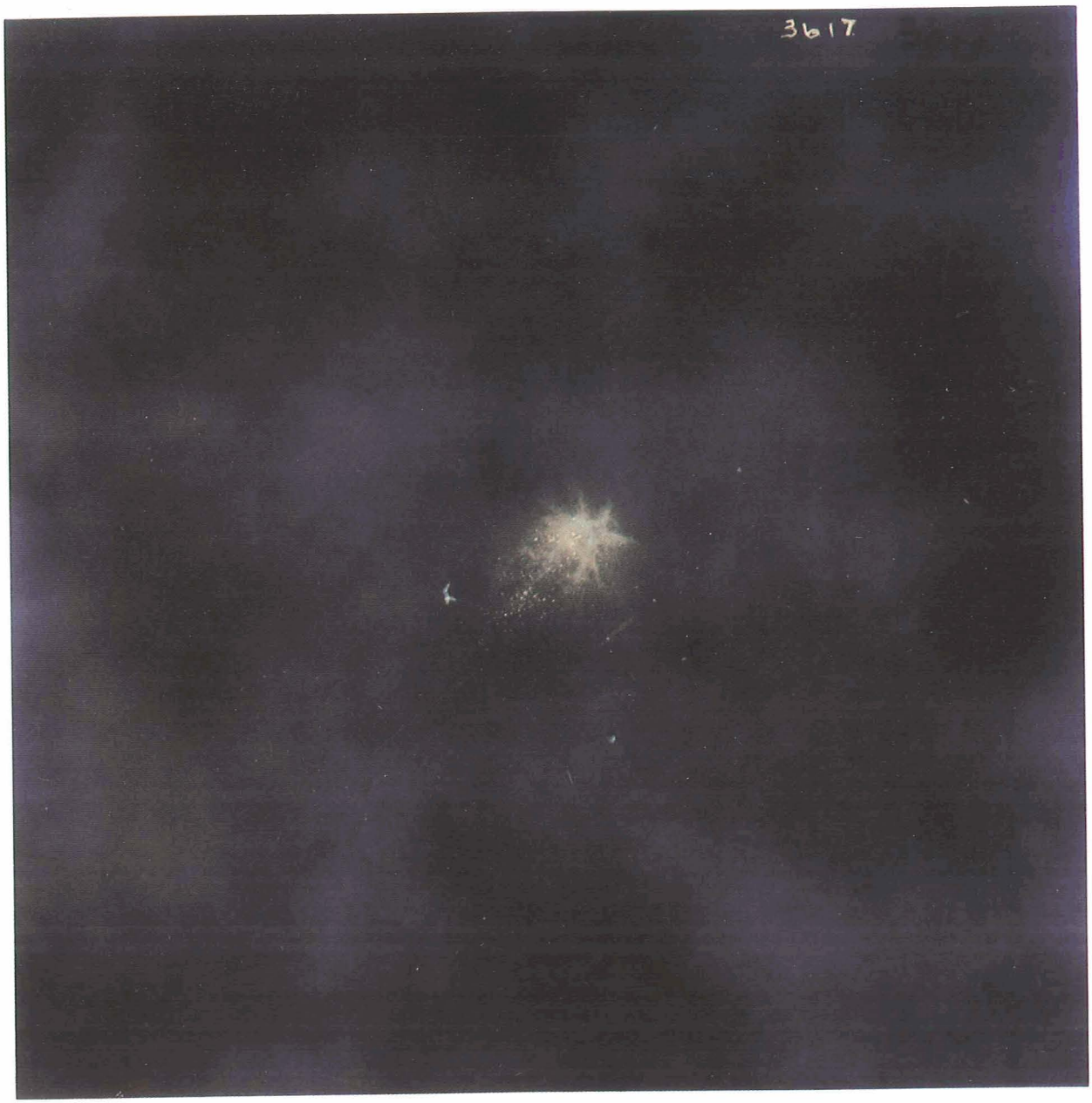
3617

SHOT # 3615

PROJECTILE: Soda Lime

D_p = 3175 μm

V = 1.98 km/s

TARGET: 1100

T = 3230 μm

D_p/T = 0.98

FRONT

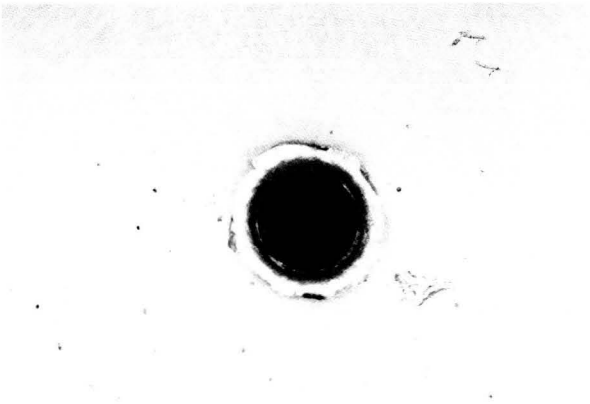

REAR

CROSS-SECTION

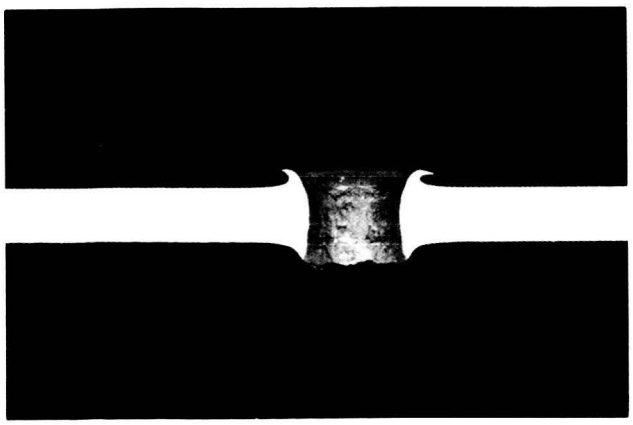

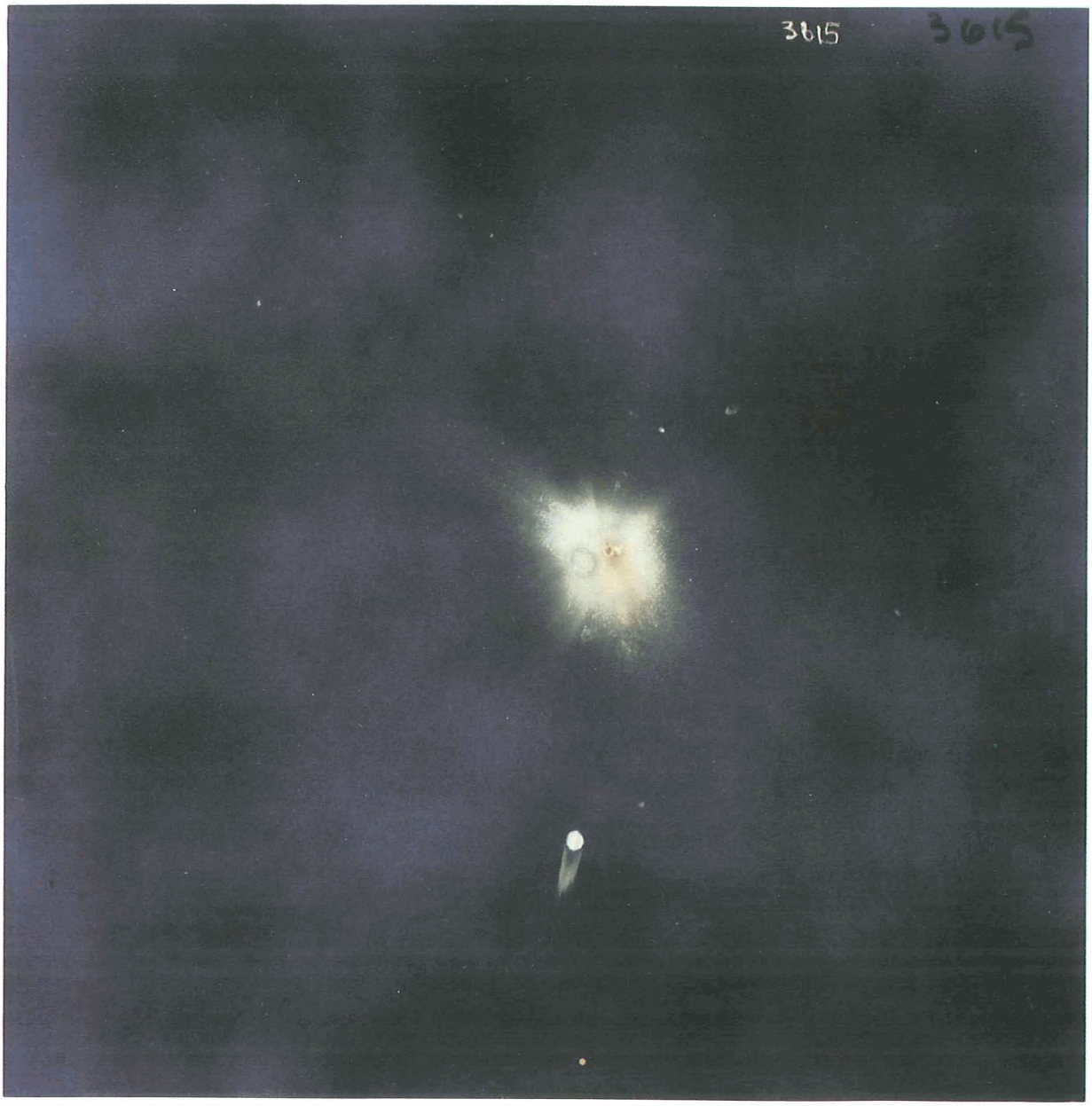
3615
3615

SHOT # 3625

PROJECTILE: Soda Lime

D_p = 3175 μm

V = 2.05 km/s

TARGET: 1100

T = 2450 μm

D_p/T = 1.30

FRONT

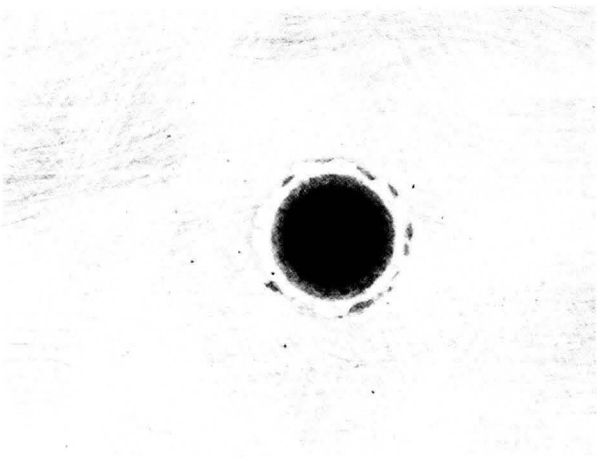

REAR

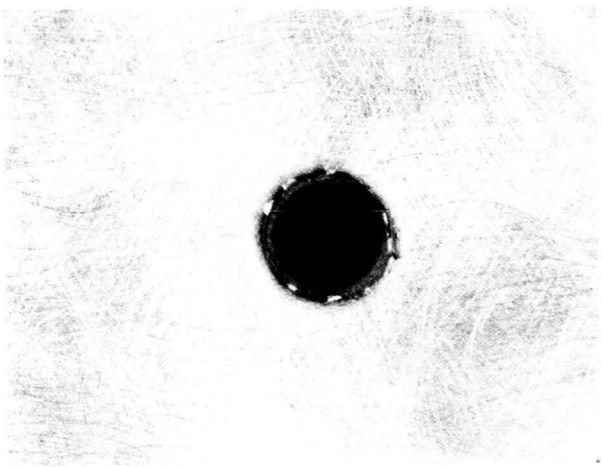

CROSS-SECTION

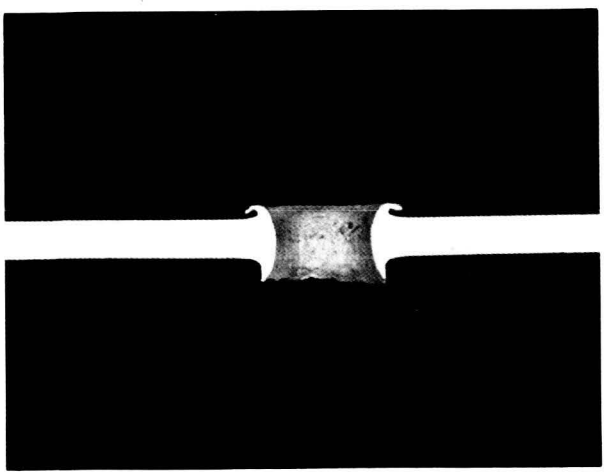

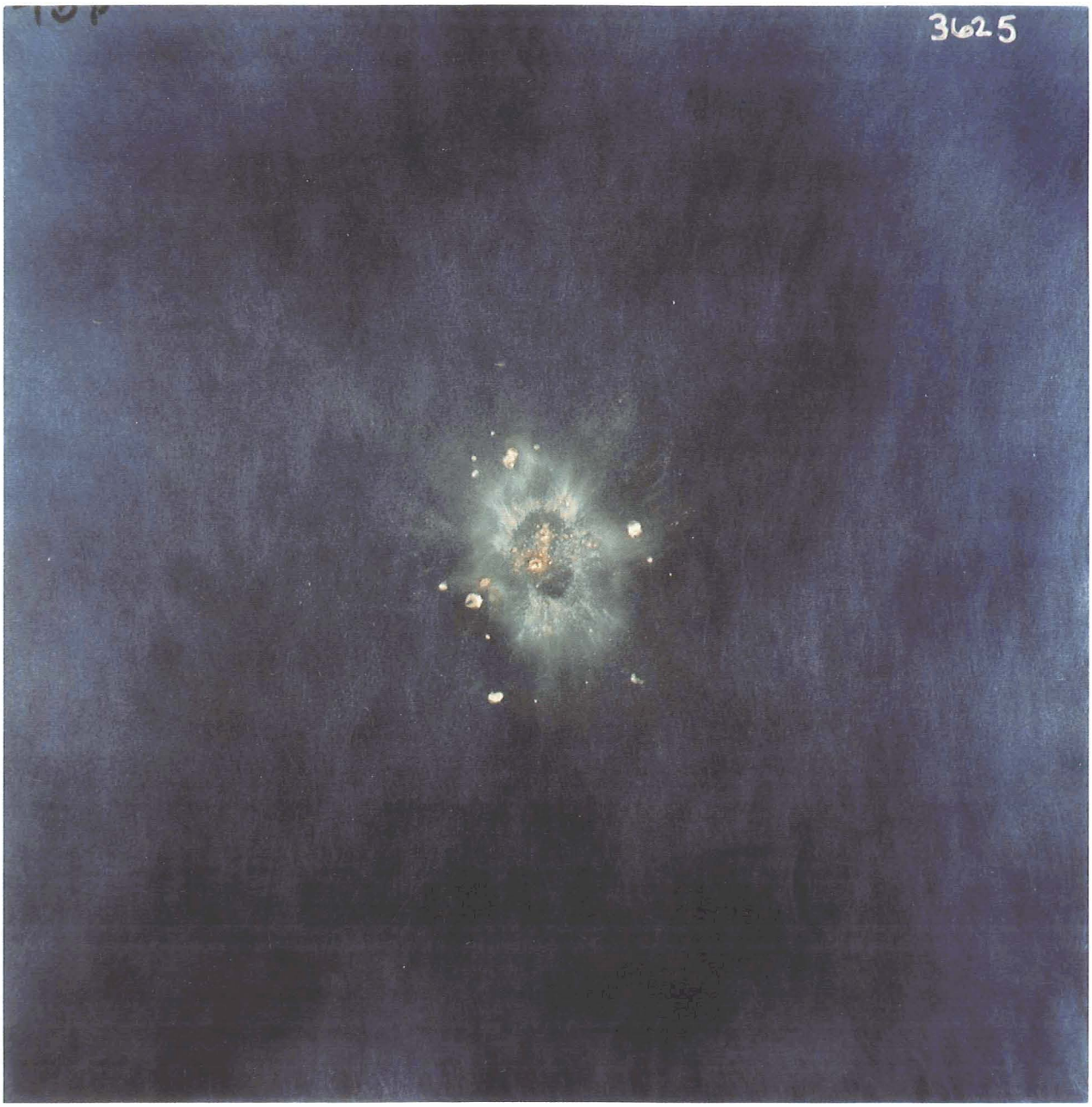
3625

SHOT # 3624

PROJECTILE: Soda Lime

D_p = 3175 μm

V = 2.04 km/s

TARGET: 1100

T = 1676 μm

D_p/T = 1.89

FRONT

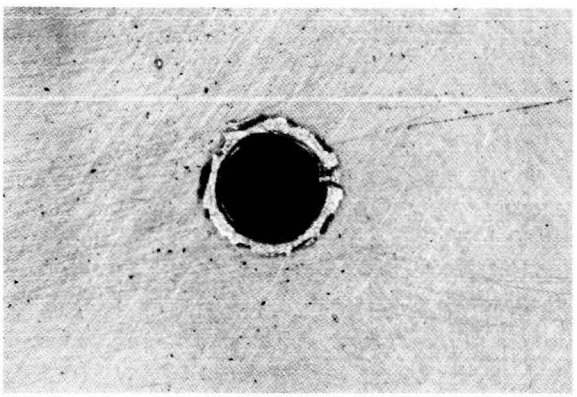

REAR

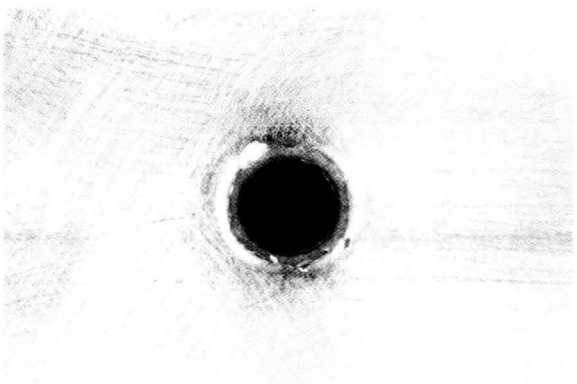

CROSS-SECTION

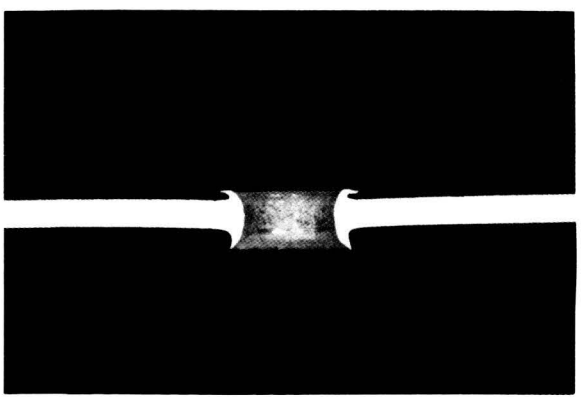

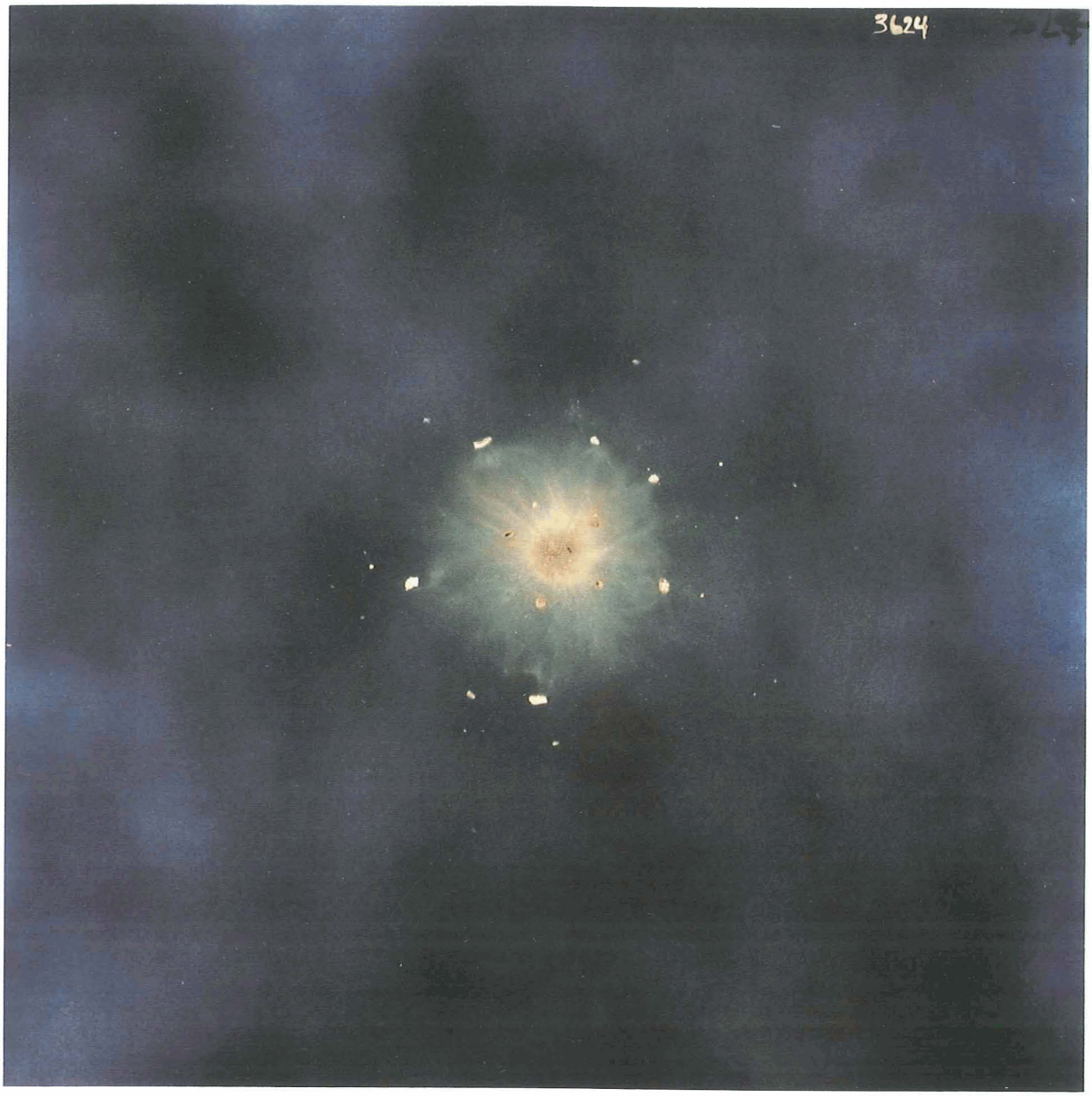
3624

SHOT # 3616

PROJECTILE: Soda Lime

D_p = 3175 μm

V = 1.99 km/s

TARGET: 1100

T = 990 μm

D_p/T = 3.21

FRONT

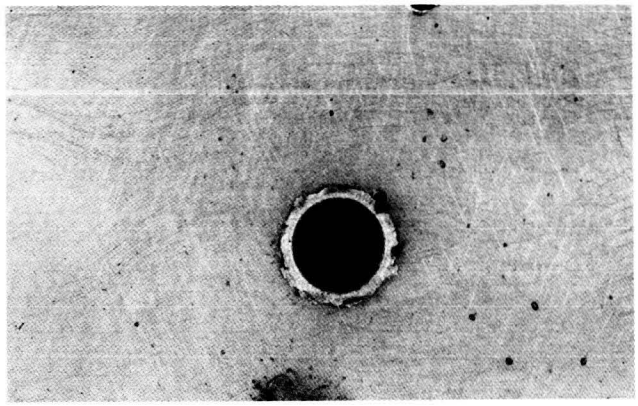

REAR

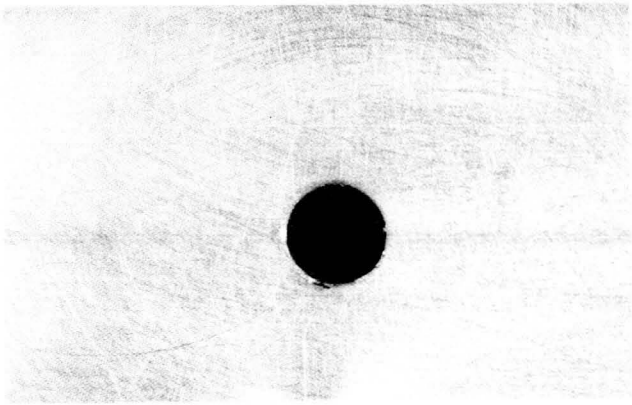

CROSS-SECTION

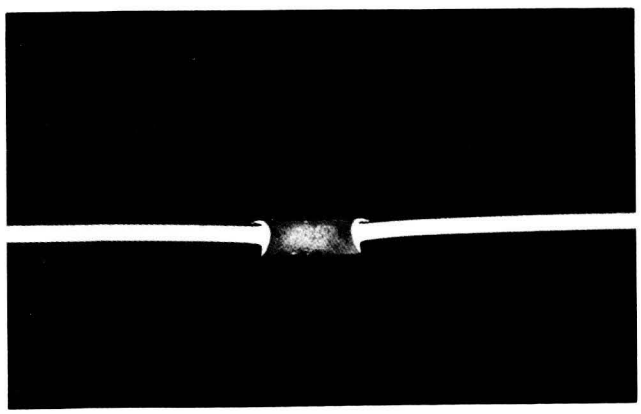

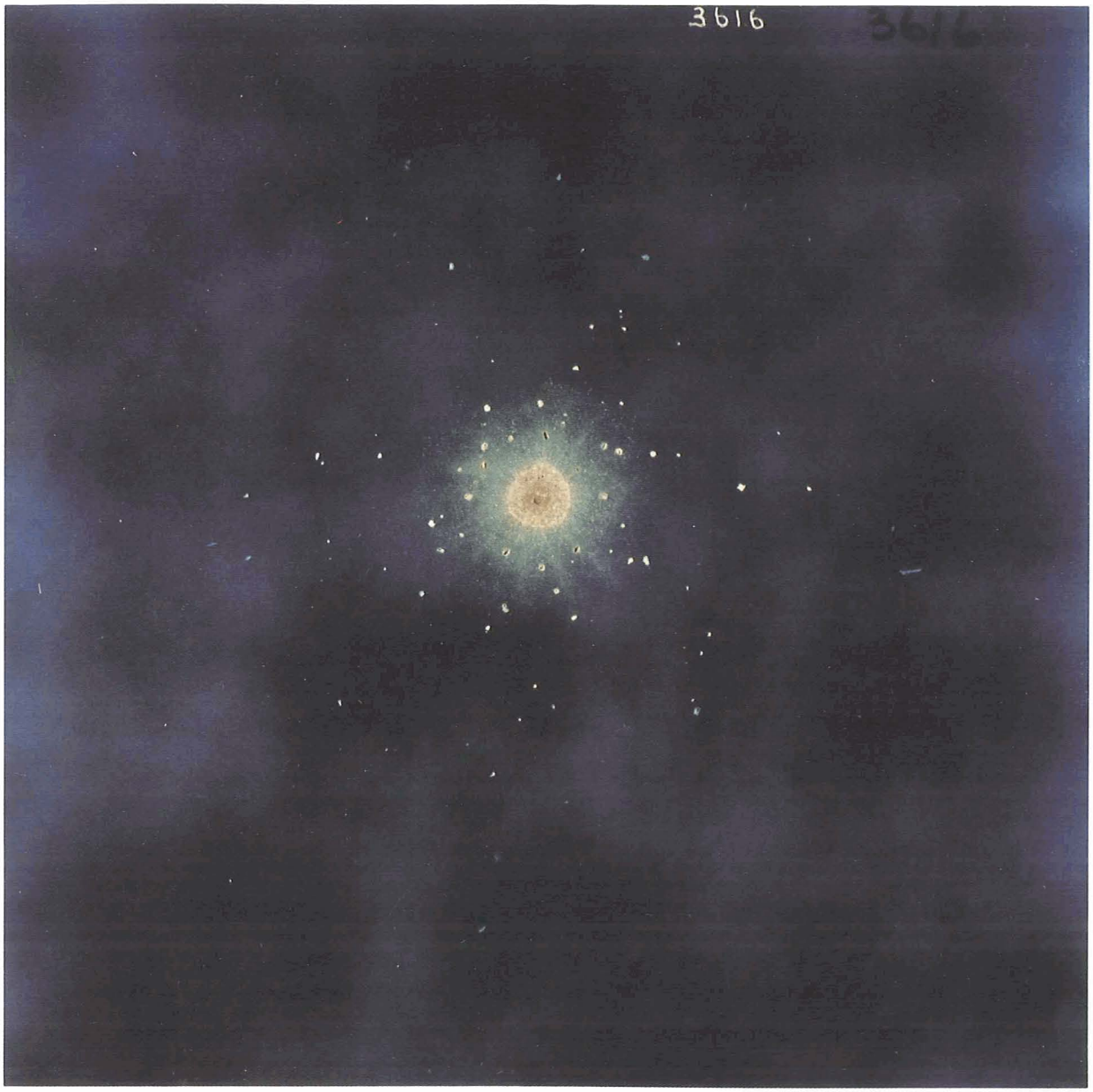
3616

SHOT # 3618

PROJECTILE: Soda Lime

D_p = 3175 μm

V = 2.05 km/s

TARGET: 1100

T = 242 μm

D_p/T = 13.12

FRONT

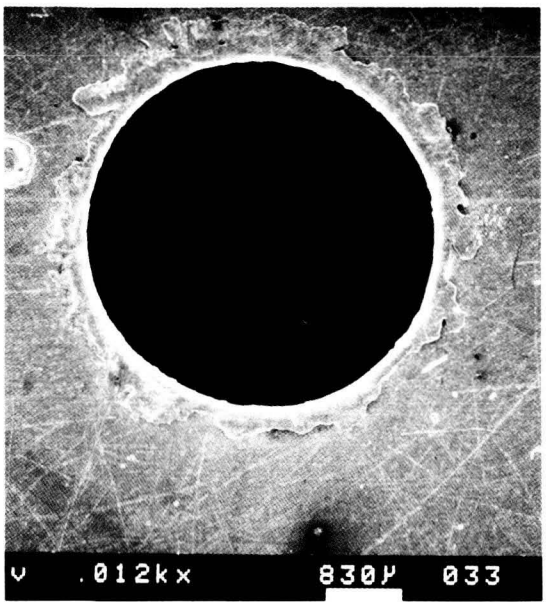

REAR

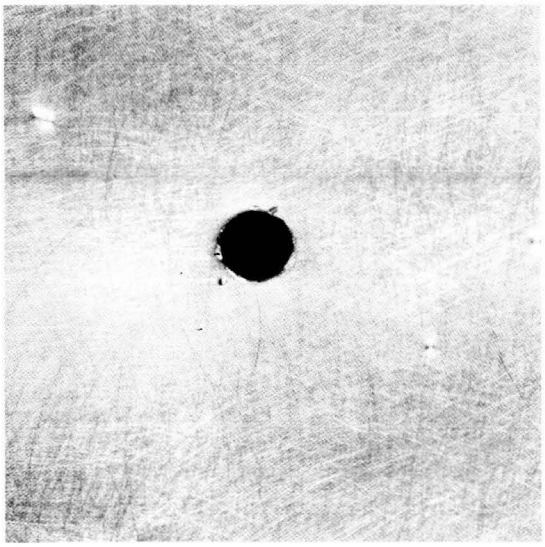

CROSS-SECTION

SHOT # 3618

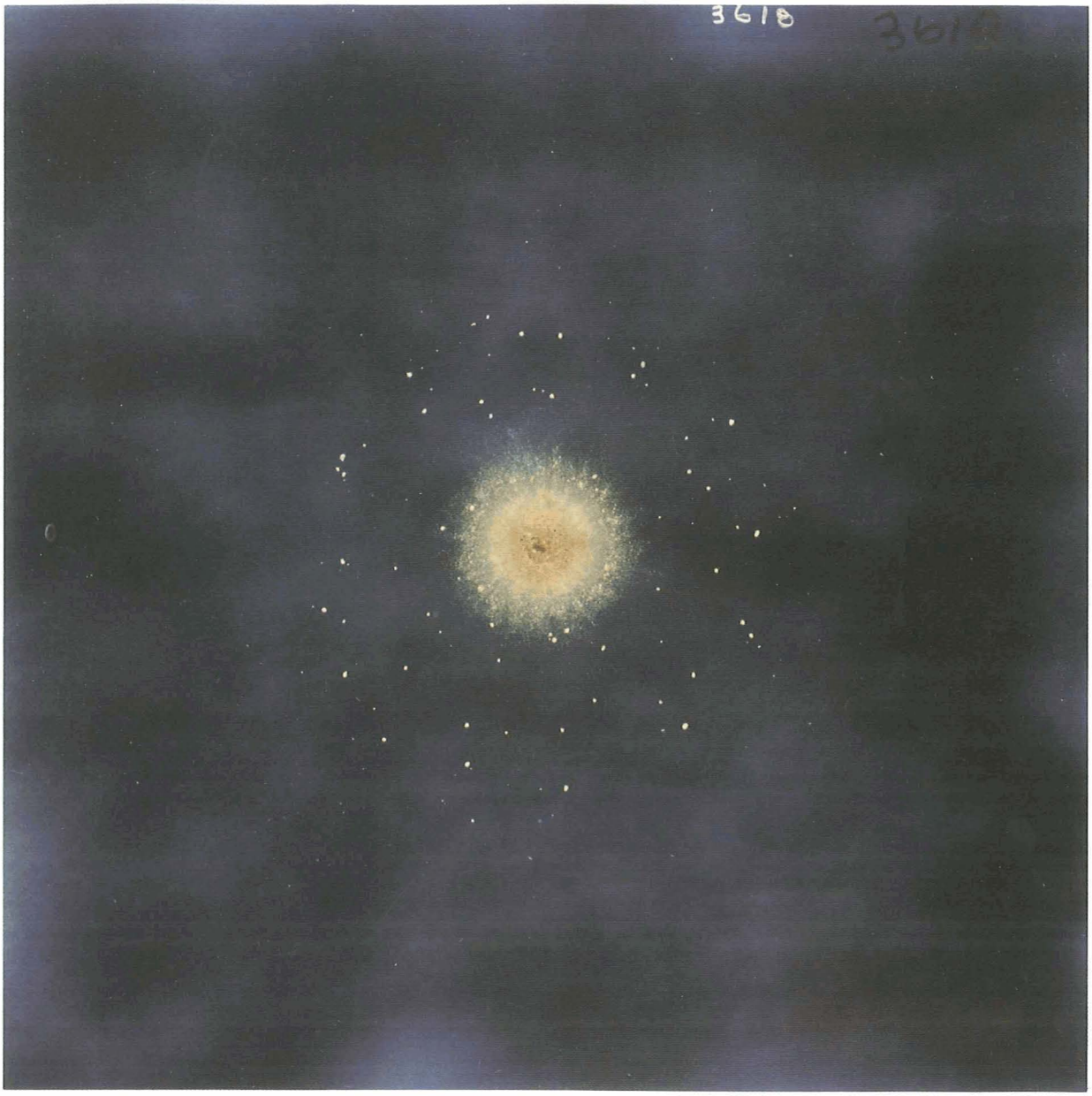

SHOT # 3619

PROJECTILE: Soda Lime

D_p = 3175 μm

V = 2.03 km/s

TARGET: 1100

T = 125 μm

D_p/T = 25.40

FRONT

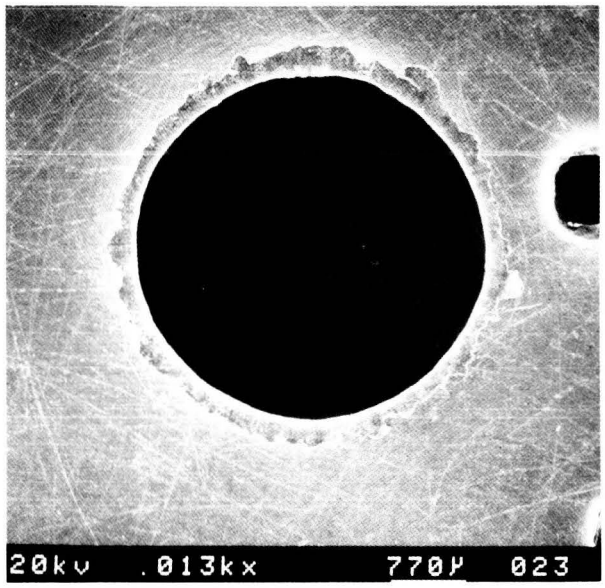

REAR

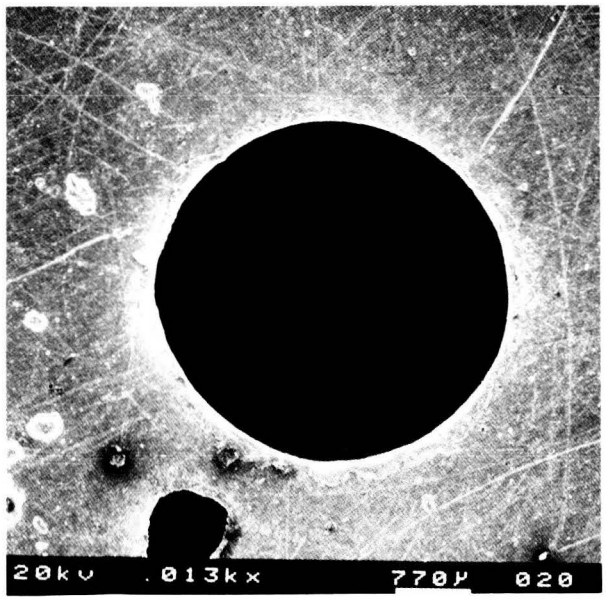

CROSS-SECTION

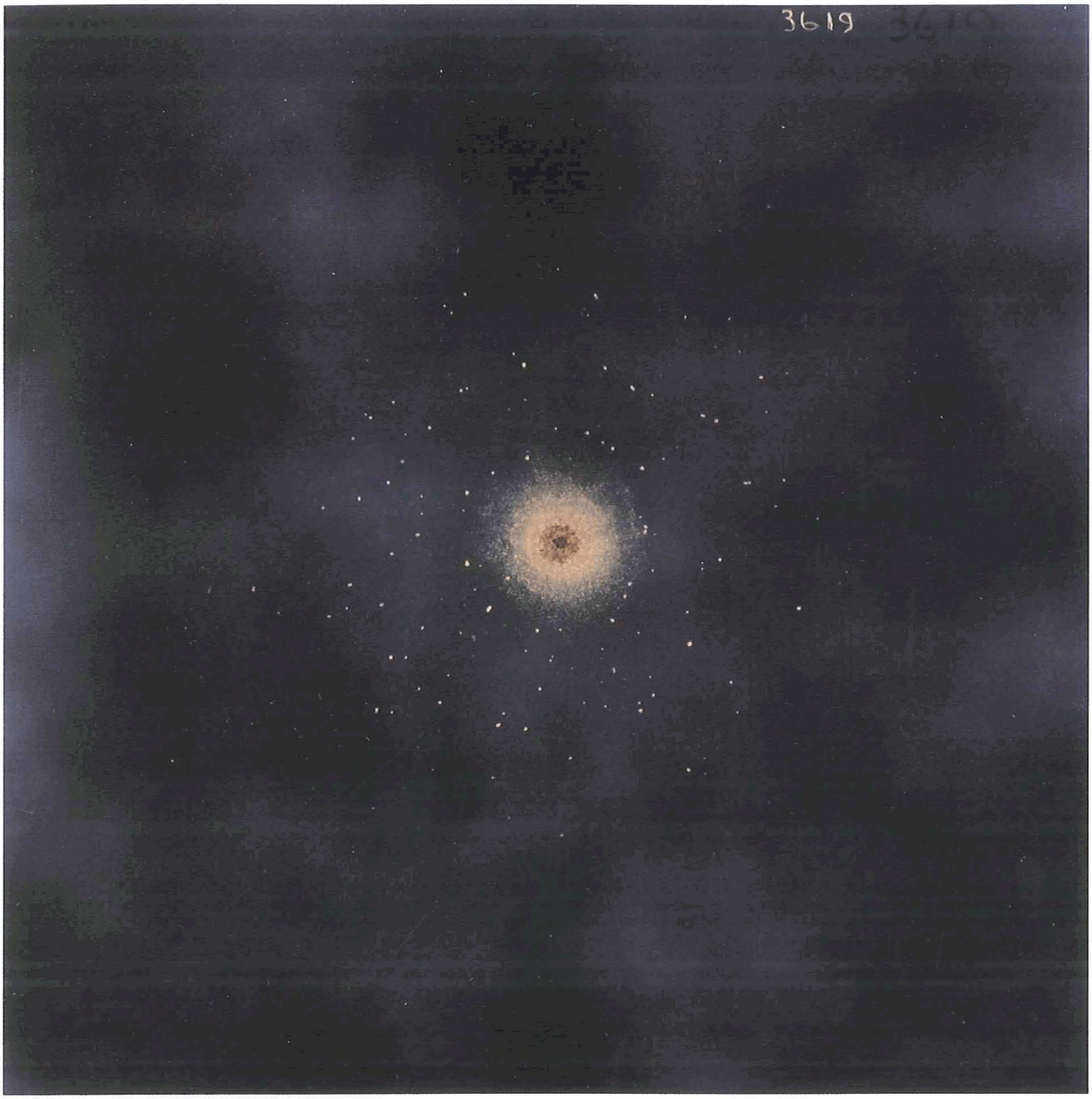
3619

SHOT # 3620

PROJECTILE: Soda Lime

D_p = 3175 μm

V = 1.99 km/s

TARGET: 1100

T = 25 μm

D_p/T = 127.00

FRONT

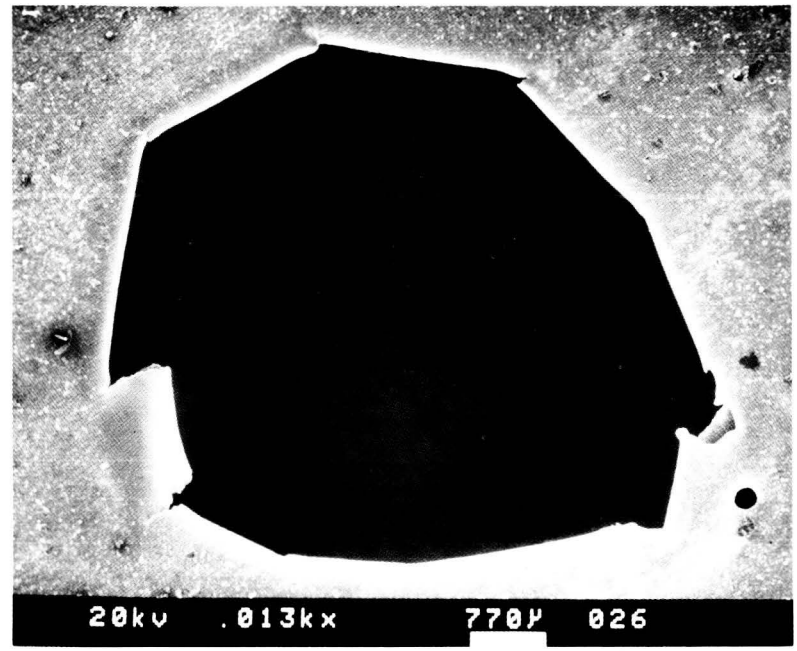

REAR

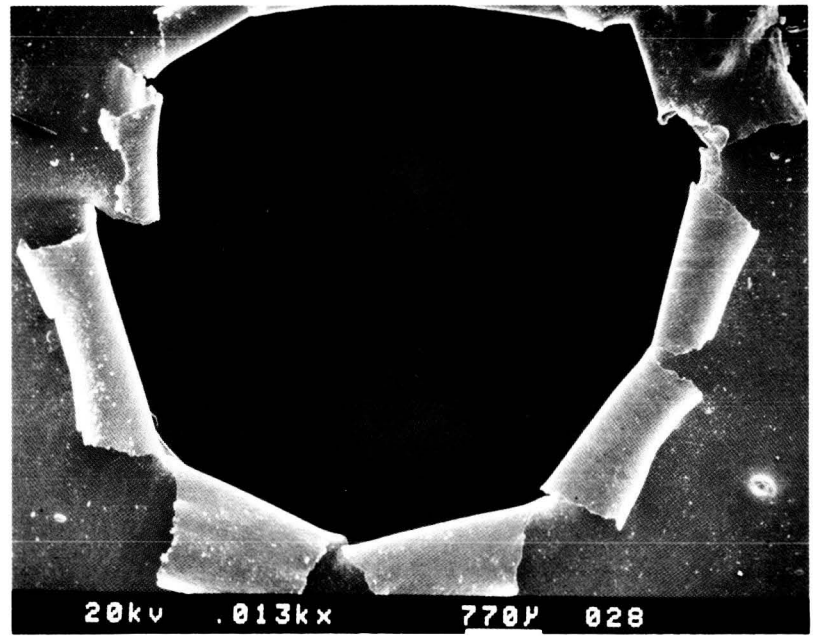

CROSS-SECTION

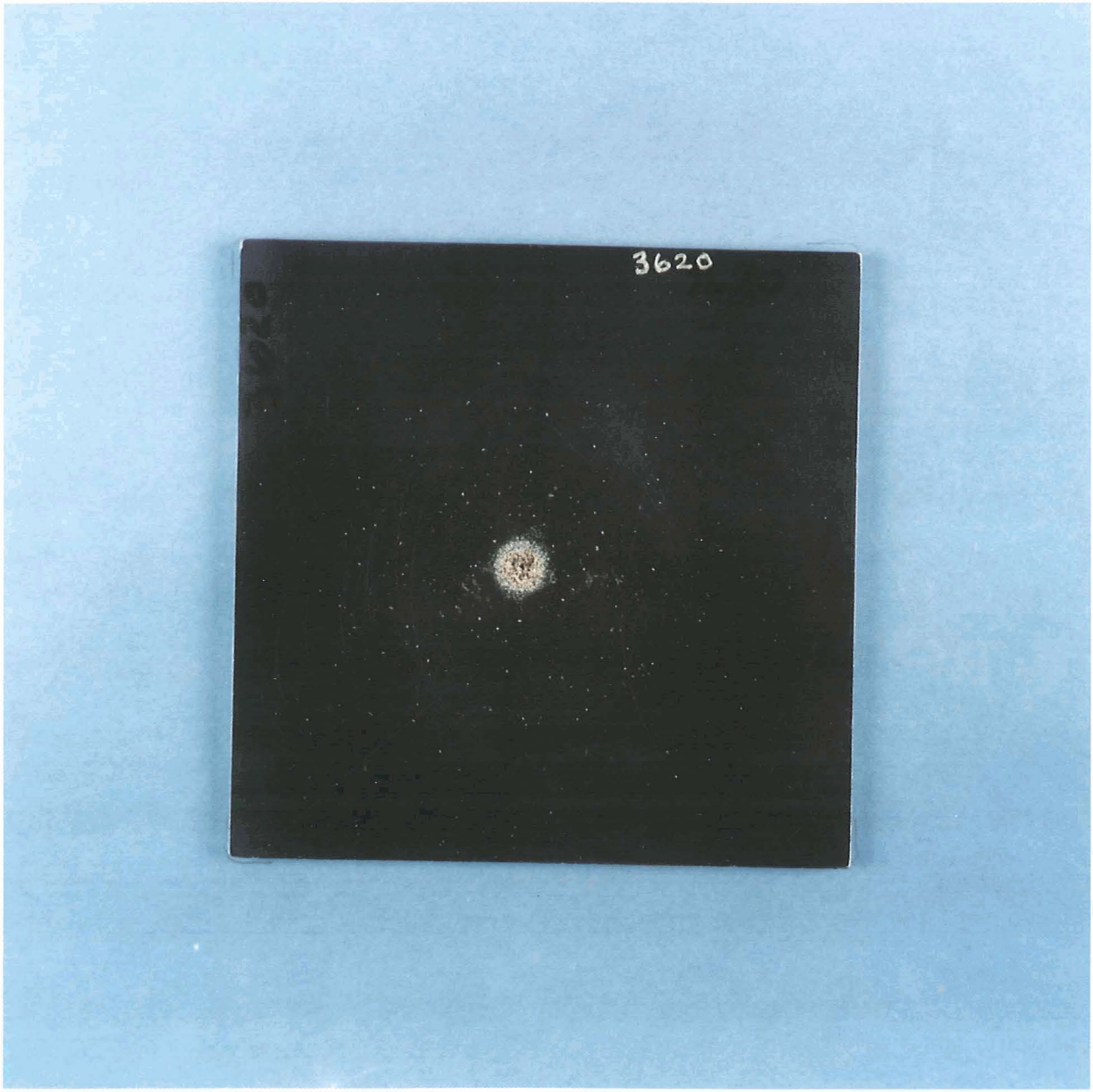
3620

SHOT # 3621

PROJECTILE: Soda Lime

D_p = 3175 μm

V = 1.86 km/s

TARGET: 1100

T = 25 μm

D_p/T = 127.00

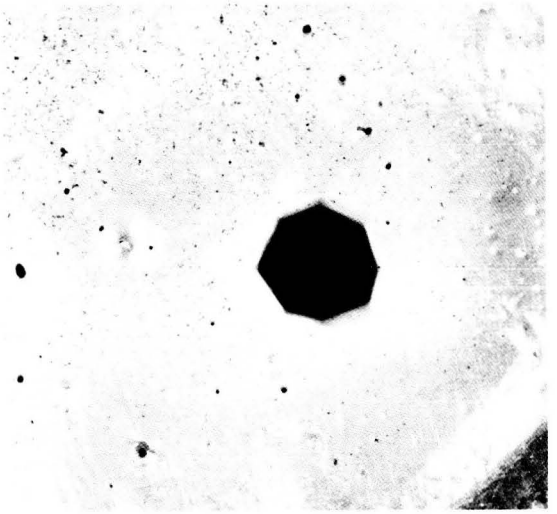

FRONT

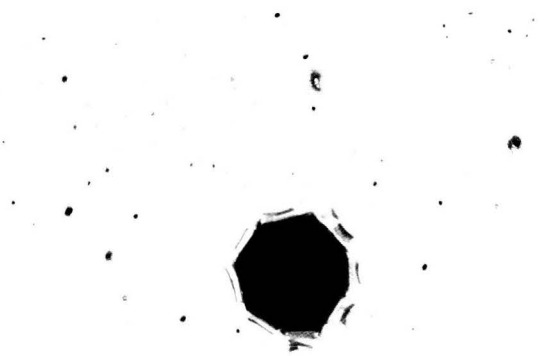

REAR

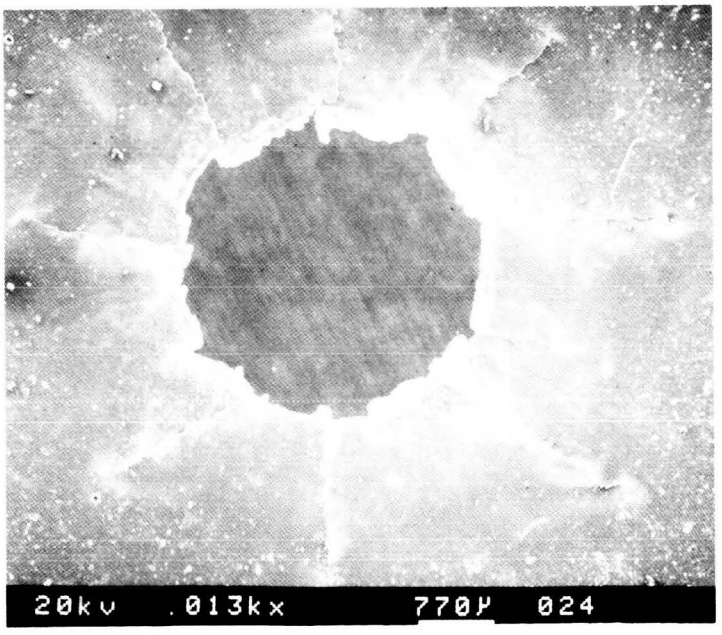

SHOT # 3621

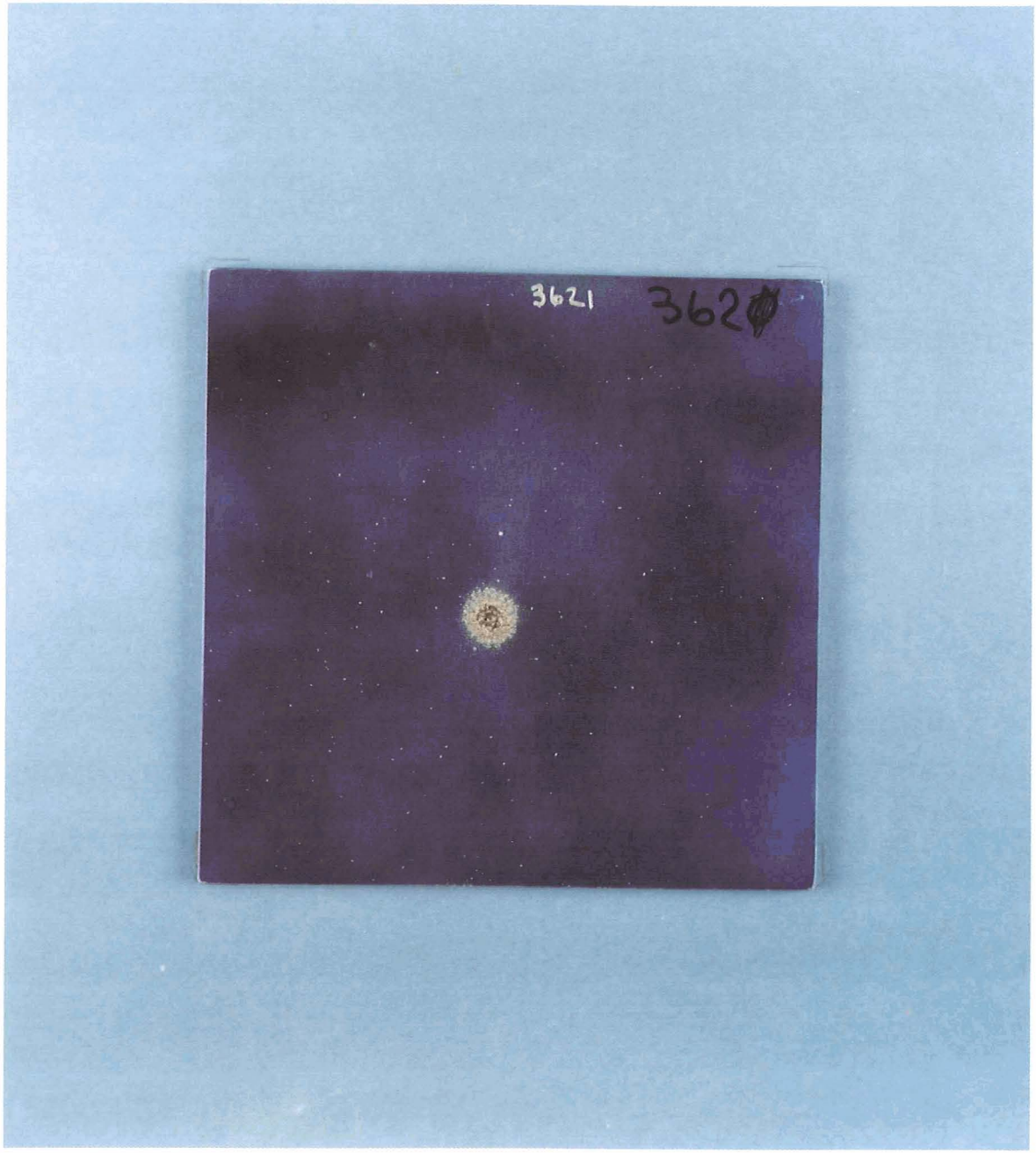

SHOT # 3622

PROJECTILE: Soda Lime

D_p = 3175 μm

V = 2.04 km/s

TARGET: 1100

T = 25 μm

D_p/T = 127.00

FRONT

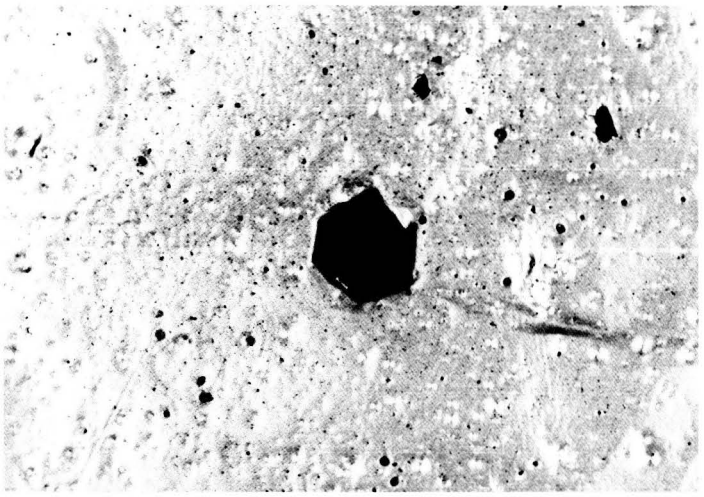

REAR

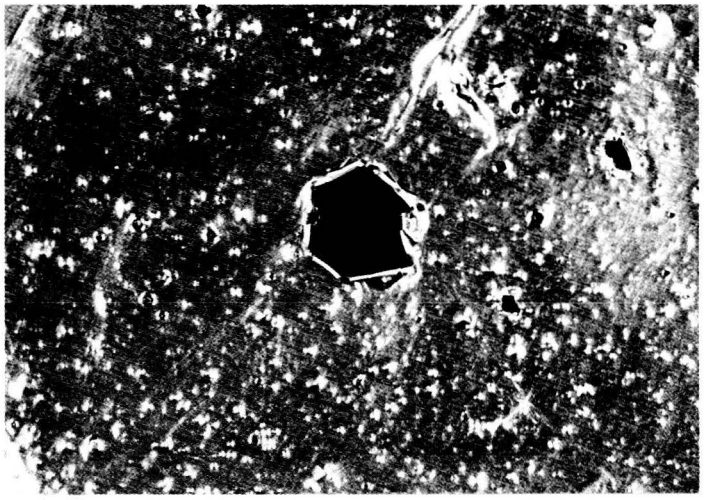

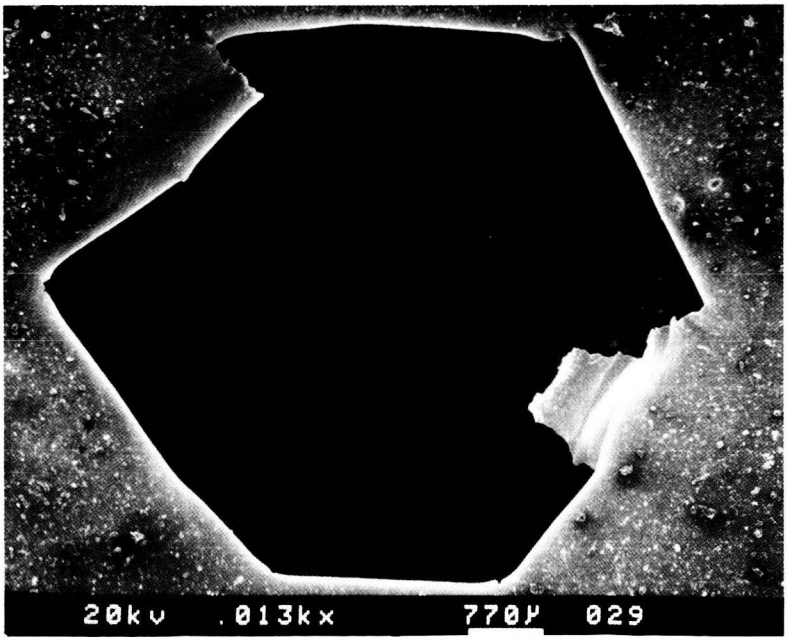

SHOT # 3622

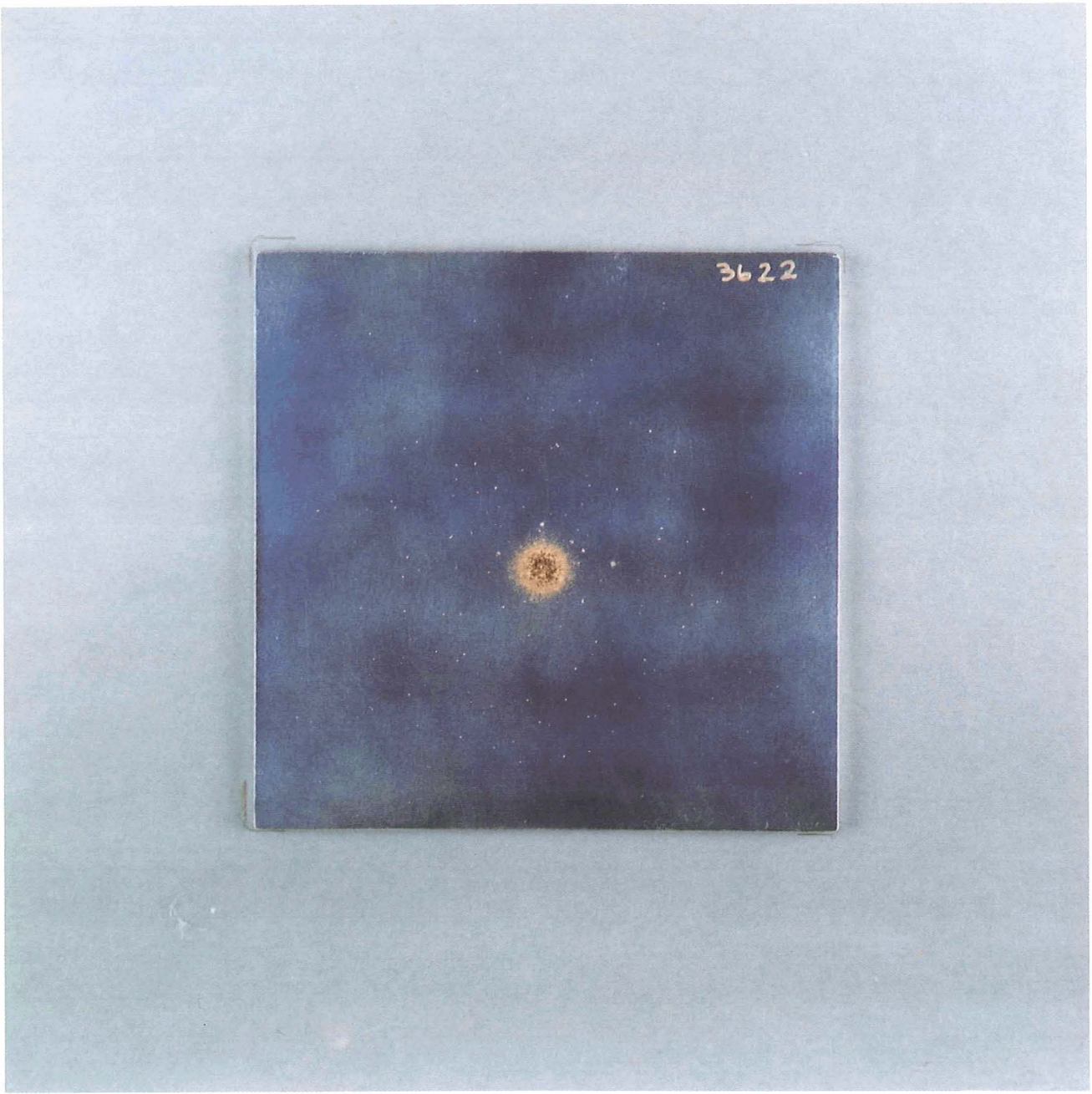

SHOT # 1154

PROJECTILE: Soda Lime
D_p = 3175 μm
V = 3.99 km/s

TARGET: 1100
T = 19250 μm
D_p/T = 0.16

FRONT

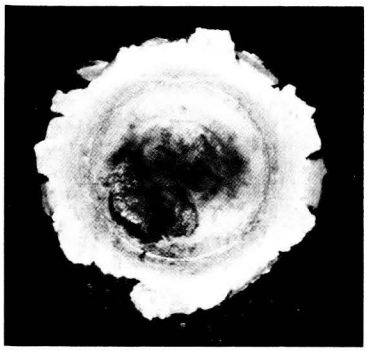

REAR

CROSS-SECTION

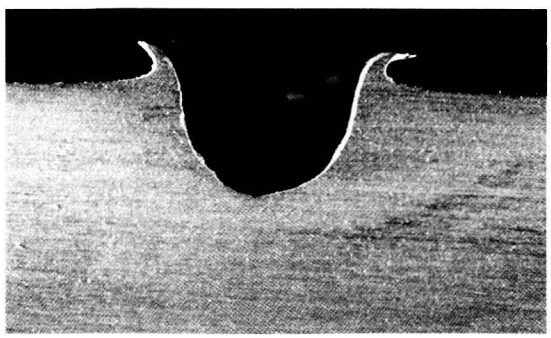

SHOT # 1152

PROJECTILE: Soda Lime
D_p = 3175 μm
V = 4.34 km/s

TARGET: 1100
T = 9525 μm
D_p/T = 0.33

FRONT

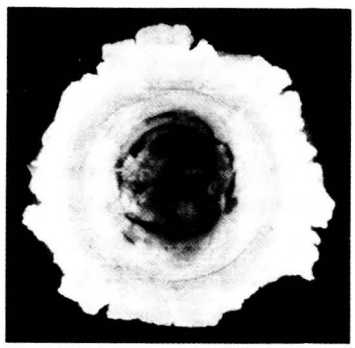

REAR

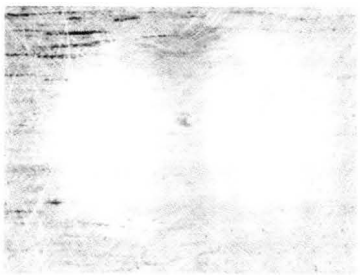

CROSS-SECTION

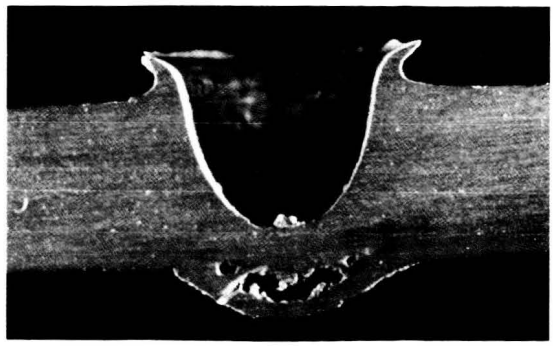

SHOT # 1185

PROJECTILE: Soda Lime
D_p = 3175 μm
V = 3.90 km/s

TARGET: 1100
T = 6883 μm
D_p/T = 0.46

FRONT

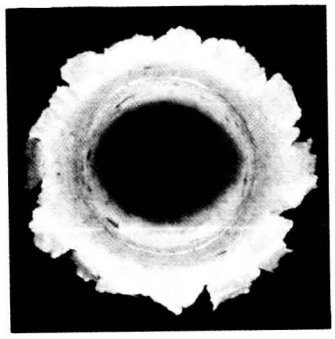

REAR

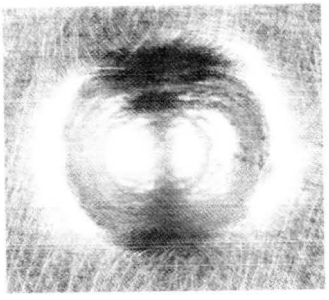

CROSS-SECTION

SHOT # 1187

PROJECTILE: Soda Lime
D_p = 3175 μm
V = 4.02 km/s

TARGET: 1100
T = 6881 μm
D_p/T = 0.46

FRONT

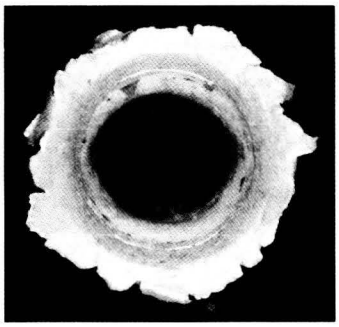

REAR

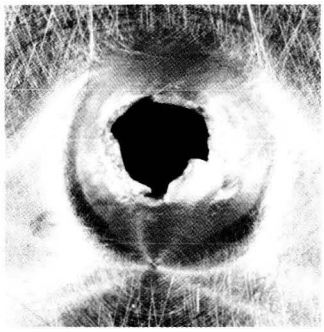

CROSS-SECTION

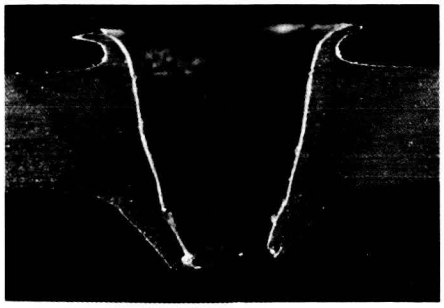

No Witness-Plate Photography

SHOT # 1186

PROJECTILE: Soda Lime
D_p = 3175 μm
V = 3.94 km/s

TARGET: 1100
T = 6550 μm
D_p/T = 0.48

FRONT

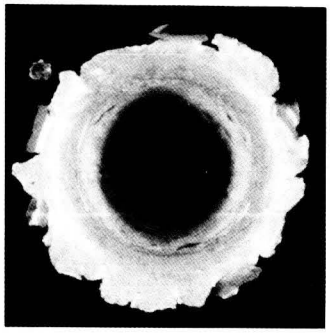

REAR

CROSS-SECTION

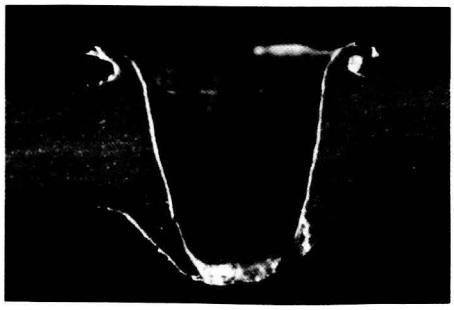

SHOT # 1184

PROJECTILE: Soda Lime

D_p = 3175 µm

V = 3.96 km/s

TARGET: 1100

T = 6400 µm

D_p/T = 0.50

FRONT

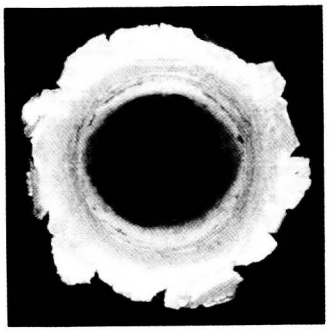

REAR

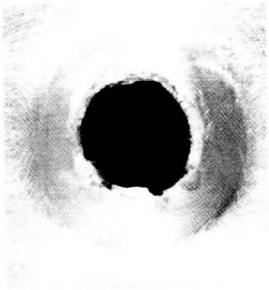

CROSS-SECTION

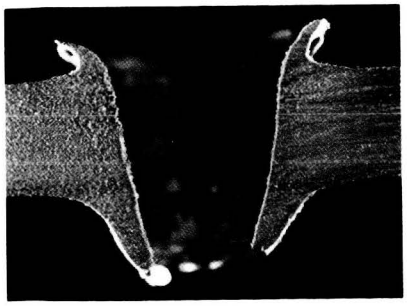

No Witness-Plate Photography

SHOT # 1165

PROJECTILE: Soda Lime
D_p = 3175 μm
V = 4.11 km/s

TARGET: 1100
T = 6250 μm
D_p/T = 0.51

FRONT

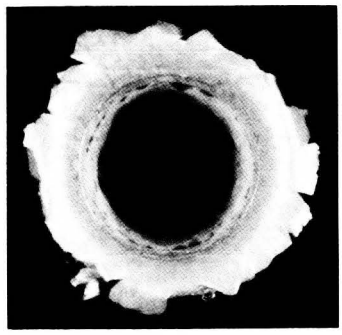

REAR

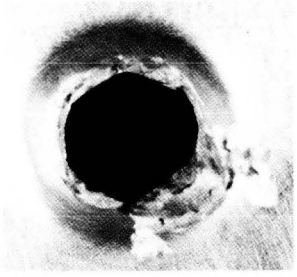

CROSS-SECTION

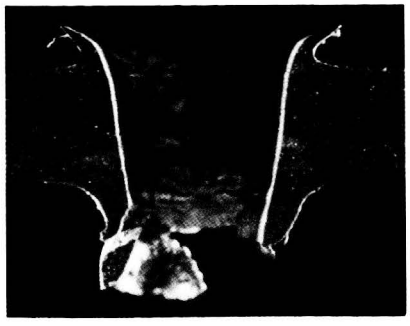

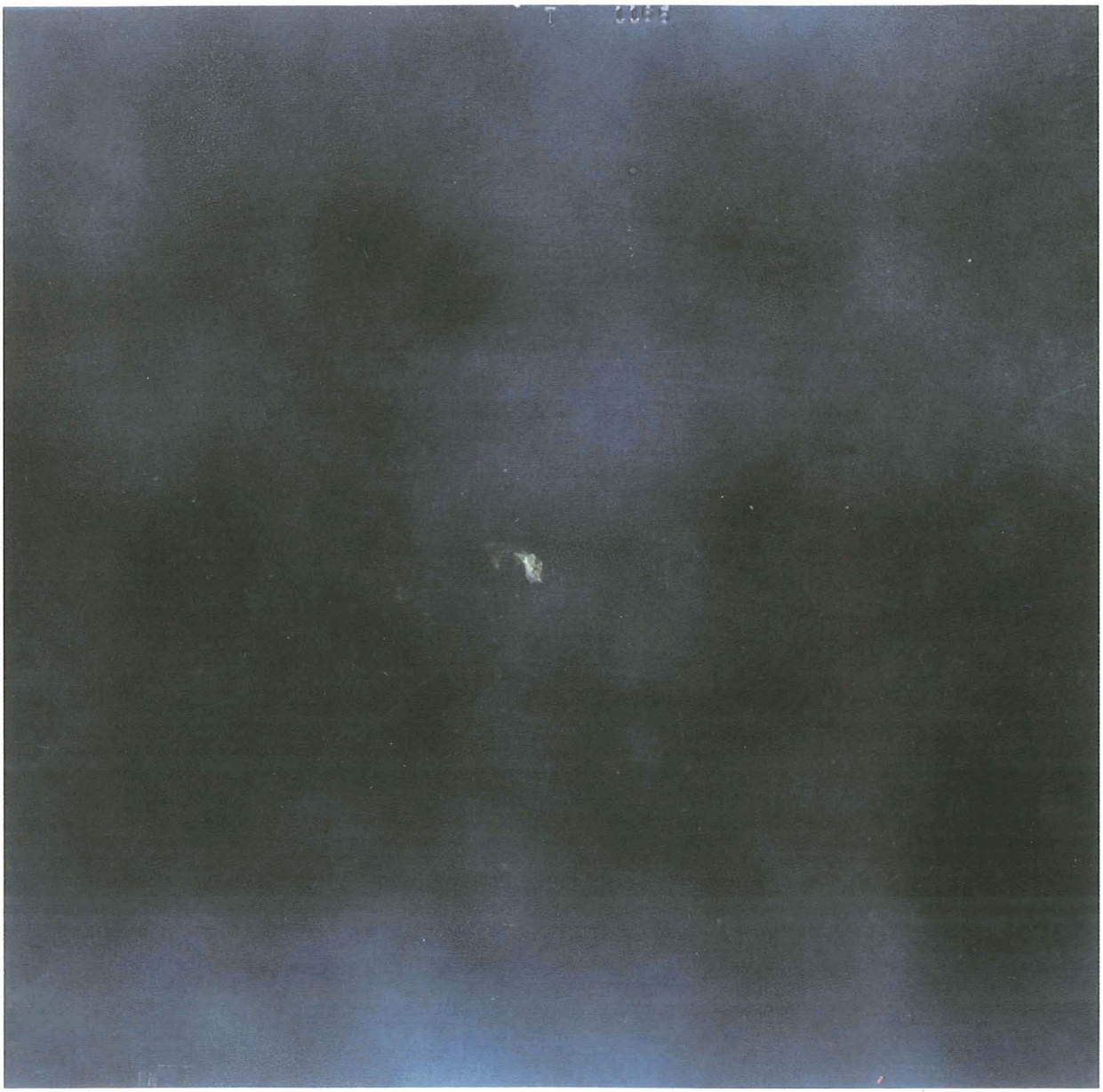

SHOT # 1153

PROJECTILE: Soda Lime
D_p = 3175 μm
V = 4.00 km/s

TARGET: 1100
T = 3152 μm
D_p/T = 1.01

FRONT

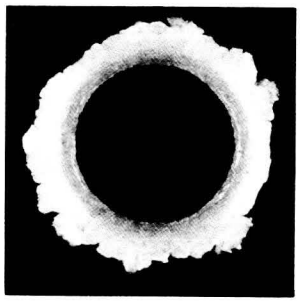

REAR

CROSS-SECTION

SHOT # 1166

PROJECTILE: Soda Lime

D_p = 3175 μm

V = 3.85 km/s

TARGET: 1100

T = 1000 μm

D_p/T = 3.18

FRONT

REAR

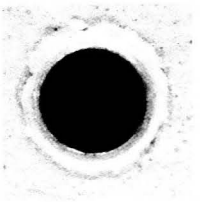

CROSS-SECTION

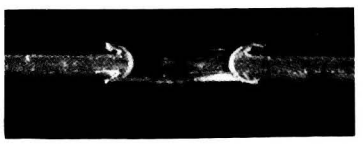

SHOT # 1166

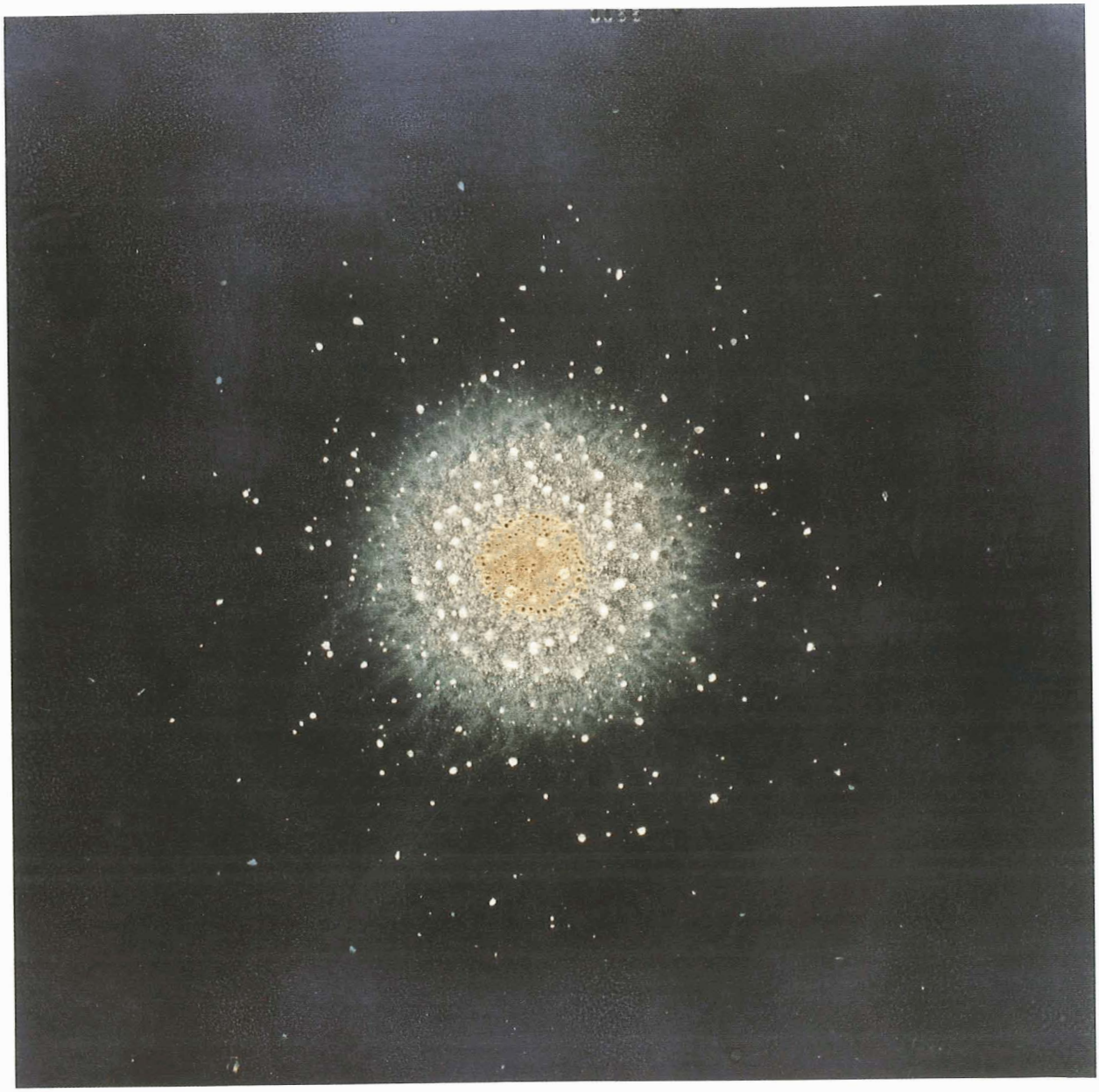

SHOT # 1163

PROJECTILE: Soda Lime

D_p = 3175 µm

V = 3.97 km/s

TARGET: 1100

T = 125 µm

D_p/T = 25.40

FRONT

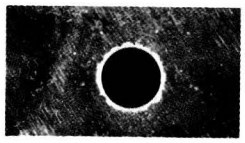

REAR

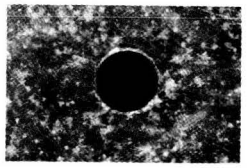

CROSS-SECTION

SHOT # 1163

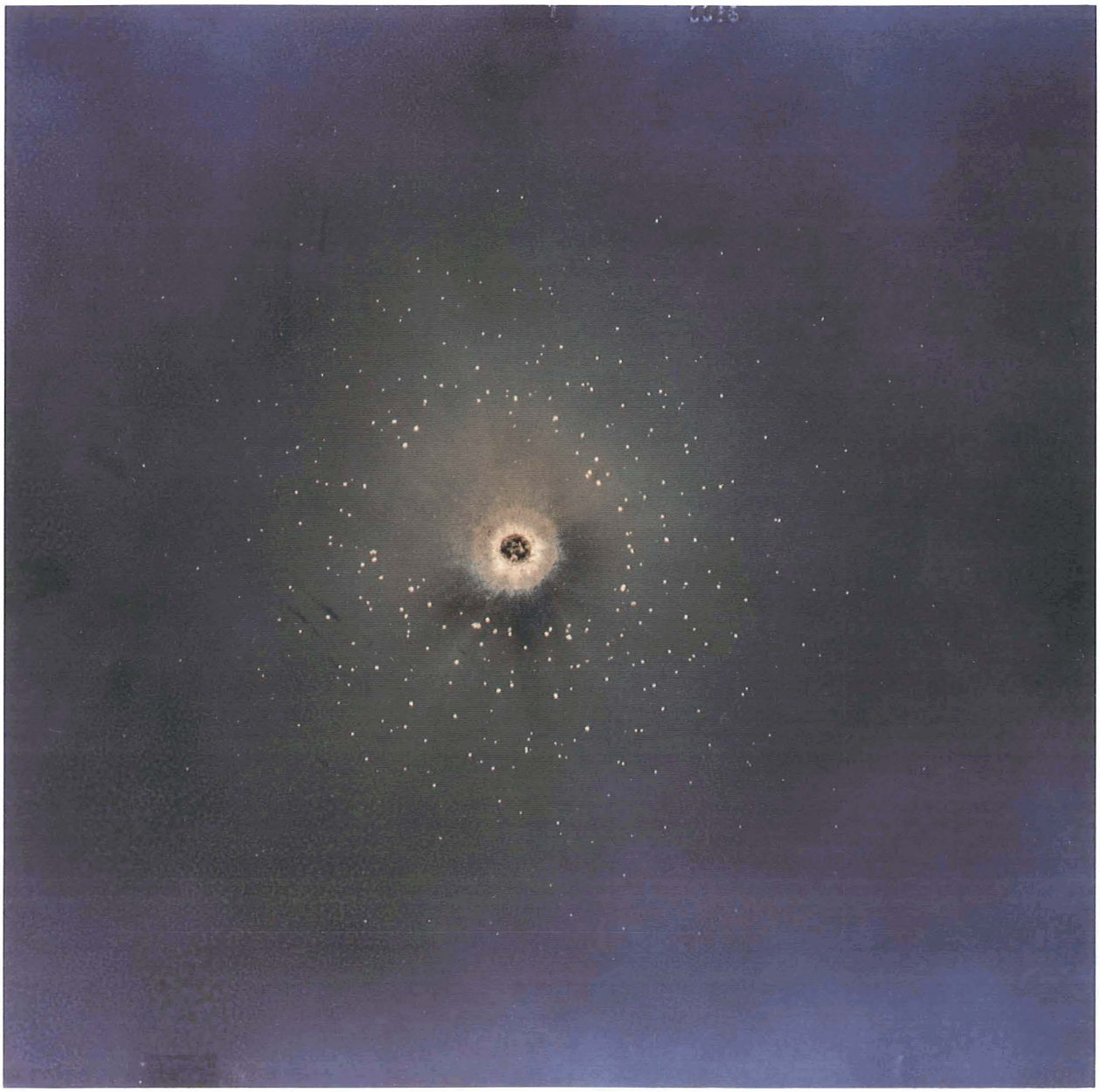

SHOT # 1149

PROJECTILE: Soda Lime

D_p = 3175 μm

V = 5.16 km/s

TARGET: 1100

T = 19500 μm

D_p/T = 0.16

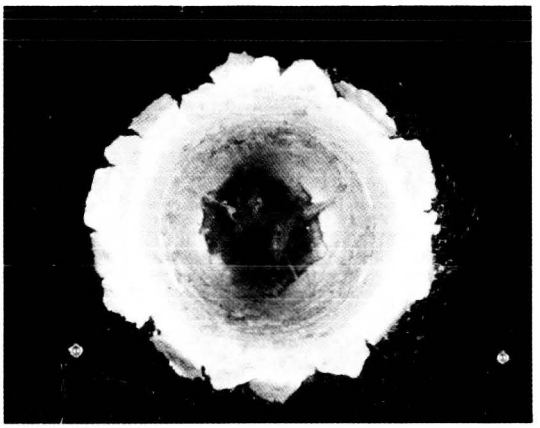

FRONT

REAR

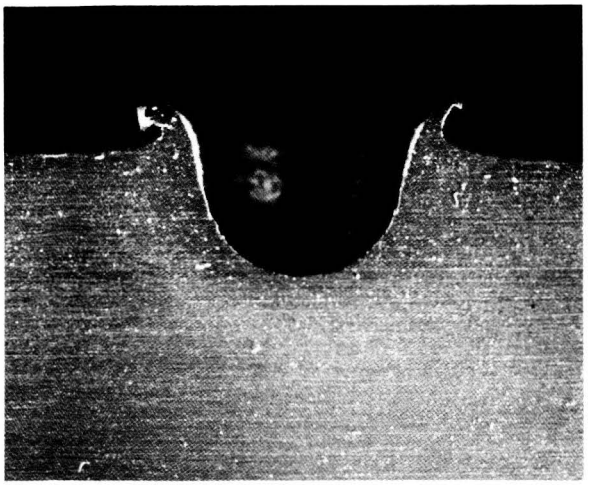

CROSS-SECTION

SHOT # 1174

PROJECTILE: Soda Lime

D_p = 3175 μm

V = 5.22 km/s

TARGET: 1100

T = 9800 μm

D_p/T = 0.32

FRONT

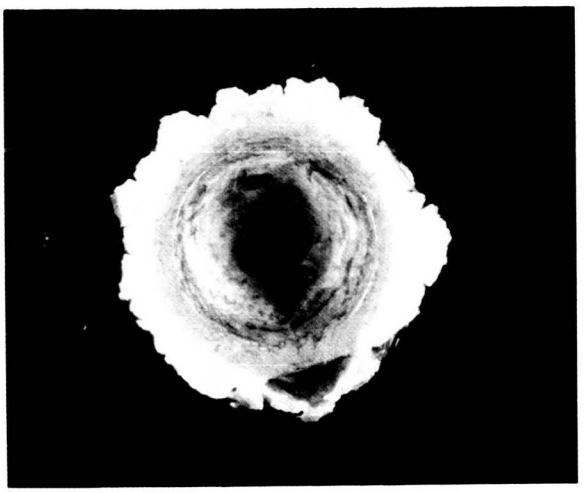

REAR

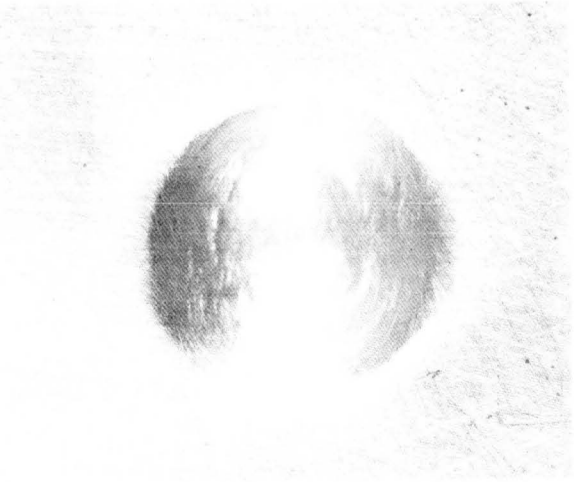

CROSS-SECTION

SHOT # 1175

PROJECTILE: Soda Lime
D_p = 3175 μm
V = 5.09 km/s

TARGET: 1100
T = 9746 μm
D_p/T = 0.33

FRONT

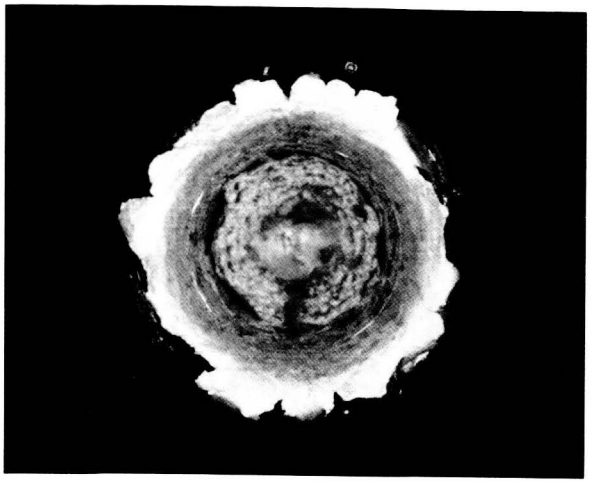

REAR

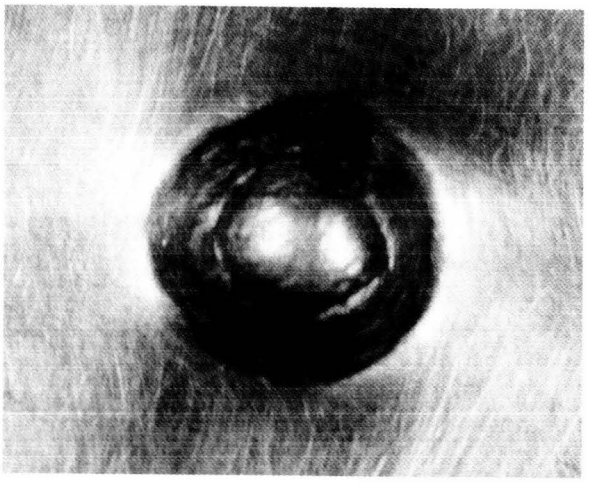

CROSS-SECTION

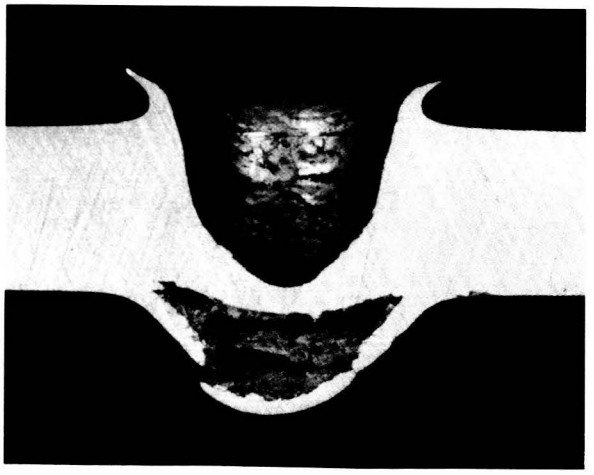

SHOT # 1176

PROJECTILE: Soda Lime
D_p = 3175 μm
V = 5.11 km/s

TARGET: 1100
T = 9300 μm
D_p/T = 0.34

FRONT

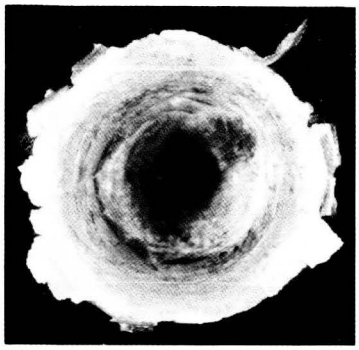

REAR

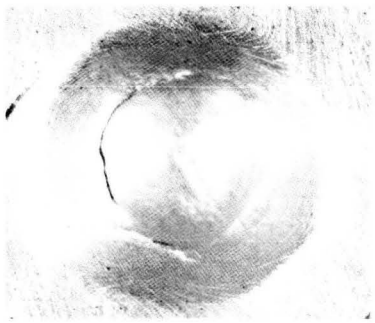

CROSS-SECTION

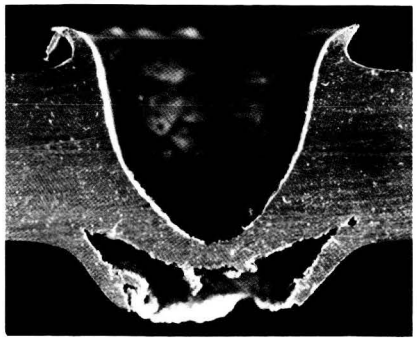

SHOT # 1178

PROJECTILE: Soda Lime
D_p = 3175 μm
V = 5.30 km/s

TARGET: 1100
T = 9050 μm
D_p/T = 0.35

FRONT

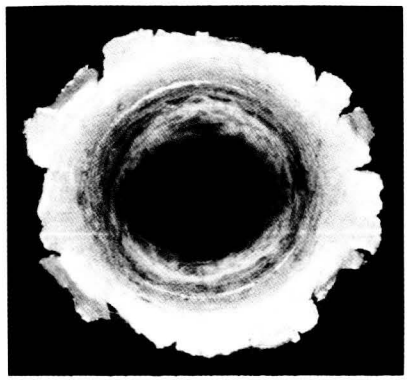

REAR

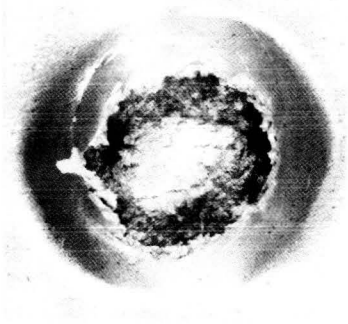

CROSS-SECTION

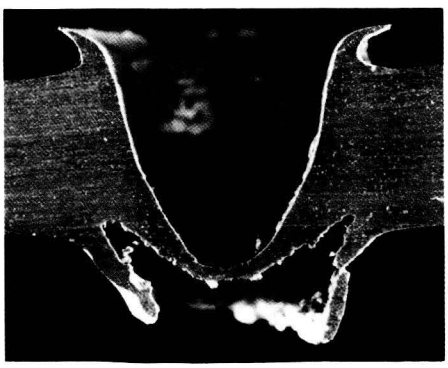

SHOT # 1178

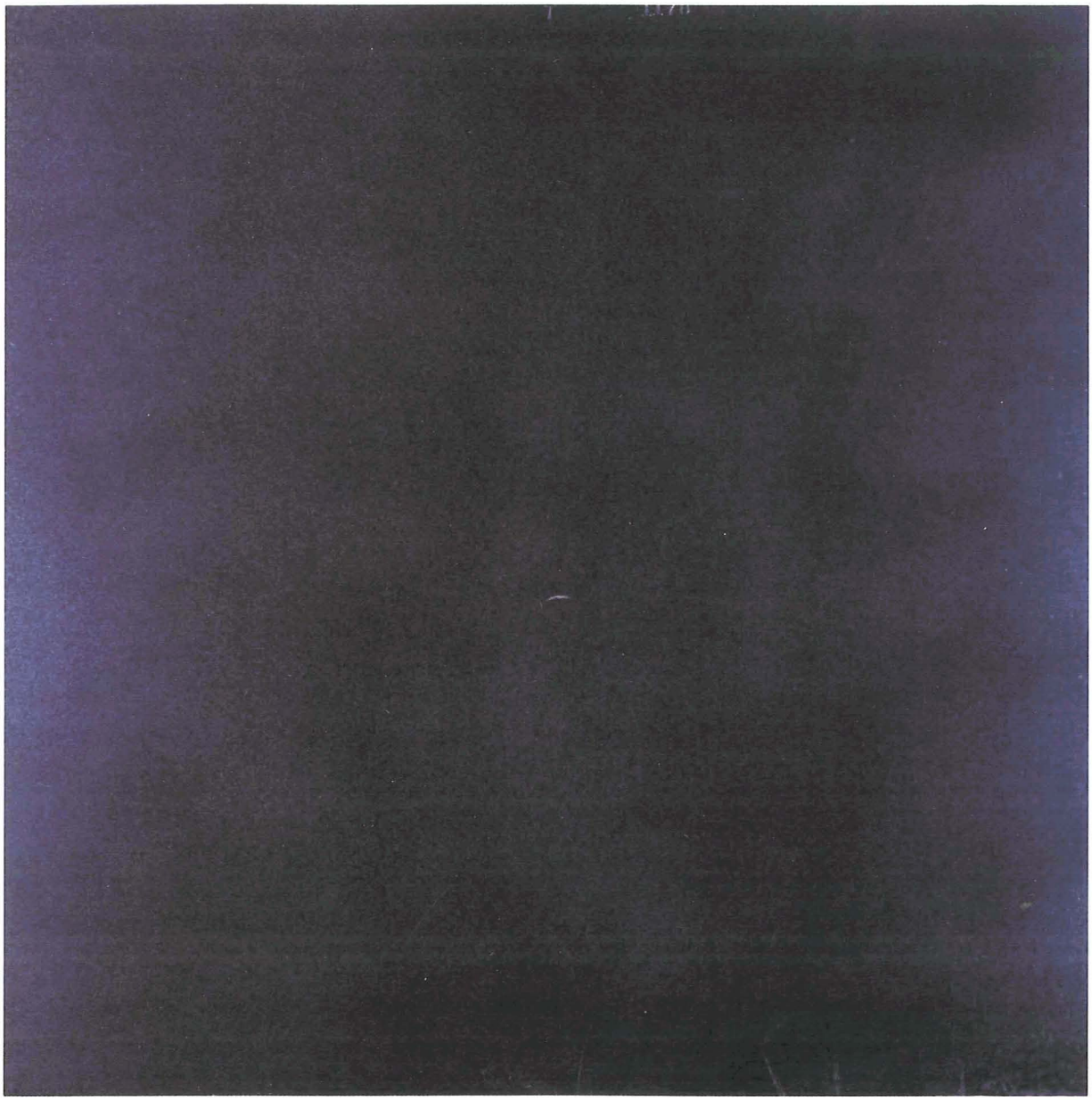

SHOT # 1179

PROJECTILE: Soda Lime
D_p = 3175 μm
V = 5.11 km/s

TARGET: 1100
T = 8842 μm
D_p/T = 0.36

FRONT

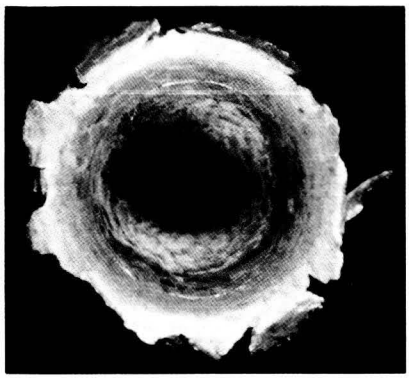

REAR

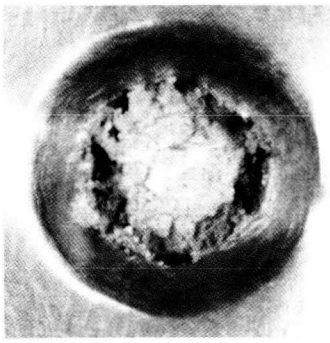

CROSS-SECTION

No Witness-Plate Photography

SHOT # 1180

PROJECTILE: Soda Lime
D_p = 3175 μm
V = 5.29 km/s

TARGET: 1100
T = 8534 μm
D_p/T = 0.37

FRONT

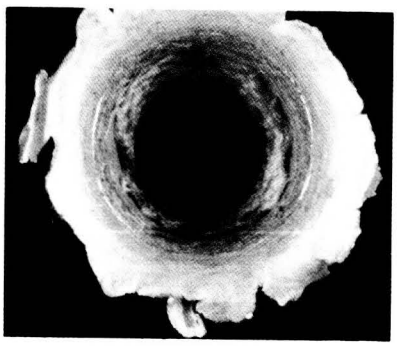

REAR

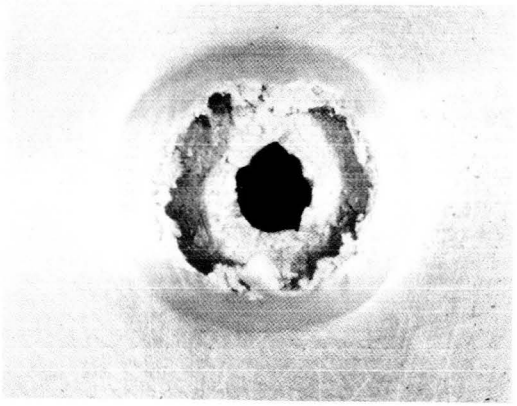

CROSS-SECTION

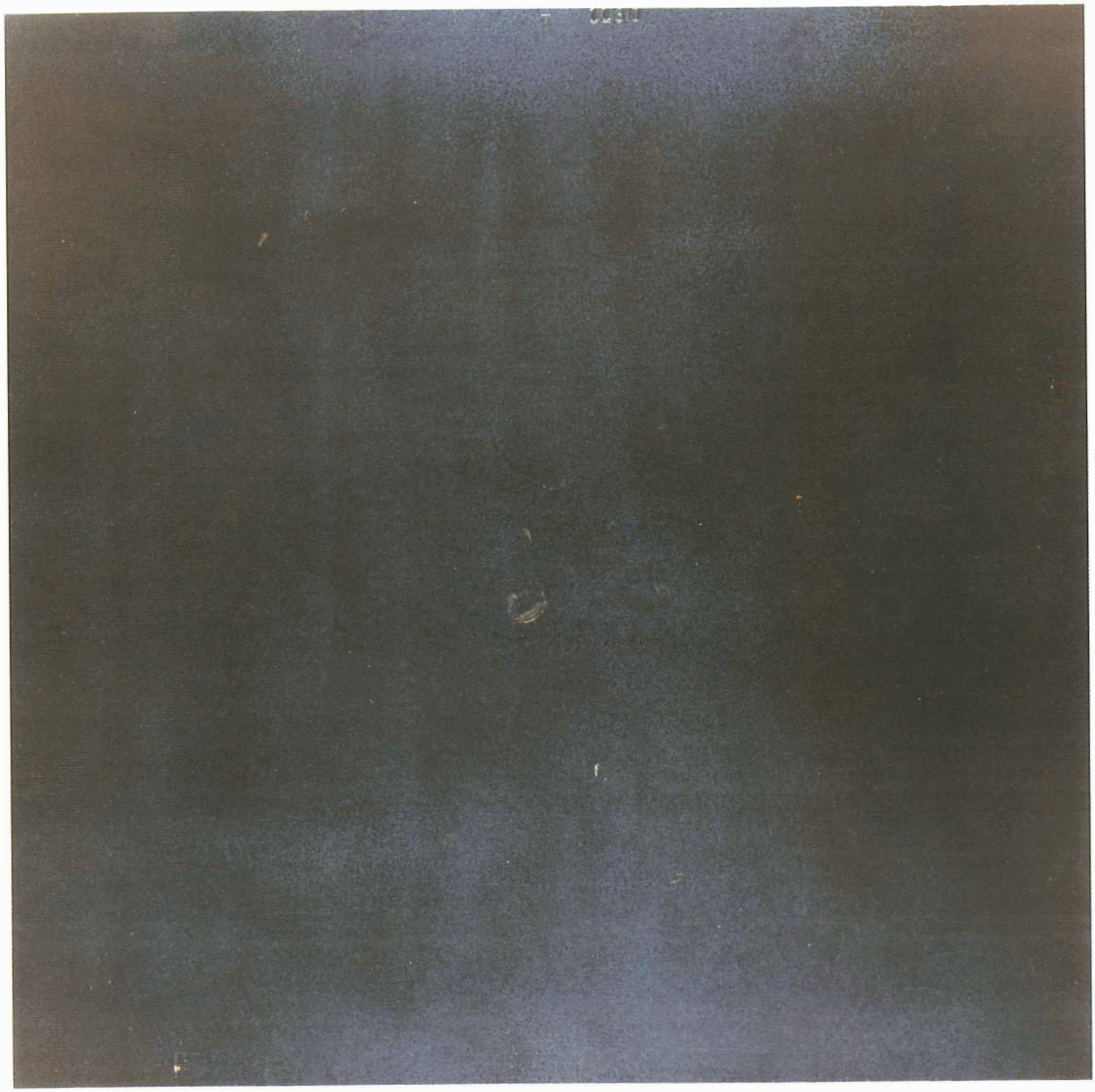

SHOT # 1160

PROJECTILE: Soda Lime
D_p = 3175 μm
V = 5.14 km/s

TARGET: 1100
T = 6250 μm
D_p/T = 0.51

FRONT

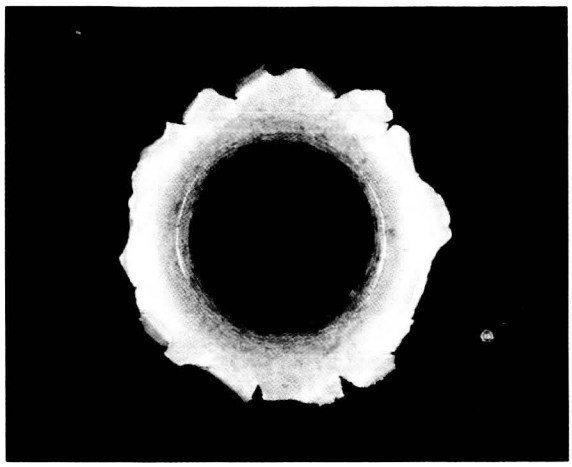

REAR

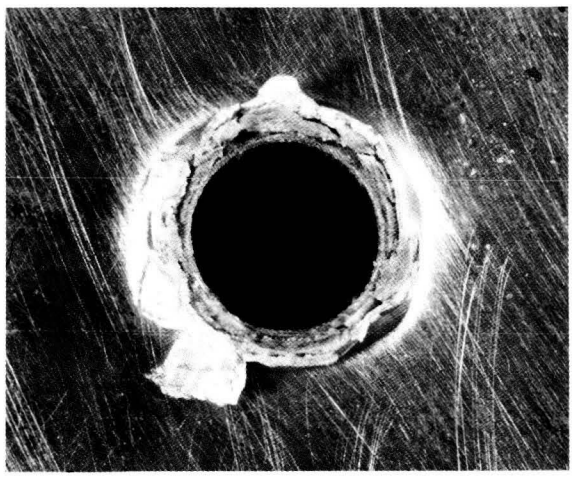

CROSS-SECTION

SHOT # 1160

SHOT # 1156

PROJECTILE: Soda Lime
D_p = 3175 μm
V = 5.17 km/s

TARGET: 1100
T = 3175 μm
D_p/T = 1.00

FRONT

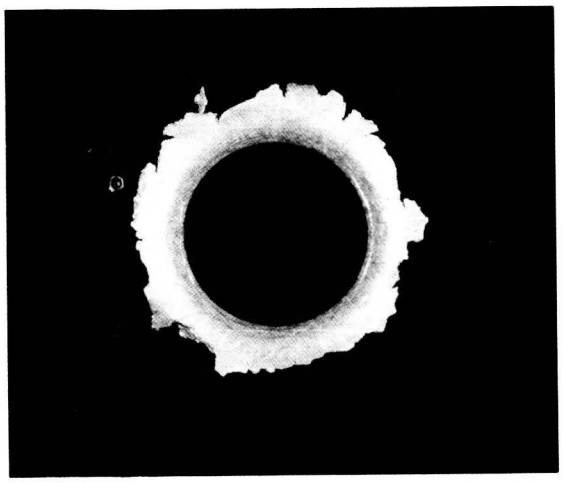

REAR

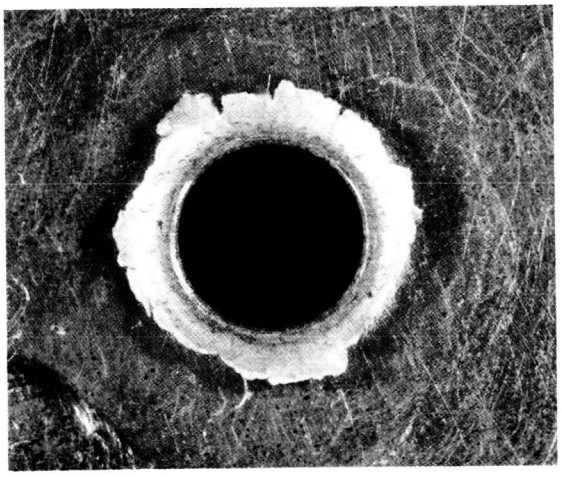

CROSS-SECTION

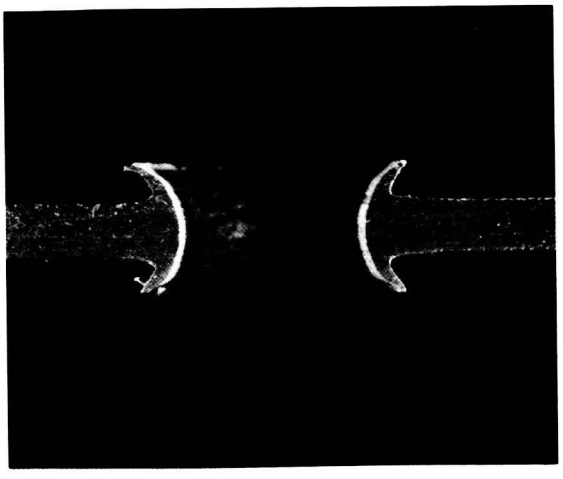

SHOT # 1156

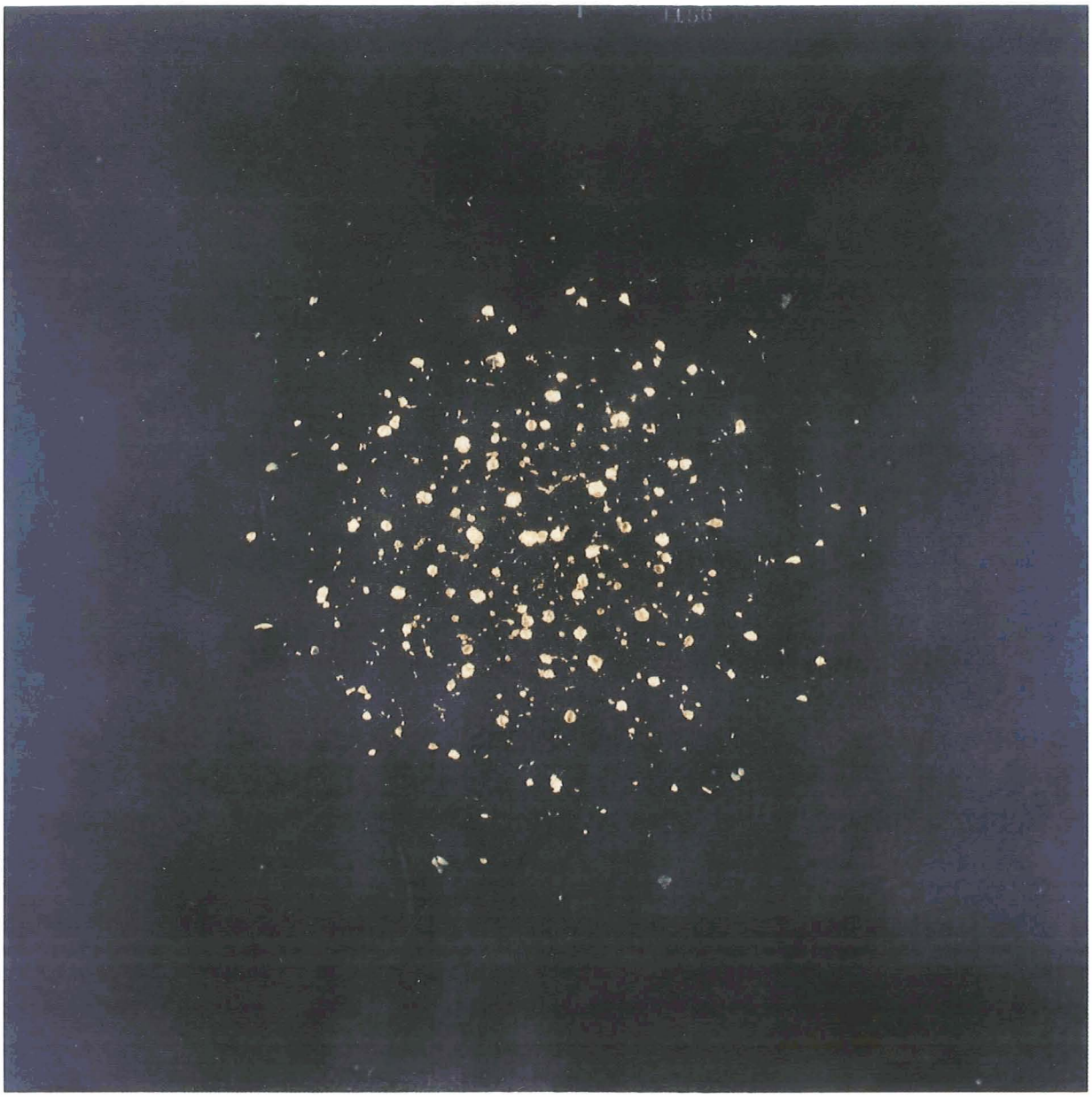

SHOT # 1159

PROJECTILE: Soda Lime
D_p = 3175 μm
V = 5.16 km/s

TARGET: 1100
T = 1020 μm
D_p/T = 3.11

FRONT

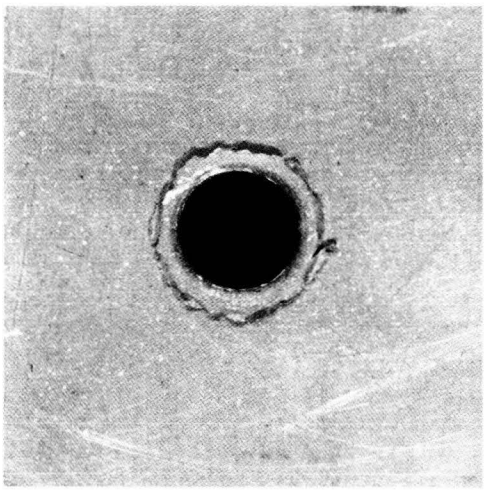

REAR

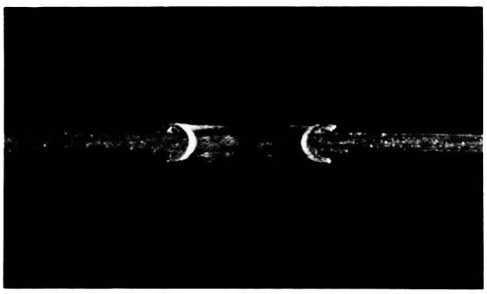

CROSS-SECTION

SHOT # 1159

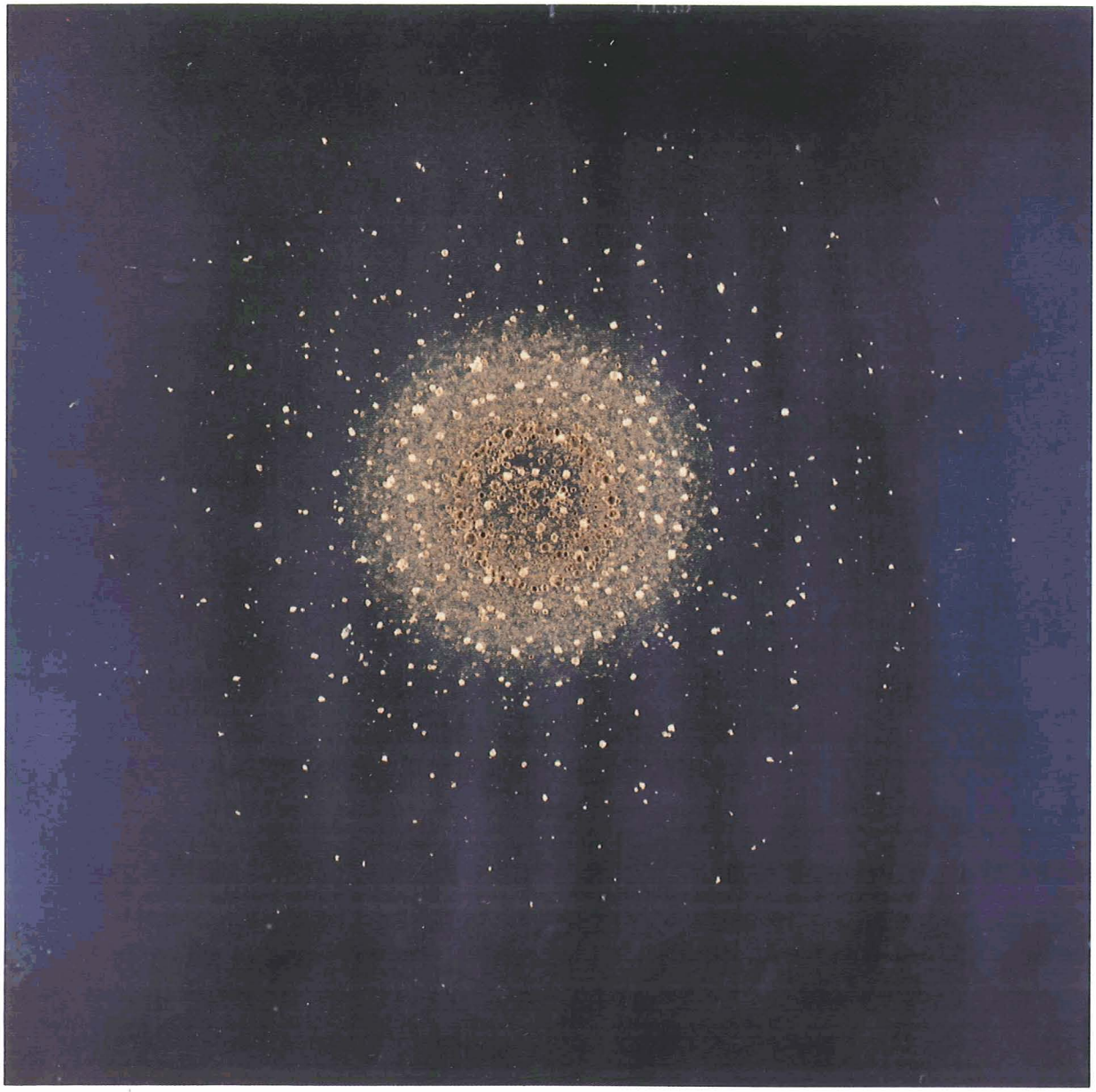

SHOT # 1161

PROJECTILE: Soda Lime

D_p = 3175 μm

V = 5.12 km/s

TARGET: 1100

T = 125 μm

D_p/T = 25.40

FRONT

No Target Photographs

REAR

CROSS-SECTION


1161

SHOT # 792

PROJECTILE: Soda Lime
D_p = 3175 μm
V = 5.69 km/s

TARGET: 1100
T = 25400 μm
D_p/T = 0.13

FRONT

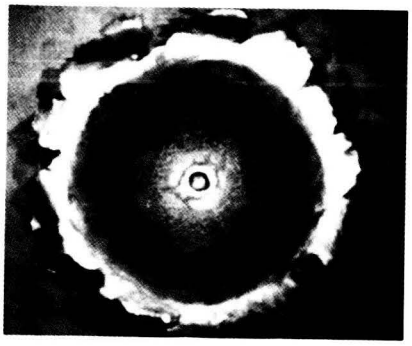

REAR

CROSS-SECTION

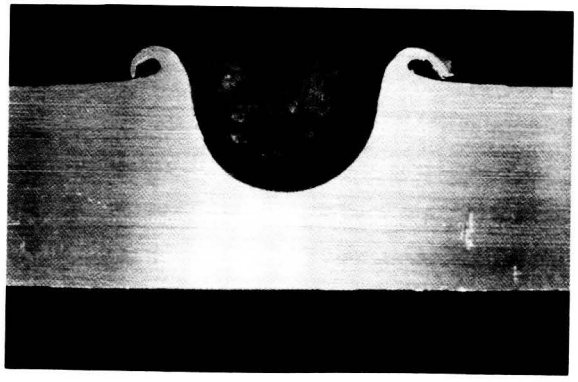

SHOT # 767

PROJECTILE: Soda Lime
D_p = 3175 μm
V = 5.84 km/s

TARGET: 1100
T = 12500 μm
D_p/T = 0.25

FRONT

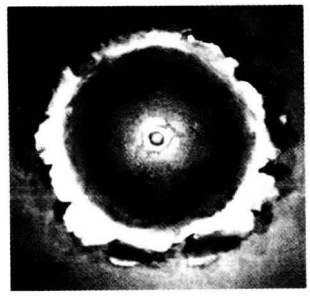

REAR

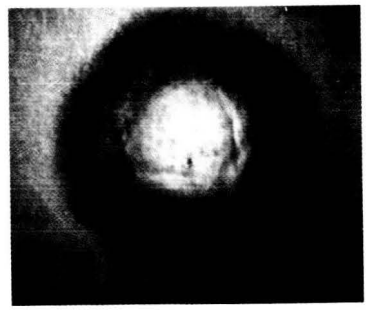

CROSS-SECTION

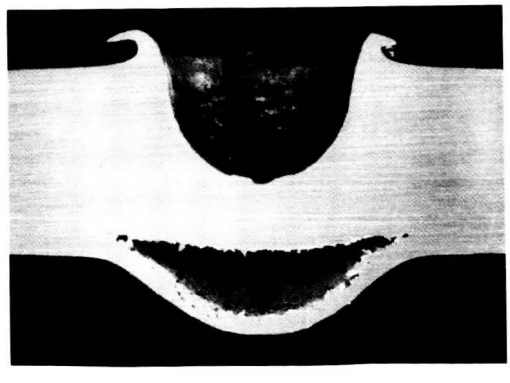

SHOT # 791

PROJECTILE: Soda Lime
D_p = 3175 μm
V = 5.84 km/s

TARGET: 1100
T = 10940 μm
D_p/T = 0.29

FRONT

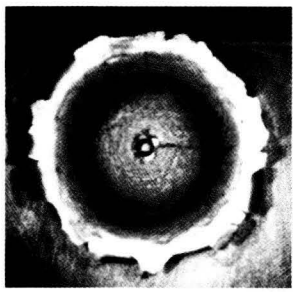

REAR

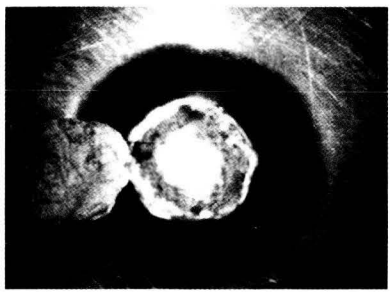

CROSS-SECTION

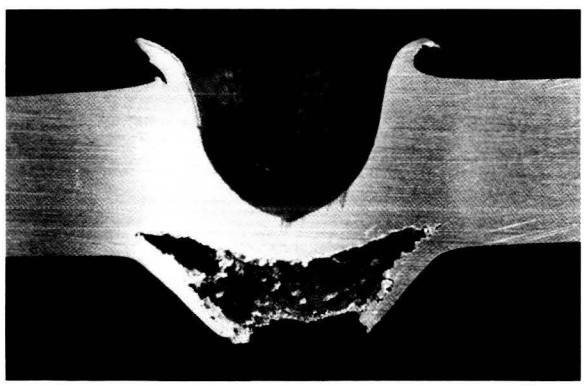

SHOT # 785

PROJECTILE: Soda Lime
D_p = 3175 μm
V = 5.91 km/s

TARGET: 1100
T = 9525 μm
D_p/T = 0.33

FRONT

REAR

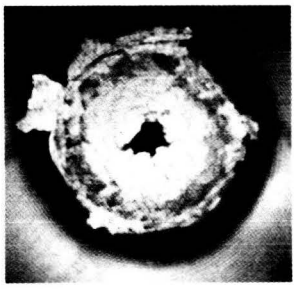

CROSS-SECTION

SHOT # 785

SHOT # 786

PROJECTILE: Soda Lime
D_p = 3175 μm
V = 5.80 km/s

TARGET: 1100
T = 9020 μm
D_p/T = 0.35

FRONT

REAR

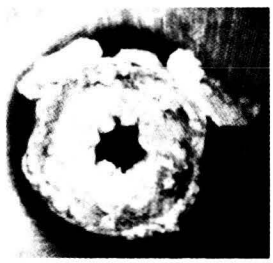

CROSS-SECTION

SHOT # 786

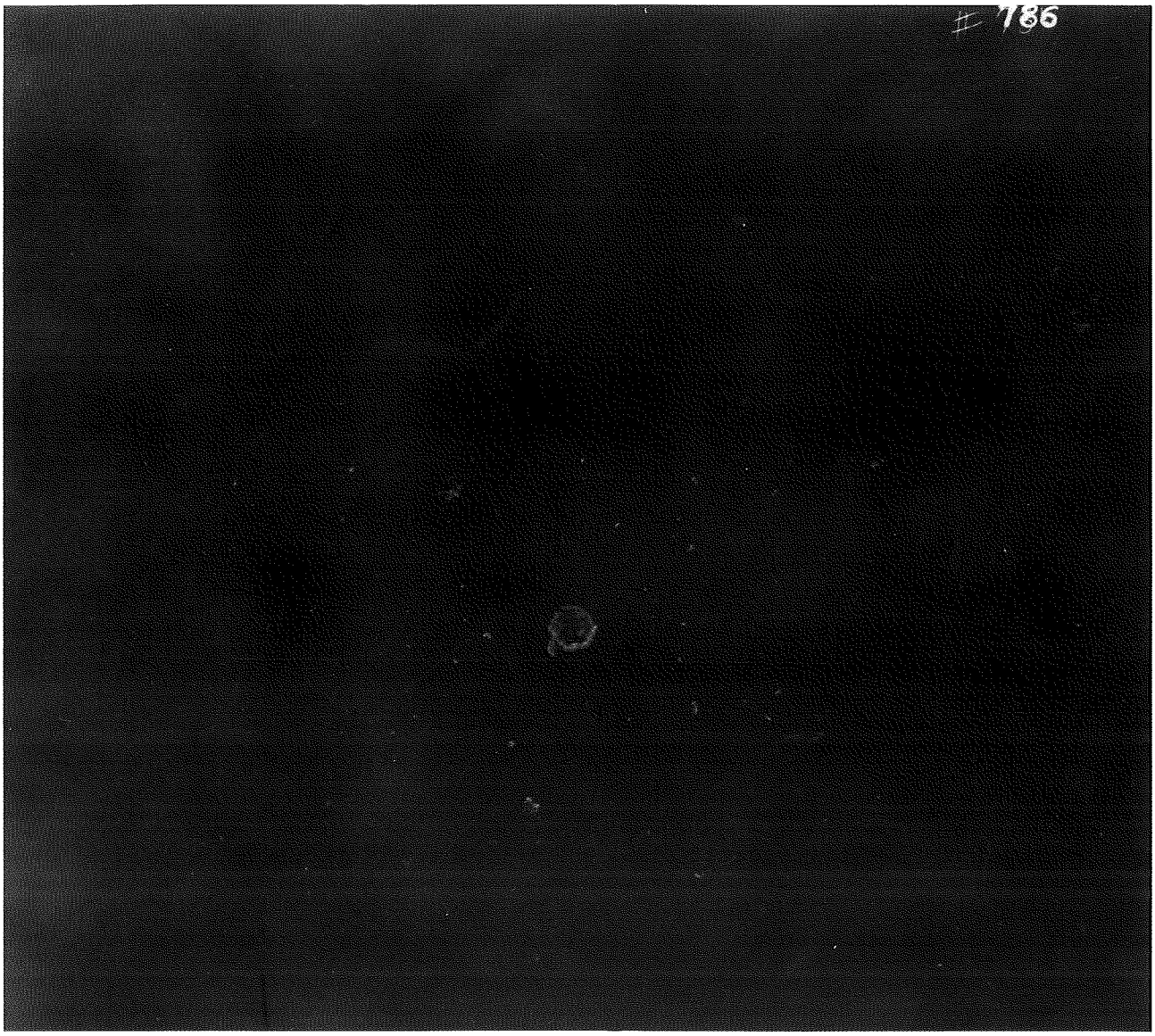

SHOT # 787

PROJECTILE: Soda Lime
D_p = 3175 μm
V = 5.81 km/s

TARGET: 1100
T = 8640 μm
D_p/T = 0.37

FRONT

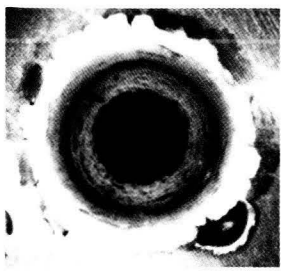

REAR

CROSS-SECTION

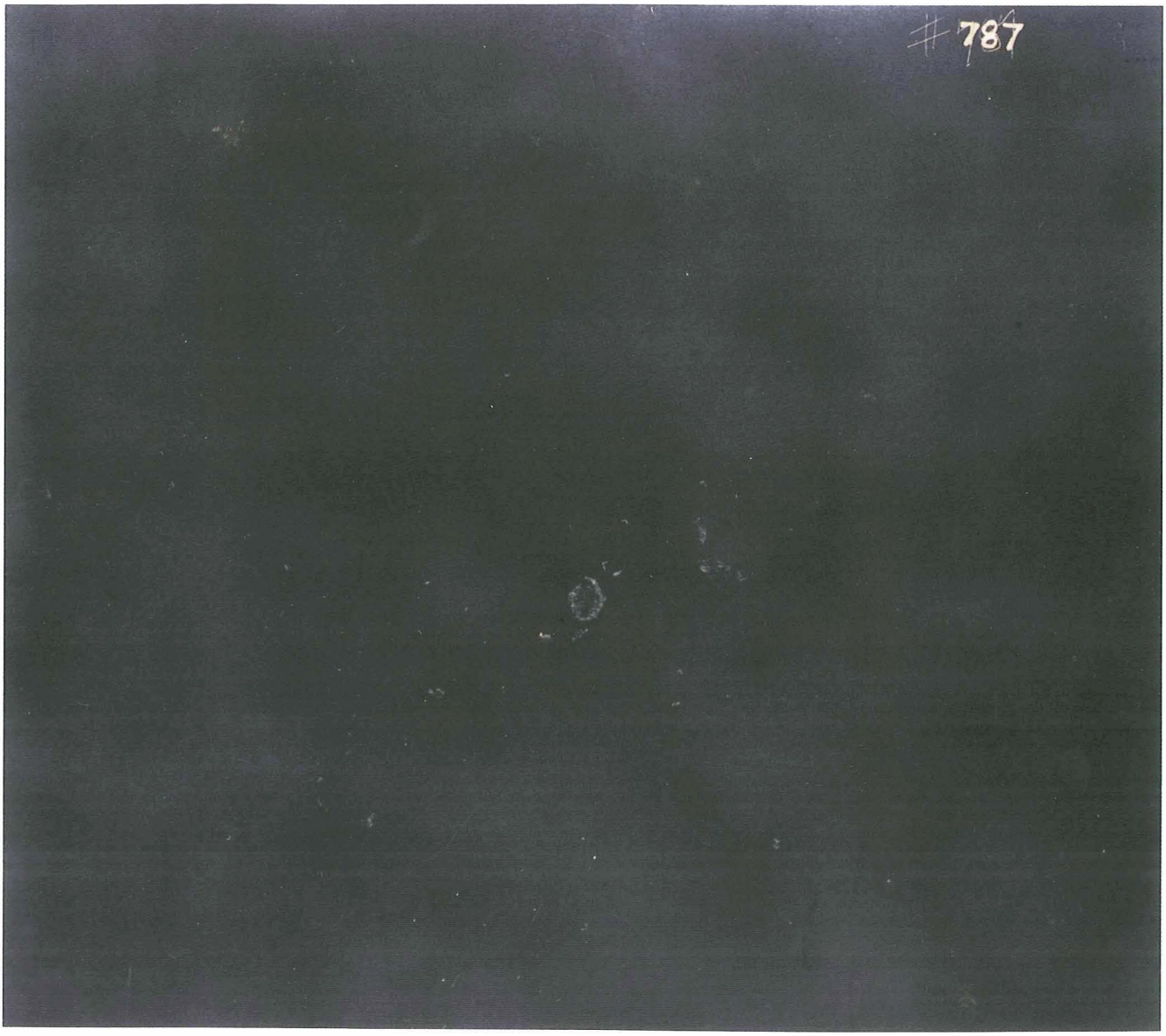
#787

SHOT # 788

PROJECTILE: Soda Lime
D_p = 3175 μm
V = 5.79 km/s

TARGET: 1100
T = 7620 μm
D_p/T = 0.42

FRONT

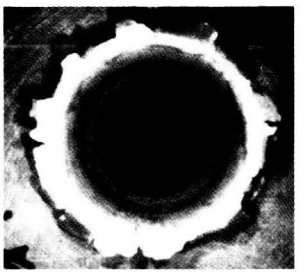

REAR

CROSS-SECTION

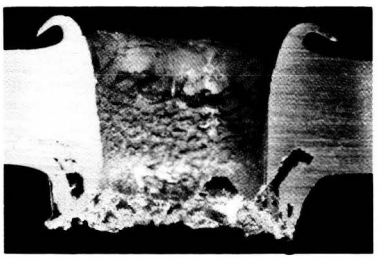

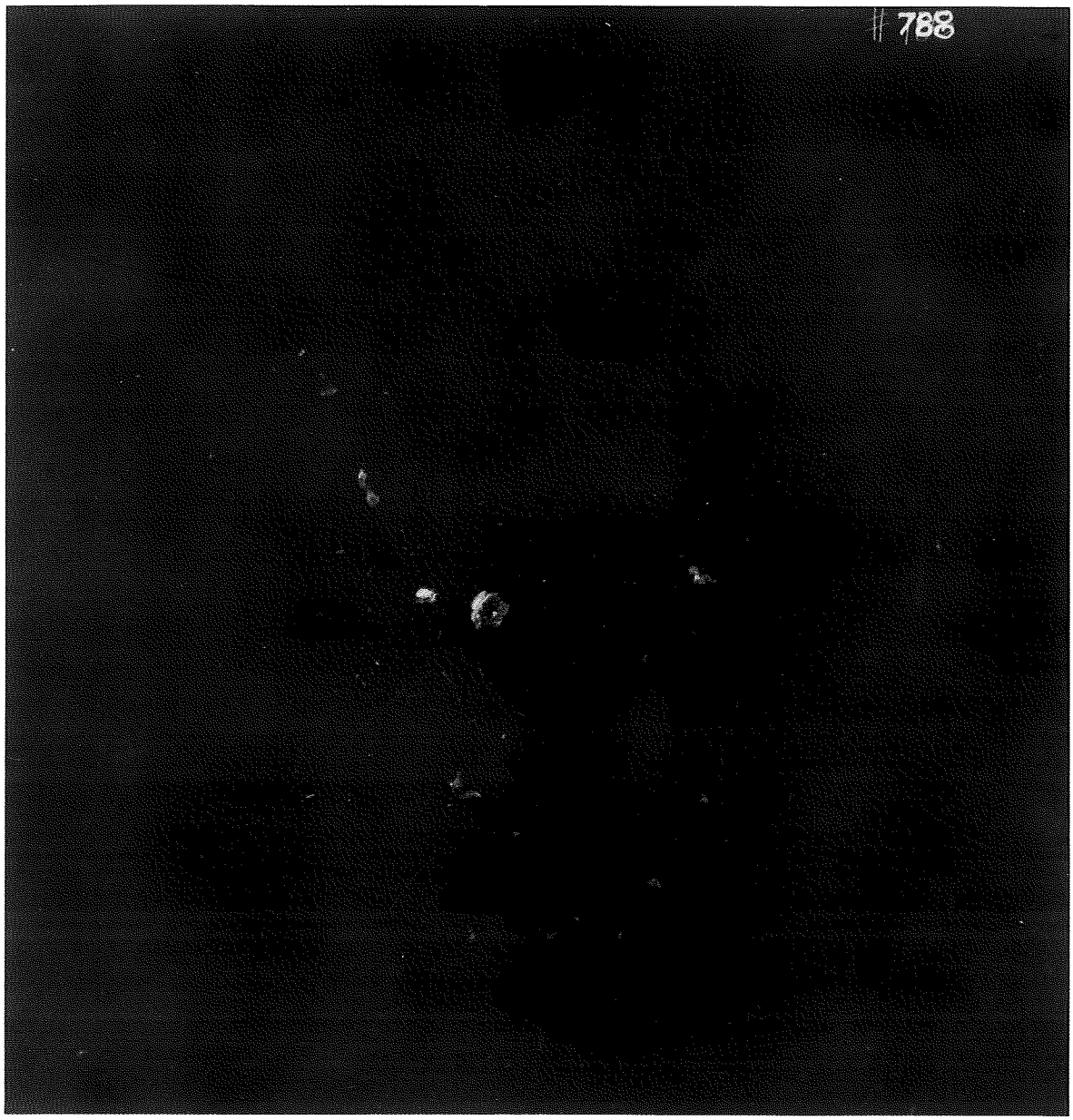
788

SHOT # 766

PROJECTILE: Soda Lime

D_p = 3175 µm

V = 5.60 km/s

TARGET: 1100

T = 6350 µm

D_p/T = 0.50

FRONT

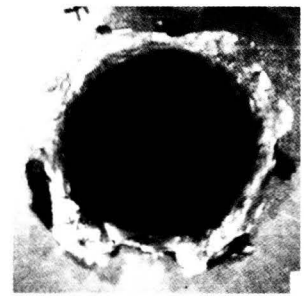

REAR

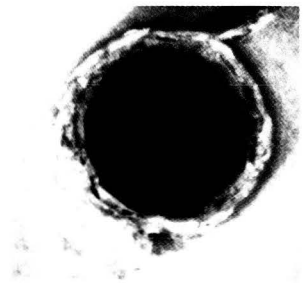

CROSS-SECTION

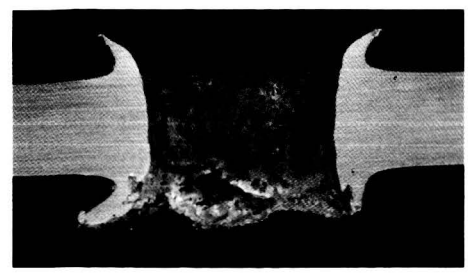


#766

SHOT # 765

PROJECTILE: Soda Lime
D_p = 3175 μm
V = 5.83 km/s

TARGET: 1100
T = 3175 μm
D_p/T = 1.00

FRONT

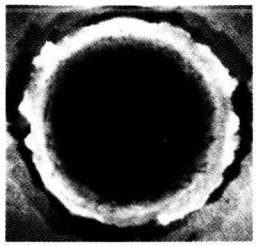

REAR

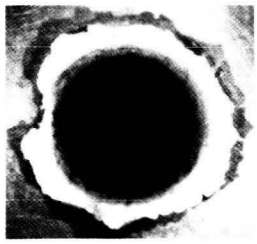

CROSS-SECTION

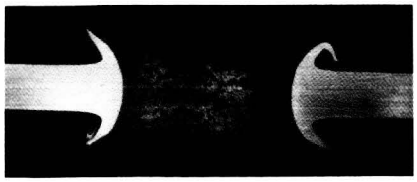

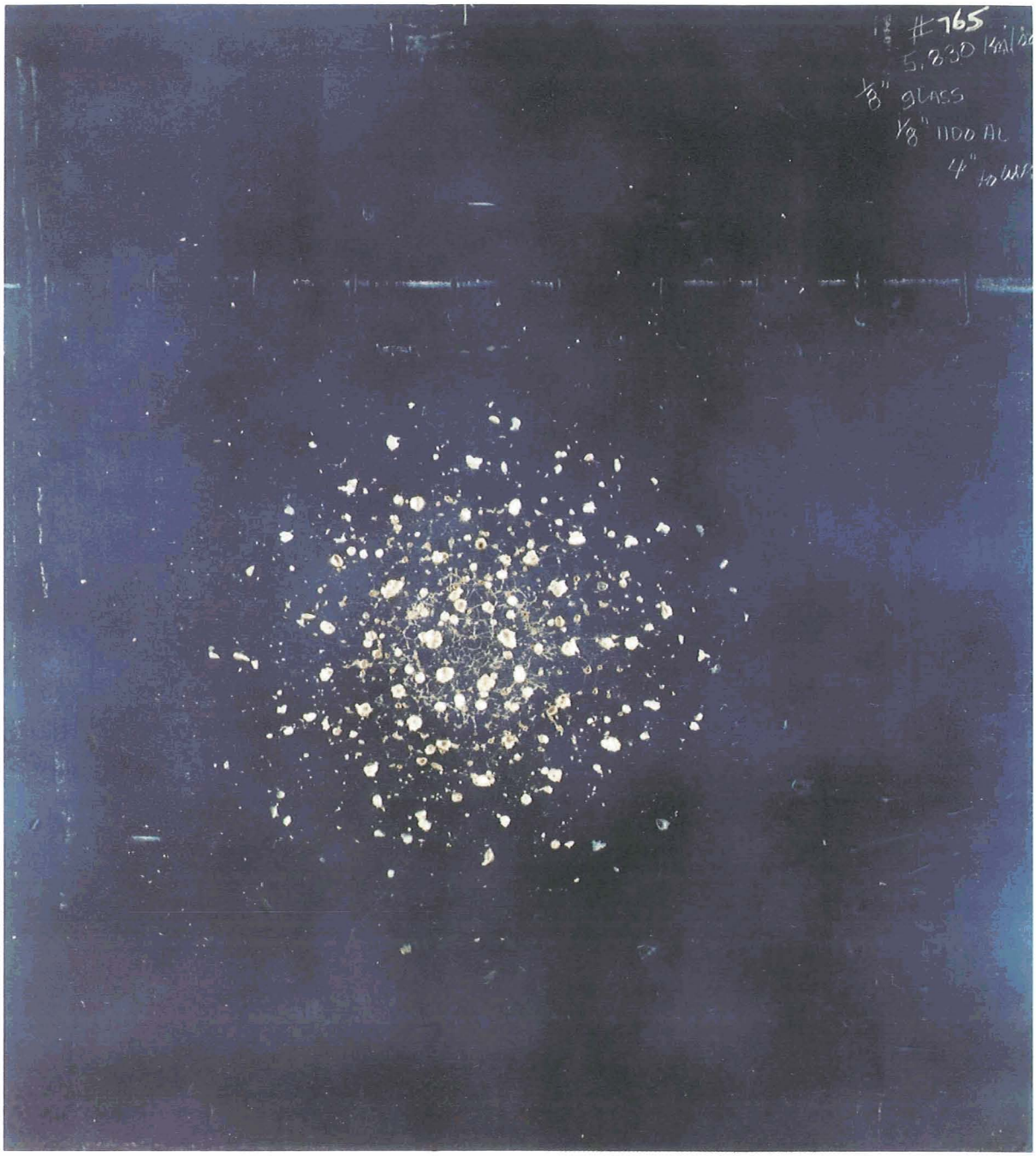
#765
5,830
1/8" GLASS
1/8" 1100 AL
4"

SHOT # 789

PROJECTILE: Soda Lime
D_p = 3175 μm
V = 5.87 km/s

TARGET: 1100
T = 1600 μm
D_p/T = 1.98

FRONT

REAR

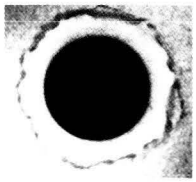

CROSS-SECTION

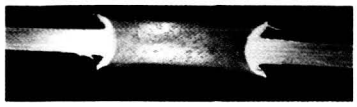


#789

SHOT # 793

PROJECTILE: Soda Lime

D_p = 3175 μm

V = 5.89 km/s

TARGET: 1100

T = 1600 μm

D_p/T = 1.98

FRONT

No Target Photographs

REAR

CROSS-SECTION

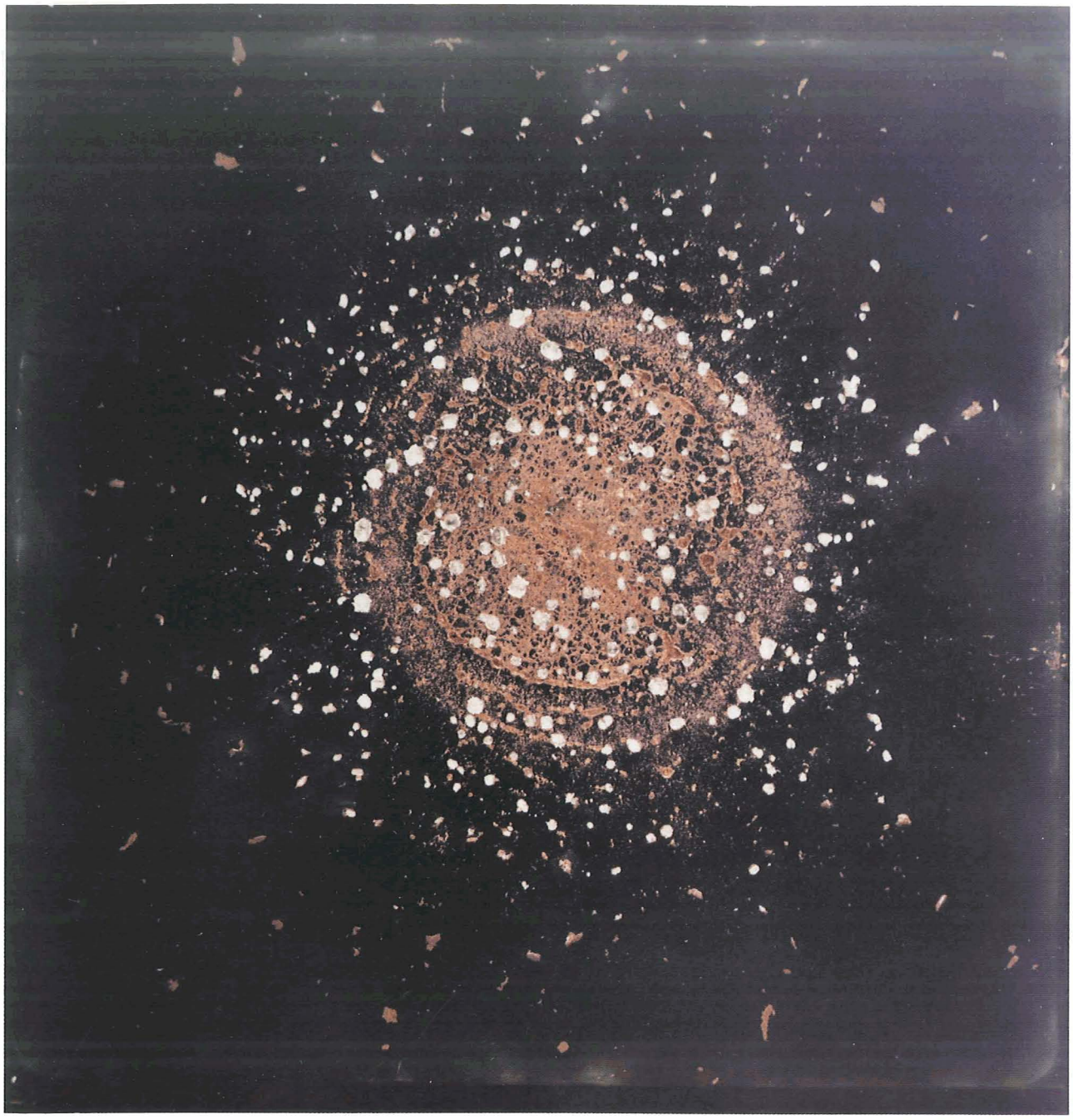

ONE CENTIMETER PER UNIT

SHOT # 794

PROJECTILE: Soda Lime

D_p = 3175 μm

V = 5.86 km/s

TARGET: 1100

T = 1325 μm

D_p/T = 2.40

FRONT

No Target Photographs

REAR

CROSS-SECTION

ONE CENTIMETER PER UNIT

SHOT # 795

PROJECTILE: Soda Lime

D_p = 3175 μm

V = 6.03 km/s

TARGET: 1100

T = 1055 μm

D_p/T = 3.01

FRONT

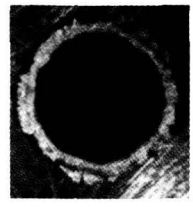

REAR

CROSS-SECTION

ONE CENTIMETER PER UNIT

SHOT # 790

PROJECTILE: Soda Lime

D_p = 3175 μm

V = 5.95 km/s

TARGET: 1100

T = 790 μm

D_p/T = 4.02

FRONT

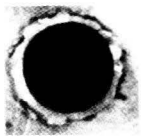

REAR

CROSS-SECTION

SHOT # 790

SHOT # 480

PROJECTILE: Soda Lime

D_p = 3175 μm

V = 5.90 km/s

TARGET: 1100

T = 305 μm

D_p/T = 10.41

FRONT

REAR

CROSS-SECTION

No Witness-Plate Photography

SHOT # 479

PROJECTILE: Soda Lime
D_p = 3175 µm
V = 6.10 km/s

TARGET: 1100
T = 204 µm
D_p/T = 15.56

FRONT

REAR

CROSS-SECTION

No Witness-Plate Photography

SHOT # 478

PROJECTILE: Soda Lime
D_p = 3175 μm
V = 6.10 km/s

TARGET: 1100
T = 102 μm
D_p/T = 31.13

FRONT

REAR

CROSS-SECTION

No Witness-Plate Photography

SHOT # 282

PROJECTILE: Soda Lime

D_p = 3175 μm

V = 6.13 km/s

TARGET: 1100

T = 38 μm

D_p/T = 83.55

FRONT

No Target Photographs

REAR

CROSS-SECTION

SHOT # 282

SHOT # 477

PROJECTILE: Soda Lime

D_p = 3175 μm

V = 6.10 km/s

TARGET: 1100

T = 38 μm

D_p/T = 83.55

FRONT

No Target Photographs

REAR

CROSS-SECTION

SHOT # 278

PROJECTILE: Bl. Gl.
D_p = 3175 μm
V = 5.69 km/s

TARGET: 1100
T = 20 μm
D_p/T = 156.25

FRONT

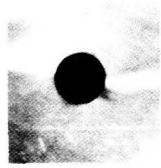

REAR

CROSS-SECTION

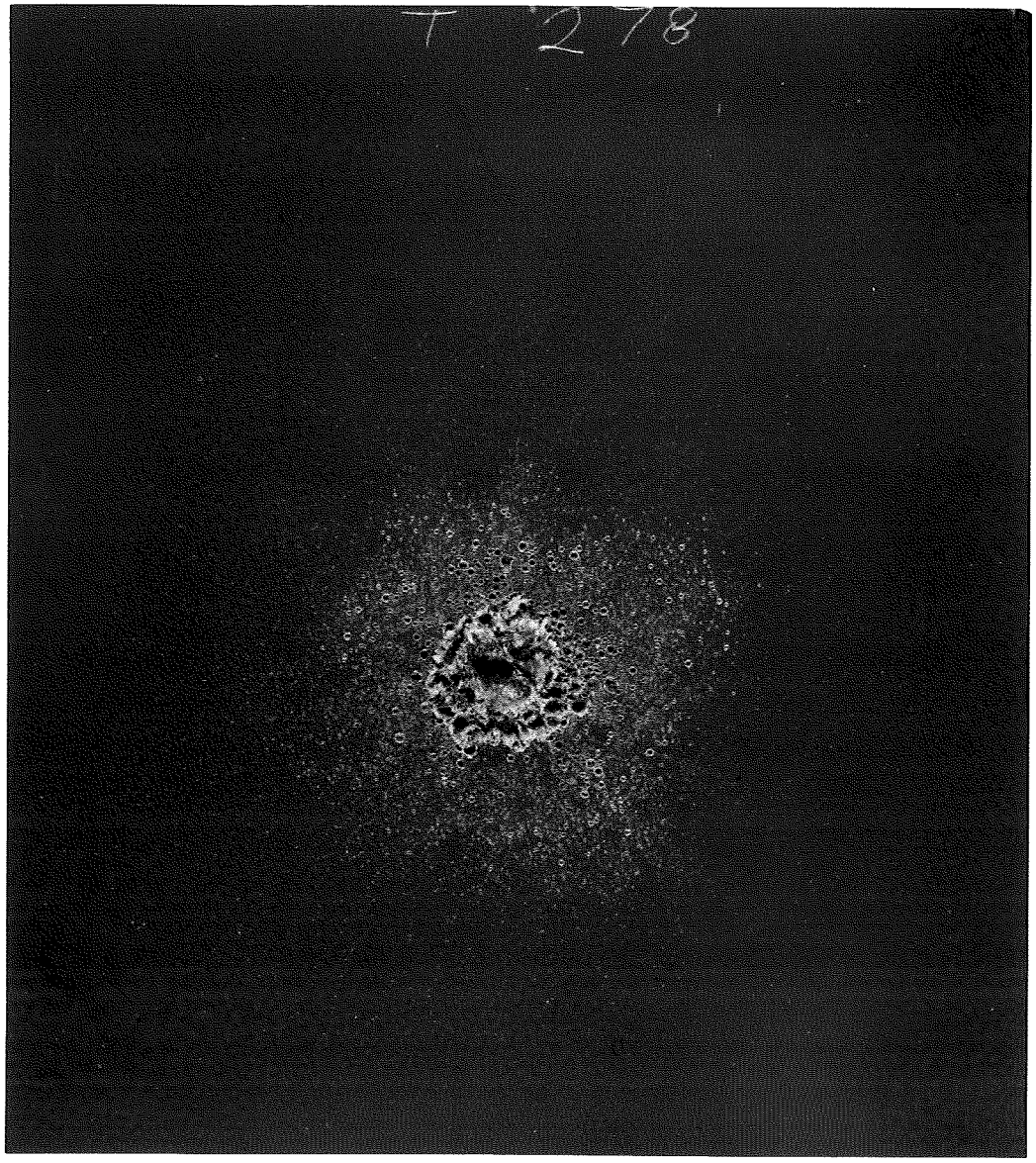
T 278

SHOT # 281

PROJECTILE: Black Glass

D_p = 3175 μm

V = 6.16 km/s

TARGET: 1100

T = 20 μm

D_p/T = 156.25

FRONT

No Target Photographs

REAR

CROSS-SECTION


T 281
281

SHOT # 894

PROJECTILE: Soda Lime

D_p = 3175 μm

V = 5.78 km/s

TARGET: 1100

T = 12 μm

D_p/T = 264.58

FRONT

No Target Photographs

REAR

CROSS-SECTION

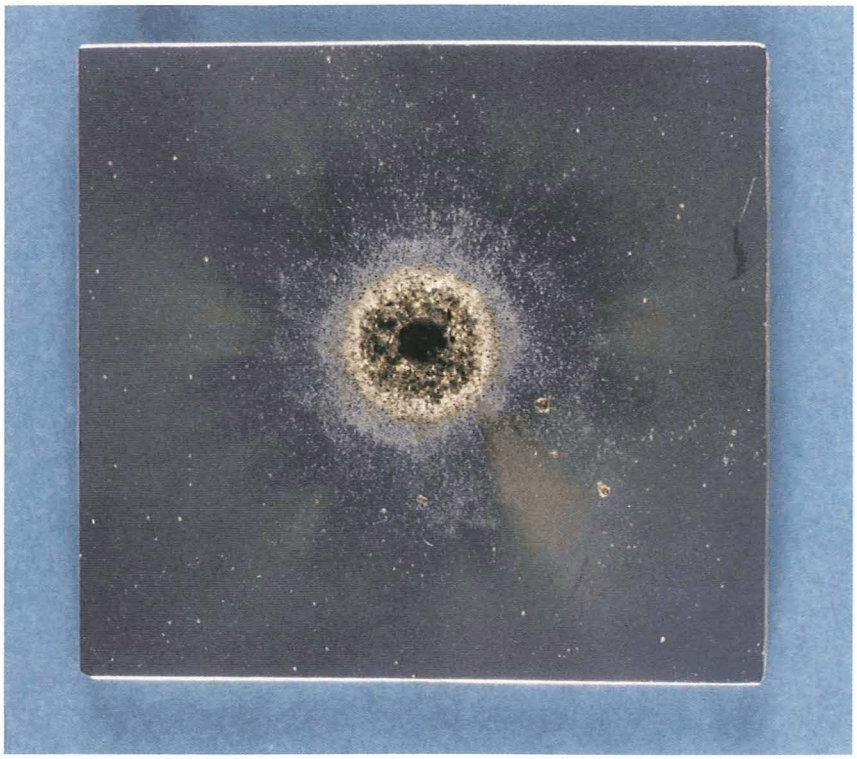

SHOT # 106

PROJECTILE: Soda Lime

D_p = 3175 μm

V = 6.96 km/s

TARGET: 1100

T = 37650 μm

D_p/T = 0.08

FRONT

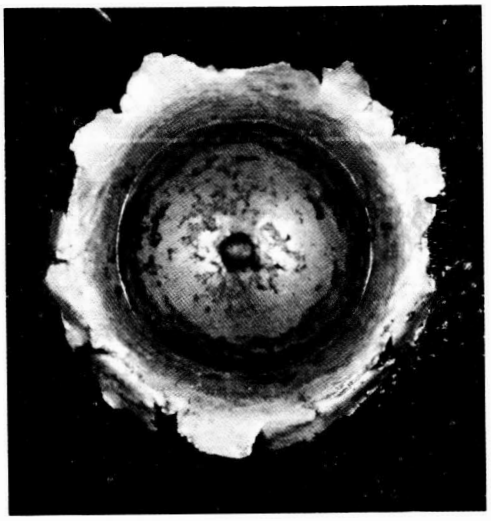

REAR

CROSS-SECTION

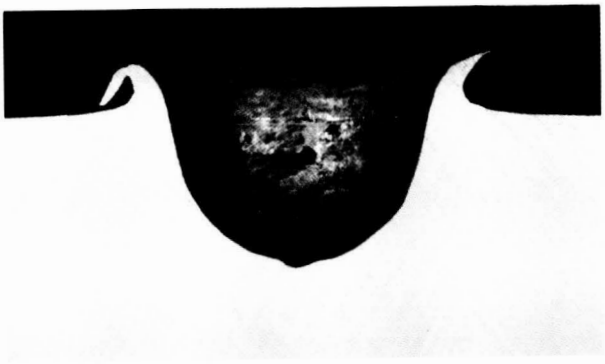

SHOT # 105

PROJECTILE: Soda Lime

D_p = 3175 μm

V = 6.83 km/s

TARGET: 1100

T = 19456 μm

D_p/T = 0.16

FRONT

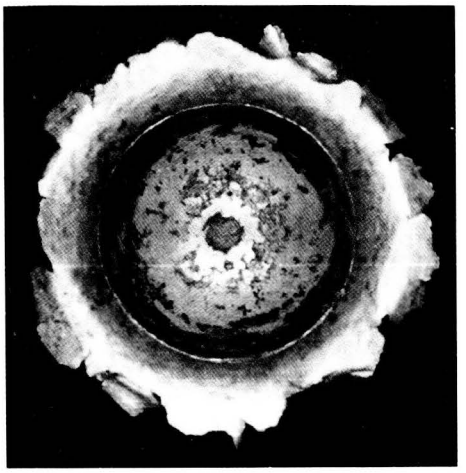

REAR

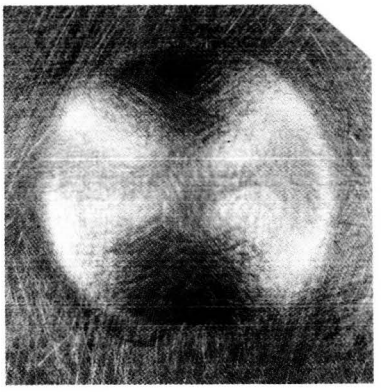

CROSS-SECTION

SHOT # 1168

PROJECTILE: Soda Lime
D_p = 3175 μm
V = 6.66 km/s

TARGET: 1100
T = 6406 μm
D_p/T = 0.50

FRONT

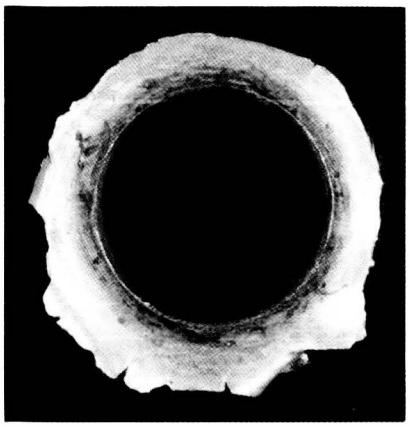

REAR

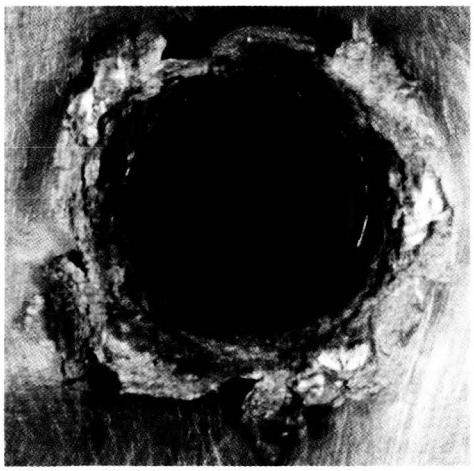

CROSS-SECTION

SHOT # 1168

SHOT # 1169

PROJECTILE: Soda Lime

D_p = 3175 μm

V = 6.64 km/s

TARGET: 1100

T = 3183 μm

D_p/T = 1.00

FRONT

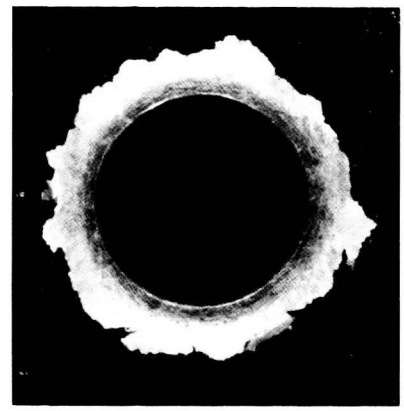

REAR

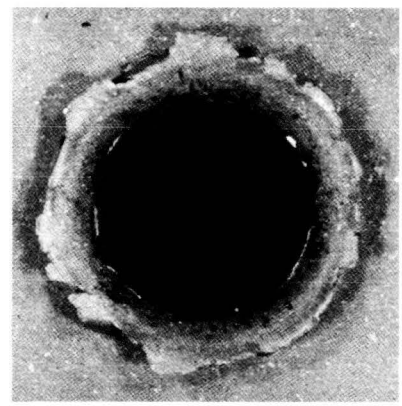

CROSS-SECTION

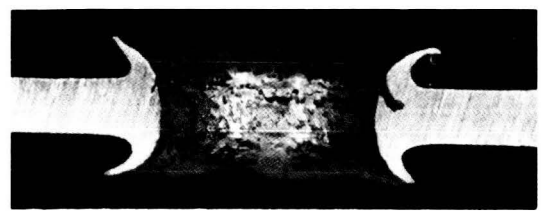

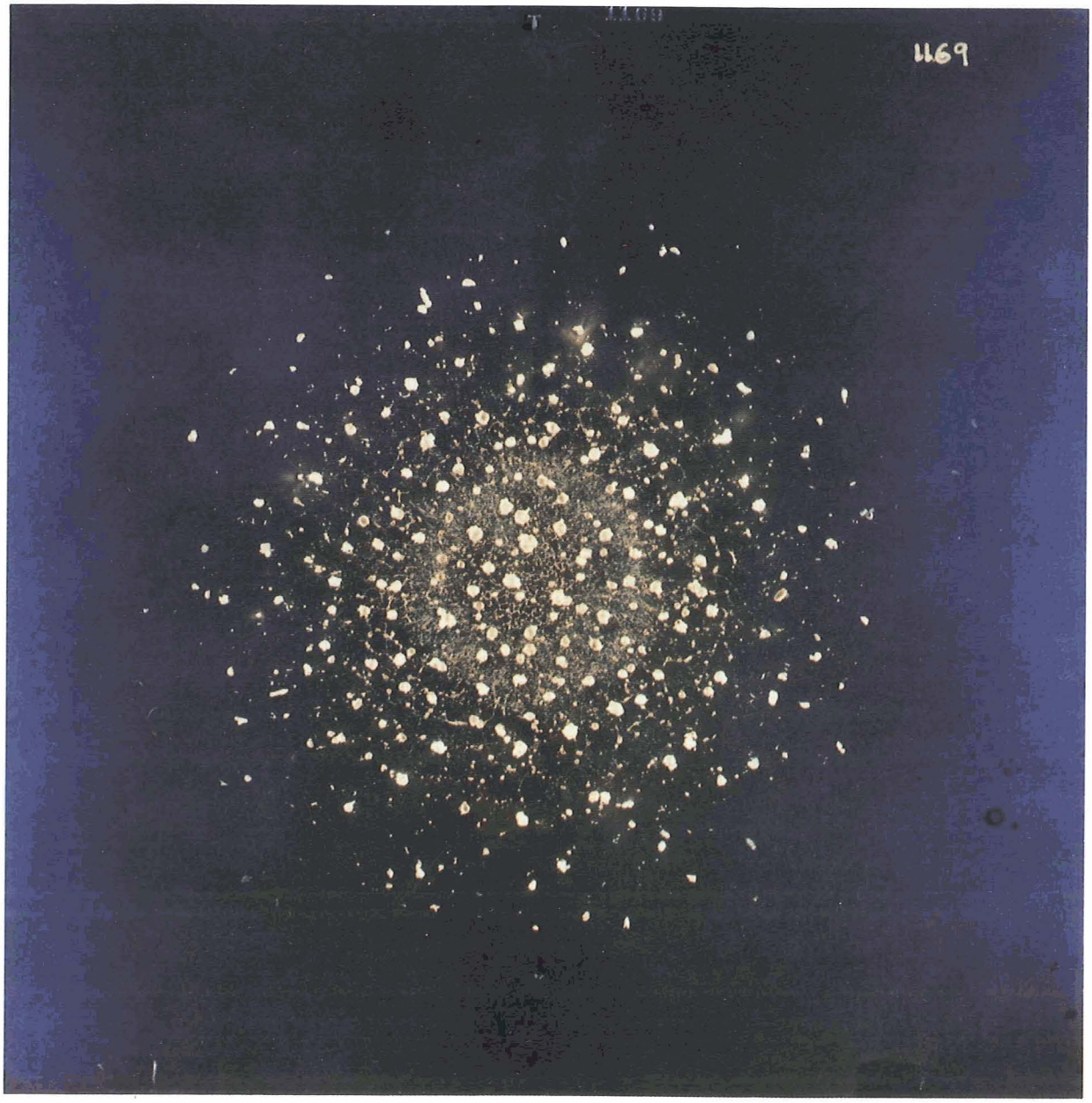
1169

SHOT # 1172

PROJECTILE: Soda Lime
D_p = 3175 μm
V = 6.52 km/s

TARGET: 1100
T = 1030 μm
D_p/T = 3.08

FRONT

REAR

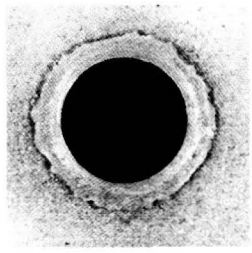

CROSS-SECTION

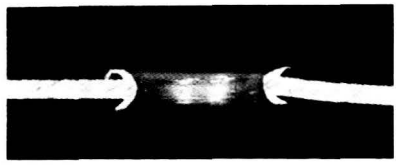


1172

SHOT # 299

PROJECTILE: Black Glass

D_p = 3175 μm

V = 6.81 km/s

TARGET: 1100

T = 37.5 μm

D_p/T = 84.67

FRONT

No Target Photographs

REAR

CROSS-SECTION

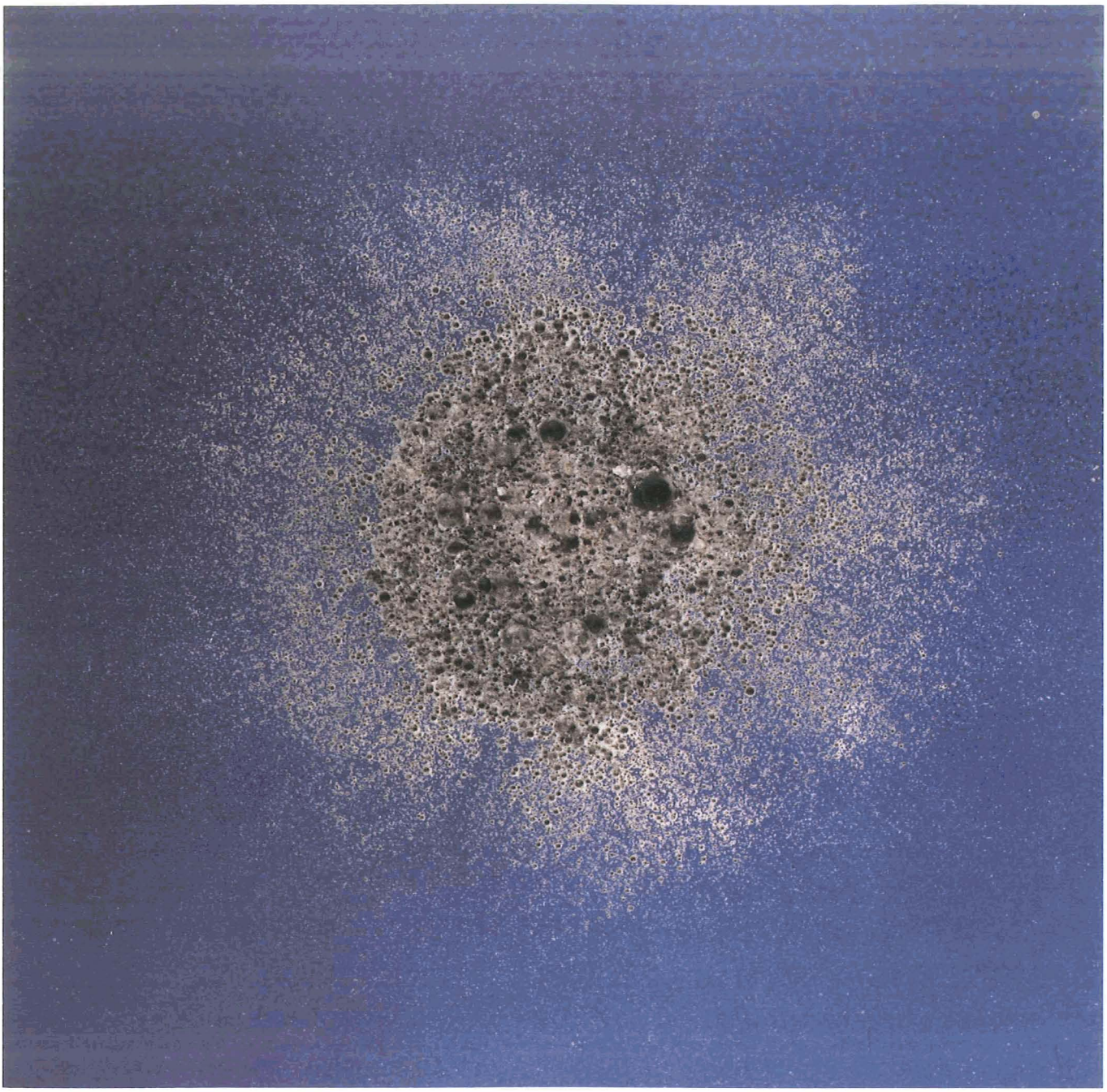

ONE CENTIMETER PER UNIT

Table 1. Initial impact conditions and first-order results cratering and penetration experiments using aluminum 1100 targets of variable thickness (T) and 3.2 mm diameter soda-lime projectiles (D_p). The cratering experiments are sorted by velocity, while the penetration experiments are arranged as a function of D_p/T for a given velocity.

SHOT #	Gun Range	Velocity (V; km/s)	Target Thickness (T; μm)	D_p/T	Crater Diameter (D_c; μm)	Rim Diameter (D_r; μm)	Lip Diameter (D_l; μm)	Hole Diameter (D_h; μm)	Rim Height (H_r; μm)	Crater Depth (P; μm)
					CRATERS					
3778	V	0.73	19500	0.16	3450					1990
3774	V	0.77	19500	0.16	3725					2275
3776	V	0.84	19500	0.16	4000					2450
3777	V	0.96	19500	0.16	4400					2775
3775	V	1.08	19500	0.16	4650					3100
3604	V	1.09	12545	0.25	4710	6000	7000		837	3320
3594	V	1.52	12471	0.25	6670	6800	8500		1171	4450
3593	V	1.88	9761	0.33	5920	7700	8800		1491	4410
3609	V	2.03	20455	0.16	6250	8400	9700		1610	4450
3610	V	2.18	24689	0.13	6740	8600	10500		1687	5140
3596	V	2.71	12621	0.25	7900	10500	12300		2127	5075
3605	V	2.74	25044	0.13	7850	10800	12500		1986	5438
3606	V	2.95	25017	0.13	8270	10900	13000		2199	5523
3607	V	3.03	24864	0.13	8540	11100	14100		2102	5807
1277	O	3.18	24359	0.13	9423	11345	14040		2199	5523
1279	O	3.45	32029	0.10	9703	11876	15748		2380	5138
1268	O	3.63	24536	0.13	9930	12470	15670		2480	5810
1278	O	3.92	24562	0.13	10864	13068	16235		2526	6262
1154	O	4.00	19125	0.17	10500	12900	15900		2520	6121
1252	O	4.17	22600	0.14	11200	13700	16700		2622	6141
1253	O	4.36	24700	0.13	11700	13755	17200		2780	6142
1266	O	4.44	37592	0.08	12085	14400	18155		2990	6178
1251	O	4.71	24600	0.13	12300	15700	19100		3000	6441
1149	O	5.16	19500	0.16	12700	16500	19100		3044	6804
1267	O	5.27	37643	0.08	13100	16400	20500		3168	6940
1248	O	5.37	24800	0.13	13200	15900	19500		3512	7108
792	O	5.69	25400	0.13	13000	17200	21550		3182	7472
1247	O	5.75	24800	0.13	13800	17000	20300		3317	7645
97	N	5.85	19660	0.16	13500	17300	21100		3804	7296
949	O	5.92	19500	0.16	13850	18300	22100		3356	7480
1249	O	6.03	24600	0.13	14300	17200	21300		3507	8050
1261	O	6.13	37643	0.08	14300	18100	21400		3607	8010
1250	O	6.30	24700	0.13	14600	17900	23000		3804	8238
1262	O	6.46	37668	0.08	14600	18800	22200		3658	8250
1297	O	6.79	37287	0.09	14986	19274	22713		3676	8575
106	N	6.96	37859	0.08	14800	18200	23000		3566	8605
1298	O	7.09	32338	0.10	15443	19515	23893		3865	8684
					~2.0 km/s Penetrations					
3612	V	1.97	19400	0.16	6300	7950	10000			
3613	V	1.94	6300	0.50	6400	7800	9600			
3614	V	1.99	4870	0.65	6600		9890	3600		
3617	V	1.98	3937	0.81	6985		9980	5518		
3615	V	1.98	3230	0.98	6300		9360	5330		
3625	V	2.05	2450	1.30	6248		9210	5580		
3624	V	2.04	1676	1.89	5740		8120	5260		
3616	V	1.99	990	3.21	6400		6980	4450		
3618	V	2.05	242	13.12			4180	3720		
3619	V	2.03	125	25.40				3450		
3620	V	1.99	25	127.00				3100		
3621	V	1.86	25	127.00				3200		
3622	V	2.04	25	127.00				3050		

Table 1. Experimental matrix and results (continued).

SHOT #	Gun Range	Velocity (V; km/s)	Target Thickness (T; μm)	D_p/T	Crater Diameter (D_c; μm)	Rim Diameter (D_r; μm)	Lip Diameter (D_l; μm)	Hole Diameter (D_h; μm)	Rim Height (H_r; μm)	Crater Depth (P; μm)
					~4.0 km/s Penetrations					
1154	O	3.99	19250	0.16	10480	12900	15900			
1152	O	4.34	9525	0.33	11200	14200	16200			
1185	O	3.90	6883	0.46	9500	12500	15400			
1187	O	4.02	6881	0.46	10600	14100	16900	4600		
1186	O	3.94	6550	0.48	10600	14000	17000	5800		
1184	O	3.96	6400	0.50	10500	13400	16300	5400		
1165	O	4.11	6250	0.51	10700	13900	17100	7500		
1153	O	4.00	3152	1.01	9600	11800	13700	8700		
1166	O	3.85	1000	3.18	6000	7600	8700	5000		
1163	O	3.97	125	25.40				3450		
					~5.0 km/s Penetrations					
1149	O	5.16	19500	0.16	12700	16500	19100			
1174	O	5.22	9800	0.32	12700	16900	19800			
1175	O	5.09	9746	0.33	12500	16100	19100			
1176	O	5.11	9300	0.34	12700	15900	18100			
1178	O	5.30	9050	0.35	12400	16600	19300			
1179	O	5.11	8842	0.36	12600	15900	19700			
1180	O	5.29	8534	0.37	12700	16700	18300	2700		
1160	O	5.14	6250	0.51	12000	15800	18700	10500		
1156	O	5.17	3175	1.00	10700	13700	15900	10100		
1159	O	5.16	1020	3.11	6900	8000	9400	5900		
1161	O	5.12	125	25.40						
					~5.9 km/s Penetrations					
792	O	5.69	25400	0.13	13000	17200	21550			
767	O	5.84	12500	0.25	13730	16600	20280			
791	O	5.84	10940	0.29	13730	15500	19310			
785	O	5.91	9525	0.33	13280	15460	19200	2240		
786	O	5.80	9020	0.35		15780	19400	3620		
787	O	5.81	8640	0.37		15910	19620	7310		
788	O	5.79	7620	0.42		16810	20310	10190		
766	O	5.60	6350	0.50		16550	20640	12400		
765	O	5.83	3175	1.00		14080	16570	11180		
789	O	5.87	1600	1.98		10860	12870	8760		
793	O	5.89	1600	1.98		10690	13010	8830		
794	O	5.86	1325	2.40		9280	11140	7360		
795	O	6.03	1055	3.01		8300	9970	6900		
790	O	5.95	790	4.02		8170	9470	6785		
480	O	5.90	305	10.41			5850	4500		
479	O	6.10	204	15.56			4850	4100		
478	O	6.10	102	31.13			3900	3425		
282	O	6.13	38	83.55				3280		
477	O	6.10	38	83.55				3280		
278	O	5.69	20	156.25				3350		
281	O	6.16	20	156.25				3215		
894	O	5.78	12	264.58				3300		
949	O	5.92	0.8	3968.75				3200		
947	O	5.82	0.8	3968.75				3277		

Table 1. Experimental matrix and results (continued).

SHOT #	Gun Range	Velocity (V; km/s)	Target Thickness (T; μm)	D_p/T	Crater Diameter (D_c; μm)	Rim Diameter (D_r; μm)	Lip Diameter (D_l; μm)	Hole Diameter (D_h; μm)	Rim Height (H_r; μm)	Crater Depth (P; μm)
					~6.7 km/s Penetrations					
106	N	6.96	37650	0.08	14800	18200	23000			
105	N	6.83	19456	0.16	14400	18150	24200			
1168	O	6.66	6406	0.50	14300	17900	20600	13300		
1169	O	6.64	3183	1.00	14200	15600	18500	13100		
1172	O	6.52	1030	3.08	7595	9271	10465	7366		
299	O	6.81	38	84.67						

Table 2. Numerical listing of all experiments and page numbers for assocaited photo documentation. NP = Not Photographed.

SHOT #	Purpose	D_p/T	Page
97	Crater @ ~5.9 km/s	0.16	A24
105	Crater @ ~6.5 km/s	0.16	A136
106	Crater @ ~7.0 km/s	0.08	A31 & A135
278	Penetration @ ~5.9 km/s	156.25	A128
281	Penetration @ ~5.9 km/s	156.25	A130
282	Penetration @ ~5.9 km/s	83.55	A124
299	Penetration @ 6.5 km/s	84.67	A144
477	Penetration @ ~5.9 km/s	83.55	A126
478	Penetration @ ~5.9 km/s	31.13	A122
479	Penetration @ ~5.9 km/s	15.56	A120
480	Penetration @ ~5.9 km/s	10.41	A118
765	Penetration @ ~5.9 km/s	1.00	A106
766	Penetration @ ~5.9 km/s	0.50	A104
767	Crater @ ~5.9 km/s	0.25	A94
785	Penetration @ ~5.9 km/s	0.33	A96
786	Penetration @ ~5.9 km/s	0.35	A98
787	Penetration @ ~5.9 km/s	0.37	A100
788	Penetration @ ~5.9 km/s	0.42	A102
789	Penetration @ ~5.9 km/s	1.98	A108
790	Penetration @ ~5.9 km/s	4.02	A116
791	Crater @ ~5.9 km/s	0.29	A95
792	Crater @ ~5.9 km/s	0.13	A22 & A93
793	Penetration @ ~5.9 km/s	1.98	A110
794	Penetration @ ~5.9 km/s	2.40	A112
795	Penetration @ ~5.9 km/s	3.01	A114
894	Penetration @ ~5.9 km/s	264.58	A132
947	Penetration @ ~5.9 km/s	3968.75	NP
949	Crater @ ~5.9 km/s	0.16	A25
1149	Crater @ ~5.0 km/s	0.16	A19 & A74
1152	Crater @ ~4.0 km/s	0.33	A57
1153	Penetration @ ~4.0 km/s	1.01	A68
1154	Crater @ ~4.0 km/s	0.16	A14 & A56
1156	Penetration @ ~5.0 km/s	1.00	A86
1159	Penetration @ ~5.0 km/s	3.11	A88
1160	Penetration @ ~5.0 km/s	0.51	A84
1161	Penetration @ ~5.0 km/s	25.40	A90
1163	Penetration @ ~4.0 km/s	25.40	A72
1165	Penetration @ ~4.0 km/s	0.51	A66
1166	Penetration @ ~4.0 km/s	3.18	A70
1168	Penetration @ 6.5 km/s	0.50	A138
1169	Penetration @ 6.5 km/s	1.00	A140
1172	Penetration @ 6.5 km/s	3.08	A142
1174	Crater @ ~5.0 km/s	0.32	A75
1175	Crater @ ~5.0 km/s	0.33	A76
1176	Crater @ ~5.0 km/s	0.34	A77
1178	Crater @ ~5.0 km/s	0.35	A78
1179	Crater @ ~5.0 km/s	0.36	A80
1180	Penetration @ ~5.0 km/s	0.37	A82
1184	Penetration @ ~4.0 km/s	0.50	A64
1185	Crater @ ~4.0 km/s	0.46	A58
1186	Penetration @ ~4.0 km/s	0.48	A62
1187	Penetration @ ~4.0 km/s	0.46	A60
1247	Crater @ ~5.8 km/s	0.13	A23
1248	Crater @ ~5.4 km/s	0.13	A21
1249	Crater @ ~5.9 km/s	0.13	A26
1250	Crater @ ~6.3 km/s	0.13	A28
1251	Crater @ ~4.7 km/s	0.13	A18
1252	Crater @ ~4.2 km/s	0.14	A15
1253	Crater @ ~4.4 km/s	0.13	A16
1261	Crater @ ~6.1 km/s	0.08	A27
1262	Crater @ ~6.5 km/s	0.08	A29
1266	Crater @ ~4.4 km/s	0.08	A17
1267	Crater @ ~5.3 km/s	0.08	A20
1268	Crater @ ~3.6 km/s	0.13	A12
1277	Crater @ ~3.2 km/s	0.13	A10
1278	Crater @ ~3.9 km/s	0.13	A13
1279	Crater @ ~3.5 km/s	0.10	A11
1297	Crater @ ~6.8 km/s	0.09	A30
1298	Crater @ ~7.1 km/s	0.10	A32
3593	Crater @ ~1.9 km/s	0.33	A3
3594	Crater @ ~1.5 km/s	0.25	A2
3596	Crater @ ~2.7 km/s	0.25	A6
3604	Crater @ ~1.1 km/s	0.25	A1
3605	Crater @ ~2.7 km/s	0.13	A7
3606	Crater @ ~3.0 km/s	0.13	A8
3607	Crater @ ~3.0 km/s	0.13	A9
3609	Crater @ ~2.0 km/s	0.16	A4
3610	Crater @ ~2.2 km/s	0.13	A5
3612	Crater @ ~2.0 km/s	0.16	A33
3613	Crater @ ~2.0 km/s	0.50	A34
3614	Penetration @ ~2.0 km/s	0.65	A35
3615	Penetration @ ~2.0 km/s	0.98	A38
3616	Penetration @ ~2.0 km/s	3.21	A44
3617	Penetration @ ~2.0 km/s	0.81	A36
3618	Penetration @ ~2.0 km/s	13.12	A46
3619	Penetration @ ~2.0 km/s	25.40	A48
3620	Penetration @ ~2.0 km/s	127.00	A50
3621	Penetration @ ~2.0 km/s	127.00	A52
3622	Penetration @ ~2.0 km/s	127.00	A54
3624	Penetration @ ~2.0 km/s	1.89	A42
3625	Penetration @ ~2.0 km/s	1.30	A40
3774	Crater @ ~0.8 km/s	0.16	NP
3775	Crater @ ~1.1 km/s	0.16	NP
3776	Crater @ ~0.8 km/s	0.16	NP
3777	Crater @ ~1.0 km/s	0.16	NP
3778	Crater @ ~0.7 km/s	0.16	NP

REPORT DOCUMENTATION PAGE

Form Approved
OMB No. 0704-0188

1. AGENCY USE ONLY (Leave Blank)	2. REPORT DATE	3. REPORT TYPE AND DATES COVERED
	June 1995	Technical Memorandum

4. TITLE AND SUBTITLE

Penetration Experiments in Aluminum 1100 Targets Using Soda-Lime Glass Projectiles

5. FUNDING NUMBERS

6. AUTHOR(S)

Friedrich Horz, Mark J. Cintala, Ronald P. Bernhard*, Frank Cardenas*, William E. Davidson*, Gerald Haynes*, Thomas H. See*, Jerry L. Winkler*

7. PERFORMING ORGANIZATION NAME(S) AND ADDRESS(ES)

Lyndon B. Johnson Space Center
Earth Science and Solar System Exploration Division
Houston, TX 77058

8. PERFORMING ORGANIZATION REPORT NUMBERS

S-801

9. SPONSORING/MONITORING AGENCY NAME(S) AND ADDRESS(ES)

National Aeronautics and Space Administration
Washington, D.C. 20546-0001

10. SPONSORING/MONITORING AGENCY REPORT NUMBER

TM-104813

11. SUPPLEMENTARY NOTES

*Lockheed Engineering and Sciences Company
Houston, TX 77058

12a. DISTRIBUTION/AVAILABILITY STATEMENT

Unclassified/Unlimited
Available from the NASA Center for AeroSpace Information (CASI)
800 Elkridge Landing Road
Linthicum Heights, MD 21090-2934
(301) 621-0390 Subject Category: 18

12b. DISTRIBUTION CODE

13. ABSTRACT *(Maximum 200 words)*

The cratering and penetration behavior of annealed aluminum 1100 targets, with thickness varied from several centimeters to ultra-thin foils < 1 micrometer thick, were experimentally investigated using 3.2 mm diameter spherical soda-lime glass projectiles at velocities from 1 to 7 km/s. The objective was to establish quantitative, dimensional relationships between initial impact conditions (impact velocity, projectile diameter, and target thickness and the diameter of the resulting crater or penetration hole). Such dimensional relationships and calibration experiments are needed to extract the diameters and fluxes of hypervelocity particles from space-exposed surfaces and to predict the performance of certain collisional shields. The cratering behavior of aluminum 1100 is fairly well predicted. However, crater depth is modestly deeper for our silicate impactors than the canonical value based on aluminum projectiles and aluminum 6061-T6 targets. The ballistic-limit thickness was also different. These differences attest to the great sensitivity of detailed crater geometry and penetration behavior on the physical properties of both the target and impactor. Each penetration experiment was equipped with a witness plate to monitor the nature of the debris plume emanating from the rear of the target. This plume consists of both projectile fragments and target debris. Both penetration hole and witness-plate spray patterns systematically evolve in response to projectile diameter/target thickness. The relative dimensions of the projectile and target totally dominate the experimental products documented in this report; impact velocity is an important contributor as well to the evolution of penetration holes, but is of subordinate significance for the witness-plate spray patterns.

14. SUBJECT TERMS

terminal ballistics, hypervelocity, space debris

15. NUMBER OF PAGES
328

16. PRICE CODE

17. SECURITY CLASSIFICATION OF REPORT	18. SECURITY CLASSIFICATION OF THIS PAGE	19. SECURITY CLASSIFICATION OF ABSTRACT	20. LIMITATION OF ABSTRACT
Unclassified	Unclassified	Unclassified	Unlimited